

**Characterization of NMR Interactions in Solids  
by Direct and Indirect Observation  
of Quadrupolar Nuclei**

by

DALMSS  
CHEM.  
S394  
1998

Robert W. Schurko

Submitted in partial fulfilment of the requirements  
for the degree of Doctor of Philosophy

at

Dalhousie University  
Halifax, Nova Scotia, Canada  
August 1998

© Copyright by Robert W. Schurko, 1998

**DALHOUSIE UNIVERSITY**

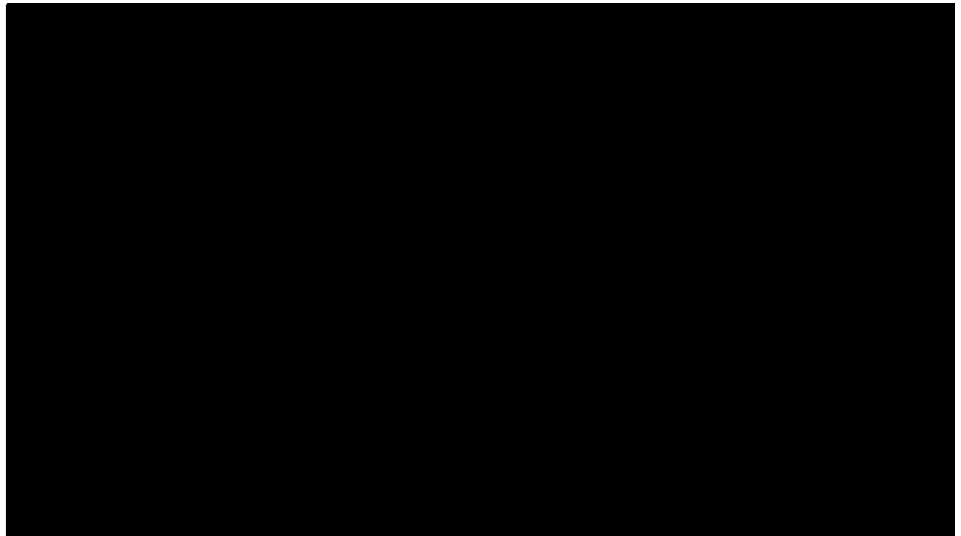
**FACULTY OF GRADUATE STUDIES**

The undersigned hereby certify that they have read and recommend to the Faculty of Graduate Studies for acceptance a thesis entitled "Characterization of NMR Interactions in Solids by Direct and Indirect Observation of Quadrupolar Nuclei"

by Robert W. Schurko

in partial fulfillment of the requirements for the degree of Doctor of Philosophy.

Dated: August 17, 1998



DALHOUSIE UNIVERSITY

DATE: August 19, 1998

AUTHOR: Robert W. Schurko

TITLE: "Characterization of NMR Interactions in Solids by  
Direct and Indirect Observation of Quadrupolar  
Nuclei"

DEPARTMENT OR SCHOOL: Department of Chemistry

DEGREE: Ph.D. CONVOCATION: October YEAR: 1998

Permission is herewith granted to Dalhousie University to circulate and to have copied for non-commercial purposes, at its discretion, the above title upon the request of individuals or institutions.

  
Signature of Author

The author reserves other publication rights, and neither the thesis nor extensive extracts from it may be printed or otherwise reproduced without the author's written permission.

The author attests that permission has been obtained for the use of any copyrighted material appearing in this thesis (other than brief excerpts requiring only proper acknowledgment in scholarly writing), and that all such use is clearly acknowledged.

*To my parents*

*Vitanda est improba siren desidia* (Horace)

## Table of Contents

Table of Contents .....	v
List of Figures .....	viii
List of Tables .....	xiii
Abstract .....	xiv
Lists of Symbols, Abbreviations and Compounds .....	xv
Acknowledgments .....	xxii
<b>Chapter 1</b>	
<b>An Introduction to Solid-State NMR</b> .....	1
1.1 Prologue .....	1
1.2 A Brief History of Nuclear Magnetic Resonance .....	3
1.3 Advances in Solid-State Nuclear Magnetic Resonance .....	5
1.4 Thesis Overview .....	7
<b>Chapter 2</b>	
<b>Basic Principles and Techniques in Solid-State NMR</b> .....	10
2.1 Introduction .....	10
2.2 NMR Interactions .....	12
2.2.1 The Zeeman Interaction .....	12
2.2.2 The Radiofrequency Hamiltonian .....	15
2.2.3 The Chemical Shielding Interaction .....	16
2.2.4 The Direct Dipolar Interaction .....	23
2.2.5 Indirect Spin-Spin Interactions .....	26
2.3 The Quadrupolar Interaction .....	27
2.3.1. The Quadrupolar Nucleus .....	27
2.3.2 The Nuclear Quadrupole Moment .....	28
2.3.3 The Electric Field Gradient .....	29
2.3.4 The Nuclear Quadrupole Interaction .....	30
2.3.5 Quadrupolar Nuclei in Magnetic Fields .....	32
2.4 Techniques in Solid-State Nuclear Magnetic Resonance .....	36
2.4.1 Magic-Angle Spinning .....	36
2.4.2 High-Power Decoupling .....	37
2.4.3 Cross Polarization .....	38
2.4.4. Solid-State NMR of Quadrupolar Nuclei - Practical Considerations .....	41
2.5 <i>Ab Initio</i> Calculations of Chemical Shielding Parameters .....	43

## Chapter 3

<b>Aluminum Chemical Shielding Anisotropy</b> .....	47
3.1 Introduction .....	47
3.2 Experimental .....	51
3.2.1. Solid-State $^{27}\text{Al}$ NMR of $\text{Cl}_3\text{AlOPCl}_3$ .....	51
3.2.2. Solid-State $^{27}\text{Al}$ NMR of Octahedral Aluminum Complexes .....	52
3.2.3. Theoretical Calculations .....	52
3.3 Characterization of Interaction Tensors by Solid-State $^{27}\text{Al}$ NMR and <i>Ab Initio</i> Techniques .....	54
3.3.1 Aluminum-27 MAS NMR .....	54
3.3.2 Solid-State Aluminum-27 NMR of Stationary Samples .....	59
3.3.3 <i>Ab Initio</i> Calculations of CS and EFG Tensors .....	74
3.4 Aluminum-27 Chemical Shielding Anisotropy in Linear Molecules ...	83
3.4.1 Theoretical Background .....	83
3.4.2 Results and Discussion .....	88
3.5 Rovibrational Corrections for Aluminum Chemical Shielding of $\text{AlCl}_3$ .....	94
3.6 Conclusions .....	96

## Chapter 4

<b>Solid-State Phosphorus-31 NMR Study of Cobaloximes</b> .....	98
4.1 Introduction .....	98
4.2 Experimental .....	101
4.3 Background .....	103
4.3.1 Cobaloximes .....	103
4.3.2 MAS NMR Spectra of Spin-1/2 Nuclei Coupled to Quadrupolar Nuclei .....	106
4.4 Results and Discussion .....	120
4.4.1 Introduction .....	120
4.4.2 Well-Characterized Cobaloximes .....	121
4.4.3 Cobaloximes for which Quadrupolar Data are Unknown ..	127
4.4.4 Temperature-Dependent Self-Decoupling of Cobalt .....	142
4.5 Conclusions .....	148

## Chapter 5

<b>Solid-State Nitrogen-15 NMR Study of Cobaloximes with <math>^{15}\text{N}</math>-labelled Pyridine and Aniline as Axial Ligands</b> .....	150
5.1 Introduction .....	150
5.2 Experimental .....	153
5.3 Theoretical Background .....	155
5.3.1 Negative Magnetogyric Ratios and Residual Dipolar Coupling .....	155
5.3.2 The Dipolar Chemical Shift Method .....	157
5.4 Nitrogen-15 CPMAS NMR Spectra of the Cobaloximes .....	160
5.4.1 $^{15}\text{N}$ -py* $\text{Co}(\text{DH})_2\text{Cl}$ (I) .....	160

5.4.2.	$^{15}\text{N}$ -anil*Co(DH) <sub>2</sub> Cl (II)	163
5.4.3	$^{15}\text{N}$ -py*Co(DH) <sub>2</sub> CH <sub>3</sub> (III)	166
5.4.4	$^{15}\text{N}$ -py*Co(DH) <sub>2</sub> Br (IV)	169
5.5	Analysis of $^{15}\text{N}$ NMR Spectra of Stationary Samples - Application of the Dipolar Chemical Shift Method to $^{59}\text{Co}$ , $^{15}\text{N}$ spin pairs	170
5.5.1	$^{15}\text{N}$ NMR of stationary samples of py*Co(DH) <sub>2</sub> Cl (I)	170
5.5.2	$^{15}\text{N}$ NMR of stationary samples of anil*Co(DH) <sub>2</sub> Cl (II)	176
5.5.3.	$^{15}\text{N}$ NMR of stationary samples of py*Co(DH) <sub>2</sub> CH <sub>3</sub> (III)	177
5.5.4.	$^{15}\text{N}$ NMR of stationary samples of py*Co(DH) <sub>2</sub> Br (IV)	179
5.6	<i>Ab initio</i> Chemical Shielding Calculations	180
5.7	Conclusions	191
<b>Chapter 6</b>		
	<b>Ongoing Projects and Future Work</b>	194
6.1	Aluminum and Gallium Chemical Shielding Anisotropy	194
6.2	Solid-State $^{31}\text{P}$ NMR Investigations of $^{31}\text{P}$ , $^{59}\text{Co}$ Spin Pairs	197
6.3	Characterization of the Nitrogen Chemical Shift Tensor in Aniline	199
<b>Chapter 7</b>		
	<b>Concluding Remarks</b>	200
<b>Appendix A</b>		
	<b>Characterization of the Phosphorus Chemical Shielding Tensor in Cl<sub>3</sub>AlOPCl<sub>3</sub></b>	202
<b>Appendix B</b>		
	<b>Solid-State Carbon-13 and Cobalt-59 NMR of Cobaloximes</b>	206
	<b>References</b>	211

## List of Figures

- Figure 2.1:** Schematic representation of the Zeeman interaction . . . . . 13
- Figure 2.2:** (A) The chemical shielding tensor represented as an ellipsoid, oriented in the Zeeman frame. (B) Simplified diagram illustrating the orientation of the chemical shielding tensor with respect to the magnetic field, as defined by polar angles  $\vartheta$  and  $\varphi$  . . . . . 18
- Figure 2.3:** Solid-state NMR spectra exhibiting chemical shielding anisotropy. (A) Non-axial CSA,  $\kappa = +0.3$ . (B) Axial CSA,  $\kappa = +1.0$ . (C) Axial CSA,  $\kappa = -1.0$  . . . . . 20
- Figure 2.4:** Comparison of the absolute chemical shielding and chemical shift scales for phosphorus. . . . . 23
- Figure 2.5:** Ellipsoidal shapes of nuclear charge distributions for prolate ( $Q > 0$ ) and oblate ( $Q < 0$ ) nuclear quadrupole moments. . . . . 29
- Figure 2.6:** Effects of the first- and second-order quadrupolar interaction on a nucleus with  $S = 5/2$  . . . . . 33
- Figure 2.7:** NMR spectra of a quadrupolar nucleus,  $S = 5/2$ , in a stationary sample, with small nuclear quadrupolar interaction (A.), and with a large nuclear quadrupolar interaction (B) . . . . . 35
- Figure 2.8:** (A)  $^{31}\text{P}$  NMR spectrum of a stationary sample of (2,4,6-tri-*t*-butylphenyl)-P=N-OSO<sub>2</sub>CF<sub>3</sub> at 4.7 T. (B) Overlaid  $^{31}\text{P}$  CPMAS NMR spectra at  $\nu_{\text{rot}} = 3010$  Hz and  $\nu_{\text{rot}} = 3405$  Hz . . . . . 37
- Figure 2.9:** Pulse sequence for cross polarization in the solid state. . . . . 39
- Figure 2.10:** Schematic diagram of Zeeman states in (A) the laboratory frame and (B) in the rf rotating frame, where cross polarization can occur. . . . 40
- Figure 3.1:** Complexes exhibiting aluminum chemical shielding anisotropy . . . 49
- Figure 3.2:** Solid-state  $^{27}\text{Al}$  MAS NMR spectrum of the central transition of Cl<sub>3</sub>AlOPCl<sub>3</sub> obtained at 9.4 T with spinning speed  $\nu_{\text{rot}} = 8$  kHz (bottom trace). Simulated  $^{27}\text{Al}$  MAS NMR spectrum (top trace) . . . . 55
- Figure 3.3:** Experimental and calculated  $^{27}\text{Al}$  MAS NMR spectra of the central transitions ( $+1/2 \leftrightarrow -1/2$ ) of (A) Al(acac)<sub>3</sub>,  $\nu_{\text{rot}} = 7853$  Hz, and (B) Al(trop)<sub>3</sub>,  $\nu_{\text{rot}} = 9955$  Hz, acquired at 9.4 T. . . . . 58

<b>Figure 3.4:</b>	(A) Euler angles describing the relative orientations of the EFG ( $\theta, \phi$ ) and CS ( $\vartheta, \varphi$ ) tensors with respect to the external magnetic field. (B) Euler angles $\alpha, \beta$ and $\gamma$ which define the orientation of the CS tensor in the EFG PAS. ....	60
<b>Figure 3.5:</b>	Experimental and calculated $^{27}\text{Al}$ NMR spectra of stationary samples of $\text{Cl}_3\text{Al}\cdot\text{OPCl}_3$ at (A) 4.7 T and (B) 9.4 T. ....	62
<b>Figure 3.6:</b>	Schematic diagram showing the relative orientation of the CS and EFG tensors. ....	63
<b>Figure 3.7:</b>	The effects of (A) the quadrupole interaction, (B) CSA and (C) combination of quadrupole interaction and CSA the solid-state NMR spectrum of a spin-5/2 quadrupolar nucleus ....	65
<b>Figure 3.8:</b>	Aluminum-27 NMR spectra of stationary samples of $\text{Al}(\text{acac})_3$ at (A) 4.7 T, (B) 9.4 T, (C) 18.8 T ....	68
<b>Figure 3.9:</b>	Experimental $^{27}\text{Al}$ NMR spectra of $\text{Al}(\text{acac})_3$ at 9.4 T and calculated spectra (A) without CSA and (B) with CSA. ....	69
<b>Figure 3.10:</b>	Aluminum-27 NMR spectra of stationary samples of $\text{Al}(\text{trop})_3$ at (A) 4.7 T, (B) 9.4 T and (C) 18.8 T ....	73
<b>Figure 3.11:</b>	Experimental $^{27}\text{Al}$ NMR spectra of $\text{Al}(\text{trop})_3$ at 18.8 T and calculated spectra (A) without CSA and (B) with CSA. ....	74
<b>Figure 3.12:</b>	(A) Theoretical orientation of the $^{27}\text{Al}$ CS tensor in the molecular frame. (B) Theoretical orientation of the EFG tensor at the aluminum nucleus. ....	77
<b>Figure 3.13:</b>	Two projections illustrating the orientations of the CS and EFG tensors in the molecular frame of $\text{Al}(\text{acac})_3$ as determined by experiment and theoretical calculations (6-31G* basis set). ....	80
<b>Figure 3.14:</b>	Two projections illustrating the orientations of the CS and EFG tensors in the molecular frame of $\text{Al}(\text{trop})_3$ as determined by experiment and theoretical calculations ....	82
<b>Figure 3.15:</b>	(A) A magnetic-dipole-allowed (symmetry-allowed) transition created by the $L_x$ operator resulting in a paramagnetic shielding contribution along the $x$ -direction (B) A symmetry-forbidden transition with no paramagnetic shielding contribution. ....	86

<b>Figure 3.16:</b>	Plot showing the linear relationship between the calculated isotropic chemical shielding and the bond length in aluminum chloride . . . .	94
<b>Figure 4.1:</b>	The molecular structure of cobaloximes . . . . .	99
<b>Figure 4.2:</b>	Asymmetric splittings in the NMR spectrum of a spin-1/2 nucleus coupled to a quadrupolar nucleus with $S = 7/2$ . . . . .	100
<b>Figure 4.3:</b>	Structure of the vitamin-B12 coenzyme. . . . .	103
<b>Figure 4.4:</b>	Relative orientation of the dipolar vector, $r_{IS}$ , and the EFG tensor. . . . .	111
<b>Figure 4.5:</b>	Energy levels of the spin-1/2 nucleus coupled to a spin-7/2 nucleus, with corresponding stick spectra. . . . .	117
<b>Figure 4.6:</b>	Relative orientations of (A) the EFG and MAS frames ( $\Xi, \xi$ ) and (B) the MAS frame and the applied magnetic field ( $\beta_M = 54.74^\circ, \omega_{rot}t$ ). . . . .	119
<b>Figure 4.7:</b>	MAS NMR spectrum of a spin-1/2 nucleus coupled to a spin-7/2 nucleus with no line broadening (lower trace) and gaussian broadening of 100 Hz (upper trace) . . . . .	120
<b>Figure 4.8:</b>	Experimental and calculated $^{31}\text{P}$ CPMAS NMR isotropic centrebands of $\text{PPh}_3\text{Co}(\text{DH})_2\text{Me}$ (I) at (A) 4.7 T and (B) 9.4 T . . . . .	122
<b>Figure 4.9:</b>	Experimental and calculated $^{31}\text{P}$ CPMAS NMR spectra of $\text{PBu}_3\text{Co}(\text{DH})_2\text{Cl}$ (II) at 9.4 T and 155 K. . . . .	124
<b>Figure 4.10:</b>	Experimental and calculated $^{31}\text{P}$ CPMAS NMR spectra of $\text{PPh}_3\text{Co}(\text{DH})_2\text{CH}_3$ (III) at (A) 4.7 T and (B) 9.4 T . . . . .	126
<b>Figure 4.11:</b>	Experimental and calculated $^{31}\text{P}$ CPMAS NMR spectra of $\text{P}(\text{tol})_3\text{Co}(\text{DH})_2\text{Cl}$ (IV) at (A) 4.7 T and (B) 9.4 T and $\text{PPh}_3\text{Co}(\text{DH})_2\text{N}_3$ (V) at (C) 4.7 T and (D) 9.4 T. . . . .	131
<b>Figure 4.12:</b>	Experimental and calculated $^{31}\text{P}$ CPMAS NMR spectra of $\text{PMe}_3\text{Co}(\text{DH})_2\text{Me}$ (X) at (A) 4.7 T and (B) 9.4 T. . . . .	132
<b>Figure 4.13:</b>	Experimental and calculated $^{31}\text{P}$ CPMAS NMR spectra of $\text{P}(p\text{-ClC}_6\text{H}_4)_3\text{-Co}(\text{DH})_2\text{Me}$ (XII) at (A) 4.7 T and (B) 9.4 T, $\text{P}(\text{Me}_2\text{Ph})\text{Co}(\text{DH})_2\text{Me}$ (XIII) at (C) 4.7 T and (D) 9.4 T, and $\text{P}(\text{Et}_2\text{Ph})\text{Co}(\text{DH})_2\text{Me}$ (XIV) at (E) 4.7 T and (F) 9.4 T. . . . .	133
<b>Figure 4.14:</b>	(A) Experimental and calculated $^{31}\text{P}$ CPMAS NMR isotropic transitions of $\text{P}(\text{OPh})_3\text{Co}(\text{DH})_2\text{Me}$ (XVI) at 9.4 T. (B) Full spectrum . . . . .	135

<b>Figure 4.15:</b> Variable-temperature $^{31}\text{P}$ CPMAS NMR spectra of $\text{PBu}_3\text{Co}(\text{DH})_2\text{Cl}$ (II).	143
<b>Figure 4.16:</b> Calculated variable-temperature solution NMR spectra of a spin-1/2 nucleus spin-coupled to a spin-7/2 nucleus.	145
<b>Figure 4.17:</b> Variable-temperature $^{31}\text{P}$ CPMAS NMR of (A) $\text{PEt}_3\text{Co}(\text{DH})_2\text{Me}$ (XVIII) and (B) $\text{PBu}_3\text{Co}(\text{DH})_2\text{N}_3$ (XIX) at 9.4 T	147
<b>Figure 5.1:</b> The relative orientations of the magnetic field, $\mathbf{B}_0$ , and the dipolar vector, $\mathbf{r}_{IS}$ , with respect to the CS tensor.	158
<b>Figure 5.2:</b> Stationary powder pattern of a spin-1/2 nucleus dipolar- and $J$ -coupled to a spin-7/2 nucleus	160
<b>Figure 5.3:</b> Experimental and calculated $^{15}\text{N}$ CPMAS NMR spectra of the isotropic peak of $^{15}\text{N}$ -enriched $\text{py}^*\text{Co}(\text{DH})_2\text{Cl}$ (I) at (A) 4.7 T and (B) 9.4 T	161
<b>Figure 5.4:</b> Experimental and calculated $^{15}\text{N}$ CPMAS NMR spectra of the isotropic peak of $^{15}\text{N}$ -enriched $\text{anil}^*\text{Co}(\text{DH})_2\text{Cl}$ (II) at (A) 4.7 T and (B) 9.4 T	164
<b>Figure 5.5:</b> Experimental and calculated $^{15}\text{N}$ CPMAS NMR spectra of the isotropic transition of $^{15}\text{N}$ -enriched $\text{py}^*\text{Co}(\text{DH})_2\text{CH}_3$ (III), (A) 4.7 T and (B) 9.4 T	167
<b>Figure 5.6:</b> Experimental and calculated $^{15}\text{N}$ NMR spectra of stationary samples of $^{15}\text{N}$ -enriched $\text{py}^*\text{Co}(\text{DH})_2\text{Cl}$ at (A) 4.7 T and (B) 9.4 T. Corresponding first-derivative spectra given in (C) and (D)	171
<b>Figure 5.7:</b> Experimental and calculated $^{15}\text{N}$ NMR spectra of stationary samples of $^{15}\text{N}$ -enriched $\text{anil}^*\text{Co}(\text{DH})_2\text{Cl}$ at (A) 4.7 T and (B) 9.4 T. Corresponding first-derivative spectra given in (C) and (D).	177
<b>Figure 5.8:</b> Experimental and calculated $^{15}\text{N}$ NMR spectra of stationary samples of $^{15}\text{N}$ -enriched $\text{py}^*\text{Co}(\text{DH})_2\text{CH}_3$ at (A) 4.7 T and (B) 9.4 T	178
<b>Figure 5.9:</b> Nitrogen chemical shielding tensor orientation in $^{15}\text{N}$ - $\text{py}^*\text{Co}(\text{DH})_2\text{Cl}$ as determined by experimental methods and GIAO calculations	183
<b>Figure 5.10:</b> Nitrogen chemical shielding tensor orientation in $^{15}\text{N}$ - $\text{py}^*\text{Co}(\text{DH})_2\text{CH}_3$ as determined by experimental methods and GIAO calculations.	184

<b>Figure 5.11:</b> Perpendicular ( $\delta_{\perp}$ ), tangential ( $\delta_{\tau}$ ) and radial ( $\delta_{\parallel}$ ) components of the nitrogen shielding tensor in pyridine . . . . .	186
<b>Figure 5.12:</b> Nitrogen chemical shielding tensor orientation in $^{15}\text{N}$ -anil*Co(DH) <sub>2</sub> Cl as determined by experimental methods and GIAO calculations . . . . .	189
<b>Figure 5.13:</b> (A) The nitrogen CS tensor in ammonia. (B) The nitrogen CS tensor in aniline, top view. (C) The nitrogen CS tensor in aniline, side view. (D) The nitrogen CS tensor in anil*Co(DH) <sub>2</sub> Cl (II), side view . . . . .	190
<b>Figure 6.1:</b> Structure of aluminum phthalocyanine. . . . .	195
<b>Figure 6.2:</b> Solid-state $^{69}\text{Ga}$ and $^{71}\text{Ga}$ NMR spectra of stationary samples of Ga(acac) <sub>3</sub> at 9.4 T. . . . .	196
<b>Figure 6.3:</b> Structure of (PPh <sub>3</sub> ) <sub>2</sub> (NO)Co( $\eta^2$ -C <sub>60</sub> ). . . . .	198
<b>Figure 6.4:</b> Solid-state $^{31}\text{P}$ CPMAS NMR spectra of (PPh <sub>3</sub> ) <sub>2</sub> (NO)Co( $\eta^2$ -C <sub>60</sub> ) and (PPh <sub>3</sub> ) <sub>3</sub> Co(NO) at 9.4 T. . . . .	199
<b>Figure A.1:</b> Experimental and calculated solid-state $^{31}\text{P}$ NMR spectra of a stationary sample of Cl <sub>3</sub> AlOPCl <sub>3</sub> at 9.4 T. . . . .	203
<b>Figure A.2:</b> Experimental and theoretical phosphorus CS tensor orientations in Cl <sub>3</sub> AlOPCl <sub>3</sub> . . . . .	204
<b>Figure B.1:</b> Solid-state $^{13}\text{C}$ CPMAS NMR spectrum of 25% $^{13}\text{C}$ -enriched PPh <sub>3</sub> Co(DH) <sub>2</sub> *CH <sub>3</sub> at 4.7 T. . . . .	207
<b>Figure B.2:</b> Solid-state $^{13}\text{C}$ CPMAS NMR spectrum of 30% $^{13}\text{C}$ -enriched pyrCo(DH) <sub>2</sub> *CH <sub>3</sub> at 4.7 T. . . . .	208
<b>Figure B.3:</b> Experimental (bottom) and calculated (top) solid-state $^{59}\text{Co}$ NMR spectra of PPh <sub>3</sub> Co(DH) <sub>2</sub> CH <sub>3</sub> at 9.4 T . . . . .	209

## List of Tables

<b>Table 3.1:</b>	Tabulation of experimental quadrupolar and chemical shift data obtained from NMR experiments on complexes exhibiting aluminum chemical shielding anisotropy . . . . .	56
<b>Table 3.2:</b>	Experimental and Calculated Aluminum-27 CS Tensors in $\text{AlCl}_3 \cdot \text{OPCl}_3$ . . . . .	76
<b>Table 3.3:</b>	Experimental and Calculated Aluminum-27 CS Tensors in $\text{Al}(\text{acac})_3$ and $\text{Al}(\text{trop})_3$ . . . . .	78
<b>Table 3.4:</b>	Experimental and calculated aluminum-27 chemical shielding parameters for a series of linear Al-containing molecules . . . . .	90
<b>Table 3.5:</b>	Experimental and calculated aluminum-27 nuclear quadrupole coupling constants for a series of linear Al-containing molecules . . .	93
<b>Table 4.1:</b>	NMR parameters for fully characterized cobaloximes . . . . .	121
<b>Table 4.2:</b>	NMR parameters for phosphine- and phosphite-substituted cobaloximes, $\text{LCo}(\text{DH})_2\text{X}$ , and uncoordinated neutral ligands, L . .	129
<b>Table 4.3:</b>	Comparison of $^1J(^{59}\text{Co}, ^{31}\text{P})$ and $^1J(^{103}\text{Rh}, ^{31}\text{P})$ in cobaloximes and rhodoximes ( $\text{LRh}(\text{DH})_2\text{X}$ ) . . . . .	141
<b>Table 5.1:</b>	Parameters obtained from the $^{15}\text{N}$ CPMAS NMR spectra of $^{15}\text{N}$ -labelled cobaloximes . . . . .	162
<b>Table 5.2:</b>	Comparison of $^1J(^{59}\text{Co}, ^{15}\text{N})$ and $^1J(^{103}\text{Rh}, ^{15}\text{N})$ in cobaloximes and rhodoximes ( $\text{LRh}(\text{DH})_2\text{X}$ ) . . . . .	168
<b>Table 5.3:</b>	Parameters obtained from dipolar chemical shift analysis of $^{15}\text{N}$ NMR spectra of stationary samples of $^{15}\text{N}$ -labelled cobaloximes . .	175
<b>Table 5.4:</b>	Comparison of experimental and calculated $^{15}\text{N}$ chemical shielding tensors . . . . .	181
<b>Table A.1:</b>	Experimental and Calculated Phosphorus Chemical Shift Tensors in $\text{Cl}_3\text{AlPOCl}_3$ . . . . .	203

## Abstract

Modern solid-state NMR techniques have been applied for the characterization of NMR interaction tensors in isolated spin systems involving quadrupolar nuclei. Several examples are presented, which include the use of solid-state aluminum-27 NMR for direct observation of the quadrupolar aluminum nucleus in several complexes, and the indirect observation of the quadrupolar cobalt nucleus in the  $^{31}\text{P}$  and  $^{15}\text{N}$  NMR spectra of cobaloximes. *Ab initio* calculations of chemical shielding and electric field gradient tensors are compared to experimental results, and utilized to confirm experimentally determined tensor orientations.

Some of the first definitive examples of aluminum chemical shielding anisotropy are presented in this thesis. In the  $\text{Cl}_3\text{AlOPCl}_3$  complex, the span of the aluminum chemical shielding tensor is found to be 60 ppm. In hexacoordinate aluminum complexes, very small spans ranging from 3.8 to 9.0 ppm are observed. The appearance of the  $^{27}\text{Al}$  NMR spectra of stationary samples is dependent upon the relative orientation of the chemical shielding and electric field gradient tensors. As well, in the linear AlNC and AlCl molecules, large spans are calculated from recently reported nuclear spin-rotation constants.

Solid-state  $^{31}\text{P}$  and  $^{15}\text{N}$  magic-angle spinning NMR spectra display distorted eight-peak multiplets arising from spin-spin coupling interactions with  $^{59}\text{Co}$ , which is a spin-7/2 nucleus. It is possible to obtain values of the one-bond  $J$ -couplings,  $^1J(^{59}\text{Co}, ^{31}\text{P})$  and  $^1J(^{59}\text{Co}, ^{15}\text{N})$ , which are unavailable from solution NMR experiments. The distortions are due to unaveraged dipolar interactions, which arise from the presence of the quadrupolar interaction. Several cobaloximes have  $^{31}\text{P}$  NMR spectra which are broad at room temperature, but exhibit splittings at low temperatures. The broad spectra are attributed to the rapid spin-lattice relaxation of  $^{59}\text{Co}$ . Splittings are observed in the  $^{15}\text{N}$  NMR spectra of stationary samples of cobaloximes with pyridine- $^{15}\text{N}$  and aniline- $^{15}\text{N}$  substituted into the axial positions, which arise from spin-spin coupling interactions with  $^{59}\text{Co}$ . The orientations of nitrogen chemical shielding tensors were determined with dipolar chemical shift analysis.

## List of Symbols

$\alpha, \beta, \gamma$	Euler angles: relative orientation of the CS and EFG tensors
$\alpha, \beta$	spin states, $\alpha = +1/2, \beta = -1/2$
$\alpha^C, \beta^C$	polar angles: relative orientation of CS tensor and dipolar vector
$\alpha^D, \beta^D$	polar angles: relative orientation of EFG tensor and dipolar vector
$\beta_M$	magic angle, $\sim 54.74^\circ$
$\gamma_I, \gamma_S$	magnetogyric ratios of spins $I, S$
$\gamma_r$	Sternheimer factor
$\Delta v_{ii}$	dipolar splitting, at $\delta_{ii}$
$\delta_{11}, \delta_{22}, \delta_{33}$	principal components of the chemical shift tensor
$\delta_{iso}$	isotropic chemical shift
$\Delta J = J_{\parallel} - J_{\perp}$	anisotropy in indirect spin-spin coupling
$\Delta K$	anisotropy in $K$
$\eta$	quadrupolar asymmetry parameter
$\theta, \phi$	polar angles: relative orientation of EFG tensor and $\mathbf{B}_0$
$\Theta, \Phi$	polar angles: relative orientation of dipolar vector and $\mathbf{B}_0$
$\vartheta, \varphi$	Euler angles: relative orientation of CS tensor and $\mathbf{B}_0$
$\theta_p$	pulse tip angle
$\kappa$	skew (of the chemical shielding tensor)
$\mu$	magnetic moment of a nucleus
$\nu_0$	Larmor frequency, $s^{-1}$
$\nu_Q$	nuclear quadrupole frequency, $s^{-1}$
$\nu_{rot}$	rotor (sample) spinning frequency, $s^{-1}$

$\nu_S$	Larmor frequency, spin $S$
$\Xi, \xi$	polar angles: relative orientation of EFG tensor and MAS frame
$\sigma$	chemical shielding tensor
$\sigma_{11}, \sigma_{22}, \sigma_{33}$	principal components of the chemical shielding tensor
$\sigma^d$	diamagnetic shielding tensor
$\sigma_{\text{iso}}$	isotropic chemical shielding
$\sigma^p$	paramagnetic shielding tensor
$\tau_{\text{AQ}}$	acquisition time
$\tau_c$	correlation time for molecular motion
$\tau_{\text{CT}}$	contact time (CP experiment)
$\tau_p$	pulse width (pulse duration)
$\tau_S$	spin-lattice relaxation time for quadrupolar nucleus
$\Omega$	span (of the chemical shielding tensor)
$\omega_0$	Larmor frequency, $\text{rad s}^{-1}$
$\omega_Q$	nuclear quadrupole frequency, $\text{rad s}^{-1}$
$\omega_{\text{rot}}$	rotor (sample) spinning frequency, $\text{rad s}^{-1}$
$a_1$	cubic force constant
$B$	molecular rotation constant
$B_0$	external applied magnetic field
$B_0$	external magnetic field strength
$B_1, B_2$	external applied radiofrequency fields
$B_1$	radiofrequency field strength
$C_Q$	nuclear quadrupolar coupling constant

$C_1$	nuclear spin-rotation constant
$d$	residual dipolar shift
<b>D</b>	dipolar tensor
$e$	electron charge
$eq, eq_{zz}$	largest component of EFG tensor, $V_{33}$
$eQ$	nuclear quadrupole moment
$g_N$	nuclear $g$ -factor
$\mathcal{H}$	hamiltonian operator
$\hbar = h/2\pi$	Planck's constant
$I$	nuclear spin number, $I = 1/2$
<b>I</b>	nuclear spin angular momentum operator
$I_+, I_-$	raising and lowering operators, spin $I$
$I_z$	$z$ -component angular momentum operator, spin $I$
<b>J</b>	<b>J</b> -tensor
$J_{\text{iso}}$	isotropic indirect spin-spin coupling ( $J$ -coupling)
$K$	reduced indirect spin-spin coupling constant
$k_B$	Boltzmann constant
$L_{x,y,z}$	angular momentum operator
<b>M</b>	macroscopic bulk magnetization
$m_I$	magnetic quantum number, spin $I$
$m_S, m$	magnetic quantum number, spin $S$
<b>Q</b>	nuclear quadrupole moment ( $\text{m}^2$ )
<b>R</b>	rotational operator

$R_{dd}$	direct dipolar coupling constant
$r_e$	equilibrium bond length
$R_{eff}$	effective dipolar coupling constant
$\mathbf{r}_{IS}$	internuclear vector, or dipolar vector
$r_o$	bond length
$\mathbf{S}$	nuclear spin angular momentum operator
$S$	nuclear spin number, $S > 1/2$
$S_+, S_-$	raising and lowering operators, spin $S$
$S_z$	$z$ -component angular momentum operator, spin $S$
$T_1$	spin-lattice relaxation time
$T_2$	spin-spin relaxation time
$T_2^*$	effective spin-spin relaxation time
$\mathbf{V}$	EFG tensor
$V_{11}, V_{22}, V_{33}$	principal components of the EFG tensor
$Z$	atomic number

## List of Abbreviations

B3LYP	Becke's 3-parameter exchange functional and the correlation functional of Lee, Yang & Parr
CHF	coupled Hartree-Fock
CP	cross polarization
CS	chemical shielding
CSA	chemical shielding anisotropy
CSGT	continuous set of gauge transforms
DAS	dynamic-angle spinning
DFT	density functional theory
DOR	double rotation
ECP	effective core potential
EFG	electric field gradient
GIAO	gauge-including atomic orbital
IGLO	individualized gauge for localized orbitals
LORG	localized orbital/localized origin
MAS	magic-angle spinning
MP2	second-order Møller-Plesset perturbation theory
MQMAS	multiple quantum magic-angle spinning
o.d.	outer diameter
PAS	principal axis system
PFG	partial field gradient
RHF	restricted Hartree-Fock

## Chemical Abbreviations

acac	acetylacetonate
anil	aniline
Bu	<i>n</i> -butyl
Bz	benzyl
DH	dimethylglyoxime
Et	ethyl
Me	methyl
Ph	phenyl
py	pyridine
TMHD	2,2,6,6-tetramethyl-3,5-heptanedionato
tol	tolyl
trop	tropolonate

## List of Compounds

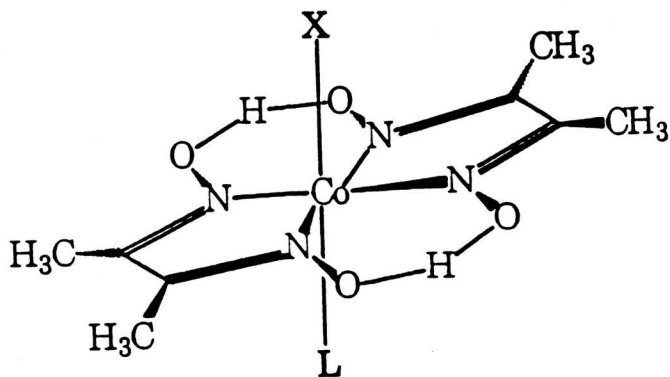
### Chapter 3 Aluminum Compounds

I	$\text{Cl}_3\text{AlOPCl}_3$	aluminum(III) chloride phosphoryl chloride
II	$\text{Al}(\text{acac})_3$	tris(acetylacetonato)aluminum(III)
III	$\text{Al}(\text{trop})_3$	tris(tropolonato)aluminum(III)
IV	$\text{Al}(\text{TMHD})_3$	tris(2,2,6,6-tetramethyl-3,5-heptanedionato)aluminum(III)
V	$\text{Al-N}\equiv\text{C}$	aluminum(I) isocyanide
VI	$\text{AlCl}$	aluminum(I) chloride

## Chapter 4 Phosphorus-Substituted Cobaloximes, $\text{LCo}(\text{DH})_2\text{X}$

L = neutral ligand, X = anionic species

- I  $\text{PPh}_3, \text{Me}$
- II  $\text{PBu}_3, \text{Cl}$
- III  $\text{PPh}_3, \text{Cl}$
- IV  $\text{P}(p\text{-tol})_3, \text{Cl}$
- V  $\text{PPh}_3, \text{N}_3$
- VI  $\text{PMePh}_2, \text{Cl}$
- VII  $\text{PMe}_2\text{Ph}, \text{N}_3$
- VIII  $\text{PBz}_3, \text{Cl}$
- IX  $\text{PBz}_3, \text{N}_3$
- X  $\text{PMe}_3, \text{Me}$
- XI  $\text{P}(p\text{-FC}_6\text{H}_4)_3, \text{Me}$
- XII  $\text{P}(p\text{-ClC}_6\text{H}_4)_3, \text{Me}$
- XIII  $\text{P}(\text{Me}_2\text{Ph}), \text{Me}$
- XIV  $\text{P}(\text{Et}_2\text{Ph}), \text{Me}$
- XV  $\text{P}(\text{OEt})_3, \text{N}_3$
- XVI  $\text{P}(\text{OPh})_3, \text{Me}$
- XVII  $\text{PPh}_3, \text{Br}$
- XVIII  $\text{PEt}_3, \text{Me}$
- XIX  $\text{PBu}_3, \text{N}_3$



## Chapter 5 Nitrogen-Substituted Cobaloximes, $\text{LCo}(\text{DH})_2\text{X}$

- I  $\text{pyCo}(\text{DH})_2\text{Cl}$
- II  $\text{anilCo}(\text{DH})_2\text{Cl}$
- III  $\text{pyCo}(\text{DH})_2\text{CH}_3$
- IV  $\text{pyCo}(\text{DH})_2\text{Br}$

## Acknowledgments

First and foremost, I would like to thank Professor Rod Wasylishen for being an excellent teacher and supervisor. Rod has encouraged me to work very hard over the past few years, and has provided me with much needed guidance in my studies. I thank him for giving me the opportunity to spend the past four years in his laboratory, and for exhibiting "extreme" patience with me in regard to some of my work habits.

I also extend thanks to past and present members of our research group. Dr. Klaus Eichele was an immense help to me during my stay at Dalhousie, and spent much time instructing me on spectrometer operation, computer programming and the finer points of laboratory safety. I also thank Scott Kroeker, who has read large portions of this thesis and several manuscripts, and provided me with invaluable comments and criticisms. I am indebted to Guy Bernard and Myrlene Gee, who aside from providing me with endless amusement in the lab, spent many hours of their free time poring over this thesis as my proof-reading team. I also thank Dr. Mike Lumsden for his help with spectrometer operation over the past four years.

I would like to thank several other members of the department, who have been exceptional friends and colleagues. First, I would like to thank Chuck Macdonald for his friendship and support, as well as for some substantial financial loans, which are now paid in full. Chuck also spent much time preparing samples and packing NMR rotors for me in the Burford glove box. I also thank Denise Walsh, Andrew Phillips and Richard Warren for providing many interesting compounds for examination by solid-state NMR. I also am indebted to Dr. T. Stan

Cameron, who loaned me his nitrogen Dewar, and spent days with me setting up variable-temperature NMR experiments. Thanks also goes to Elinor Cameron, who performed a number of crystal structure database searches. I also very grateful to Cameron Dickinson, who agreed (for a price) to check through all of my references, much to my surprise.

I am grateful to Dr. John H. Nelson (University of Nevada at Reno), who provided the initial cobaloxime samples, and to Dr. Scott Moore and Dr. Luigi Marzilli (Emory University), who provided most of the methylcobaloximes examined in this thesis. I thank Hans Foerster for running aluminum NMR spectra using Bruker's high-field magnet (18.8 T).

I thank the Killam Foundation and Walter C. Sumner Foundation for graduate fellowships.

Finally, I would like to thank my parents and family, who have supported and encouraged me from when I started at University of Manitoba, during my stay at Dalhousie, and as I move on to whatever lies ahead.

# Chapter 1

## An Introduction to Solid-State NMR

### 1.1 Prologue

Solid materials have been of great importance to humankind throughout the ages, from the primitive development of tools from naturally occurring minerals; to the application of materials such as wood, copper, and iron; up to the modern, synthetic materials of today. Tremendous effort has been put forth during the last century in the production of such sophisticated materials, but no less energy has been expended in the characterization of the physical and chemical properties of solid materials. The field of science dedicated to the design and characterization of solid matter and materials is broadly defined as solid-state science. In particular, solid-state chemistry has become an extremely important area of solid-state science, and is concerned with the synthesis of new solid materials, identification of the products, characterization of the physical and chemical properties, structural determination, and engineering of methods for the design and production of materials with specific properties in both microscopic and macroscopic quantities.

Characterization of the properties of solid materials can reveal much about their underlying chemistry. A wide variety of techniques is available for such purposes, including diffraction methods, vibrational spectroscopy, calorimetric techniques, optical techniques, X-ray photoelectron spectroscopy and magnetic measurements. One of the newest and fastest-growing techniques for elucidation of

chemical structures in solid materials is solid-state nuclear magnetic resonance spectroscopy.

Many chemists associate nuclear magnetic resonance spectroscopy with the liquid state, since a majority of organic, inorganic and biochemical materials are characterized by NMR spectra of neat liquids or dilute samples in an appropriate solvent. In an isotropic solution, molecules rapidly tumble in a chaotic fashion, generally resulting in the averaging of the various NMR parameters to their isotropic values, and the observation of discrete, well-defined peaks in the NMR spectra. There is a moderate amount of information available from the solution NMR spectra of spin-1/2 nuclei, such as chemical shifts and indirect spin-spin interactions ( $J$ -couplings), which aid in the determination of molecular structure. As well, nuclear magnetic relaxation data yield information on the overall motion of the molecule in solution, as well as internal modes of motion within the molecule. Solution NMR spectra of quadrupolar nuclei usually only provide information on isotropic chemical shifts and spin-spin relaxation times, the latter of which is dominated by the presence of the quadrupolar nucleus. Information on the nature of the quadrupolar nucleus or other spin-spin interactions is usually not apparent, as quadrupolar nuclei generally relax very efficiently in solution, resulting in NMR signals that are often very broad and featureless. Similar line-broadening effects are sometimes observed in spectra of spin-1/2 nuclei which are  $J$ -coupled to quadrupolar nuclei. For example, spin-spin couplings between  $^{35/37}\text{Cl}$  and  $^{13}\text{C}$  nuclei, or  $^{14}\text{N}$  and  $^{13}\text{C}$  nuclei, are almost never observed in solution.

NMR spectra of solid samples are more complex, since isotropic averaging of

NMR interactions does not generally occur in the solid state. Rather, motion is relatively restricted in solids, such that the orientation-dependent, *anisotropic* characteristics of NMR interactions are apparent in the spectra. NMR interactions vary in magnitude depending on their orientation with respect to the applied magnetic field. Because of a multitude of orientation-dependent interactions, the solid-state NMR spectra of polycrystalline powder samples are generally quite broad, and often appear to have very little definition. In fact, solid-state NMR spectra contain much more information than solution spectra. Determination of the magnitudes and orientation dependence of chemical shielding, dipolar coupling, *J*-coupling and quadrupolar interactions provides valuable chemical information about the solid material. The difficulty lies in the acquisition and interpretation of solid-state NMR spectra, and the extraction of pertinent information. Fortunately, many techniques have been created and cultivated over the past thirty years which allow for the acquisition of solid-state NMR spectra while selectively eliminating the influences of certain interactions, and retaining spectral features which elicit the desired chemical information. Sophisticated theories have also been developed which allow for detailed spectral analysis and interpretation.

## 1.2 A Brief History of Nuclear Magnetic Resonance

Magnetic resonance first originated in the laboratories of physicists, who were interested in measuring the electron, nuclear and neutron magnetic moments by molecular beam magnetic resonance.<sup>1</sup> The first attempts at observing nuclear magnetic resonance in condensed matter were made by Gorter et al. on <sup>1</sup>H, <sup>7</sup>Li and

$^{19}\text{F}$  nuclei in simple crystalline materials.<sup>2</sup> Unfortunately for them, the spin-lattice relaxation times in these molecules were quite long and no resonances were observed. The first observations of magnetic resonance in bulk matter were made in 1945 on solid paraffin by Purcell and co-workers,<sup>3</sup> and on liquid water by Bloch et al.<sup>4</sup> A number of papers followed, leading up to the classic NMR work by Pake, which was the first investigation of dipolar interactions in the solid state.<sup>5</sup> In this proton NMR study of gypsum,  $\text{CaSO}_4 \cdot 2\text{H}_2\text{O}$ , the dependence of  $^1\text{H}$ ,  $^1\text{H}$  dipolar interactions on the orientation of the internuclear dipolar vector with respect to the applied magnetic field was examined. Pound published the first major solid-state NMR study of *quadrupolar nuclei*, investigating  $^7\text{Li}$ ,  $^{23}\text{Na}$  and  $^{27}\text{Al}$  resonances in crystals of simple inorganic salts.<sup>6</sup> Quadrupolar nuclei, one of the focal points of this thesis, will be discussed in detail in Chapter 2.

Chemical shifts were soon discovered, described in papers as NMR frequencies that were dependent upon “the chemical compound in which it [the nucleus] was contained.”<sup>7</sup> This was followed by the observation of fine structure resulting from electron-mediated nuclear spin interactions (i.e., *J*-couplings) in the  $^1\text{H}$ ,  $^{19}\text{F}$  and  $^{31}\text{P}$  solution NMR spectra in a series of simple molecules.<sup>8</sup> Forthwith, chemists realized the potential of NMR as a powerful tool for the characterization of organic molecules. Commercial NMR spectrometers became available in the mid 1950's, and solution NMR quickly became a routine procedure for detailed structural characterization and investigation of reaction mechanisms in solution, just ten years after its discovery!<sup>9</sup>

The use of solid-state NMR by chemists did not spread as rapidly, remaining

in the realm of the physicist until the mid 1960's. However, in the late 1950's it was found that rapid, physical rotation of the sample about an axis oriented at  $\Omega = 54.74^\circ$  (the *magic angle*) with respect to the applied magnetic field results in the narrowing of the broad resonances characteristic of solid-state NMR spectra.<sup>10</sup>

Interactions with a specific angular orientation dependence,  $3\cos^2\theta - 1$ , such as the dipolar interaction, are averaged by magic-angle spinning (MAS). The combination of pulsed-NMR spectrometers and Fourier-transform methods popularized the use of solid-state NMR for chemical problems.<sup>11</sup> Pines et al.<sup>12</sup> developed a technique using the concept of *cross-polarization* (CP),<sup>13</sup> which results in signal enhancement of dilute spins (e.g.,  $^{13}\text{C}$ ) by transfer of polarization from abundant spins (e.g.,  $^1\text{H}$ ). These techniques were combined with high-power proton decoupling to obtain the first high-resolution solid-state CPMAS NMR spectra, which exhibit isotropic peaks akin to those observed in solution.<sup>14</sup> Since then, an enormous number of solid-state NMR experiments have been conducted on a vast array of materials, such as crystalline organic and inorganic complexes, glasses, ceramics, minerals, plastics, metal alloys, superconductors, biological materials, etc., providing chemical and structural information which is in some cases unobtainable from other solid-state techniques.<sup>15</sup>

### 1.3 Advances in Solid-State Nuclear Magnetic Resonance

Several major technological developments have contributed to the widespread use of solid-state NMR spectroscopy in the last fifteen years.<sup>16</sup> The production of high-field, homogeneous, superconducting NMR magnets has resulted

in the extension of NMR studies to systems which could not previously be studied at lower applied magnetic fields. Typical magnetic field strengths now range from  $B_0 = 4.7$  T (200 MHz,  $^1\text{H}$ ) to  $B_0 = 18.8$  T (800 MHz,  $^1\text{H}$ ). Higher magnetic fields result in spectra exhibiting greater chemical shift dispersion, reduction of second-order quadrupolar effects on line shape, and most importantly, greater sensitivity. As well, the development of sophisticated pulse sequences and associated electronics for purposes such as the elimination and recoupling of dipolar interactions; the acquisition of isotropic, solution-like spectra for quadrupolar nuclei in the solid-state via multiple-quantum (MQ) techniques; the study of strongly dipolar-coupled abundant-spin nuclei (e.g.,  $^1\text{H}$  and  $^{19}\text{F}$ ); and so forth, has presented opportunities for NMR experiments on systems which were hitherto difficult or impossible to investigate. It is presently possible to spin samples at rates on the order of 33 kHz, which is extremely useful for acquiring MAS NMR spectra of quadrupolar nuclei, some of which have large anisotropic interactions that are not averaged at lower spinning speeds. Finally, the availability of high-speed workstations for control of experiments, processing and handling of data is also a significant contribution to the present success of NMR. These technological advancements have allowed for great strides forward in the application of solid-state NMR to materials science, particularly, in the investigation of countless materials containing quadrupolar nuclei, in the NMR of solid polymeric substances, and in the study of disordered, non-crystalline materials.

## 1.4 Thesis Overview

The main objective of this thesis is to demonstrate that the presence of quadrupolar nuclei within a molecule can be beneficial to the solid-state NMR spectroscopist, and not a bane, as it was once thought. The focus of this thesis is the characterization of a variety of NMR interactions with solid-state NMR spectra of quadrupolar nuclei, and spectra of nuclei which are affected by the presence of neighbouring quadrupolar nuclei. Such spectra are shown to provide an abundance of structural and chemical information. It is stressed that solid-state NMR experiments provide information on quadrupolar nuclei that is not procurable from analogous solution NMR studies.

This thesis covers two main topics: first, through the *direct* observation of quadrupolar nuclei using modern solid-state NMR techniques, orientation-dependent chemical shielding interactions and quadrupolar interactions are observed in the solid-state aluminum-27 NMR spectra of a variety of complexes. This research is motivated by the fact that there are very few examples of aluminum chemical shielding anisotropy in the current literature. Aluminum chemical shielding anisotropies are also calculated from available nuclear spin-rotation constants in linear molecules. Second, quadrupolar interactions, *J*-couplings, dipolar interactions and chemical shielding tensor orientations are examined by means of solid-state NMR studies of spin-1/2 nuclei which are spin coupled to quadrupolar nuclei. The interactions in *isolated spin pairs* (i.e.,  $^{59}\text{Co}$ ,  $^{15}\text{N}$  and  $^{59}\text{Co}$ ,  $^{31}\text{P}$ ) are characterized in a series of pseudo-octahedral complexes known as cobaloximes, through *indirect* observation of quadrupolar nuclei. Solid-state MAS

NMR spectra of the spin-1/2 nuclei allow for the determination of indirect spin-spin couplings which are inaccessible from analogous solution NMR experiments.

Further, distorted multiplets are observed resulting from *residual dipolar coupling*, which is dependent upon the nature of the quadrupolar and the direct dipolar interactions. NMR spectra of spin-1/2 nuclei in stationary samples of cobaloximes provide information on the orientation dependence of chemical shielding at the spin-1/2 nucleus, due to direct dipolar coupling with the quadrupolar nucleus. In addition, it is demonstrated that comparison of experimental and theoretical (*ab initio*) chemical shielding and quadrupolar interactions serves a two-fold purpose: *ab initio* calculations aid in the determination of the orientation dependence of the NMR interactions on molecular structure and symmetry, and comparison of theoretical values to experimental values acts as a rigorous test of current computational schemes.

The thesis is organized as follows: In Chapter 2, a general discussion of the NMR interactions pertinent to this thesis is presented. Quadrupolar interactions are discussed in some detail, followed by a brief discussion of some of the techniques relevant to this work. As well, a succinct introduction to the calculation of chemical shielding and electric field gradient tensors by *ab initio* methods is given at the end of this chapter.

Chapter 3 deals with direct observation of quadrupolar nuclei ( $^{27}\text{Al}$ , spin 5/2) with solid-state NMR. Theoretical background is given on the dependence of NMR spectra of quadrupolar nuclei on contributions from both quadrupolar and chemical shielding interactions. The orientation-dependent chemical shielding and

quadrupolar interactions in the aluminum chloride phosphoryl chloride ( $\text{Cl}_3\text{AlOPCl}_3$ ) complex are discussed. Two extremes of anisotropic aluminum chemical shielding interactions are also investigated: small anisotropic interactions are observed in distorted octahedral complexes, and large anisotropic interactions are found in linear diatomic and triatomic molecules.

Chapters 4 and 5 deal with indirect observation of quadrupolar interactions ( $^{59}\text{Co}$ , spin 7/2) in the solid-state  $^{31}\text{P}$  and  $^{15}\text{N}$  NMR spectra of cobaloximes containing phosphines, phosphites, pyridine- $^{15}\text{N}$  or aniline- $^{15}\text{N}$  as axial ligands. In Chapter 4, a review of the current literature on residual dipolar coupling is given, along with a concise theoretical treatment. Unique examples of *self-decoupling* of quadrupolar nuclei are demonstrated in variable-temperature solid-state  $^{31}\text{P}$  NMR experiments. In Chapter 5, *dipolar chemical shift NMR*, a technique used to provide information about the orientation of chemical shielding tensors in the molecular frame, is discussed in some detail. Nitrogen-15 NMR spectra of stationary samples of cobaloximes exhibit dipolar and  $J$ -coupling with  $^{59}\text{Co}$ , allowing for the determination of the nitrogen chemical shielding tensors with respect to the molecular frame.

Ongoing projects and future work in both characterization of chemical shielding tensors of quadrupolar nuclei and observations of residual dipolar coupling are covered in Chapter 6. In the former case, new examples of solid-state  $^{69}\text{Ga}$  and  $^{71}\text{Ga}$  NMR spectra are discussed (spin 3/2). In the latter case, examples of residual dipolar coupling observed in the  $^{31}\text{P}$  CPMAS NMR spectra of transition metal phosphine-substituted buckminsterfullerenes are introduced. Finally, in Chapter 7, conclusions regarding the scope and objectives of this thesis are discussed.

## Chapter 2

# Basic Principles and Techniques

## in Solid-State NMR

### 2.1 Introduction

In this chapter, the nuclear magnetic resonance phenomenon is introduced, and the various NMR interactions in the solid state are discussed. This thesis is primarily concerned with interactions between isolated pairs of nuclei, and only in part with interactions between the lattice and the nuclear spins which can result in relaxation phenomena. The solid-state NMR hamiltonian for an isolated spin pair which comprises external and internal interactions is written as

$$\mathcal{H}_{\text{NMR}} = \mathcal{H}_Z + \mathcal{H}_{\text{rf}} + \mathcal{H}_{\text{CS}} + \mathcal{H}_D + \mathcal{H}_J + \mathcal{H}_Q . \quad (2.1)$$

The first two terms, the Zeeman (Z) and radiofrequency (rf) hamiltonians, are external hamiltonians which are under the control of the experimentalist. They describe the interaction of nuclear spins with the static applied magnetic field ( $\mathbf{B}_0$ ) and time-dependent radiofrequency fields ( $\mathbf{B}_1, \mathbf{B}_2$ ). The remaining terms correspond to spin interactions, and are internal hamiltonians which are explicitly derived from the nuclear magnetic properties of the system. These hamiltonians describe chemical shielding (CS), dipole-dipole (D), indirect spin-spin coupling (J) and quadrupolar interactions (Q). The spin interactions resulting from coupling of spins

with external magnetic fields, other spins or electric field gradients, can be described by second-rank tensors (*vide infra*). There are several excellent texts which provide thorough introductions to NMR interactions in the solid state, and were used for the preparation of this discussion on NMR interactions presented in this chapter.<sup>17,18,19,20,21,22,23,24,25</sup>

The nuclear magnetic resonance phenomenon originates from the intrinsic angular momentum of the nucleus,  $\mathbf{P}$ , which is directly related to a quantum mechanical quantity known as *spin*,  $\mathbf{I}$ . Both  $\mathbf{P}$  and  $\mathbf{I}$  are quantum mechanical operators, and are proportional to one another, such that  $\mathbf{P} = \hbar\mathbf{I}$ . The magnitude of the nuclear spin angular momentum, or spin, is given by  $P = \hbar[I(I + 1)]^{1/2}$ , where  $I$  is the *nuclear spin quantum number*, and  $\hbar$  is Planck's constant,  $h$ , divided by  $2\pi$ . Most nuclei possess the property of spin; those that do not are normally referred to as magnetically non-active or spin-0 nuclei (e.g.,  $^{12}\text{C}$ ,  $^{16}\text{O}$ , etc.). Spin-1/2 nuclei are by far the most commonly observed nuclei in NMR experiments, including  $^1\text{H}$ ,  $^{13}\text{C}$ ,  $^{15}\text{N}$ ,  $^{19}\text{F}$  and  $^{31}\text{P}$ . Quadrupolar nuclei have nuclear spin quantum numbers greater than 1/2, and constitute ca. 70% of NMR active nuclei. However, NMR spectra of quadrupolar nuclei are often more difficult to acquire and interpret. For the remainder of the thesis,  $I$  will be used to denote the spin-1/2 nucleus, and  $S$  will denote the quadrupolar nucleus. The quadrupolar nuclei considered in this thesis are the half-integer quadrupolar nuclei  $^{27}\text{Al}$  ( $S = 5/2$ ),  $^{59}\text{Co}$  ( $S = 7/2$ ) and  $^{69/71}\text{Ga}$  ( $S = 3/2$ ).

For simplicity, the present discussion is confined to nuclei of spin  $I = 1/2$ . The spin angular momentum is proportional to the magnetic moment,  $\mu$ , of the nucleus,

$$\boldsymbol{\mu} = \gamma \hbar \mathbf{I} \quad (2.2)$$

where  $\gamma$  is the *magnetogyric ratio*. Each NMR-active isotope possesses a specific magnetogyric ratio. In the classical description of NMR, the macroscopic bulk magnetization,  $\mathbf{M}$ , results from the sum of the projections of magnetic moments along the direction of the external applied magnetic field,  $\mathbf{B}_0$ .

## 2.2 NMR Interactions

### 2.2.1 The Zeeman Interaction

The fundamental interaction responsible for nuclear magnetic resonance is the Zeeman interaction. In the *high-field approximation*, it is assumed that the Zeeman interaction is much larger than all of the spin interactions. In the absence of an applied magnetic field, the energy of an isolated nucleus of spin  $I = 1/2$  is independent of the *magnetic quantum number*,  $m_I$ , where  $m_I = \pm 1/2$ . However, upon application of a magnetic field of strength  $B_0$  (conventionally applied along the  $z$ -direction in the laboratory frame,  $\mathbf{B}_0 = (0, 0, B_0)$ ), the nuclear spin energy is split into two levels corresponding to  $m_I$ . Classically, the potential energy of magnetization,  $\mathbf{M}$ , in a magnetic field,  $\mathbf{B}_0$ , depends upon the orientation of the magnetic moments with respect to the field,

$$E = -\mathbf{M} \cdot \mathbf{B}_0 = -|\mathbf{M}| |\mathbf{B}_0| \cos\chi = -M_z B_0 \quad (2.3)$$

where the angle  $\chi$  defines their relative orientations, and  $M_z$  is the bulk

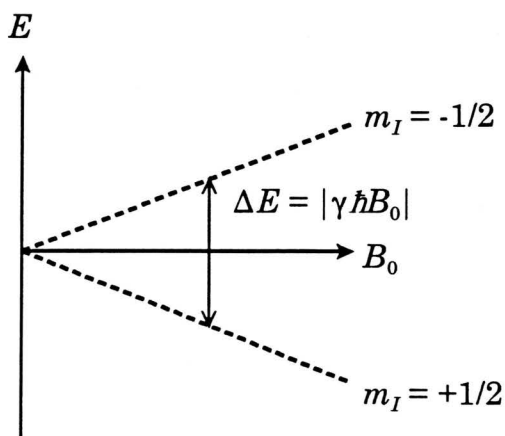


**Figure 2.1** Schematic representation of the Zeeman interaction.

magnetization along the  $z$ -direction.

The quantum mechanical expression for the Zeeman interaction,

$$\mathcal{H}_z = -\boldsymbol{\mu} \cdot \mathbf{B}_0 = -\gamma \hbar \mathbf{I}_z \cdot \mathbf{B}_0 \quad (2.4)$$

yields expressions for the energy levels corresponding to the spin states,  $m_I$ :

$$E_m = -\gamma \hbar m_I B_0 \quad (2.5)$$

There are  $(2I + 1)$  non-degenerate energy levels, separated by an energy difference of  $|\gamma \hbar B_0|$ . The Zeeman interaction for an isolated spin-1/2 nucleus is pictured in Fig.

2.1. The  $m_I = +1/2$  state is often denoted as  $\alpha$ , and the  $m_I = -1/2$  state as  $\beta$ . In eq.

2.4,  $I_z$  is a quantum mechanical spin operator, which is discussed in detail

elsewhere.<sup>25</sup>

It is possible to induce transitions with the selection rule  $\Delta m_I = \pm 1$  by applying electromagnetic radiation of the appropriate frequency. For an isolated nucleus, NMR transition energies are given by

$$h\nu_0 = |\gamma \hbar B_0 \Delta m_I| \quad (2.6)$$

where  $\nu_0$  is the *Larmor frequency*,  $\nu_0 = |\gamma/2\pi|B_0$ . The Larmor frequency is also written in terms of  $\text{rad s}^{-1}$ , as  $\omega_0 = \gamma B_0$ , which can be used to simplify the appearance of certain equations.

NMR is a relatively insensitive technique compared to other forms of spectroscopy such as vibrational and rotational spectroscopy, due to the very small energy and population differences between spin states. For the spin-1/2 case, the classical Boltzmann distribution gives the relative number of spins in each state:

$$\frac{N_\beta}{N_\alpha} = \exp(-\hbar\omega_0/k_B T) \quad (2.7)$$

where  $N_i$  correspond to populations of the  $\alpha$  and  $\beta$  spin states, and  $k_B$  is the Boltzmann constant. At normal temperatures,  $k_B T$  is very large compared to  $\hbar\omega_0$ . Under the so-called *high-temperature approximation*, the above equation can be expanded and truncated such that the population difference between  $\alpha$  and  $\beta$  spins,  $\Delta N$ , is given by

$$\Delta N = N_\alpha - N_\beta = N\Delta E/2k_B T = N\gamma\hbar B_0/2k_B T \quad (2.8)$$

where  $N$  is the total number of spins in the sample. Examination of the above equations reveals that the population difference, and hence the sensitivity of the NMR experiment increases as the strength of the applied magnetic field increases.

### 2.2.2 The Radiofrequency Hamiltonian

Electromagnetic radiation from the rf region of the spectrum ( $\mathbf{B}_1$ ,  $\mathbf{B}_2$ ) is applied perpendicular to the direction of the applied magnetic field ( $\mathbf{B}_0$ ) in NMR experiments, near or at the Larmor frequency of the nucleus being observed. In pulse NMR experiments, pulses of fixed durations are utilized to induce transitions over set frequency ranges, and are used for the creation, observation or suppression of NMR coherences. Normally, the length of the pulse is short (1 to 20  $\mu\text{s}$ ) with respect to the spin-lattice ( $T_1$ ) and spin-spin ( $T_2$ ) relaxation times, which describe the decay of longitudinal ( $M_z$ ) and transverse ( $M_{x,y}$ ) magnetization, respectively. The radiofrequency hamiltonian describes the interactions between the applied radiofrequency field,  $\mathbf{B}_1$ , and the nuclear spins:

$$\mathcal{H}_{\text{rf}} = -h\omega_1 \sum_k I_{xk} \cos[(\omega_0 + \zeta)t + \epsilon] - I_{yk} \sin[(\omega_0 + \zeta)t + \epsilon] \quad (2.9)$$

where  $\zeta$  is the resonance offset in  $\text{rad s}^{-1}$ ,  $\omega_1 = \gamma B_1$ , and  $\epsilon$  is a phase offset. The nuclear spins interact with  $\mathbf{B}_1$  in the same way that they interact with  $\mathbf{B}_0$ , excepting that  $\mathbf{B}_1$  oscillates in time, and  $\mathbf{B}_0$  is static. For a pulse along the  $x$ -direction of the Zeeman frame,

$$\mathcal{H}_{1x} = -\gamma h B_1 I_x = -h\omega_1 I_x \quad (2.10)$$

where  $I_x$  is a nuclear spin operator. Application of such a pulse tips the magnetization from the  $z$ -direction (along the magnetic field) onto the  $y$ -axis of the Zeeman frame. The duration of the pulse,  $\tau_p$ , determines the tip angle,  $\theta_p$ , according to  $\theta_p = \gamma B_1 \tau_p$ .

### 2.2.3 The Chemical Shielding Interaction

#### A. Chemical Shielding

If the Zeeman interaction was the sole interaction present in NMR experiments, NMR would be of very little use to chemists, as only nuclei with disparate magnetogyric ratios would be differentiated. However, the external magnetic field generates currents in the electron clouds surrounding the nuclei, which in turn produce secondary magnetic fields at the nuclei, which are proportional to  $B_0$ . If the charge distribution about a nucleus is spherically symmetric, the induced field at the nucleus,  $B'$ , opposes the applied magnetic field. For rapidly tumbling molecules in solution,  $B'$  is related to the external field by the *chemical shielding constant*,  $\sigma$ :

$$B' = -\sigma B_0 \quad (2.11)$$

which means the local field is defined by

$$B_{\text{loc}} = (1 - \sigma)B_0 \quad (2.12)$$

The chemical shielding constant is expressed in dimensionless units, ppm, obtained from measurements in Hz divided by  $\nu_0$ . These units are independent of the applied magnetic field, and are therefore molecular characteristics.

There are several sources contributing to the secondary magnetic fields. Ramsey partitioned the chemical shielding interaction into two major components: the *diamagnetic* and *paramagnetic* shielding interactions.<sup>26</sup> Diamagnetic nuclear

shielding arises from circulation of electrons in the  $s$  orbitals and filled shells surrounding the nucleus and is dependent on the ground state of the molecule. The diamagnetic contribution to chemical shielding is normally associated with increased shielding, with the local field at the nucleus antiparallel to the external magnetic field. Paramagnetic shielding, which arises from the non-spherical orbitals, is associated with the orbital angular momentum of electrons, and is therefore dependent on excited states of the molecule. Paramagnetic contributions normally result in deshielding, with local fields at the nuclei aligned parallel with  $\mathbf{B}_0$ . The partitioning of chemical shielding into diamagnetic and paramagnetic contributions, and interpretation of chemical shielding using Ramsey's theory are further discussed in Chapters 3 and 5.

Chemical shielding is an orientation-dependent property, i.e., the magnetic shielding at a nucleus in a molecule depends on the relative orientation of the molecule with respect to the applied magnetic field. Thus, chemical shielding can be described by a second-rank Cartesian tensor,  $\sigma$ , in which nine independent values specify the orientation of the chemical shielding (CS) tensor with respect to the laboratory frame. The CS tensor can be written as a sum of symmetric (six independent elements) and antisymmetric (three independent elements) second-rank tensors.<sup>27</sup> Only the symmetric portion of the CS tensor makes a contribution to observed chemical shielding;<sup>27</sup> thus, the antisymmetric components are not considered here. In its own principal axis system (PAS), the chemical shielding tensor is expressed in terms of three principal components which are defined from least to most shielded as  $\sigma_{11} \leq \sigma_{22} \leq \sigma_{33}$ :

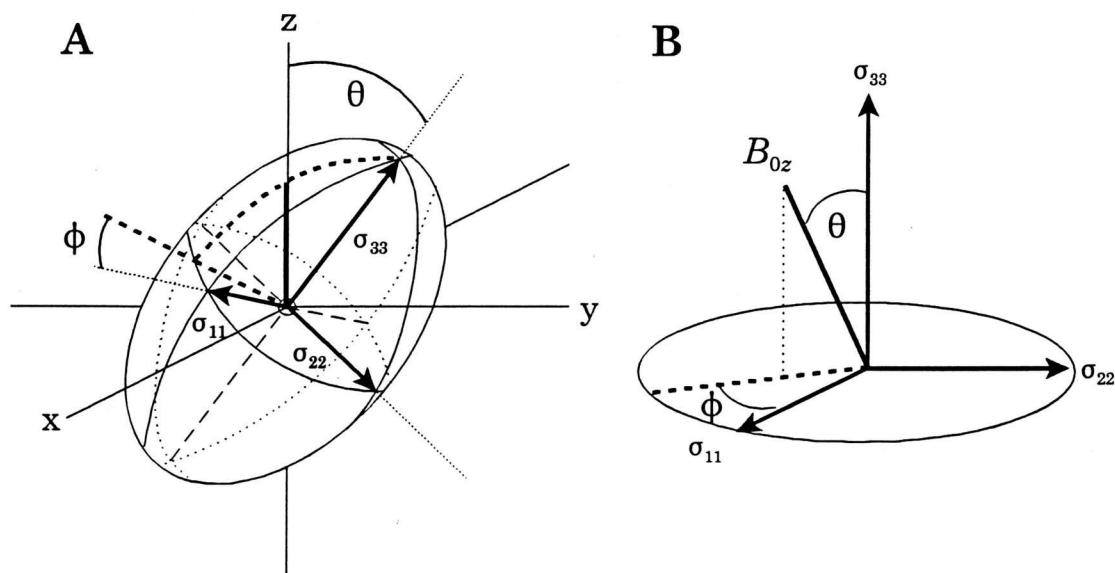


**Figure 2.2** (A) The chemical shielding tensor represented as an ellipsoid, oriented in the Zeeman frame. (B) Simplified diagram illustrating the orientation of the chemical shielding tensor with respect to the magnetic field, as defined by polar angles  $\vartheta$  and  $\phi$ .

$$\sigma = \begin{bmatrix} \sigma_{xx} & \sigma_{xy} & \sigma_{xz} \\ \sigma_{yx} & \sigma_{yy} & \sigma_{yz} \\ \sigma_{zx} & \sigma_{zy} & \sigma_{zz} \end{bmatrix}_{\text{sym}} \xrightarrow{\text{transform}} \begin{bmatrix} \sigma_{11} & 0 & 0 \\ 0 & \sigma_{22} & 0 \\ 0 & 0 & \sigma_{33} \end{bmatrix} \quad \text{CS PAS} \quad (2.13)$$

A pictorial representation of a chemical shielding tensor is given in Fig. 2.2. The chemical shielding hamiltonian can therefore be written as

$$\mathcal{H}_{\text{CS}} = \gamma h \mathbf{I} \cdot \sigma \cdot \mathbf{B}_0 \quad (2.14)$$

which describes chemical shielding as the coupling of the spin  $I$  and the applied magnetic field  $\mathbf{B}_0$  with the chemical shielding tensor,  $\sigma$ .

The orientation of the CS tensor with respect to  $\mathbf{B}_0$  is defined by the polar angles  $\vartheta$  and  $\varphi$  (Fig. 2.2). The frequency of spin  $I$  can then be expressed as

$$\nu_I(\vartheta, \varphi) = \nu_0 - \nu_{\text{CS}} \quad (2.15)$$

where

$$\nu_{\text{CS}} = \nu_0 (\sigma_{11} \sin^2 \vartheta \cos^2 \varphi + \sigma_{22} \sin^2 \vartheta \sin^2 \varphi + \sigma_{33} \cos^2 \vartheta) \quad (2.16)$$

The presence of the chemical shielding interaction gives rise to the characteristic solid-state NMR powder patterns pictured in Fig. 2.3.

## B. Describing the Chemical Shielding Tensor

The orientation of the CS tensor in the molecular frame can generally be determined from single-crystal NMR studies, with the relative orientation of the two frames given by three Euler angles.<sup>28</sup> However, in most instances single crystals suitable for such NMR studies are not available, hence, experiments must be conducted upon microcrystalline powder samples, in which the molecules, and therefore the CS tensors, assume random distributions with respect to the magnetic field. Thus, NMR spectra of stationary samples of microcrystalline powders contain information on the orientation dependence of the chemical shielding interaction. Analysis of such spectra yields the principal components of the CS tensor, but no knowledge is gained regarding the orientation of the CS tensor with respect to the frame of the molecule.

At this time, three CS parameters are specified which completely define the

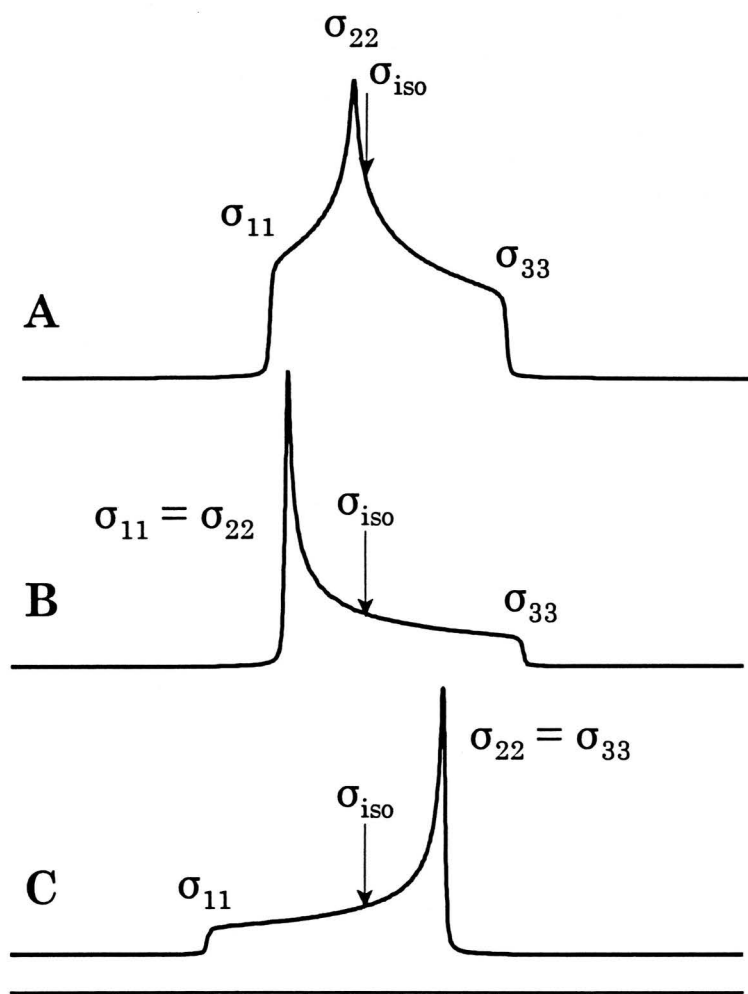


**Figure 2.3** Solid-state NMR spectra exhibiting chemical shielding anisotropy. (A) Non-axial CSA,  $\kappa = +0.3$ . (B) Axial CSA,  $\kappa = +1.0$ . (C) Axial CSA,  $\kappa = -1.0$ . Isotropic shielding is the same for all spectra. See text for definition of CSA.

CS tensor in terms of its principal components. First, the *isotropic chemical shielding* is given by

$$\sigma_{\text{iso}} = (\sigma_{11} + \sigma_{22} + \sigma_{33})/3 \quad (2.17)$$

The breadth of the powder pattern arising from the presence of chemical shielding anisotropy (*vide infra*) is described by the *span*,

$$\Omega = \sigma_{33} - \sigma_{11} \quad (2.18)$$

with the shape of the powder pattern defined by the *skew*,

$$\kappa = 3(\sigma_{\text{iso}} - \sigma_{22})/\Omega \quad (2.19)$$

where  $-1 \leq \kappa \leq 1$ .<sup>29</sup> If  $\kappa = +1.0$ , the CS tensor is said to be *axially symmetric*, with  $\sigma_{33}$  as the unique component. Similarly, if  $\kappa = -1.0$ , the CS tensor is axially symmetric with  $\sigma_{11}$  as the unique component. Unfortunately, no standard convention exists within the current literature for describing CS tensors, though this method is thought to be the most intuitive.

Presently, there is no standard definition for *chemical shielding anisotropy* (CSA) in the literature. In this thesis, chemical shielding anisotropy is defined as magnetic shielding at a nucleus which varies when measured in different directions. Since the CS tensor describes the anisotropy of magnetic shielding, a CS tensor with a large span can also be said to have a large CSA, and a CS tensor with a skew different from 1.0 or -1.0 is said to exhibit non-axial CSA. The orientation dependence of chemical shielding observed in powder NMR spectra of stationary samples is implicit in this definition, since it arises from the presence of chemical shielding anisotropy.

### C. Chemical Shift

In practice, NMR spectroscopists measure the chemical shift of a nucleus, which is simply the nuclear magnetic shielding with respect to some reference

compound. For example, in  $^1\text{H}$  and  $^{13}\text{C}$  solution NMR, tetramethylsilane (TMS) is used as a chemical shift standard. Chemical shielding and chemical shift are related as follows:<sup>30</sup>

$$\begin{aligned}\delta &= (v_{\text{sample}} - v_{\text{ref}}) / v_{\text{ref}} \times 10^6 \\ &= \sigma_{\text{ref}} - \sigma_{\text{sample}}\end{aligned}\quad (2.20)$$

The principal components of the chemical shift tensor are defined such that  $\delta_{11} \geq \delta_{22} \geq \delta_{33}$ , where  $\delta_{33}$  corresponds to the most shielded principal component of the chemical shielding tensor. The CS tensor parameters defined above can also be rewritten in terms of the principal components of the chemical shift tensor, with  $\delta_{\text{iso}} = (\delta_{11} + \delta_{22} + \delta_{33})/3$ ,  $\Omega = (\delta_{11} - \delta_{33})$  and  $\kappa = 3(\delta_{22} - \delta_{\text{iso}})/\Omega$ . Under these conventions, the span and skew have identical meanings in terms of the anisotropy and shape of the magnetic shielding tensor, regardless of whether chemical shieldings or chemical shifts are being considered, thus allowing for the interchangeable use of these terms to describe chemical shift anisotropy and chemical shielding anisotropy.

The *absolute chemical shielding* of a nucleus in simple molecules can be determined using procedures outlined by Jameson and Mason.<sup>30,31</sup> These molecules can be used as references for comparing the chemical shieldings and chemical shifts of molecules in which the absolute chemical shielding is unknown. This is useful for comparing theoretically calculated chemical shieldings to experimentally known chemical shifts. Absolute chemical shielding scales have been established for many of the important NMR-active nuclei.<sup>30</sup> The relationship between chemical shielding and chemical shift for phosphorus<sup>32</sup> is shown in Fig. 2.4.

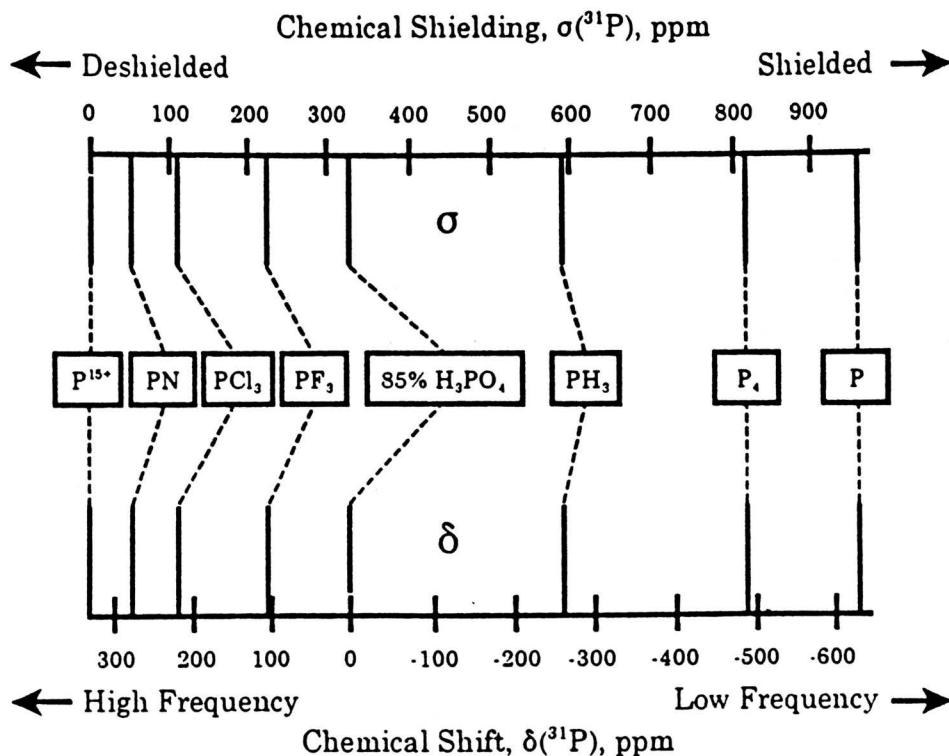


**Figure 2.4** Comparison of the absolute chemical shielding and chemical shift scales for phosphorus. The standard chemical shift reference is 85%  $\text{H}_3\text{PO}_4(\text{aq})$ , with  $\delta_{\text{iso}} = 0.0$  ppm and  $\sigma_{\text{iso}} = 328.35$  ppm.<sup>32</sup>

## 2.2.4 The Direct Dipolar Interaction

The direct dipolar interaction<sup>33</sup> is akin to the classical interaction between magnetic dipoles, and plays important roles in determining the appearance of the NMR line shapes of stationary samples as well as in nuclear relaxation. The dipolar hamiltonian for two spins,  $I$  and  $S$ , can be written in a similar form to the CS hamiltonian,

$$\mathcal{H}_D = \mathbf{I} \cdot \mathbf{D} \cdot \mathbf{S} \quad (2.21)$$

where  $\mathbf{D}$  is the dipolar coupling tensor,

$$\mathbf{D} = hR_{\text{dd}} \begin{bmatrix} (1 - 3x^2) & -3xy & -3xz \\ -3xy & (1 - 3y^2) & -3yz \\ -3xz & -3yz & (1 - 3z^2) \end{bmatrix} . \quad (2.22)$$

In the absence of molecular motion,  $\mathbf{D}$  is a symmetric, traceless tensor. In a completely general coordinate system, this interaction is written as

$$\mathcal{H}_{\text{D}} = hR_{\text{dd}}[\mathbf{I} \cdot \mathbf{S} - 3(\mathbf{I} \cdot \mathbf{r}_{IS})(\mathbf{S} \cdot \mathbf{r}_{IS})/r_{IS}^2] . \quad (2.23)$$

Here,  $R_{\text{dd}}$  is the *direct dipolar coupling constant*, and is given by

$$R_{\text{dd}} = \left( \frac{\mu_0}{4\pi} \right) \frac{\gamma_I \gamma_S \hbar}{2\pi} \langle r_{IS}^{-3} \rangle \quad (2.24)$$

where  $r_{IS}$  is the internuclear separation. It is important to note that the magnitude of  $R_{\text{dd}}$  is dependent upon the inverse cube of the motionally-averaged internuclear distance, designated by  $\langle r_{IS}^{-3} \rangle$ . In rigid systems, measurements of the dipolar coupling constant can be used to infer internuclear distances, in the absence of anisotropic indirect spin-spin interactions (*vide infra*).

The direct dipolar hamiltonian is often expanded in terms of spherical polar coordinates, to give the dipolar "alphabet" hamiltonian:<sup>17</sup>

$$\mathcal{H}_D = hR_{dd}(A + B + C + D + E + F)$$

where

$$\begin{aligned} A &= I_z S_z (1 - 3\cos^2\Theta) \\ B &= - (1/4)(I_+ S_- + I_- S_+)(1 - 3\cos^2\Theta) \\ C &= - (3/2)(I_+ S_z + I_z S_+) \sin\Theta \cos\Theta \exp(-i\Phi) \\ D &= - (3/2)(I_- S_z + I_z S_-) \sin\Theta \cos\Theta \exp(i\Phi) \\ E &= - (3/4)(I_+ S_+) \sin^2\Theta \exp(-2i\Phi) \\ F &= - (3/4)(I_- S_-) \sin^2\Theta \exp(2i\Phi) \end{aligned} \quad (2.25)$$

where  $I_z$ ,  $I_+$ ,  $I_-$ ,  $S_z$ ,  $S_+$  and  $S_-$  are nuclear spin operators, and  $\Theta$  and  $\Phi$  are polar angles describing the orientation of the dipolar vector,  $\mathbf{r}_{IS}$ , with respect to the external magnetic field. Term  $A$  is referred to as the secular dipolar coupling. For heteronuclear two-spin systems at high magnetic fields,  $A$  is the only term that contributes to perturbations in the Zeeman hamiltonian, and therefore to changes in transition frequencies and line intensities. The flip-flop term,  $B$ ; the single quantum terms  $C$  and  $D$ ; and the double-quantum terms,  $E$  and  $F$ ; cause mixing of the Zeeman states, and can make significant contributions to nuclear magnetic relaxation.

Dipolar interactions between  $I$  and  $S$  result in  $2S + 1$  orientation-dependent splittings in solid-state NMR spectra of  $I$ . The presence of dipolar splittings can be beneficial, providing information on the orientation dependence of chemical shielding and dipolar interactions within the molecular frame, and as mentioned, yielding information on internuclear distances. In isotropic solution, dipolar interactions are averaged to zero by the rapid tumbling of the molecules. The effects of the dipolar interaction on NMR spectra of stationary samples is discussed in Chapter 5. Dipolar couplings between many abundant nuclei (e.g.,  $^1\text{H}$ ) and a dilute

nucleus (e.g.,  $^{13}\text{C}$ ) can result in a complicated powder pattern and severe broadening of the spectrum. Fortunately, methods are available for the suppression of such undesirable interactions, such as high-power proton (or abundant-spin) decoupling and magic-angle spinning. These methods are discussed later in this chapter.

### 2.2.5 Indirect Spin-Spin Interactions

The indirect spin-spin hamiltonian describing  $J$ -coupling between  $I$  and  $S$  can be expressed as

$$\mathcal{H}_J = h\mathbf{I} \cdot \mathbf{J} \cdot \mathbf{S} \quad (2.26)$$

where the  $\mathbf{J}$  tensor describes orientation dependence of the  $J$ -coupling with respect to the magnetic field. The  $\mathbf{J}$  tensor is a general second-rank tensor; however, for the purpose of this discussion it will be assumed that the  $\mathbf{J}$  tensor is axially symmetric with the unique component coincident with  $\mathbf{r}_{IS}$ . In contrast to the direct dipolar tensor, the trace of the  $\mathbf{J}$  tensor is non-zero.<sup>33</sup> The isotropic average of the  $\mathbf{J}$  tensor, given by  $(1/3)\text{Tr}(\mathbf{J})$ , is the isotropic  $J$ -coupling,  $J_{\text{iso}}$ . The anisotropy of the  $\mathbf{J}$  tensor is denoted as  $\Delta J$ , and is defined as

$$\Delta J = J_{\parallel} - J_{\perp} \quad (2.27)$$

Solid-state NMR is capable of eliciting information on the magnitude of  $\Delta J$ ; however, it has an identical orientation dependence to the dipolar coupling tensor.<sup>33,34</sup> Thus, contributions to line shape from  $R_{\text{dd}}$  and  $\Delta J$  are impossible to separate, and the two parameters are often treated together using the *effective dipolar coupling constant*

$$R_{\text{eff}} = R_{\text{dd}} - \Delta J/3 \quad . \quad (2.28)$$

Indirect spin-spin coupling between  $I$  and  $S$  results in splitting of the peak in the  $I$  spectrum into  $2S + 1$  evenly spaced lines, and vice versa. Unlike the dipolar interaction, the indirect spin-spin coupling is not averaged to zero by fast, random motion; thus,  $J_{\text{iso}}$  can be observed in both solution and solid-state NMR spectra.

## 2.3 The Quadrupolar Interaction

### 2.3.1. The Quadrupolar Nucleus

One focus of this thesis is quadrupolar nuclei, and as such, the quadrupolar interaction is discussed in more detail than previous interactions. Besides having a nuclear magnetic moment, quadrupolar nuclei possess an electric quadrupole moment, referred to as the *nuclear quadrupole moment*. The interaction of the nuclear quadrupole moment with a nonvanishing electric field gradient (EFG) at the nuclear site results in modification of the Zeeman energy levels, and dominates the appearance of the NMR spectrum. The nature of the EFG depends on the local electronic environment and symmetry about the nucleus. Accordingly, if the characteristics of the EFG can be determined from NMR experiments, much can be learned about the chemistry of a molecule.

Most of the elements in the periodic table have at least one isotope with a quadrupole moment.<sup>35</sup> Quadrupolar nuclei of integer spin have an odd number of both protons and neutrons (there are only seven nuclei with integer spins), while the

remainder of the quadrupolar nuclei have half-integer spins (i.e., 3/2, 5/2, 7/2 and 9/2) resulting from an odd number of total nucleons. Of the quadrupolar nuclei with integer spins, NMR experiments are almost exclusively done on  $^2\text{H}$  and  $^{14}\text{N}$ .

Discussion in this thesis will focus on the properties of half-integer spin nuclei.

Since a majority of the nuclei in the periodic table are quadrupolar nuclei, and because they occur in a vast number of molecular systems, it is of great interest to both chemists and physicists to better understand the nature and properties of quadrupolar nuclei and the effects they generate within such molecules. Most of the isotopes in the periodic table can be examined by radiofrequency methods, with a good number of such studies conducted in the solid state; thus, measurement of quadrupolar interactions is very important in the study of structure and motion in solids.<sup>36</sup>

### 2.3.2 The Nuclear Quadrupole Moment

The non-spherical charge distributions of quadrupolar nuclei give rise to an inherent nuclear property known as the *nuclear quadrupole moment*. Nuclear quadrupole moments are known approximately for most quadrupolar nuclei.<sup>37</sup> The nuclear quadrupole moment is defined with respect to the nuclear spin-axis, with cylindrical symmetry about this axis. If the ellipsoid is lengthened along the direction of the spin axis, the quadrupole moment,  $Q$ , is positive, and the ellipsoid is said to be *prolate*. If the ellipsoid is flattened down this axis, it is an *oblate* spheroid, and  $Q$  is negative (Fig. 2.5). If  $\rho_n(\mathbf{r})$  is the nuclear charge density, then the nuclear quadrupolar moment is defined by

$$eQ = \int \rho_n(\mathbf{r})(3z^2 - r^2) d\mathbf{r} \quad (2.29)$$

which is measured in units of charge. A greater proportion of nuclei have positive  $Q$  values (i.e., prolate). The quadrupole moment can be described by a symmetrical, traceless tensor,  $\mathbf{Q}$ , but is treated as a scalar quantity.<sup>38</sup>

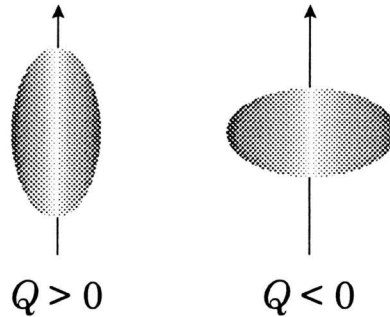


**Figure 2.5** Ellipsoidal shapes of nuclear charge distributions for prolate ( $Q > 0$ ) and oblate ( $Q < 0$ ) nuclear quadrupole moments.

### 2.3.3 The Electric Field Gradient

The EFG at a nucleus arises from the distribution of electronic charge about the nucleus. The EFG is described by a traceless, symmetric tensor,  $\mathbf{V}$ , which has nine elements of the form

$$V_{jk} = \left( \frac{\partial^2 V}{\partial \alpha_j \partial \alpha_k} \right)_0 \quad (2.30)$$

where  $\alpha_{i,j,k} = x, y, z$ .  $\mathbf{V}$  can be written as a symmetrical second-rank tensor with five independent elements, which results from the vanishing trace (i.e. from Laplace's equation,  $\nabla^2 V = 0$  at the nuclear origin) and  $V_{jk} = V_{kj}$ . One can reduce the number of

elements to three, without any loss of generalization, by diagonalizing this matrix with the selection of an appropriate set of orthogonal  $x$ ,  $y$  and  $z$  axes (the so-called principal axis system). The relative magnitudes of the principal components of the EFG tensor are:

$$|V_{33}| \geq |V_{22}| \geq |V_{11}| \quad (2.31)$$

where the  $V_{33}$  is the direction of the maximum field gradient. The two parameters used to describe the tensor  $\mathbf{V}$  in its PAS are the *electric field gradient*,  $eq_{zz} = V_{33}$ , and the asymmetry parameter,  $\eta$ , which is written as

$$\eta = \frac{V_{11} - V_{22}}{V_{33}} \quad (2.32)$$

where  $\eta$  must lie in the range  $0 \leq \eta \leq 1$ . The asymmetry parameter is a measure of deviation from cylindrical symmetry. A *spherically symmetric* EFG (i.e.,  $V_{33} = 0$ , therefore no quadrupolar interaction) occurs in sites of high symmetry such as perfectly octahedral or tetrahedral lattice sites, whereas an *axially symmetric* EFG has  $\eta = 0$  (i.e.,  $V_{11} = V_{22}$ ), and occurs in sites of relatively high symmetry.

### 2.3.4 The Nuclear Quadrupole Interaction

Several excellent articles and texts describe the nuclear quadrupole interaction and its derivation in great detail.<sup>20,38,39,40,41</sup> As well, there are several exceptional sources describing the solid-state NMR of quadrupolar nuclei.<sup>23,35,42,43</sup> The detailed description given in these references is beyond the scope of this thesis.

The brief explanation of the quadrupolar interaction in this section and the discussion on the solid-state NMR spectra of quadrupolar nuclei in following section are derived from the aforementioned reference material.

Nuclear quadrupole moments only interact with very strong electric field gradients; however, it is impossible to produce an external EFG that would have any appreciable interaction with the nuclear quadrupole moment. Strong EFGs exist within molecules, resulting from the interaction of electrostatic charges near the nucleus. It is reemphasized that subtle distortions in molecular or ionic structure significantly alter the magnitude and orientation of the EFG in the molecular frame. Changes in the EFG are observed in the interaction between the nuclear quadrupole moment and the EFG, which is known as the *nuclear quadrupole interaction*.

The general form of the quadrupolar hamiltonian is written in a similar manner to all of the other internal spin interactions, as

$$\mathcal{H}_Q = \frac{e^2Qq}{6S(2S - 1)} \mathbf{S} \cdot \mathbf{V} \cdot \mathbf{S} \quad (2.33)$$

This is expanded into the expression for the quadrupolar hamiltonian in its PAS:

$$\mathcal{H}_Q = \frac{e^2Qq_{zz}}{4S(2S - 1)} \left[ (3S_z^2 - S^2) + \frac{\eta}{2}(S_+^2 + S_-^2) \right] \quad (2.34)$$

where  $S_{\pm} = S_x \pm iS_y$ . The constant  $e^2Qq_{zz}/h$  is referred to as the *nuclear quadrupole coupling constant*, and is denoted by the symbol  $C_Q$ . The nuclear quadrupole coupling constant is often expressed in terms of the *nuclear quadrupolar frequency*,

$$\nu_Q = \frac{3C_Q}{2S(2S - 1)} . \quad (2.35)$$

The above equation can also be expressed in  $\text{rad s}^{-1}$ , with  $\omega_Q = 2\pi\nu_Q$ . The magnitude of the quadrupolar interaction can range from kHz to hundreds of MHz. In this thesis, we investigate cases where the Zeeman interaction is larger than the quadrupolar interaction (i.e.,  $\nu_0 \gg \nu_Q$ ). In this instance the quadrupolar hamiltonian is treated as a small perturbation on the Zeeman hamiltonian.

### 2.3.5 Quadrupolar Nuclei in Magnetic Fields

The quadrupolar hamiltonian is rearranged into a form with components that commute with the Zeeman spin operator,  $S_z$ :

$$\mathcal{H}_Q = \mathcal{H}_Q^{(1)} + \mathcal{H}_Q^{(2)} . \quad (2.36)$$

where  $\mathcal{H}_Q^{(1)}$  and  $\mathcal{H}_Q^{(2)}$  are first- and second-order quadrupolar hamiltonians. Full expressions for these hamiltonians are given elsewhere.<sup>40,42</sup> The effect of the first-order quadrupolar interaction on the NMR spectrum can be written as

$$\nu_{m_S, m_S-1}^{(1)} = (\nu_Q/4) (1 - 2m_S) (3\cos^2\theta - 1 + \eta\sin^2\theta\cos 2\phi) . \quad (2.37)$$

where  $\theta$  and  $\phi$  are polar angles describing the orientation of the EFG tensor with

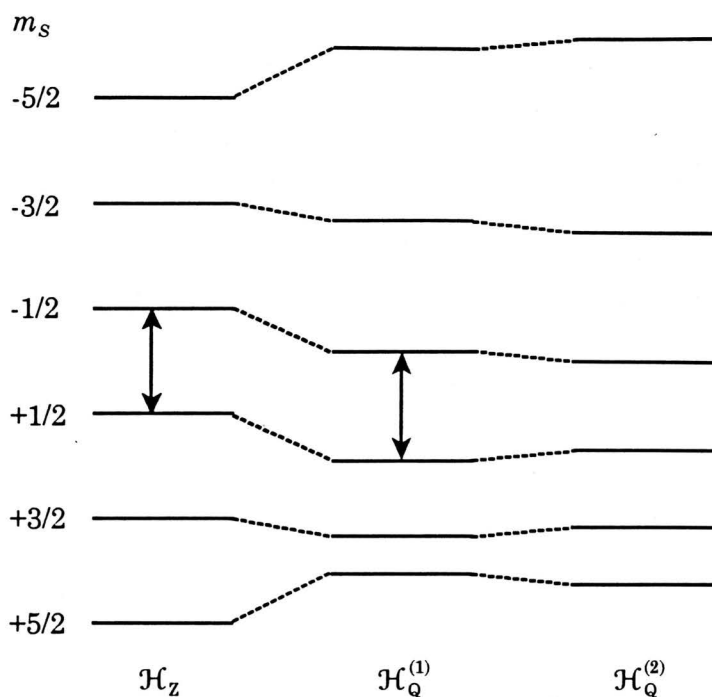


**Figure 2.6** Effects of the first- and second-order quadrupolar interaction on a nucleus with  $S = 5/2$ . The shifts caused by the second-order quadrupolar interaction are exaggerated in this figure.

respect to the applied magnetic field. There are three important implications of this equation. First of all, the *central transition* ( $+1/2 \leftrightarrow -1/2$ ) is not affected by the first-order quadrupolar interaction, since the energy levels of the  $+1/2$  and  $-1/2$  spin states are shifted by the same amount in the same direction (Fig 2.6). Second, the non-central, or *satellite transitions*, are spread out over a range on the order of  $\nu_Q$ . In the presence of a large quadrupolar interaction on the order of MHz, it is therefore common to only observe the central transition. Finally, since there is a geometrical term of  $(3\cos^2\theta - 1)$  present, this interaction can in principle be averaged by rapid magic-angle spinning.

As the quadrupolar interaction becomes larger, the central transition is

dramatically affected by the second-order quadrupolar interaction, resulting in a shift of the isotropic chemical shift away from the centre of gravity of the spectrum (known as the *second-order quadrupole shift*). Since  $\nu_Q$  must be small for satellite transitions to be observed, second-order effects are neglected here. The effects of the second-order quadrupolar interaction on the central transition are given by<sup>35,42</sup>

$$\begin{aligned} \nu_{+1/2,-1/2}^{(2)} &= (\nu_Q^2/12\nu_0)\{(3/2)\sin^2\theta[(A+B)\cos^2\theta - B] \\ &\quad - \eta\cos 2\phi\sin^2\theta[(A+B)\cos^2\theta + B] \\ &\quad + (\eta^2/6)[A - (A+4B)\cos^2\theta - (A+B)\cos^2 2\phi(\cos^2\theta - 1)^2]\} \end{aligned} \quad (2.38)$$

where

$$\begin{aligned} A &= 24m_S(m_S - 1) - 4S(S + 1) + 9 \\ B &= (1/4)[6m_S(m_S - 1) - 2S(S + 1) + 3] \end{aligned} \quad (2.39)$$

The second-order quadrupolar transition cannot be completely averaged by MAS, so the acquisition of isotropic, solution-like spectra of quadrupolar nuclei in the solid-state is difficult. However, techniques such as Double Rotation (DOR),<sup>44</sup> Dynamic Angle Spinning (DAS)<sup>45</sup> and more recently Multiple-Quantum Magic-Angle Spinning (MQMAS)<sup>46</sup> NMR have been developed for such purposes. Nonetheless, MAS still averages the dipolar and anisotropic chemical shielding interactions that may be manifested in the spectra of quadrupolar nuclei (*vide infra*).

NMR powder patterns arise from the random distribution of crystallites with respect to the magnetic field. In each crystallite, the EFG at a particular nucleus is fixed; thus, the powder pattern results from the superposition of frequency and intensity contributions for all combinations of the angles  $\theta$  and  $\phi$ . Powder patterns

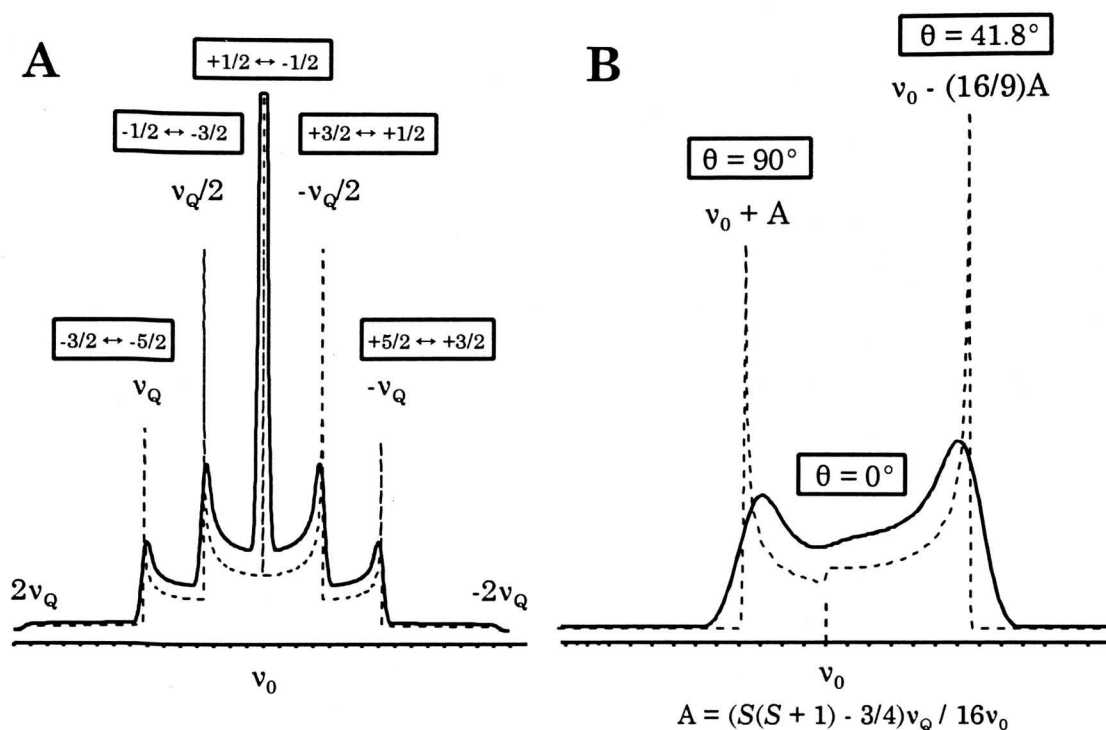


**Figure 2.7** NMR spectra of a quadrupolar nucleus,  $S = 5/2$ , in a stationary sample, with small nuclear quadrupolar interaction (A.), and with a large nuclear quadrupolar interaction (B). Only the central transition is observable in the latter case. Dashed lines show idealized powder patterns with no line broadening. Spectrum (A) results from the superposition of five powder patterns corresponding to transitions between the Zeeman states of the quadrupolar nucleus.

are shown (Fig. 2.7) which depict the effects of the first-order quadrupolar interaction, where all of the transitions are visible, and for the second-order quadrupolar interaction, where only the central transition is observed.

In Fig. 2.7A, the central transition is truncated, and is much more intense than the broadened satellite transitions. The second-order quadrupolar interaction is negligible, since  $\nu_Q$  is very small. The appearance of the spectrum in Fig. 2.7B arises solely from the effect of the second-order quadrupolar interaction on the central transition.

Only the effects of the quadrupolar interaction on the solid-state NMR spectra of quadrupolar nuclei have been discussed in this section. The combined effects of quadrupolar and chemical shielding interactions are considered in Chapter 3. In Chapters 4 and 5, the effects of the quadrupolar interaction on the NMR spectra of spin-1/2 nuclei which are spin-coupled to quadrupolar nuclei are examined.

## 2.4 Techniques in Solid-State Nuclear Magnetic Resonance

### 2.4.1 Magic-Angle Spinning

High-resolution solid-state NMR spectra can be obtained for a variety of nuclei using a combination of magic-angle spinning, cross-polarization and high-power abundant-spin decoupling. As mentioned previously, mechanical rotation of the sample at the magic angle averages anisotropic interactions with the geometrical dependence ( $3\cos^2\Omega - 1$ ), which equals zero if  $\Omega = 54.74^\circ$ .<sup>10,47</sup> Such interactions include anisotropic chemical shielding, weak heteronuclear and homonuclear dipolar interactions and first-order quadrupolar broadening. When the spinning rate,  $\nu_{\text{rot}}$ , is less than the breadth of the anisotropic interaction (in Hz), the MAS NMR spectrum consists of an isotropic peak(s) flanked by a series of *spinning sidebands* (Fig. 2.8), which are separated from one another by a frequency equivalent to  $\nu_{\text{rot}}$ . For nuclei exhibiting chemical shielding anisotropy, the positions and intensities of the spinning sidebands, often referred to as the *spinning sideband manifold*, can be analyzed using the Herzfeld-Berger method to yield the principal

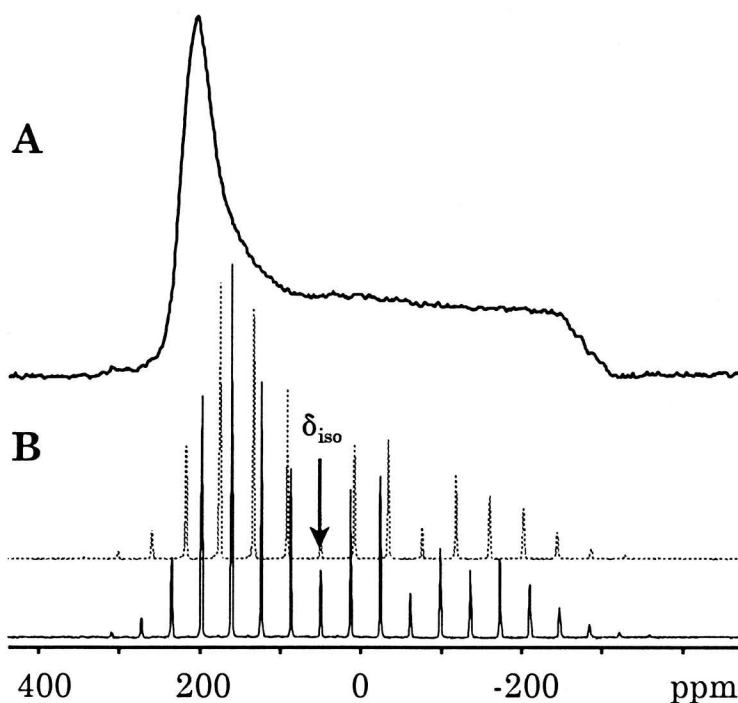


**Figure 2.8** (A)  $^{31}\text{P}$  NMR spectrum of a stationary sample of (2,4,6-tri-*t*-butylphenyl)P=N-OSO<sub>2</sub>CF<sub>3</sub> at 4.7 T. (B) Overlaid  $^{31}\text{P}$  CPMAS NMR spectra at  $\nu_{\text{rot}} = 3010$  Hz (lower trace) and  $\nu_{\text{rot}} = 3405$  Hz (upper trace).

components of the chemical shift tensor.<sup>48</sup>

## 2.4.2 High-Power Decoupling

High-power decoupling is normally applied in solid-state NMR spectra to suppress large direct dipolar interactions between dilute nuclei (e.g.,  $^{15}\text{N}$ ,  $^{31}\text{P}$ , etc.) and abundant nuclei (e.g.,  $^1\text{H}$ ,  $^{19}\text{F}$ ).<sup>49,50,51,52</sup> Decoupling also has the effect of removing indirect spin-spin coupling interactions between nuclei. For proton decoupling, a strong, continuous wave (CW) rf field is applied at or near the  $^1\text{H}$  Larmor frequency. The efficiency of decoupling is determined by (i) the amplitude of  $\nu_{1\text{H}}$  compared with the heteronuclear dipolar interaction and (ii) modulation of the

heteronuclear dipolar interaction by mutual spin flips, or *spin diffusion* of the abundant nuclei. Decoupling efficiency is measured by the peak widths in the NMR spectrum of the dilute nucleus. Factors such as thermal motion in the solid<sup>18</sup> and rf transmitter offset<sup>51</sup> for the abundant spin can have deleterious peak broadening effects. Large decoupling fields (> 100 kHz) are necessary to remove the dipolar coupling between <sup>1</sup>H and common nuclei such as <sup>13</sup>C, <sup>27</sup>Al and <sup>31</sup>P, corresponding to power outputs on the order of hundreds of watts.

### 2.4.3 Cross Polarization

Cross polarization refers to the NMR technique for transferring abundant spin polarization to dilute spins, where the abundant and dilute spins are dipolar coupled.<sup>13,53,54</sup> The benefits are two-fold: first, the signal intensity of the dilute spin is increased, optimally by a factor equal to  $\gamma_{\text{abund}}/\gamma_{\text{dilute}}$ . For example, <sup>1</sup>H CP to <sup>13</sup>C can result in a signal intensity gain of approximately  $\gamma_{1\text{-H}}/\gamma_{13\text{-C}} \approx 4$ . Second, and more important, the spin-lattice relaxation times of the dilute nuclei are not important for determining the length of the relaxation delay,  $\tau_R$ , between acquisitions; rather, the  $T_1$  of the abundant nucleus is the rate-determining factor. For protons, the spin-lattice relaxation times are generally much shorter than for nuclei such as <sup>13</sup>C, <sup>15</sup>N and <sup>31</sup>P. Thus, solid-state CP NMR experiments on samples with dilute nuclei possessing long  $T_1$ 's are subject to better S/N and reduced experimental time. In this section, <sup>1</sup>H are the abundant spins and <sup>13</sup>C the dilute spins, for ease of discussion.

A typical CP pulse sequence is pictured in Fig. 2.9. In the rotating frame, the

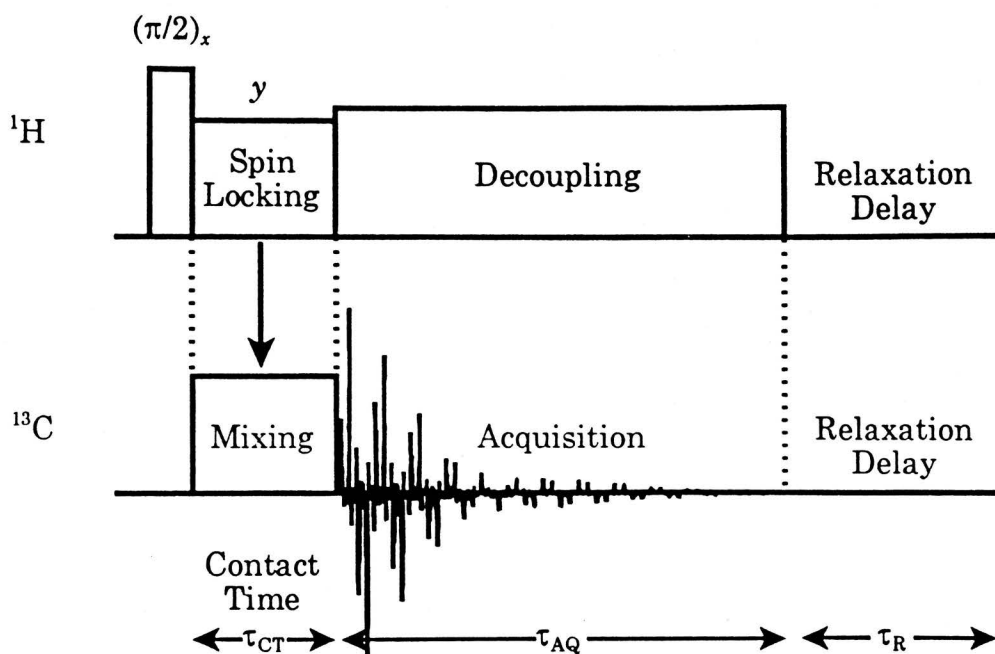
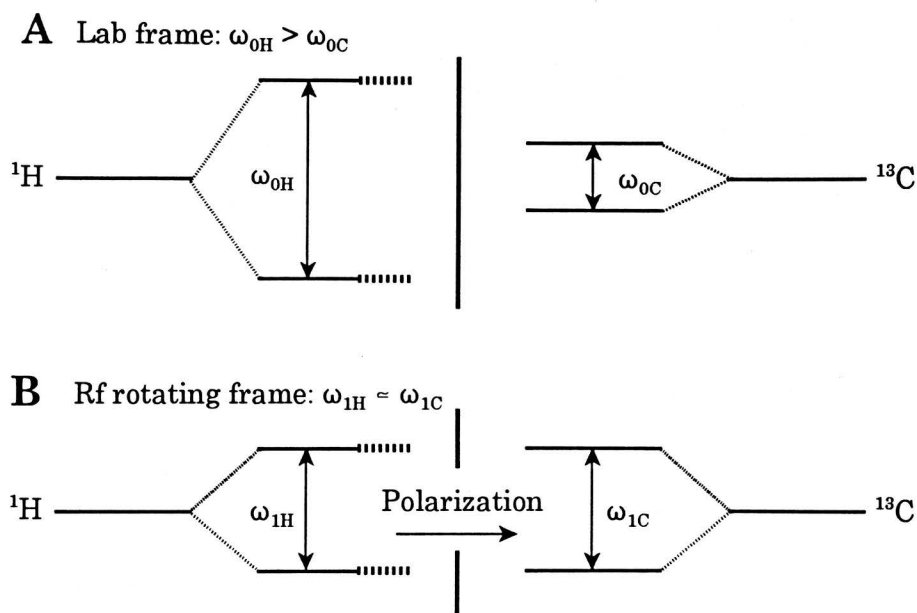


Figure 2.9 Pulse sequence for cross polarization in the solid state.

$(\pi/2)_x$  pulse tips the  $^1\text{H}$  magnetization along into the  $y$ -direction, where it is then *spin locked*. While the  $^1\text{H}$  magnetization is spin locked, an rf pulse is applied on the  $^{13}\text{C}$  channel which spin locks the  $^{13}\text{C}$  magnetization. The period of spin locking is known as the *contact time*,  $\tau_{\text{CT}}$ , and is usually on the order of milliseconds. The amplitudes of the  $^1\text{H}$  and  $^{13}\text{C}$  rf fields are matched so that the frequencies are equivalent, i.e.,  $\omega_{1\text{H}} \approx \omega_{1\text{C}}$ , or

$$\gamma_{\text{H}} B_{1\text{H}} = \gamma_{\text{C}} B_{1\text{C}} \quad (2.40)$$

which is known as the Hartmann-Hahn condition.<sup>13</sup> During the contact time, spin polarization is transferred from the protons to the carbon nuclei. High-power decoupling is normally applied on the  $^1\text{H}$  channel, while acquisition is carried out on



**Figure 2.10** Schematic diagram of Zeeman states in (A) the laboratory frame and (B) in the rf rotating frame, where cross polarization can occur. The hatched lines of the  $^1\text{H}$  spin states represent broadening due to H-H dipolar interactions.

the  $^{13}\text{C}$  channel, for time  $\tau_{\text{Aq}}$ .

The schematic diagram depicting the mechanism of cross polarization is given in Fig. 2.10.<sup>54</sup> Cross polarization involves flip-flop transitions or mutual spin flips of dipolar-coupled heteronuclear spin pairs. Protons and carbon nuclei subject to the Zeeman interaction have very different Larmor frequencies, and the probability of mutual spin flips resulting from dipolar coupling is very low (Fig. 2.10A).<sup>54</sup> In the presence of rf fields for both nuclei, the total hamiltonian of each becomes oscillatory time dependent in the lab frame. The interaction of the spin systems can be considered in a different frame of reference, known as the *doubly rotating frame* (Fig. 2.10B). In this frame, the oscillatory time dependence of the rf fields disappears, and the Zeeman splittings in the rf rotating frame are given by

$\omega_{1H}$  and  $\omega_{1C}$ . Under the Hartmann-Hahn matching condition, the Zeeman splittings for protons and carbon nuclei are equal, hence energy transfer from the abundant spin reservoir to the dilute spin occurs.

#### 2.4.4. Solid-State NMR of Quadrupolar Nuclei - Practical Considerations

In this section, some general concerns regarding the acquisition of solid-state NMR spectra are outlined, as they pertain to the aluminum complexes examined in this thesis.<sup>43,55</sup> Excitation of quadrupolar nuclei and pulse response are considered, along with necessary delays in the pulse sequence to acquire proper NMR spectra.

The choice of proper pulse widths and amplitudes is very important for obtaining undistorted spectra, since quadrupolar nuclei have several transitions which must be uniformly excited. In the case of a small quadrupolar interaction on the order of kHz, it is sometimes possible to apply a strong rf field, such that  $\omega_{rf} > \omega_Q$ . In this case, all of the transitions can be uniformly excited; this is referred to as *non-selective excitation*. In the aluminum complexes in this thesis, the quadrupolar interactions are on the order of MHz, and  $\omega_{rf} \ll \omega_Q$ , and only the central ( $+1/2 \leftrightarrow -1/2$ ) transition is prominent. In this case, *selective excitation* of the central transition must be applied. The signal intensity is modulated as a function of pulse length,  $\tau_p$ , and applied rf field,  $\omega_{rf}$ , in both cases. The signal intensity in the case of non-selective excitation is given as  $F(\tau_p) = [3(S+1/2)/4S(S+1)]\sin(\omega_{rf}\tau_p)$ . For selective excitation, the intensity is reduced by a factor of  $S+1/2$ :  $F(\tau) = [3/4S(S+1)] \cdot \sin((S+1/2)\omega_{rf}\tau_p)$ .<sup>42,55</sup>

The relationship between pulse width, rf field amplitude and the pulse tip

angle for a particular quadrupolar nucleus and NMR spectrometer can be determined using a model compound with a very small quadrupolar interaction, or on a solution sample. The  $90^\circ$  pulse and corresponding rf frequency,  $\omega_{\text{rf}} = 2\pi\nu_{\text{rf}}$  can be easily determined for samples where non-selective excitation can be applied, since the response of the system to pulses will be similar to that of a spin-1/2 nucleus. Signal intensities resulting from non-selective and selective excitation experiments become equivalent in the limit  $\sin(\theta_p) \approx \theta_p$ . Therefore, for the samples requiring selective excitation, the proper pulse length resulting in high intensity and uniform excitation of the central transition is given by  $\tau_p \leq (\pi/2)/2\pi\nu_{\text{rf}}(S+1/2)$  (i.e.,  $90^\circ$  non-selective pulse widths are reduced by a factor of  $S + 1/2$ ).<sup>42,55</sup> To uniformly excite a large bandwidth (e.g.,  $> 50$  kHz), the rf field,  $\nu_{\text{rf}}$  must be larger than the region of interest; hence pulse widths must be very short (usually between 0.5 and 2  $\mu\text{s}$ ).

Another important consideration is the *pre-acquisition delay*, which is the length of time between the pulse and the acquisition. When a rf pulse is applied, only a very small fraction of the pulse energy is taken up by the spins, which is stored for the time  $T_1$ , and observable for the time  $T_2^*$ . The latter time corresponds to an effective spin-spin relaxation time, in which the transverse magnetization decays due to magnetic field inhomogeneity ( $T_2^* < T_2$ ). The remaining pulse energy is stored in the rf circuitry, and released during a span of time known as the *dead time*. The dead time, which is of great significance in NMR experiments, is the time during which no signal is detectable, due to the presence of the excess pulse energy in the receiver coil and corresponding decay to amplitudes on the order of NMR signals.<sup>56</sup> The electronic dead time, which is dependent only on the electronic

circuitry of the probe, is given by  $\tau_{\text{dead}} = 20Q_F/2\pi\nu_0$ ,<sup>57</sup> where  $Q_F$  is the quality factor of the probe (higher quality factors are desirable for high power pulses needed to excite large bandwidths and better sensitivity, so there is a trade-off). Typical dead times in experiments in this thesis are on the order of microseconds. Thus, for samples with long values of  $T_2^*$ , or at high frequencies, the dead time is not always a crucial factor. However, for quadrupolar nuclei which have very short  $T_2^*$  values, or for nuclei with small Larmor frequencies, the signal can often substantially decay during the pre-acquisition delay, resulting in odd spectral artifacts and loss of signal. Very short dead times are therefore desirable, though not always achievable on modern-day NMR spectrometers.

A way around this problem is the use of *spin echoes*,<sup>58</sup> which involve pulse sequences of the form:  $\pi/2 - \tau_1 - \pi - \tau_2 - \tau_{\text{AQ}}$ , where  $\tau_1$  and  $\tau_2$  are delays on the order of tens of microseconds. Acquisitions of spin echoes, and subsequent left shifting and transform of the free-induction decay (FID) can lead to spectra of central transitions which are relatively free of peak and baseline distortions. Another option is linear back-prediction methods, which can fill in missing points at the start of the FID. For the aluminum complexes studied in this thesis, single-pulse selective excitation experiments could be used, since  $T_2^*$  values are longer than the experimental dead times. However, for the gallium complexes discussed in Chapter 6, and for cobalt complexes in Appendix B, spin-echo pulse sequences had to be applied.

## 2.5 *Ab Initio* Calculations of Chemical Shielding Parameters

A significant portion of this thesis is dedicated to the theoretical

determination of chemical shielding parameters. There are many articles and reviews in the literature which give detailed background on *ab initio* calculations of CS parameters, and methods by which they are calculated.<sup>59,60,61,62,63,64</sup> It is the intent of this section of the thesis to show (i) why *ab initio* calculations were utilized in this work, (ii) what techniques were used for calculating chemical shieldings, and (iii) important factors which influence the results of shielding calculations.

*Ab initio* calculations of chemical shielding tensors represent one of the most rigorous tests of current computational schemes, and are an exceptional complement to experimentally determined data. Comparison of experimental and theoretical CS tensors, as opposed to just the isotropic chemical shifts, provide an excellent measure of the quality of the calculation. At the present levels of theory, *ab initio* calculations do not usually provide very accurate CS tensor principal components in larger systems; nonetheless, qualitative trends can be reproduced, such as how the CS tensor changes upon altering the chemistry or geometry of a molecule. CS calculations are remarkably useful for predicting the orientation of the CS tensor in the molecular frame.<sup>65</sup> This is useful in situations where the orientation of the CS tensor cannot be determined directly from the solid-state NMR spectra, or for comparison with systems in which the CS tensor orientation is partially or fully known from experiment.

The gauge-including atomic orbital (GIAO) method<sup>66</sup> is used for all of the CS calculations reported in this thesis, as implemented in the Gaussian 94 suite of programs.<sup>67</sup> The GIAO approach is a non-relativistic coupled Hartree-Fock method, which employs atomic basis functions with the local gauge origin positioned at the

centre of the orbital. In the Gaussian 94 software package, the GIAO method can be used with the standard restricted Hartree-Fock (RHF) level of theory, or with density functional theory (DFT). DFT accounts for electron correlation in a semi-empirical fashion, and should, in theory, provide systematically better results than corresponding RHF calculations.<sup>60,63</sup> However, the DFT correlation functional does not include any perturbation accounting for an external magnetic field.<sup>60,68</sup> Other common coupled Hartree-Fock approaches for calculating chemical shielding include the individual gauge for localized orbitals (IGLO)<sup>69</sup> and localized orbital/localized origin (LORG)<sup>70</sup> methods, which have gauge origins in localized molecular orbitals; and the continuous set of gauge transforms (CSGT) method of Keith and Bader, which is based on the individual gauges for atoms in molecules (IGAİM) method.<sup>71</sup>

There are several important factors to consider before proceeding with CS calculations.<sup>60</sup> The first is the level of theory at which the calculations are performed. For example, in situations where electron correlation may be very important, it would be unwise to simply use RHF calculations. For very large systems, DFT calculations may be preferred, since they require less CPU time than RHF calculations. Second is the choice of *basis set*, which can drastically influence the calculated parameters. Calculations carried out on atoms like carbon, nitrogen and phosphorus, or on systems with multiple bonds, require that large basis sets like 6-31G\* and 6-311G\* be used. For smaller systems, larger basis sets are desirable since the degree of gauge independence increases with larger basis sets. The third factor is the geometry of the system under investigation. If the molecular geometry of the system is unknown, geometry optimization calculations of the

molecule may be carried out. For larger molecules which have known crystal structures, it is possible to use these geometries for chemical shielding calculations. It is *crucial* to mention at this juncture that calculations are normally performed on isolated molecules with rigid structures, and do not take into account intermolecular effects and solid-state interactions such as crystal packing forces, vibrations, etc. Thus, it is expected that some of the difference between experimental CS tensors determined by solid-state methods and theoretical “isolated molecule” CS tensors can be accounted for by the very different physical environments. The final consideration is of relativistic effects and calculations involving heavy atoms (in this case, the fourth row of the periodic table and beyond). In this work, CS tensors are not reported for heavy atoms, but are reported for molecules containing heavy atoms. Heavy atoms can be treated at an elementary level by the use of *effective core potentials* (ECPs),<sup>72</sup> in which inner shells of electrons are treated with an approximate method, and some relativistic effects are included.

On a final note, some *ab initio* calculations of EFG tensors are also included in this thesis. EFG tensors are dependent only upon the ground-state of the molecule, and are therefore easily calculated in comparison to CS tensors. They serve the same functions as the theoretical CS tensors, in helping to confirm and/or determine tensor orientations, and to observe changes in the EFG with alterations in molecular structure and chemistry. The EFG is a local property, and is very sensitive to the basis set.<sup>73</sup> Thus, very large basis sets must be applied for calculations of EFG tensors, which makes calculations on atoms beyond the third row of the periodic table impractical.

## Chapter 3

# Aluminum Chemical Shielding Anisotropy

### 3.1 Introduction

The aluminum-27 nucleus (nuclear spin  $I = 5/2$ ) is well suited for solid-state NMR studies,<sup>74</sup> due to its high natural abundance (100%), relatively large magnetic moment and small nuclear quadrupole moment.<sup>37</sup> For materials in which  $C_Q(^{27}\text{Al})$  is on the order of MHz, it is possible to easily obtain and analyze solid-state  $^{27}\text{Al}$  magic-angle spinning NMR spectra, since the central transition ( $+1/2 \leftrightarrow -1/2$ ) is dependent only upon the second-order quadrupolar interaction and the isotropic chemical shift.<sup>74</sup> Solid-state  $^{27}\text{Al}$  NMR has especially found use in materials science for the study of a variety of substances including zeolites, ceramics, cements, glasses, etc.<sup>74,75,76,77</sup> Numerous isotropic  $^{27}\text{Al}$  chemical shifts have been reported, indicating a chemical shift range of ca. 300 ppm;<sup>78,79</sup> however, there are very few reports of  $^{27}\text{Al}$  chemical shielding anisotropy in the literature. In contrast, carbon-13 chemical shift anisotropies have been reported for hundreds of compounds even though the  $^{13}\text{C}$  chemical shift range is comparable to that of  $^{27}\text{Al}$ .<sup>80</sup>

Samoson and coworkers reported the first evidence of  $^{27}\text{Al}$  CSA in a study of trialuminum tris(orthophosphate) hydrate,  $\text{AlPO}_4 \cdot 2\text{H}_2\text{O}$ , which contains one tetrahedral and two pentacoordinate aluminum sites.<sup>81</sup> They found that it was difficult to simulate NMR spectra of the pentacoordinate sites without including orientation-dependent chemical shifts; however, the overlap of signals arising from

chemically distinct sites rendered an exact determination of the magnitude of the CSA impossible. Recently, Vosegaard and Jakobsen reported aluminum CSA in sapphire ( $\alpha$ -Al<sub>2</sub>O<sub>3</sub>).<sup>82</sup> From single-crystal <sup>27</sup>Al NMR experiments, they were able to determine the magnitude of the CSA as well as the orientations of the aluminum CS and EFG tensors in the molecular frame. Aside from these examples of aluminum CSA, the only other interaction which influences the line shape of solid-state NMR spectra in a similar fashion is the Knight shift,<sup>83</sup> which has been observed in the <sup>27</sup>Al NMR spectra of binary aluminum-metal alloys.<sup>84</sup> However, the Knight shift is only functional in conducting or semiconducting materials.

Only a handful of *ab initio* calculations of <sup>27</sup>Al chemical shieldings have appeared in the literature,<sup>85</sup> with no reports of theoretical <sup>27</sup>Al CS tensors. Recent *ab initio* studies have focussed either on first-row elements<sup>86</sup> or <sup>31</sup>P chemical shielding tensors.<sup>87</sup>

In this chapter, several new examples of <sup>27</sup>Al chemical shielding anisotropy are characterized in systems of varying geometry, including molecules with aluminum in a pseudo-tetrahedral environment, in pseudo-octahedral environments, and in linear molecules. The magnitude of the <sup>27</sup>Al CSA is shown to be extremely dependent upon molecular geometry. Aluminum CS and EFG tensors are characterized by combinations of experimental and theoretical methods. A summary of known aluminum CSAs and associated quadrupolar parameters is given in Table 3.1.

Our research group has recently submitted a report of <sup>27</sup>Al CSA in aluminum trichloride phosphoryl trichloride, Cl<sub>3</sub>AlOPCl<sub>3</sub> (I).<sup>88</sup> The results of this study are

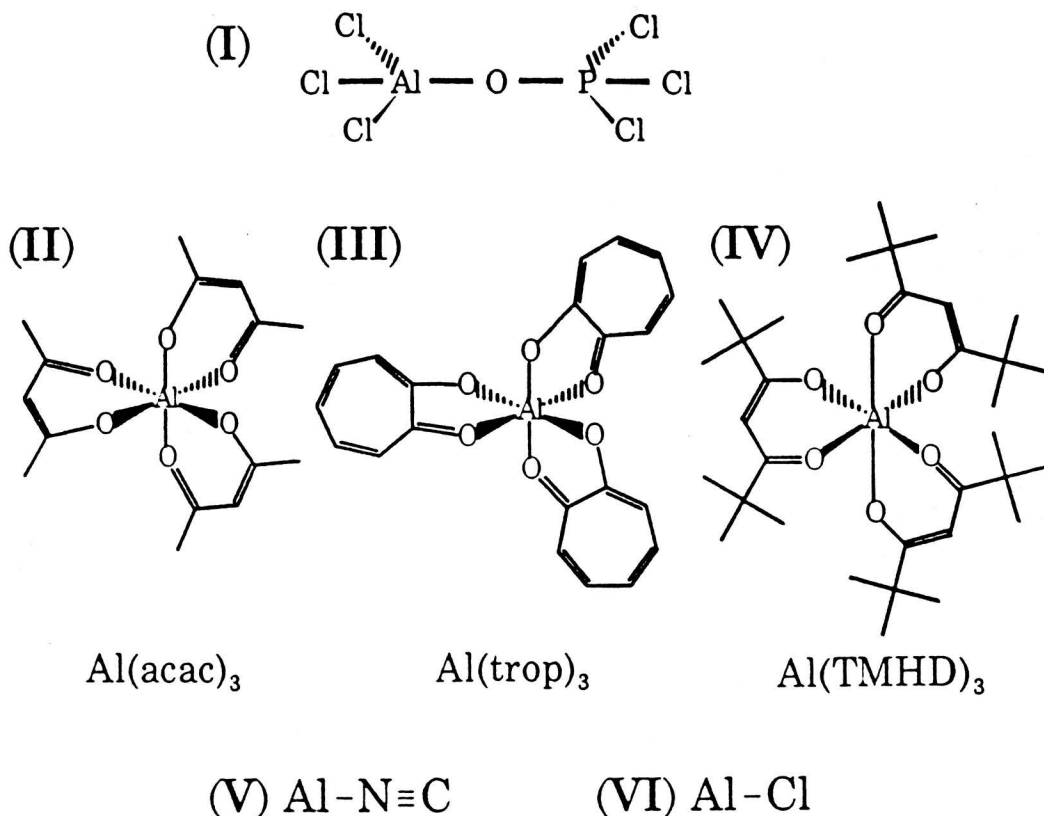


Figure 3.1 Complexes exhibiting aluminum chemical shielding anisotropy.

discussed in Section 3.3 of this chapter. This is the first definitive example of  $^{27}\text{Al}$  chemical shielding anisotropy determined from solid-state NMR spectra of a polycrystalline powder.  $\text{Cl}_3\text{AlOPCl}_3$  and other analogous systems, (Group 13 Lewis acid - phosphine oxide complexes) have been of interest for over one-hundred years.<sup>89,90</sup> Compound I is of particular interest, since the P-O-Al bond angle is close to  $180^\circ$  and the molecule has a near- $C_{3v}$  symmetry (Fig. 3.1).<sup>91</sup> The effects of the  $^{27}\text{Al}$  CSA, the nuclear quadrupole interaction and the relative orientation of the chemical shielding and electric field gradient tensors on the appearance of the  $^{27}\text{Al}$  NMR spectra are discussed in detail. Comparison of experimentally determined and theoretically calculated CS and EFG tensors at aluminum provides information on

the orientations of these tensors in the molecular frame.

Other new examples of  $^{27}\text{Al}$  CSA characteristic of two extremes are also presented in this chapter - small values in pseudo-octahedral complexes (Section 3.3) and relatively large values in diatomic and linear triatomic molecules (Section 3.4).<sup>92</sup> The small  $^{27}\text{Al}$  CSAs observed in the octahedrally-coordinated aluminum complexes tris(acetylacetonato)aluminum(III),  $\text{Al}(\text{acac})_3$  (II), tris(tropolonato)aluminum(III),  $\text{Al}(\text{trop})_3$  (III), and tris(2,2,6,6-tetramethyl-3,5-heptanedionato)aluminum(III),  $\text{Al}(\text{TMHD})_3$  (IV), are obtained from  $^{27}\text{Al}$  NMR spectra of stationary samples at three different fields. The orientation of the CS and EFG tensors are inferred by the high molecular symmetry, and by comparison with theoretically calculated interaction tensors.

Previously measured  $^{27}\text{Al}$  nuclear spin-rotation constants for aluminum (I) isocyanide,  $\text{AlNC}$  (V),<sup>93,94</sup> and aluminum (I) chloride,  $\text{AlCl}$  (VI),<sup>95</sup> are utilized to calculate the  $^{27}\text{Al}$  CS tensor parameters for these molecules. It is interesting to note that the large spans of these CS tensors ( $\Omega > 400$  ppm, *vide infra*) are comparable to the entire  $^{27}\text{Al}$  CS range. RHF and DFT calculations of the  $^{27}\text{Al}$  CS tensors and the EFG at the aluminum nucleus were also done on these systems, as well as for two complementary systems,  $\text{AlF}$  and  $\text{AlH}$ . Variation in chemical shielding tensor parameters are described qualitatively in terms of molecular orbital theory.

## 3.2 Experimental

### 3.2.1. Solid-State $^{27}\text{Al}$ NMR of $\text{Cl}_3\text{AlOPCl}_3$

The  $\text{Cl}_3\text{AlOPCl}_3$  (I) complex was synthesized by A.D. Phillips. Equimolar amounts of  $\text{OPCl}_3$  and  $\text{AlCl}_3$  were combined in  $\text{CH}_2\text{Cl}_2$  under an inert atmosphere, and recrystallized from the same solvent.<sup>91</sup> Solid-state aluminum-27 MAS NMR spectra and spectra of a stationary sample of I were acquired at  $B_0 = 4.7$  T and 9.4 T on Bruker MSL-200 and AMX-400 NMR spectrometers, respectively. Crystals of I were powdered and packed into 4 mm and 7 mm o.d. zirconium oxide rotors under an inert atmosphere. MAS spectra were acquired with spinning rates between 2.5 and 8 kHz. Aluminum-27 chemical shifts were referenced with respect to  $\text{Al}(\text{H}_2\text{O})_6^{3+}(\text{aq})$  ( $\delta_{\text{iso}}(^{27}\text{Al}) = 0$  ppm) in a solution of 0.1 M  $\text{Al}(\text{NO}_3)_3(\text{aq})$ . The aqueous standard was also used to determine the  $90^\circ$  pulse for  $^{27}\text{Al}$  ( $3.5 \mu\text{s}$ ,  $\nu_{\text{rf}} \sim 70$  kHz), which was then set at  $1.0 \mu\text{s}$  for the solid samples. Dead times of up to  $20 \mu\text{s}$  were applied. Relaxation delays of 4 to 6 s were used with approximately 3400 and 9100 transients accumulated for MAS and static  $^{27}\text{Al}$  spectra, respectively. Peaks were broadened by 100 Hz (MAS) and 400 Hz (stationary sample) with exponential multiplication of the FID. NMR spectra were simulated with the program WSolids, which was developed in this laboratory. This program incorporates the space-tiling method of Alderman, Solum and Grant as an efficient means of simulating solid-state NMR powder patterns.<sup>96</sup>

### 3.2.2. Solid-State $^{27}\text{Al}$ NMR of Octahedral Aluminum Complexes

Tris(acetylacetonato) aluminum(III) (IUPAC name: tris-(2,4-pentanedionato-*O,O'*)aluminum) and tris-(2,2,6,6-tetramethyl-3,5-heptanedionato)-aluminum(III), both 99.5 % pure, were obtained from Aldrich and used without any further purification. Tris(tropolonato) aluminum (III) (IUPAC name: tris-(2-hydroxybenzaldehydato-*O,O'*)aluminum) was synthesized by R. Warren according to a procedure in the literature<sup>97</sup> and recrystallized from methanol.

Solid-state  $^{27}\text{Al}$  NMR spectra were acquired at 4.7 T, 9.4 T and 18.8 T ( $\nu_0(^{27}\text{Al}) = 52.13, 104.26$  and  $208.49$  MHz) on Bruker MSL-200, AMX-400 and DSX-800 NMR spectrometers, respectively. The highest field spectra were obtained by H. Foerster of Bruker, Germany. MAS NMR spectra were acquired with samples at spinning rates ranging from 4.0 to 10.5 kHz, with the accumulation of 256 to 2048 scans. For stationary samples, 1000 to 10000 transients were accumulated. All spectra were acquired with the application of high-power proton decoupling. Aluminum chemical shift referencing and determination of the  $90^\circ$  pulse in solution were done as described above. Pulse widths and relaxation delays were  $1.0\ \mu\text{s}$  and 2 to 4 s, respectively, with dead times ranging from 10 to  $40\ \mu\text{s}$ .

### 3.2.3. Theoretical Calculations

Theoretical chemical shielding calculations were performed using the Gaussian 94 suite of programs<sup>67</sup> on an IBM RS6000/580 workstation. Calculations were conducted on all systems, except  $\text{Al}(\text{TMHD})_3$ , for which an experimentally-determined molecular geometry is not available. Gauge Including Atomic Orbital

(GIAO)<sup>66</sup> calculations of the <sup>27</sup>Al shielding tensors were performed using both RHF and DFT levels of theory. DFT calculations utilized Becke's three-parameter hybrid exchange functional<sup>98</sup> and the correlation functional of Lee, Yang and Parr<sup>99</sup> (i.e., B3LYP DFT calculations). The 6-31G\* and 6-311G\* basis sets were used for all molecules, with 6-31G\*\* and 6-311G\*\* employed for calculations on AlH. The diffuse basis sets, 6-31+G\* and 6-311+G\*, were also utilized for calculations on I.

The molecular geometries used for calculations on I, II and III were taken from previously determined X-ray crystal structures,<sup>91,100,101</sup> with carbon-hydrogen bond lengths in II and III optimized using RHF theory with the 6-311G\*\* basis set. Calculations on linear molecules were conducted with both experimentally determined geometries (*vide infra*) and theoretically optimized geometries. Geometry optimizations of AlNC, AlCl, AlF and AlH were carried out at both RHF and MP2 levels of theory using the 6-311G\*(\*) basis set.

Since there is no established absolute chemical shielding scale for <sup>27</sup>Al, calculated <sup>27</sup>Al chemical shifts were referenced with respect to AlH<sub>4</sub><sup>-</sup>, which has a calculated chemical shielding of  $\sigma_{\text{iso}}(\text{Al}) = 512 \text{ ppm}^{\text{85d}}$  and a measured chemical shift of  $\delta_{\text{iso}}(^{27}\text{Al}) = 101 \text{ ppm}$  with respect to the standard Al(H<sub>2</sub>O)<sub>6</sub><sup>3+</sup> (aq).<sup>102</sup> Incidentally, Farrar and co-workers recently reported a calculation of  $\sigma_{\text{iso}}(\text{Al}) = 612 \text{ ppm}$  for Al(H<sub>2</sub>O)<sub>6</sub><sup>3+</sup> which gives a calculated chemical shift difference of 100 ppm,<sup>85a</sup> in excellent agreement with the experimentally determined difference in chemical shielding.<sup>103</sup>

Theoretical EFG calculations were carried out at RHF, DFT and MP2 levels of theory, using basis sets listed above. Calculated EFG tensors were converted

from atomic units (a.u.) to MHz<sup>104</sup> by multiplying the largest component of the EFG tensor,  $V_{33}$ , by  $eQ/h \times 9.7177 \times 10^{21}$  V m<sup>-2</sup>, where  $Q$  (<sup>27</sup>Al) =  $1.403 \times 10^{-29}$  m<sup>2</sup> (Ref. 37).

### 3.3 Characterization of Interaction Tensors by Solid-State <sup>27</sup>Al NMR and *Ab Initio* Techniques

This section is outlined as follows: in Section 3.3.1, the <sup>27</sup>Al MAS spectra of compounds I through IV are discussed. In Section 3.3.2, the combined effects of quadrupolar and anisotropic chemical shielding interactions on the NMR spectrum of a stationary solid samples are illustrated. New examples of <sup>27</sup>Al CSA are reported here, along with discussion of the orientations of the interaction tensors. The experimental CS and EFG tensors of I, II and III are compared with *ab initio* calculations of both CS and EFG tensors in Section 3.3.3.

#### 3.3.1 Aluminum-27 MAS NMR

##### A. Introduction

The NMR hamiltonian for an isolated quadrupolar nucleus can be written as

$$\mathcal{H} = \mathcal{H}_Z + \mathcal{H}_Q + \mathcal{H}_{CS} \quad (3.1)$$

In moderate to high applied magnetic fields, the quadrupolar and CS hamiltonians can be treated as perturbations on the Zeeman hamiltonian. Under conditions of fast magic-angle spinning,<sup>10</sup> anisotropic CS interactions become negligible, and the

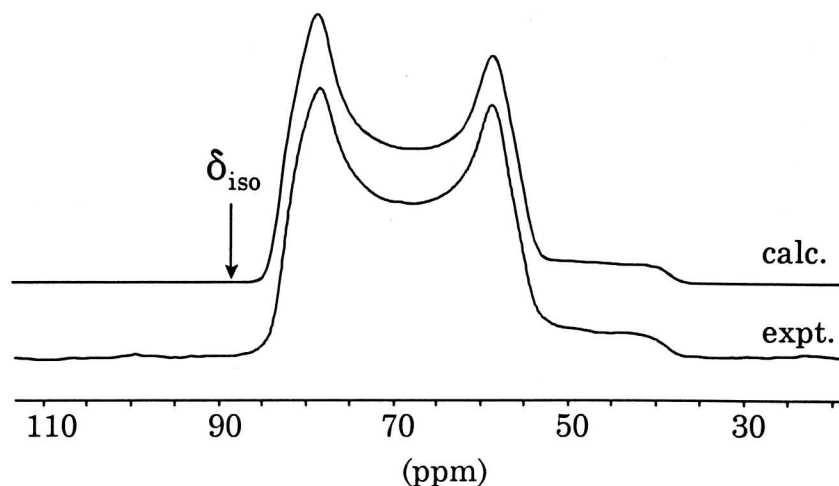


**Figure 3.2** Solid-state  $^{27}\text{Al}$  MAS NMR spectrum of the central transition of  $\text{Cl}_3\text{AlOPCl}_3$  obtained at 9.4 T with spinning speed  $\nu_{\text{rot}} = 8$  kHz (bottom trace). Simulated  $^{27}\text{Al}$  MAS NMR spectrum (top trace). Position of the isotropic shift is affected by the second-order quadrupolar interaction.

line shape of the central transition ( $+1/2 \leftrightarrow -1/2$ ) of the quadrupolar nucleus is therefore dependent only upon the second-order quadrupolar interaction.<sup>105</sup>

Accordingly, the position and line shape of the central transition are dependent only upon three parameters: the magnitude of the nuclear quadrupole coupling constant,  $C_Q$ , the quadrupolar asymmetry parameter,  $\eta$ , and the isotropic chemical shift,  $\delta_{\text{iso}}$ .

## B. $\text{Cl}_3\text{AlOPCl}_3$ (I)

The solid-state  $^{27}\text{Al}$  MAS NMR spectrum of the central transition of **I** obtained at 9.4 T is pictured in Fig. 3.2. The crystallographic space group of **I** has been determined as  $P2_1/m$  with  $Z = 2$ .<sup>91</sup> The molecules in the unit cell are crystallographically equivalent; therefore, the principal components of their CS and

EFG tensors are identical. The calculated spectrum (Fig. 3.2) was obtained from the following parameters:  $\delta_{\text{iso}}(^{27}\text{Al}) = 88(1)$  ppm,  $C_{\text{Q}}(^{27}\text{Al}) = 6.0(1)$  MHz and  $\eta = 0.15(1)$ .

The isotropic chemical shift is similar to other  $^{27}\text{Al}$  shifts of  $\text{AlCl}_3$  complexes measured in both the solution and solid state<sup>79,106,107</sup> and is comparable with solution NMR data acquired for I.<sup>90</sup> The magnitude of  $C_{\text{Q}}$  is large enough that the satellite transitions are not observed. The quadrupolar asymmetry parameter and high molecular symmetry allow some qualified conclusions about the orientation of the EFG tensor in the molecular frame. According to the X-ray crystal structure,<sup>91</sup> the chlorine atoms bonded to the aluminum and phosphorus atoms are arranged in

**Table 3.1:** Tabulation of experimental quadrupolar and chemical shift data obtained from NMR experiments on complexes exhibiting aluminum chemical shielding anisotropy. Errors are given in parentheses.

Complex	Quadrupolar Parameters		Chemical Shift Parameters			Euler Angles (degrees) <sup>a</sup>			Ref.
	$C_{\text{Q}}$ (MHz)	$\eta$	$\delta_{\text{iso}}$ (ppm) <sup>b</sup>	$\Omega$ (ppm)	$\kappa$	$\alpha$	$\beta$	$\gamma$	
$\text{AlPO}_4\text{-21}$ (site 1,2) <sup>c</sup>	7.35	0.5	15.8	44	0.64	90	70	90	76
	5.8	0.7	14.2						
$\alpha\text{-Al}_2\text{O}_3$	2.403(15)	0.01(1)	18.8(3)	17.5(6)	0.96(4)	0	3	0	77
$\text{Cl}_3\text{AlOPCl}_3$	6.0(1)	0.15(1)	88(1)	60(1)	-0.70(2)	90	90	0	83
$\text{Al}(\text{acac})_3$	3.03(1)	0.15(1)	0.0(3)	3.8(3)	0.70(3)	90	90	0	87
$\text{Al}(\text{trop})_3$	4.43(1)	0.08(2)	36.6(2)	9.0(3)	-0.25(5)	90	81	7	87
$\text{Al}(\text{TMHD})_3$	3.23(2)	0.10(1)	1.5(3)	6.7(5)	0.4(1)	90	90	0	87

- a. Errors in Euler angles given in text.  
b. Referenced with respect to an external sample of 0.1 M  $\text{Al}(\text{NO}_3)_3$  (aq),  $\delta_{\text{iso}}(^{27}\text{Al})$  of  $\text{Al}(\text{H}_2\text{O})_6^{3+} = 0$  ppm.  
c. No errors quoted, accurate simulations of spectra not possible (see text).

eclipsed conformations (all Cl-Al...P-Cl torsional angles are ca.  $0.0^\circ$ ), and the complex has near- $C_{3v}$  symmetry, since the Al-O-P bond angle is  $176.0(4)^\circ$ . There is a unique mirror plane parallel to the approximately linear Al-O-P axis containing two chlorine atoms, with the remaining chlorine atoms related by reflection through the mirror plane. If the Al-O-P bond angle was exactly  $180^\circ$ , the local symmetry would dictate that  $\eta = 0$  with the largest component of the EFG tensor being parallel to the Al-O bond. The small departure from linearity ( $4^\circ$ ) of the Al-O-P bond angle and the near-axial symmetry of the EFG tensor indicate that  $V_{33}$  must be oriented near the Al-O bond axis.

### C. Al(acac)<sub>3</sub> (II), Al(trop)<sub>3</sub> (III) and Al(TMHD)<sub>3</sub> (IV)

Analysis of  $^{27}\text{Al}$  MAS NMR spectra of Al(acac)<sub>3</sub> and Al(trop)<sub>3</sub> obtained at 9.4 T (Fig. 3.3) and 18.8 T, yielded the quadrupolar parameters and isotropic chemical shifts listed in Table 3.1. The results for Al(acac)<sub>3</sub> are in excellent agreement with those previously reported in the literature ( $C_Q = 3.0$  MHz,  $\eta = 0.15$ <sup>108</sup> and  $C_Q = 2.85$  MHz,  $\eta \sim 0$ <sup>109</sup>). The former data was obtained from  $^{27}\text{Al}$  MAS NMR spectra, while the latter was estimated from solid-state  $^{27}\text{Al}$  spectra of stationary samples acquired at 2.35 T. Values of  $C_Q$  and  $\eta$  for Al(TMHD)<sub>3</sub> were obtained from the analysis of  $^{27}\text{Al}$  NMR spectra acquired at 9.4 T (see Table 3.1).

Al(acac)<sub>3</sub> and Al(TMHD)<sub>3</sub> are both tris( $\beta$ -ketoenolato) complexes,<sup>110</sup> with the oxygen atoms positioned in an octahedral arrangement about the central aluminum atom. As isolated molecules, these complexes possess  $D_3$  symmetry, with each of the three diketo ligands forming a six-membered chelate ring with the aluminum. Due

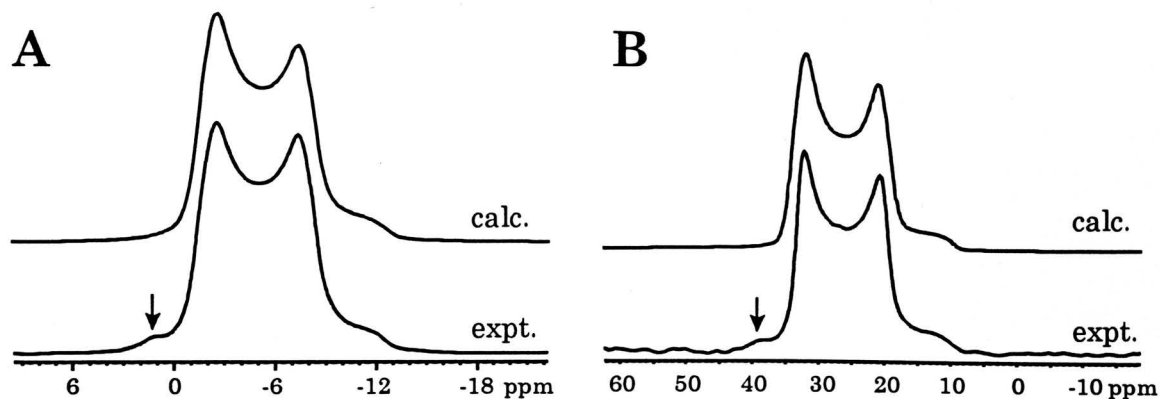


**Figure 3.3** Experimental and calculated  $^{27}\text{Al}$  MAS NMR spectra of the central transitions ( $+1/2 \leftrightarrow -1/2$ ) of (A)  $\text{Al}(\text{acac})_3$ ,  $\nu_{\text{rot}} = 7853$  Hz, and (B)  $\text{Al}(\text{trop})_3$ ,  $\nu_{\text{rot}} = 9955$  Hz, acquired at 9.4 T. The ( $\pm 3/2 \leftrightarrow \pm 1/2$ ) satellite transitions are also visible, and marked with arrows.

to the similar structural environments about the aluminum centres, the  $C_Q(^{27}\text{Al})$  and  $\delta_{\text{iso}}(^{27}\text{Al})$  of  $\text{Al}(\text{acac})_3$  and  $\text{Al}(\text{TMHD})_3$  are of comparable magnitudes. The tropolonato ions in  $\text{Al}(\text{trop})_3$  form five-membered chelate rings with the aluminum, and the interoxygen distances or “bites” are reduced<sup>101</sup> in comparison to the six-membered chelate ring of  $\text{Al}(\text{acac})_3$ .<sup>100</sup> This leads to a distorted octahedral arrangement of oxygen atoms, which gives rise to augmented electric field gradients at the aluminum site. As a result, the magnitude of  $C_Q$  in  $\text{Al}(\text{trop})_3$  is larger than those observed in the former compounds. The isotropic aluminum chemical shift is also very sensitive to changes in structure, as demonstrated by the deshielding of  $\delta_{\text{iso}}(^{27}\text{Al})$  by ca. 35 ppm compared to the six-membered chelate ring complexes.

The isotropic chemical shifts and quadrupolar parameters are consistent with those observed for a wide variety of aluminum complexes.<sup>74,79</sup> Chemical shifts of halogenated and oxygenated aluminum in tetrahedral and tetragonal environments are normally observed from ca. 60 ppm to 120 ppm, while octahedrally coordinated

aluminum atoms have chemical shifts of 50 ppm to -20 ppm.<sup>79</sup> This constant relationship between aluminum coordination and isotropic chemical shift is often applied in the analysis of aluminum NMR spectra of materials such as disordered solids, zeolites, minerals and clays, allowing for differentiation of tetrahedral and octahedral aluminum sites.<sup>74,75,76,79</sup> Quadrupolar parameters are also used in the same context, with octahedral complexes normally exhibiting smaller values of  $C_Q$ .<sup>55,74</sup> It is interesting to note that the ( $\pm 3/2 \leftrightarrow \pm 1/2$ ) transitions are observed in spectra of the octahedral complexes II, III and IV, due to the reduced values of  $C_Q$  compared with I.

### 3.3.2 Solid-State Aluminum-27 NMR of Stationary Samples

#### A. Introduction

In analyzing the NMR spectra of solid stationary samples, the effects of chemical shielding anisotropy on the line shape must be considered. There are many examples in the literature in which the CS and EFG tensor parameters have been extracted through analyses of powder NMR spectra of stationary samples,<sup>111,112,113,114</sup> and treatment of the problem is well known. A description of the theory necessary for the interpretation of such spectra is outlined in this section.

Simulation of the central transition is quite facile if the EFG and CS tensors are coincident (i.e.,  $\theta, \phi = \vartheta, \varphi$ , *vide infra*); however, this is most often not the case, and knowledge of the relative orientation of the EFG and CS tensors is necessary when simulating the NMR spectra (Fig. 3.4). Since the NMR spectrum of a

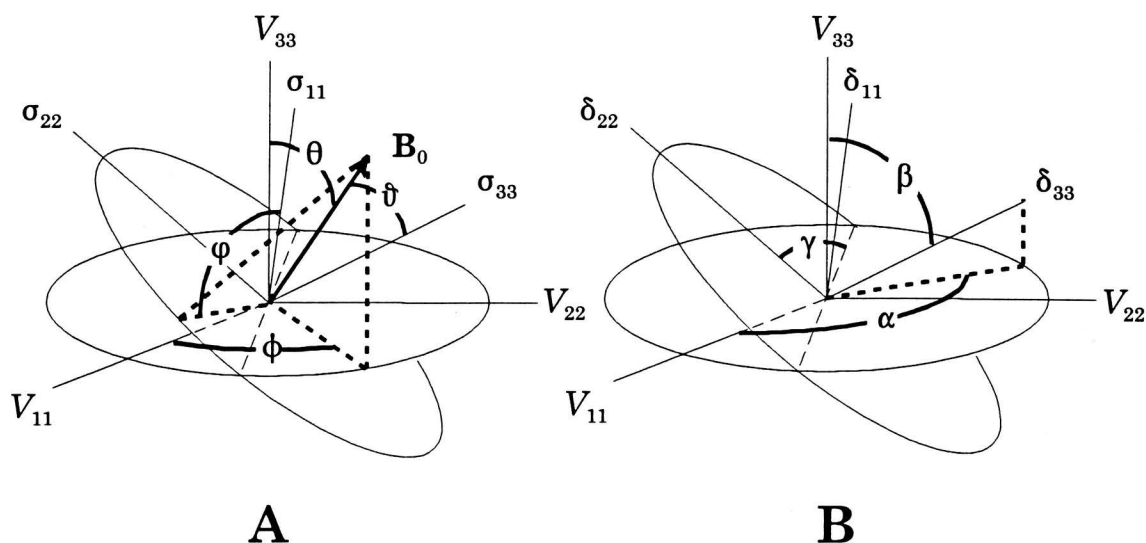


**Figure 3.4** (A) Euler angles describing the relative orientations of the EFG ( $\theta, \phi$ ) and CS ( $\vartheta, \phi$ ) tensors with respect to the external magnetic field. (B) Euler angles  $\alpha$ ,  $\beta$  and  $\gamma$  which define the orientation of the CS tensor in the EFG PAS.

quadrupolar nucleus is dependent upon the relative orientation of the EFG tensor with respect to the applied magnetic field, the convention used in this thesis is to describe the CS interaction within the PAS of the EFG. The orientation of the CS tensor in the EFG PAS is defined by three Euler angles ( $\alpha$ ,  $\beta$  and  $\gamma$ ), and the following rotational operations:<sup>113,115</sup>

$$\delta_{\text{CS}}^{(\text{Q})} = \mathbf{R}_{Z''}(\gamma) \mathbf{R}_{Y'}(\beta) \mathbf{R}_Z(\alpha) \delta_{\text{CS}}^{(\text{PAS})} \quad (3.2)$$

where  $\delta_{\text{CS}}^{(\text{Q})}$  is the chemical shift tensor in the EFG PAS,  $\delta_{\text{CS}}^{(\text{PAS})}$  is the chemical shift tensor in its own PAS, and  $\mathbf{R}$  designates rotational operators. Rotational operators in eq. 3.2, from right to left, correspond to rotation by  $\alpha$  about the coincident  $\delta_{33}$  and  $V_{33}$  axes, rotation by  $\beta$  about the  $\delta_{22}$  axis, and rotation by  $\gamma$  about the  $\delta_{33}$  axis.

Keeping in mind that the central transition is not dependent upon the first-order

quadrupolar interaction, the frequencies of the spectrum of the central transition can be calculated from:

$$\nu_{+1/2, -1/2} = \nu_0 + \nu_Q^{(2)}(\theta, \phi) - \nu_{CS}(\theta, \phi, \alpha, \beta, \gamma) \quad , \quad (3.3)$$

where  $\nu_0$  is the Larmor frequency,  $\nu_Q^{(2)}$  is the second-order quadrupolar frequency shift as defined in eq. 2.38. Trigonometric terms in the expression for  $\nu_{CS}(\theta, \phi)$  defined in eq. 2.16 are substituted by the following relations

$$\begin{aligned} \sin\theta \cos\phi &= \cos\gamma \cos\beta \sin\theta \cos(\phi - \alpha) + \sin\gamma \sin\theta \sin(\phi - \alpha) - \cos\gamma \sin\beta \cos\theta \\ \sin\theta \sin\phi &= -\sin\gamma \cos\beta \sin\theta \cos(\phi - \alpha) + \cos\gamma \sin\theta \sin(\phi - \alpha) + \sin\gamma \sin\beta \cos\theta \\ \cos\theta &= \sin\beta \sin\theta \cos(\phi - \alpha) + \cos\beta \cos\theta \end{aligned} \quad (3.4)$$

to yield the term  $\nu_{CS}(\theta, \phi, \alpha, \beta, \gamma)$  in eq. 3.3.

Powder patterns are simulated by calculating frequencies over a large number of angles,  $\theta$  and  $\phi$ , and summing the superimposed spectra, according to

$$\begin{aligned} I(\nu) &= \sum_{m=-S+1}^{+S} P(m_S) \int_0^{\pi} \int_0^{2\pi} g\{\nu - \nu_0[\delta_{11} \sin^2\theta \cos^2\phi + \delta_{22} \sin^2\theta \sin^2\phi \\ &+ \delta_{33} \cos^2\theta] - (\nu_Q^2/12\nu_0)\{(3/2)\sin^2\theta[(A+B)\cos^2\theta - B] \\ &- \eta \cos 2\phi \sin^2\theta[(A+B)\cos^2\theta + B] + (\eta^2/6)[A - (A+4B)\cos^2\theta \\ &- (A+B)\cos^2 2\phi(\cos^2\theta - 1)^2]\} \sin\theta d\theta d\phi \end{aligned} \quad (3.5)$$

where  $A$  and  $B$  are as defined in Section 2.3.5,  $P(m_S)$  is the probability of the  $(m_S, m_S-1)$  transition, and  $g(\nu)$  is a gaussian broadening function. Only the second-order quadrupolar interaction is considered in the above equation. The stationary NMR spectrum of the central transition of a quadrupolar nucleus can be computed

from the knowledge of eight parameters: the quadrupolar parameters,  $C_Q$  and  $\eta$ ; the CS parameters,  $\delta_{iso}$ ,  $\Omega$  and  $\kappa$ ; and the polar angles,  $\alpha$ ,  $\beta$  and  $\gamma$ , which define the relative orientation of the EFG and CS tensors.

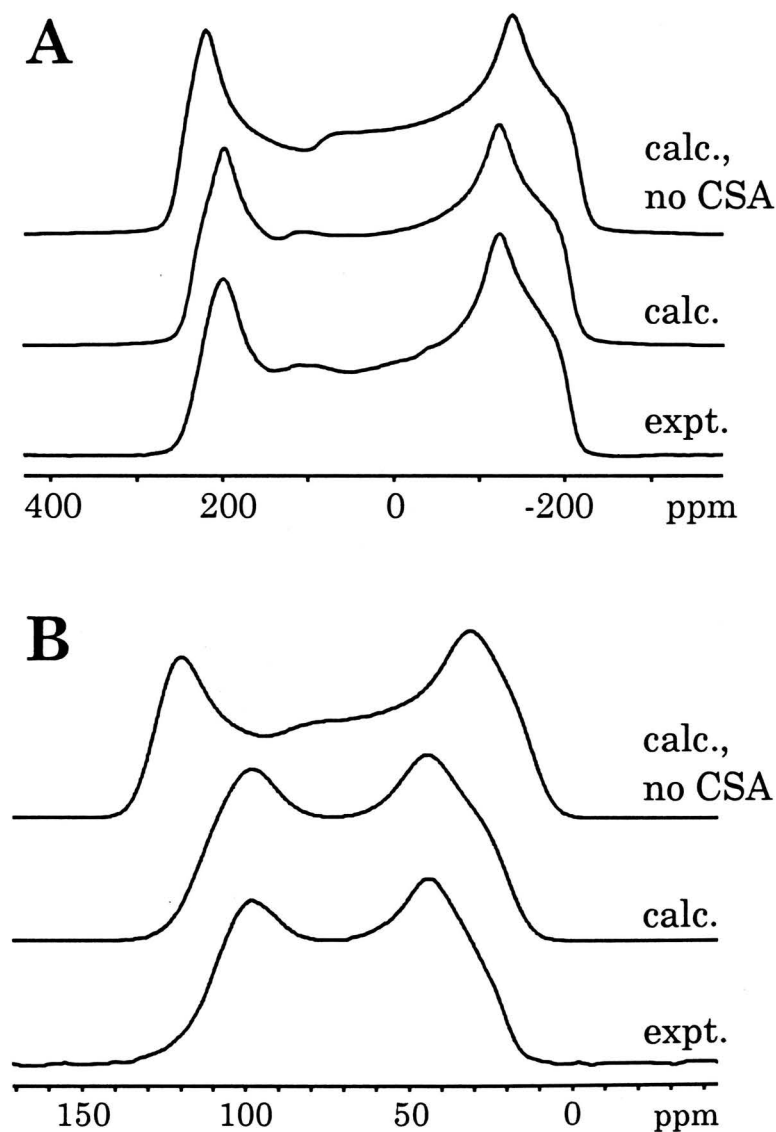


**Figure 3.5** Experimental and calculated  $^{27}\text{Al}$  NMR spectra of stationary samples of  $\text{Cl}_3\text{Al}\cdot\text{OPCl}_3$  at (A) 4.7 T and (B) 9.4 T. Calculated spectra are presented which include and exclude aluminum chemical shielding anisotropy. All other parameters are the same.

## B. Aluminum Chemical Shielding Anisotropy in $\text{Cl}_3\text{AlOPCl}_3$ (I)

Experimental and calculated  $^{27}\text{Al}$  NMR spectra of the central transition of a stationary sample of I, at both 4.7 T and 9.4 T, are presented in Fig. 3.5. The top traces are  $^{27}\text{Al}$  NMR spectral simulations including the parameters obtained from the  $^{27}\text{Al}$  MAS NMR spectra, with the assumption that the  $^{27}\text{Al}$  CSA is zero.

Comparison of the top simulations with the experimental spectra reveals that the positions of the discontinuities and the overall width of the transition are different, clearly indicating that there is an additional interaction determining the overall line shape of the powder pattern. The difference is especially noticeable at the higher field (Fig. 3.5B), since the effects of chemical shielding on the spectrum are augmented. Utilizing the quadrupolar parameters and isotropic chemical shift obtained from simulation of the MAS NMR spectra, the best-fit calculated stationary spectra are obtained from the additional parameters:  $\Omega = 60(1)$  ppm,  $\kappa = -0.70(2)$ ,  $\alpha = 90^\circ(10)$ ,  $\beta = 90^\circ(5)$  and  $\gamma = 0^\circ(5)$ . This corresponds to  $^{27}\text{Al}$  CS tensor principal components of  $\delta_{11} = 125(1)$  ppm,  $\delta_{22} = 74(1)$  ppm, and  $\delta_{33} = 65(1)$  ppm. Agreement

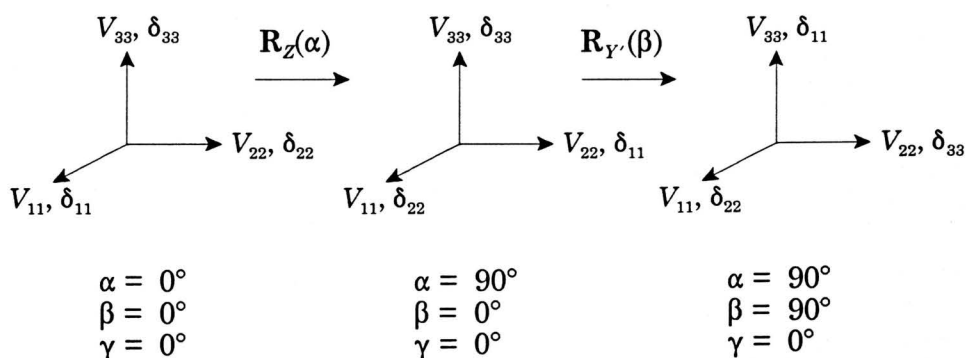


**Figure 3.6** Schematic diagram showing the relative orientation of the CS and EFG tensors.

between experimental and calculated spectra at all fields is quite good. Parameters were varied until best fits (i.e., experimental spectra were reproduced) were obtained at both  $B_0 = 4.7$  T and 9.4 T. Uncertainties in spectral parameters (given in parentheses) were estimated by visual comparison of experimental and calculated spectra.

The polar angles reveal that the CS tensor is oriented such that the least shielded component,  $\delta_{11}$ , is parallel to the largest component of the EFG tensor,  $V_{33}$ , which must be along or close to the direction of the Al-O bond axis. The relative orientation of the other principal components of the two interaction frames are known (i.e.,  $\delta_{22}$  is parallel to  $V_{11}$  and  $\delta_{33}$  is parallel to  $V_{22}$ , see Fig. 3.6). From these spectra, it is not possible to determine their orientations with respect to the molecular frame, other than to say that one set is perpendicular to the mirror plane in the molecule and the other set is parallel to this plane. *Ab initio* calculations of CS and EFG tensors in  $\text{Cl}_3\text{AlOPCl}_3$  are discussed in the next section of this chapter, and aid in the determination of the interaction tensor orientations.

Second moment analysis<sup>116</sup> reveals that the broadening of the central transition results mainly from dipolar coupling of the aluminum nucleus with the three directly bonded chlorine nuclei and the phosphorus nucleus (from the X-ray structure the direct dipolar coupling constants are calculated to be  $R_{\text{dd}}(^{27}\text{Al}, ^{35}\text{Cl}) = 330$  Hz and  $R_{\text{dd}}(^{27}\text{Al}, ^{31}\text{P}) = 383$  Hz, respectively).

A calculated NMR spectrum of the central transition for a spin-5/2 nucleus in a stationary powder sample with an axially symmetric EFG tensor and no chemical shift anisotropy is pictured in Fig. 3.7A (shown twice for the purpose of comparison

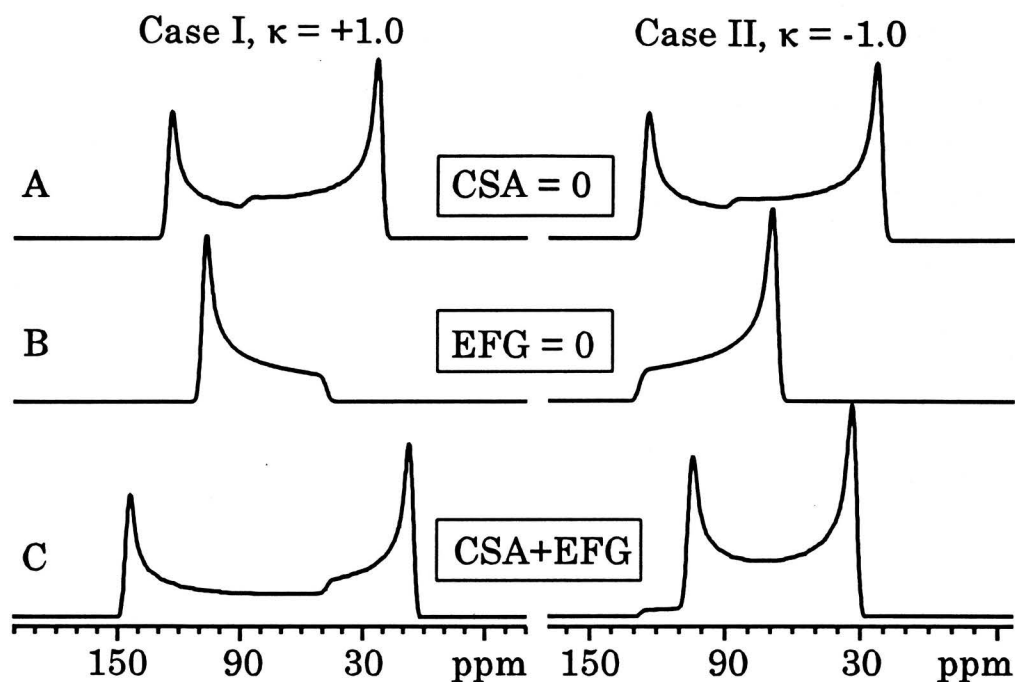


**Figure 3.7** The effects of (A) the quadrupole interaction, (B) CSA and (C) combination of quadrupole interaction and CSA the solid-state NMR spectrum of a spin-5/2 quadrupolar nucleus. Parameters are:  $C_Q = 6.0$  MHz,  $\eta = 0.0$ ,  $\delta_{\text{iso}} = 88$  ppm,  $\Omega = 60$  ppm,  $\beta = 0^\circ$ .

with the spectra below). The discontinuities in the spectrum correspond (moving from high to low frequency) to orientations in which the unique component of the EFG tensor is perpendicular to ( $\theta = 90^\circ$ ), parallel to ( $\theta = 0^\circ$ ) and oriented at  $41.8^\circ$  with respect to the external magnetic field,  $B_0$ . The isotropic chemical shift is not located at the centre of gravity of the spectrum due to the second-order quadrupole shift.

To consider the effects of CSA on the appearance of an NMR spectrum of a spin-5/2 nucleus, we first examine two NMR powder patterns of nuclei in which the CS and Zeeman interactions are the only interactions present (i.e.,  $EFG = 0$ ). These

simulated spectra are pictured in Fig. 3.7B. In Case I,  $\delta_{11} = \delta_{22}$  (i.e., the unique component is  $\delta_{33}$ ) and the skew,  $\kappa = +1.0$ . Discontinuities occur in this spectrum (from high to low frequency) at points at which the unique component of the CS tensor is perpendicular ( $\vartheta = 90^\circ$ ) and parallel ( $\vartheta = 0^\circ$ ) to the external magnetic field. In Case II,  $\kappa = -1.0$  and  $\delta_{11}$  is the unique component. Discontinuities occur at the same relative orientations of the unique CS tensor component and magnetic field; however, the parallel orientation is now at higher frequency than the perpendicular orientation. In both cases, the isotropic chemical shift occurs at the centre of gravity of the spectrum, where  $\vartheta = 54.74^\circ$ .

Finally, the combined effects of CSA and the quadrupolar interaction are pictured in Fig. 3.7C. If both quadrupolar interactions and CS interactions from Case I ( $\kappa = +1.0$ ) are present, the breadth of the NMR spectrum increases. Conversely, if CS interactions from Case II are present ( $\kappa = -1.0$ ), the breadth of the spectrum decreases. This information allows one to use simulated spectra to determine (i) if there is CS anisotropy in the NMR spectrum of the central transition of a quadrupolar nucleus and (ii) the skew of the CS tensor at the quadrupolar nucleus. This methodology was also applied to the results of Woessner and Timken, who reported a  $^{27}\text{Al}$  NMR spectrum of a stationary sample of low albanite, but were unable to satisfactorily simulate the spectrum by considering the quadrupolar interaction alone.<sup>117</sup> We performed spectral simulations which reveal that the spectral appearance is due to a small  $^{27}\text{Al}$  CSA of 18(2) ppm and  $\beta = 20(2)^\circ$ . The smaller CSA and  $C_Q$  (3.37 MHz) relative to those observed in I are in accordance with the increased symmetry of a tetrahedrally coordinated  $\text{AlO}_4$  centre in albanite

compared to the pseudo-tetrahedral  $\text{AlCl}_3$  centre in I.

### C. Aluminum CSA in Distorted Octahedral Compounds

The majority of publications concerning solid-state  $^{27}\text{Al}$  NMR involve materials and complexes possessing four and six oxygen-coordinated aluminum centres.<sup>23,74,79</sup> In many cases, the materials investigated are disordered solids, or there are multiple aluminum sites present; consequently, broad and/or overlapping powder patterns make it very difficult to extract CS tensor information from the spectra.  $\text{Al}(\text{acac})_3$  and  $\text{Al}(\text{trop})_3$  are ideal compounds to study, since known crystal structures<sup>100,101</sup> reveal that (i) there is nearly octahedral symmetry about the aluminum centres, and (ii) there is only one crystallographically distinct aluminum nucleus per unit cell. In addition, both complexes have approximate  $C_3$  and  $C_2$  rotation axes which are normal to one another, where one might expect the principal components of the EFG and CS tensors to be directed.<sup>118,119,120</sup> For example, in the case of  $\text{Co}(\text{acac})_3$ , single-crystal  $^{59}\text{Co}$  NMR measurements indicate that the unique principal components of the cobalt CS and EFG tensors are close to the local  $C_3$  axis, with the remaining principal components approximately normal to this axis.<sup>120</sup> Although there is no crystal structure of  $\text{Al}(\text{TMHD})_3$  in the literature, it is clear from the well-known chemistry of the  $\beta$ -ketoenolato complexes and the  $^{27}\text{Al}$  NMR results (*vide infra*) that the aluminum is hexacoordinate with pseudo-octahedral symmetry.

**$\text{Al}(\text{acac})_3$ .** Solid-state  $^{27}\text{Al}$  NMR spectra of stationary samples of  $\text{Al}(\text{acac})_3$  at three different fields are pictured in Fig. 3.8, along with the calculated spectra. Analysis

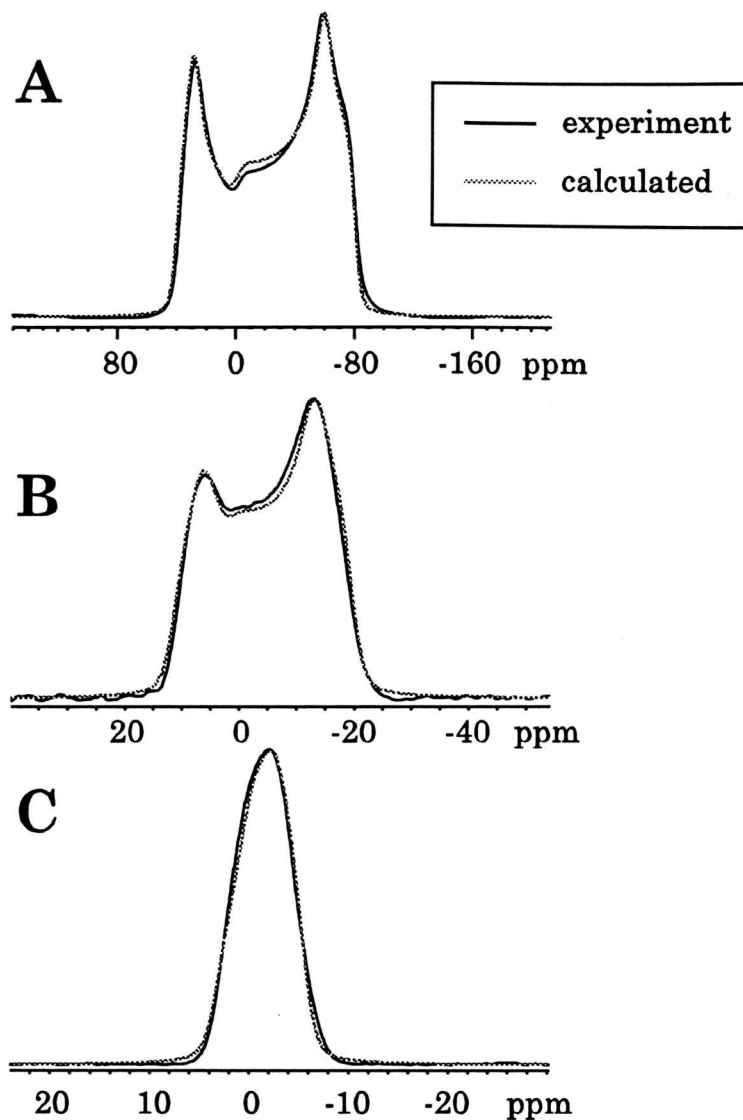


**Figure 3.8** Aluminum-27 NMR spectra of stationary samples of  $\text{Al}(\text{acac})_3$  at (A) 4.7 T, (B) 9.4 T, (C) 18.8 T.

of these spectra yielded the following parameters:  $C_Q(^{27}\text{Al}) = 3.03(1)$  MHz,  $\eta = 0.15(1)$ ,  $\delta_{\text{iso}} = 0.0(3)$  ppm,  $\Omega = 3.8(3)$  ppm and  $\kappa = 0.70(3)$ . The relative orientation of the EFG and CS tensors is given by the Euler angles  $\alpha = 90^\circ(\pm 15^\circ)$ ,  $\beta = 90^\circ(\pm 10^\circ)$  and  $\gamma = 0^\circ(\pm 30^\circ)$ , which sets the least shielded component of the CS tensor,  $\delta_{11}$ , along the direction of the largest component of the EFG tensor,  $V_{33}$ ,  $\delta_{22}$  along  $V_{11}$ , and  $\delta_{33}$

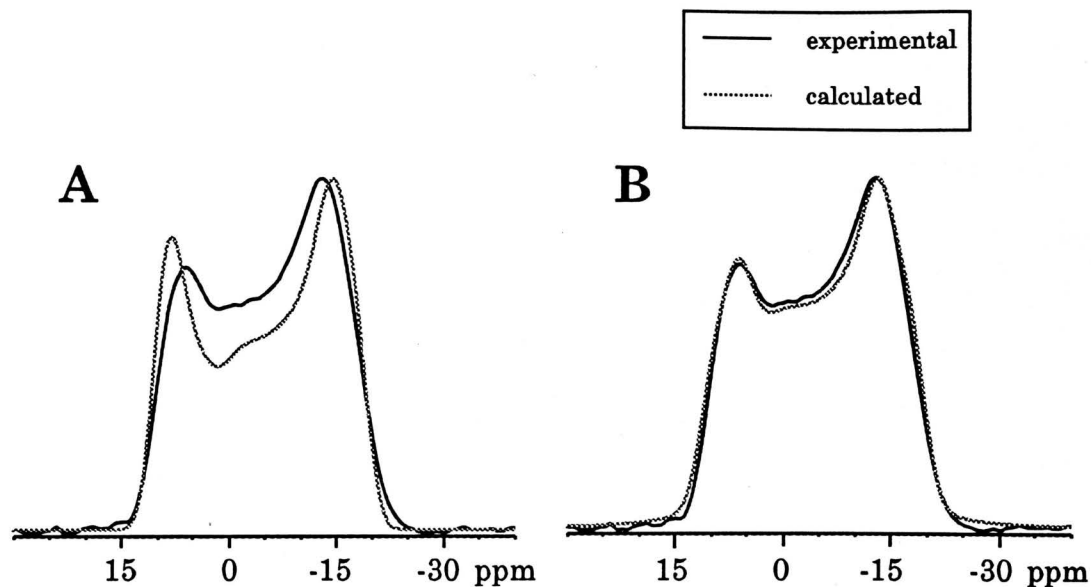


**Figure 3.9** Experimental  $^{27}\text{Al}$  NMR spectra of  $\text{Al}(\text{acac})_3$  at 9.4 T and corresponding calculated spectra (A) without CSA and (B) with CSA.

along  $V_{22}$ . Since  $\delta_{11}$  and  $\delta_{22}$  are similar, altering the value of  $\gamma$  does not significantly change the shape of the central transition. Consequently, the error in  $\gamma$  is significantly larger than those in  $\alpha$  and  $\beta$ . The span of the shielding tensor is very small; however, comparison of experimental and calculated spectra (with and without the CSA) reveal that there is clearly a CSA effect present on the  $^{27}\text{Al}$  NMR line shape (see Fig. 3.9).

In many cases, single-crystal NMR studies have been used to elicit information on the orientation of NMR interaction tensors in the molecular frame.<sup>6,28,121</sup> When suitable single crystals are unavailable and only powder NMR spectra can be obtained, it is sometimes possible to utilize (i) molecular symmetry, and/or (ii) theoretical CS or EFG tensors to predict the orientation of the interaction tensors in the molecule. The aluminum EFG tensor of  $\text{Al}(\text{acac})_3$  has near-axial symmetry ( $\eta = 0.15$ ), which indicates that  $V_{33}$  is the quasi-unique component, and

the value of the skew,  $\kappa = 0.7$ , signifies that the CS tensor is also almost axially symmetric, with  $\delta_{33}$  as the quasi-unique component. Note, that the term *quasi-unique* is used to describe a single principal component that is distinctly separated from the other two components which are of similar magnitude, in tensors that are close to being axially symmetric. Based on the roughly axially symmetric interaction tensors and the relative orientation of the EFG and CS frames, two possible orientations of the interaction tensors with respect to the molecular frame are suggested. One possible orientation has  $V_{33}$  (the quasi-unique EFG principal component) oriented near or along the direction of the approximate  $C_3$  axis, which positions  $\delta_{11}$  near or along this axis as well. The other possibility has the most shielded principal component,  $\delta_{33}$ , aligned near the  $C_3$  axis, placing  $V_{22}$  along this direction as well. In both cases, one set of remaining principal components would be directed along or near one of the *three*  $C_2$  symmetry axes present in the molecule.

One might expect to find both of the quasi-unique components of the EFG and CS tensors (i.e.,  $V_{33}$  and  $\delta_{33}$ ) aligned along the  $C_3$  symmetry axis. However, calculated spectra incorporating these tensor orientations indicate that this is not the case. The EFG is a ground-state property, predominantly dependent upon the arrangement of nearest neighbours about the central nucleus, whereas CS is a second-order property, dependent upon the virtual as well as the ground electronic state of the molecule.<sup>122</sup> In addition, the magnitude of the  $^{27}\text{Al}$  CSA is very small compared to the overall shielding range of  $^{27}\text{Al}$ , whereas  $C_Q(^{27}\text{Al})$  is of small to moderate magnitude (small values of  $C_Q(^{27}\text{Al})$  range from 0.3 - 0.6 MHz, in alums,<sup>23,123</sup> to values on the order of 25 to 45 MHz, in monomeric and dimeric

organoaluminum compounds).<sup>124</sup> Therefore, the orientation of the quasi-unique component of the EFG tensor should be dictated by molecular symmetry, whereas the CS tensor orientation is somewhat more ambiguous, predominantly due to the nominal magnitude of the CSA. From these arguments, it is proposed that the most probable orientation of the EFG and CS tensors in  $\text{Al}(\text{acac})_3$  is one in which  $V_{33}$  and  $\delta_{11}$  are along or near the  $C_3$  symmetry axis. No additional information can be gained from experimental data regarding the orientation of the remaining principal components with respect to the molecular frame; however, it is reiterated that from the Euler angles and the crystal structure of  $\text{Al}(\text{acac})_3$ , it is known that  $\delta_{22}$  is oriented along or close to  $V_{11}$ , and  $\delta_{33}$  near to  $V_{22}$ , with one set of these components aligned in the direction of one of the  $C_2$  symmetry axes. Again, it is stated that *ab initio* calculations of the interaction tensors presented later in this chapter help to elucidate their orientation in the molecular frame.

**$\text{Al}(\text{TMHD})_3$ .** Analyses of  $^{27}\text{Al}$  NMR spectra of stationary samples of  $\text{Al}(\text{TMHD})_3$  at 4.7 T and 9.4 T yielded the following parameters:  $C_Q(^{27}\text{Al}) = 3.23(2)$  MHz,  $\eta = 0.10(1)$ ,  $\delta_{\text{iso}} = 1.5(3)$  ppm,  $\Omega = 6.7(5)$  ppm and  $\kappa = 0.4(1)$ , with Euler angles  $\alpha = 90^\circ(\pm 25^\circ)$ ,  $\beta = 90^\circ(\pm 10^\circ)$  and  $\gamma = 0^\circ(\pm 30^\circ)$ . The magnitudes of  $C_Q$ ,  $\Omega$  and  $\kappa$  suggest that there is a slightly less symmetric environment about the central aluminum atom in comparison to  $\text{Al}(\text{acac})_3$ . The relative orientation of the CS and EFG tensors is the same as in  $\text{Al}(\text{acac})_3$ , which suggests that these tensors may be oriented in the molecular frame in a similar manner as those in  $\text{Al}(\text{acac})_3$ . The quoted errors in the CS parameters for  $\text{Al}(\text{TMHD})_3$  are slightly larger than those for  $\text{Al}(\text{acac})_3$  (or

$\text{Al}(\text{trop})_3$ , *vide infra*), since spectra were not obtained and analyzed at 18.8 T, where the effects of anisotropic chemical shielding are more pronounced.

**$\text{Al}(\text{trop})_3$ .** Similar analyses were completed on the  $^{27}\text{Al}$  NMR spectra of  $\text{Al}(\text{trop})_3$ , with the following results:  $C_Q(^{27}\text{Al}) = 4.43(1)$  MHz,  $\eta = 0.08(2)$ ,  $\delta_{\text{iso}} = 36.6(2)$  ppm,  $\Omega = 9.0(3)$  ppm and  $\kappa = -0.25(5)$ . Experimental and calculated spectra at three fields are presented in Fig. 3.10, and a comparison of spectra with and without CSA are displayed in Fig. 3.11. The larger CSA with respect to those in  $\text{Al}(\text{acac})_3$  and  $\text{Al}(\text{TMHD})_3$  and the non-axial CS tensor are presumably the result of diminished octahedral symmetry about the central aluminum nucleus (*vide supra*).<sup>100,101</sup> In addition to a near- $C_3$  symmetry axis, there is also a *unique*  $C_2$  rotation axis positioned normal to the  $C_3$  axis, resulting from the fact that two of the tropolone moieties are identical in terms of bond lengths, angles and torsional angles with respect to the central aluminum nucleus. As in the case of  $\text{Al}(\text{acac})_3$ , it is very likely that two principal components of each of the interaction tensors are aligned along the directions of these symmetry axes. The non-axial CS tensor makes it difficult to assess which of the CS principal components may be aligned in the direction of the unique  $C_2$  and approximate  $C_3$  symmetry axes. However, the small quadrupolar asymmetry parameter ( $\eta = 0.08$ ) once again indicates near-axial symmetry in the EFG tensor, which would strongly imply that  $V_{33}$  lies along or in the direction of the  $C_3$  axis. The relative orientation of the EFG and CS PASs in  $\text{Al}(\text{trop})_3$  are given by  $\alpha = 90^\circ(\pm 5^\circ)$ ,  $\beta = 81^\circ(\pm 2^\circ)$  and  $\gamma = 7^\circ(\pm 2^\circ)$ , setting  $\delta_{11}$  at  $9^\circ$  from the direction of  $V_{33}$ ; therefore,  $\delta_{11}$  is the principal CS component that is situated near the approximate- $C_3$

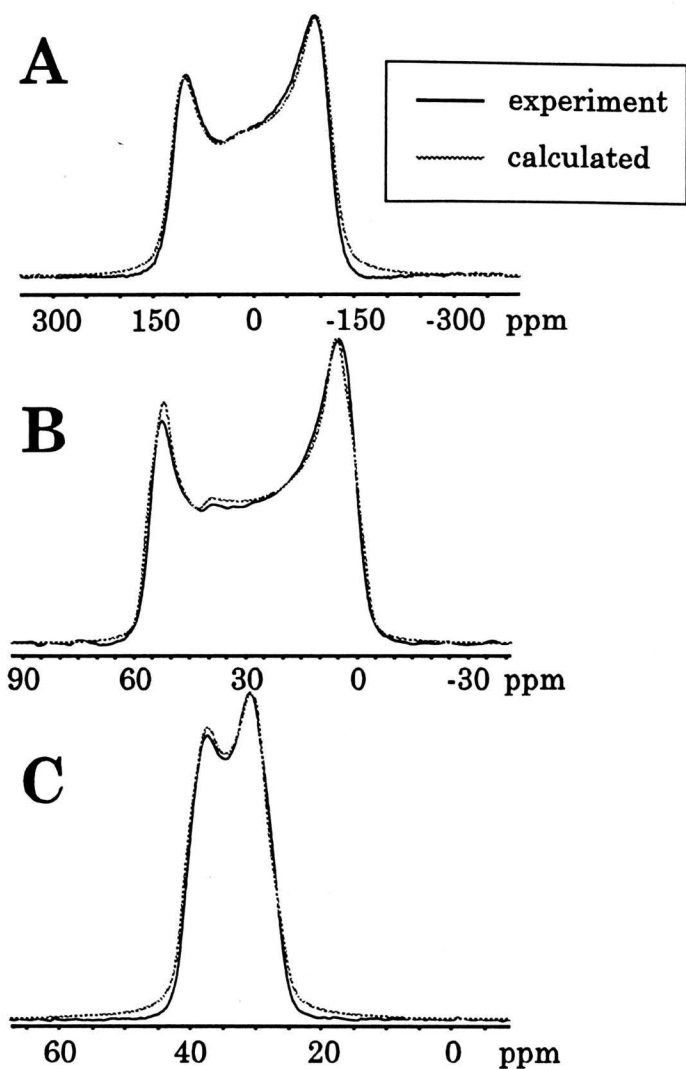


**Figure 3.10** Aluminum-27 NMR spectra of stationary samples of  $\text{Al}(\text{trop})_3$  at (A) 4.7 T, (B) 9.4 T and (C) 18.8 T.

axis. The calculated spectra are sensitive to small changes in the Euler angles, due to the increased magnitude of the CSA in  $\text{Al}(\text{trop})_3$ ; hence, the errors in the Euler angles are significantly smaller in comparison to those for  $\text{Al}(\text{acac})_3$  and  $\text{Al}(\text{TMHD})_3$ . Again, no further information can be gained on the orientation of the other principal components relative to the molecular frame, except to say that one CS and EFG

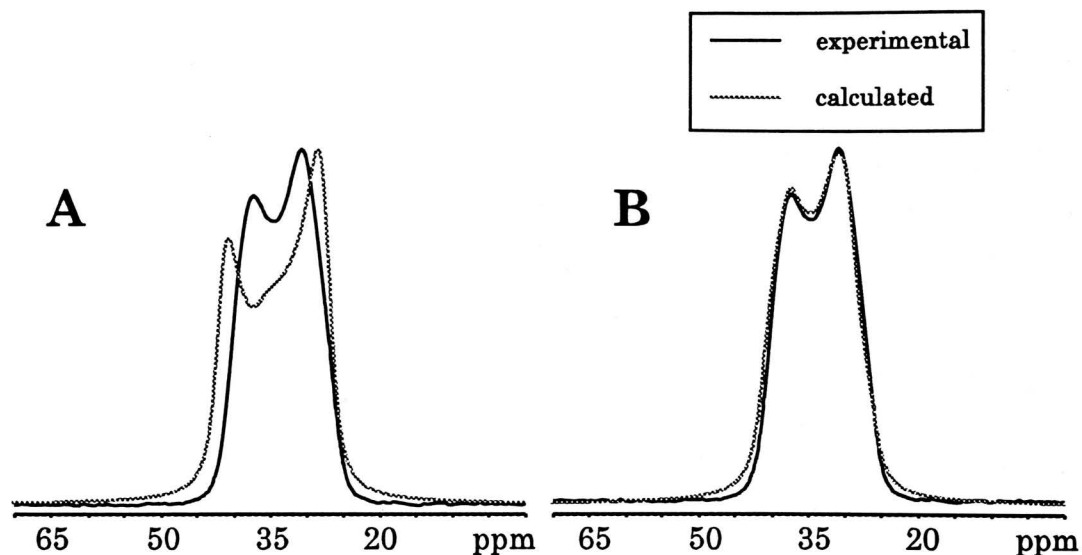


**Figure 3.11** Experimental  $^{27}\text{Al}$  NMR spectra of  $\text{Al}(\text{trop})_3$  at 18.8 T and corresponding calculated spectra (A) without CSA and (B) with CSA.

principal component should be aligned in the direction of the unique  $C_2$  axis. The Euler angles reveal that, as in the case of  $\text{Al}(\text{acac})_3$ ,  $\delta_{22}$  is oriented approximately in the direction of  $V_{11}$ , and  $\delta_{33}$  is approximately along  $V_{22}$ . Pictorial representations of the CS and EFG tensor orientations of **I**, **II** and **III** are given in the next section, in which *ab initio* calculations are applied to these systems.

### 3.3.3 *Ab initio* calculations of CS and EFG tensors

#### A. Introduction

*Ab initio* calculations of CS and EFG tensors presented in this section serve several purposes. First, they allow for comparison between experimentally-derived and theoretically-calculated interaction tensors. Second, the parameters from calculations performed with RHF and DFT methods available under the Gaussian

94 platform are compared.<sup>125</sup> Third, the effects of basis set on the CS and EFG tensor principal components are tabulated. Finally, theoretical CS and EFG tensor orientations are obtained for comparison with those garnered from experiment.

### B. *Ab initio* calculations of CS and EFG tensors in $\text{Cl}_3\text{AlOPCl}_2$

A comparison of the experimental and theoretical  $^{27}\text{Al}$  CS tensors of **I** is presented in Table 3.2. Experimental CS parameters are most closely predicted by the RHF/6-31G\* and B3LYP/6-31G\* calculations. Interestingly, all of the CS principal components become deshielded (most notably,  $\delta_{11}$ ) with the use of the larger basis set (6-311G\*). The addition of diffuse functions (i.e., 6-31+G\* and 6-311+G\*) has little effect on the calculated results. In some instances, continually increasing the size of the basis set will have little or no effect on the resulting parameters; this is known as *basis set saturation*.<sup>60</sup> This was observed for calculations on **II** and **III** as well. Taking this and the large amounts of CPU time required for such calculations into consideration, calculations employing diffuse basis functions are only reported for **I**. The DFT calculations were completed in roughly two-thirds of the CPU time required for analogous RHF calculations.

The orientation of the  $^{27}\text{Al}$  CS tensor in the molecular frame (Fig. 3.12) is also obtained from the calculations. RHF and DFT calculations predict almost identical tensor orientations regardless of basis set. The least shielded component of the CS tensor is oriented  $1.2^\circ$  from the direction of the Al-O bond vector, with  $\delta_{33}$  contained within and  $\delta_{22}$  perpendicular to the mirror plane. The theoretical orientation of  $\delta_{11}$  is in agreement with the experimental  $^{27}\text{Al}$  CS tensor orientation.

**Table 3.2:** Experimental and Calculated Aluminum-27 CS Tensors in  $\text{Cl}_3\text{AlOPCl}_3^a$ 

	$\delta_{11}$ (ppm)	$\delta_{22}$ (ppm)	$\delta_{33}$ (ppm)	$\delta_{\text{iso}}$ (ppm)	$\Omega$ (ppm)	$\kappa$	$C_Q$ (MHz)	$\eta$
Expt.	125	74	65	88	60	-0.70	6.0(1)	0.15(1)
RHF								
6-31G*	115.9	58.5	53.8	76.1	62.0	-0.85	-7.6	0.11
6-31+G*	120.1	61.1	55.9	79.0	64.3	-0.84	-7.4	0.12
6-311G*	162.5	93.6	87.6	114.6	74.9	-0.84	-10.0	0.11
6-311+G*	161.3	92.8	86.9	113.7	74.4	-0.84	-9.7	0.12
DFT(B3LYP)								
6-31G*	142.6	81.6	77.0	100.4	65.6	-0.86	-6.5	0.11
6-31+G*	148.6	79.4	73.6	100.5	75.0	-0.85	-7.0	0.10
6-311G*	214.0	130.7	124.6	156.4	89.4	-0.86	-9.4	0.11
6-311+G*	213.5	130.8	124.7	156.3	88.9	-0.86	-9.3	0.11

<sup>a</sup> Experimental chemical shifts referenced with respect to  $\text{Al}(\text{H}_2\text{O})_6^{3+}(\text{aq})$ ,  $\delta(^{27}\text{Al}) = 0$  ppm. Theoretical chemical shifts referenced with respect to  $\text{AlH}_4^-$ ,  $\delta(^{27}\text{Al}) = 101$  ppm (see experimental).

The EFG tensor at the aluminum nucleus was also calculated using several different basis sets (Table 3.2). The values of  $C_Q$  calculated by both RHF and DFT methods with 6-31G\* and 6-31+G\* basis sets are reasonably close to the experimental nuclear quadrupolar coupling constant, while larger basis sets overestimate its magnitude. The sign of  $C_Q$ , which cannot be determined from the solid-state NMR experiments described here, is calculated to be negative. The quadrupolar asymmetry parameter is calculated as 0.11 or 0.12, in good agreement with the experimental  $\eta = 0.15$ , which is thought to be the result of the near- $C_{3v}$  symmetry at the aluminum nucleus ( $V_{11} \neq V_{22}$ ). The largest component of the EFG

tensor is oriented  $1.4^\circ$  from the Al-O bond axis, with the remaining components perpendicular to this axis (Fig. 3.12). The theoretical relative orientation of the CS and EFG tensor is in good agreement with the experimentally-derived orientation, where the CS tensor is related to the EFG PAS by Euler angles  $\alpha = 90^\circ$ ,  $\beta = 90^\circ$  and  $\gamma = 0^\circ$ .

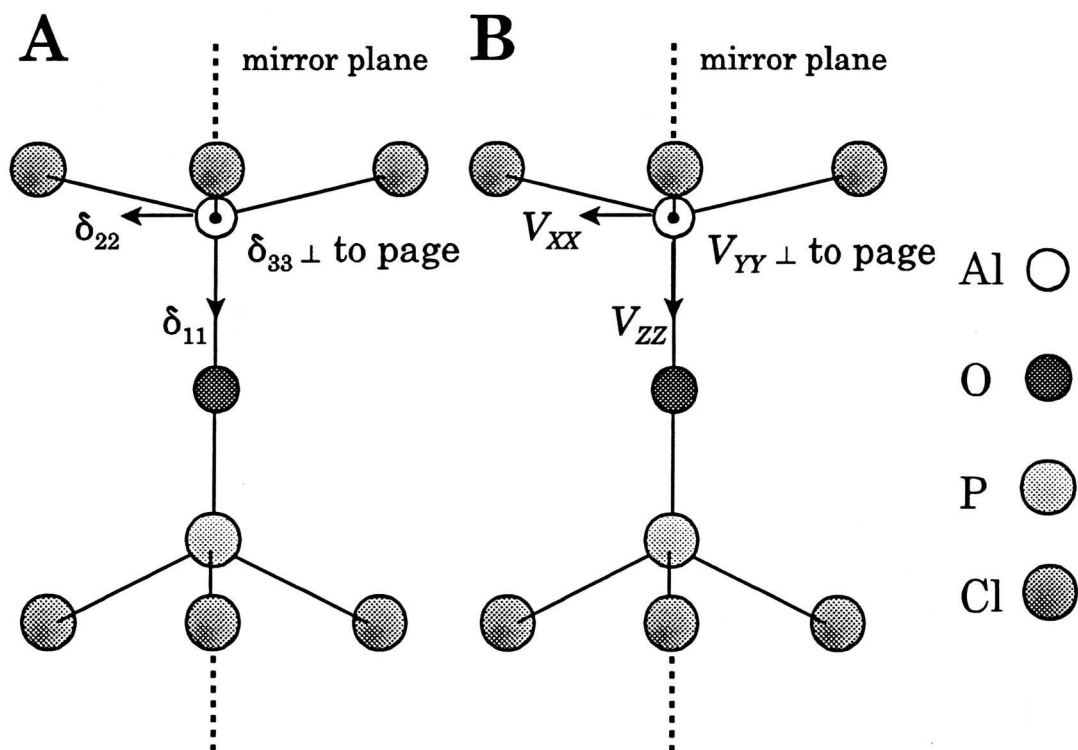


**Figure 3.12** (A) Theoretical orientation of the  $^{27}\text{Al}$  CS tensor in the molecular frame. (B) Theoretical orientation of the EFG tensor at the aluminum nucleus.

### C. *Ab initio* calculations of CS and EFG tensors in $\text{Al}(\text{acac})_3$ and $\text{Al}(\text{trop})_3$

$\text{Al}(\text{acac})_3$ . In order to further establish the orientation of the interaction tensors with respect to the molecular frame, it is worthwhile to compare theoretical CS and

**Table 3.3:** Experimental and Calculated Aluminum-27 CS Tensors in Al(acac)<sub>3</sub> and Al(trop)<sub>3</sub>

Complex	Chemical Shift Principal Components (ppm) <sup>a</sup>			Chemical Shift Parameters			Quadrupolar Parameters	
	$\delta_{11}$	$\delta_{22}$	$\delta_{33}$	$\delta_{\text{iso}}$ (ppm)	$\Omega$ (ppm)	$\kappa$	$C_Q$ (MHz)	$\eta$
Al(acac) <sub>3</sub>								
Experimental	1.5	0.9	-2.3	0.0	3.8	0.7	3.03	0.15
RHF/6-31G*	-6.8	-9.3	-9.9	-8.6	3.1	-0.6	2.11	0.05
B3LYP/6-31G*	17.1	15.9	15.3	16.1	1.8	-0.3	2.30	0.03
RHF/6-311G*	12.2	5.4	4.9	7.5	7.3	-0.9	2.37	0.05
B3LYP/6-311G*	45.6	39.2	38.6	41.1	7.0	-0.8	2.85	0.04
Al(trop) <sub>3</sub>								
Experimental	41.5	35.9	32.5	36.6	9.0	-0.3	4.43	0.08
RHF/6-31G*	20.8	13.4	10.6	14.9	10.2	-0.4	3.36	0.04
B3LYP/6-31G*	49.6	47.6	43.3	46.8	6.4	0.4	3.40	0.03
RHF/6-311G*	46.9	36.7	32.9	38.8	14.0	-0.5	3.31	0.10
B3LYP/6-311G*	90.1	80.4	75.2	81.9	14.9	-0.3	4.00	0.07

<sup>a</sup> Calculated <sup>27</sup>Al chemical shifts are referenced as described in Table 3.2 and experimental section.

EFG tensor orientations on the octahedral aluminum complexes with experimental results (see Table 3.3).

Both RHF and DFT(B3LYP) CS calculations with 6-31G\* and 6-311G\* basis sets predict CSA at the aluminum nucleus. Several interesting observations can be made. The CS calculations carried out with the 6-31G\* basis set are closest to the

experimentally observed values, though the improved results with the smaller basis set are likely fortuitous. The RHF/6-31G\* calculations predict a span of 3.1 ppm, which is quite close to the measured value of 3.8(3) ppm. The RHF and DFT 6-311G\* calculations overestimate the span of the CS tensor by ca. 3 ppm or more. Both RHF and DFT calculations predict a negative skew, implying that  $\delta_{11}$  is the quasi-unique principal CS tensor component, contrary to the experimental results. Both methods using the 6-31G\* basis set underestimate  $C_Q$  by 0.7 to 0.9 MHz; however, calculations with the 6-311G\* basis set (notably B3LYP) yield values of  $C_Q$  that are close to the experimentally determined  $C_Q$ . In all cases, the calculated  $\eta$  values indicate an EFG tensor of near-axial symmetry.

The most interesting feature of these calculations is the predicted orientations of the CS and EFG tensors in the molecular frame and relative to one another. RHF calculations using either the 6-31G\* or 6-311G\* basis set and B3LYP/6-311G\* calculations yield orientations in which  $V_{33}$  and  $\delta_{11}$  are between 6° and 7° apart, aligned approximately along the direction of the molecular  $C_3$  axis, in agreement with the first set of experimentally proposed tensor orientations (Section 3.3.2). The relative orientation of EFG and CS tensors, for example in the RHF/6-31G\* calculations, is described by the Euler angles  $\alpha = 88.3^\circ$ ,  $\beta = 87.9^\circ$  and  $\gamma = 6.8^\circ$ , with other calculations giving similar data. These results are very close to the experimental orientation [ $\alpha = 90^\circ(\pm 15^\circ)$ ,  $\beta = 90^\circ(\pm 10^\circ)$  and  $\gamma = 0^\circ(\pm 30^\circ)$ ]. The orientations of the CS and EFG tensors in the molecular frame are pictured in Fig. 3.13. Despite the fact that the theoretical orientations of the CS and EFG tensors are in agreement with experiment, there are some discrepancies in the orientations

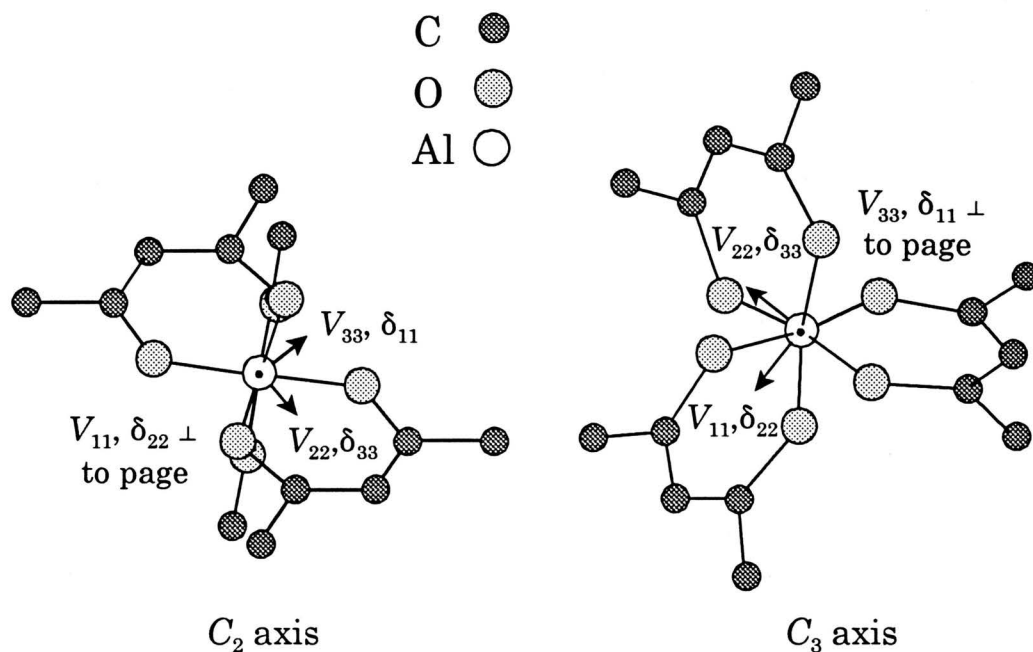


**Figure 3.13** Two projections illustrating the orientations of the CS and EFG tensors in the molecular frame of  $\text{Al}(\text{acac})_3$  as determined by experiment and theoretical calculations (6-31G\* basis set).  $V_{33}$  and  $\delta_{11}$  are aligned along an approximate  $C_3$  rotational axis, with  $V_{11}$  and  $\delta_{22}$  roughly oriented with the  $C_2$  symmetry axis.

of the remaining components in the molecular frame, depending on the type of basis set applied in the calculation. The RHF/6-31G\* calculations place  $V_{11}$  and  $\delta_{22}$  approximately along a  $C_2$  rotation axis, separated by  $7.0^\circ$ , with  $\delta_{33}$  and  $V_{22}$  set  $3.3^\circ$  apart and normal to both symmetry axes. In contrast, both the RHF and B3LYP 6-311G\* calculations set  $\delta_{33}$  and  $V_{22}$  at ca.  $16^\circ$  apart and near a  $C_2$  axis, with  $V_{11}$  and  $\delta_{22}$  normal to the rotational symmetry axes. It is not surprising that there is some discrepancy between calculations with different methods and basis sets in the orientation of CS and EFG tensors in the molecular frame, since the magnitude of

the CSA is very small and the “non-unique” components are very close to one another. At this point, no conclusion can be drawn about which set of principal components lies along the direction of one of the  $C_2$  symmetry axes, but the theoretical relative orientations of the EFG and CS tensors obtained from RHF/6-31G\*, RHF/6-311G\* and B3LYP/6-311G\* calculations are in reasonable agreement with the experimentally determined orientations. B3LYP/6-31G\* calculations yield CS tensor orientations which do not correspond to those observed experimentally or obtained using other basis sets.

**Al(trop)<sub>3</sub>.** Aluminum-27 CS tensors calculated using Hartree-Fock methods with the 6-31G\* basis set are in very good agreement with the experimentally determined values - notably, the experimental and theoretical spans and skews are very close to one another (Table 3.3). The DFT calculations with the same basis set underestimate the span considerably (ca. 3 ppm), and predict a skew of opposite sign. Calculations carried out using the larger 6-311G\* basis set overestimate the span by 5 ppm or greater, but also predict negative skews, in accordance with experiment. All calculations predict deshielding at the  $^{27}\text{Al}$  nucleus in Al(trop)<sub>3</sub> relative to Al(acac)<sub>3</sub>, ranging from 20 to 40 ppm, which is in qualitative agreement with the measured deshielding of 36.6 ppm. All calculations slightly underestimate the magnitude of  $C_Q$ , with B3LYP/6-311G\* calculations predicting the asymmetry parameter quite accurately.

Several interesting results regarding the tensor orientations are extracted from these computations (Fig 3.14). RHF/6-31G\*, 6-311G\* and B3LYP/6-311G\*

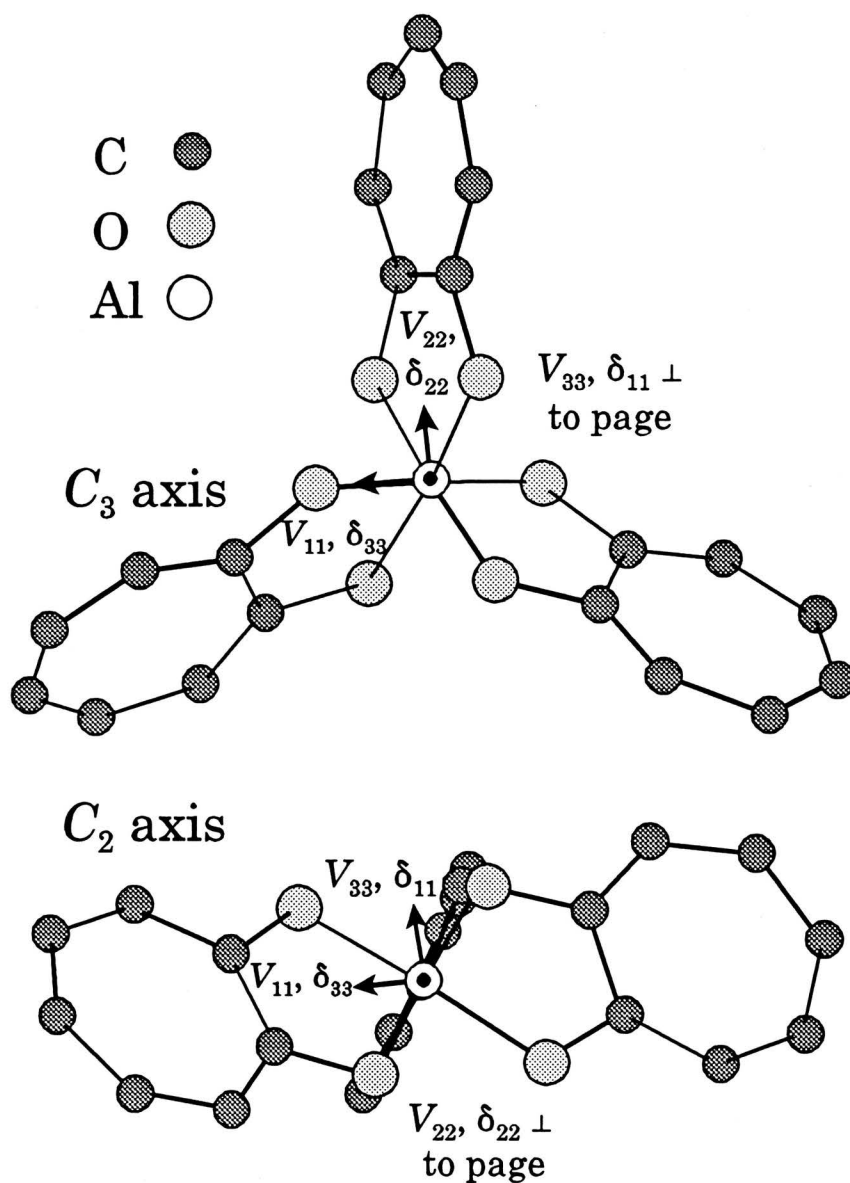


**Figure 3.14** Two projections illustrating the orientations of the CS and EFG tensors in the molecular frame of  $\text{Al}(\text{trop})_3$  as determined by experiment and theoretical calculations. Theoretical calculations place  $V_{33}$  and  $\delta_{11}$  along the unique  $C_3$  symmetry axis, with  $V_{22}$  and  $\delta_{22}$  along the direction of a  $C_2$  symmetry axis.

calculations reveal that the  $V_{33}$  and  $\delta_{11}$  are in the direction of the near- $C_3$  axis, and are  $3.5^\circ$  to  $8.5^\circ$  apart, in close agreement with our experimental results. However,

the calculations place  $V_{11}$  and  $\delta_{33}$  at ca.  $7.7(6)^\circ$  from one another and  $V_{22}$  and  $\delta_{22}$  at ca.  $2.0^\circ$  apart, in contrast to the relative orientations of these components determined experimentally. Interestingly, the  $\delta_{22}$  and  $V_{22}$  components fall along the direction of the unique  $C_2$  axis (in agreement with our earlier suggestion), with  $V_{11}$  and  $\delta_{33}$  normal to the two symmetry axes. In general, the theoretically-calculated parameters are quite close to experimental values for  $\text{Al}(\text{trop})_3$ , the only discrepancy being the relative orientation of the CS and EFG tensors. Nevertheless, given that  $V_{11} \approx V_{22}$ , this is not a serious incongruity.

### 3.4 Aluminum-27 Chemical Shielding Anisotropy in Linear Molecules

#### 3.4.1 Theoretical Background

It is possible to obtain absolute chemical shielding data from the recently reported  $^{27}\text{Al}$  nuclear spin-rotation constants,  $C_1$ , which have been obtained from high-resolution microwave spectroscopic studies of the linear molecules aluminum (I) isocyanide<sup>93,94</sup> and aluminum (I) chloride.<sup>95</sup> The spin-rotation data yields “experimental” values of the CS tensor components parallel and perpendicular to the molecular axis (i.e.,  $\sigma_{\parallel}$  and  $\sigma_{\perp}$ ). Because these are highly reactive molecules, it is impractical to measure experimental chemical shifts of other aluminum-containing compounds relative to  $\text{AlNC}$  or  $\text{AlCl}$ . Nevertheless, the experimental data presented here serve as a benchmark for checking the reliability of theoretical calculations.

As discussed in Chapter 2, the chemical shielding tensor can be expressed according to the sum of the diamagnetic and the paramagnetic shielding tensors.<sup>26</sup>

$$\sigma = \sigma^d + \sigma^p \quad (3.6)$$

The diamagnetic shielding tensor is dependent only upon the ground electronic state of the molecule, and for a nucleus,  $A$ , is given as

$$\sigma_{A\alpha\beta}^d = \frac{\mu_0}{4\pi} \frac{e^2}{2m} \langle 0 | \sum_i \frac{(\mathbf{r}_i \cdot \mathbf{r}_{iA} \delta_{\alpha\beta} - r_{i\alpha} r_{i\beta})}{r_{iA}^3} | 0 \rangle \quad (3.7)$$

where  $\mu_0$  is the permeability of free space,  $e$  and  $m$  are the charge and mass of the electron,  $|0\rangle$  are ground-state wavefunctions,  $\alpha$  and  $\beta$  are Cartesian components ( $x$ ,  $y$ ,  $z$ ) of the diamagnetic CS tensor,  $\delta_{\alpha\beta}$  is the Krönecker delta, and  $\mathbf{r}_i$  and  $\mathbf{r}_{iA}$  are the position vectors of electron  $i$  with respect to the origin of coordinates (the *gauge origin*) and the nucleus, respectively. In a closed-shell atom in an applied magnetic field, electron circulation about the direction of the field induces a magnetic field at the nucleus proportional and opposite in direction to the magnetic field (i.e., shielding). From eq. 3.7, it is seen that shielding decreases as  $r_{iA}$  increases. The degree of diamagnetic shielding also increases with increasing atomic number,  $Z$ .<sup>126</sup>

For linear molecules, Flygare and co-workers<sup>127</sup> have shown that the diamagnetic shielding contribution can be obtained from

$$\sigma_{\perp}^d = \sigma_{\text{free atom}}^d + \frac{\mu_0}{4\pi} \frac{e^2}{2m} \sum_n \frac{Z_n}{r_n} \quad (3.8)$$

and

$$\sigma_{\parallel}^d \approx \sigma_{\text{free atom}}^d \quad (3.9)$$

where  $\sigma_{\text{free atom}}^d$  have been calculated for nuclei up to  $Z = 86$  from ground state atomic orbital wavefunctions,<sup>126</sup> and  $Z_n$  and  $r_n$  are the atomic number and distance of the  $n$ th nucleus from the origin nucleus, respectively.

Chemical shielding at a nucleus within a molecule is considerably more complicated than for a free atom. The electron cloud about the nucleus is no longer spherically symmetrical, since it is involved in chemical bonding. In addition, the circulation of electrons is inhibited by electrostatic interactions with other nuclei in the molecule. Thus, the difficulty in chemical shielding computations arises when calculating the paramagnetic shielding tensor, which involves excited state molecular orbitals. The paramagnetic shielding tensor at a nucleus,  $A$ , is given as<sup>26</sup>

$$\begin{aligned} \sigma_{A\alpha\beta}^p = & -\frac{\mu_0}{4\pi} \frac{e^2}{2m^2} \sum_{k \neq 0} (E_k - E_0)^{-1} \times [ \langle 0 | \sum_i L_{i\alpha} | k \rangle \langle k | \sum_i \frac{L_{i\alpha\beta}}{r_{iA}^3} | 0 \rangle \\ & + \langle 0 | \sum_i \frac{L_{iA\alpha}}{r_{iA}^3} | k \rangle \langle k | \sum_i L_{i\beta} | 0 \rangle ] \end{aligned} \quad (3.10)$$

where  $E_k - E_0$  is the energy difference between ground and excited states ( $|k\rangle$ ), and  $L_i$  and  $L_{iA}$  are the orbital angular momentum operators of the  $i$ th electron with respect to the gauge origin and nucleus, respectively. The equation is summed over all excited states,  $k$ . The angular momentum operators in eq. 3.10 describe the mixing of ground and excited state orbitals. This mixing is often described as "rotation of charge," in which the mixing of ground and excited states correspond to rotation of charge about the direction of the magnetic field.

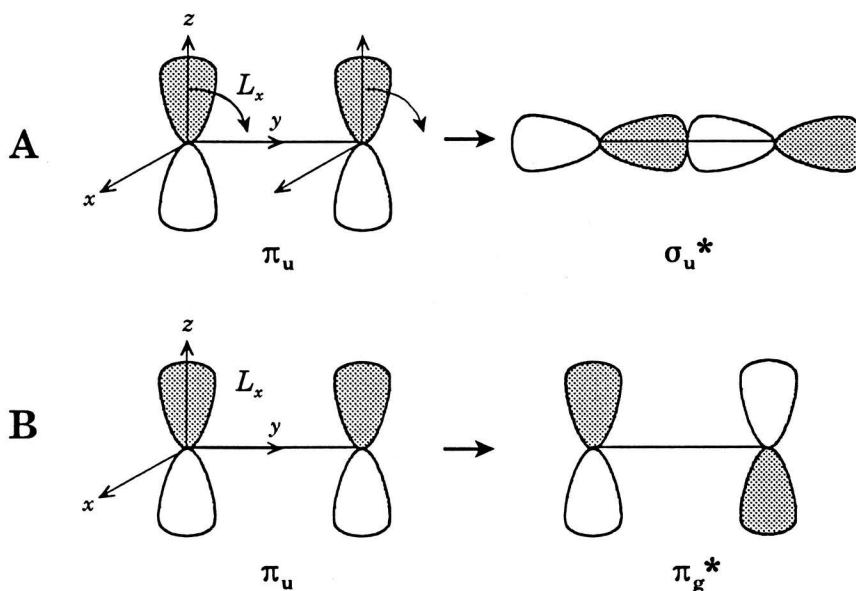


**Figure 3.15** (A) A magnetic-dipole-allowed (symmetry-allowed) transition created by the  $L_x$  operator resulting in a paramagnetic shielding contribution along the  $x$ -direction (B) A symmetry-forbidden transition with no paramagnetic shielding contribution.

The mixing of ground- and excited-state orbitals by the  $L_x$  angular momentum operator is shown in Fig. 3.15.<sup>128</sup> In 3.15A, a symmetry-allowed or *magnetic-dipole-allowed*  $\pi_u$ - $\sigma_u^*$  transition is pictured, corresponding to transformation of the  $p_z$  into  $p_y$  atomic orbitals, and the mixing of  $\pi_u$  and  $\sigma_u^*$  molecular orbitals. The paramagnetic shielding contribution (i.e., normally deshielding) is along the direction of the angular momentum operator, perpendicular to the directions of the mixing orbitals. In Fig. 3.15B, a symmetry forbidden transition is pictured, meaning that there is no contribution to paramagnetic shielding from mixing of these orbitals. This qualitative picture of charge rotation is useful for understanding the origin of paramagnetic shielding contributions in molecules discussed in this chapter and in Chapter 5.

Theoretical treatment of the paramagnetic chemical shielding contribution is improved by the inclusion of electron correlation;<sup>60,63,87,129</sup> notwithstanding, due to the high computational times involved in performing such calculations, the majority of reported shielding calculations are obtained with Hartree-Fock methods. Highly polarized basis sets are required to accurately calculate paramagnetic shielding contributions, and as a result, RHF theory often tends to overestimate the paramagnetic shielding component. Density functional theory implicitly includes electron correlation; however, the quality of the DFT calculation is largely dependent on the calibre of the semi-empirical correlation functional used in the calculation,<sup>68,125,130</sup> as discussed in Section 2.5.

Experimental values of the paramagnetic shielding tensor can be calculated from the nuclear spin-rotation tensor data following procedures outlined by Flygare and co-workers.<sup>127</sup> In the case of linear molecules,

$$\sigma_{\perp}^p = - \frac{m_p}{2m_e g_N} \frac{C_{\perp}}{B} - \frac{\mu_0}{4\pi} \frac{e^2}{2m_e} \sum_n \frac{Z_n}{r_n} \quad (3.11)$$

where  $m_p$  and  $m_e$  are the proton and electron masses,  $g_N$  is the nuclear  $g$ -factor (1.4565 for  $^{27}\text{Al}$ ), and  $B$  is the molecular rotational constant in Hz ( $B = h/8\pi^2 I$ ). The sign preceding the first term of eq. 3.11 is often written as positive;<sup>31,127</sup> however, the correct sign depends upon the convention used for the sign of the nuclear spin-rotation constant.<sup>131</sup> Here we follow the sign convention of Gerry and co-workers.<sup>131a</sup> The most important point is that the first term of eq. 3.11 is almost always negative. Known exceptions are for the fluorine nuclei of ClF, BrF, IF and SF<sub>2</sub>.<sup>132</sup> There is no

paramagnetic shielding contribution along the molecular  $C_\infty$  axis in linear molecules;<sup>127</sup> therefore, the total parallel chemical shielding component is given by eq. 3.9. This can be easily understood in terms of the charge-rotation model presented above.

### 3.4.2 Results and Discussion

Consider the AlNC molecule, for which internuclear distances of  $r_o(\text{Al,N}) = 1.849 \text{ \AA}$ ,  $r_o(\text{N,C}) = 1.171 \text{ \AA}$ ,<sup>93</sup> and a  $^{27}\text{Al}$  spin-rotation constant of  $C_\perp = 3.850(84)$  kHz,<sup>94</sup> have been determined. From the above equations, one obtains  $\sigma_\parallel = 789.9$  ppm<sup>126</sup> and  $\sigma_\perp = 384.3(8.9)$  ppm (from  $\sigma_\perp^d = 871.21(3)$  ppm and  $\sigma_\perp^p = -486.9(8.9)$  ppm), for an isotropic chemical shielding of  $\sigma_{\text{iso}} = (2\sigma_\perp + \sigma_\parallel)/3 = 519.5(9.0)$  ppm. The span of the chemical shielding tensor is given by  $\Omega = \sigma_\parallel - \sigma_\perp = 405.6(9.0)$  ppm. Similar calculations can be carried out for AlCl, which has  $r_e(\text{Al,Cl}) = 2.12983(1) \text{ \AA}$ <sup>133</sup> and  $C_\perp = 5.54(16)$  kHz,<sup>95</sup> which gives  $\sigma_\parallel = 789.9$  ppm and  $\sigma_\perp = 313(17)$  ppm (from  $\sigma_\perp^d = 902.34(1)$  ppm and  $\sigma_\perp^p = -589(17)$  ppm), for  $\sigma_{\text{iso}} = 472(17)$  ppm,  $\Omega = 477(17)$  ppm. These results are summarized and compared to theoretically calculated values in Table 3.4.

GIAO NMR chemical shielding calculations were carried out on AlNC, AlCl, AlF and AlH, using both experimentally determined molecular geometries<sup>134,135</sup> and theoretically optimized structures. Several striking features are evident when comparing the theoretical and experimental results (Table 3.4). For both AlNC and AlCl, the theoretical shielding parameters are in good agreement with the experimental values, notably those calculated values obtained with the RHF and

DFT methods using the 6-311G\* basis set. Calculations on AlNC and AlCl were performed using both MP2/6-311G\* geometry optimized structures as well as the structures deduced from the experimental rotational constants. The experimental AlCl bond length,  $r_e(\text{Al,Cl}) = 2.1298 \text{ \AA}$ ,<sup>133</sup> is quite close to the MP2/6-311G\* bond length, and as a result, the chemical shielding parameters are quite similar. However, for AlNC the experimental value determined for  $r_e(\text{Al,N})$ , 1.849Å,<sup>93</sup> is significantly different from the theoretical equilibrium bond length.

In comparison to the span calculated for AlCl ( $\Omega = 487.6 \text{ ppm}$ , RHF/6-311G\*), a very large span is predicted for AlH ( $\Omega = 985.0 \text{ ppm}$ ) and a smaller span is calculated for AlF ( $\Omega = 329.8 \text{ ppm}$ ). It is possible to qualitatively rationalize the increasing span (i.e.,  $\Omega(\text{AlF}) < \Omega(\text{AlCl}) < \Omega(\text{AlH})$ ) in terms of magnetic dipole allowed  $\sigma \rightarrow \pi^*$  mixing. From RHF Mulliken population and natural bond order analyses<sup>136</sup> with both the 6-31G\* and 6-311G\* basis sets, several interesting results are noted. In all three molecules, the HOMO and the LUMO are  $\sigma$  and  $\pi^*$  molecular orbitals, respectively, with large contributions from the valence shell atomic orbitals of the aluminum atom. The energy difference between the HOMO and LUMO decreases in a linear fashion with respect to chemical shielding (i.e.,  $\Delta E(\text{AlF}) > \Delta E(\text{AlCl}) > \Delta E(\text{AlH})$ ). The relationship between the CS and  $\Delta E$  stems from the dependence of the paramagnetic shielding contribution on the excited electronic states (see eq. 3.10).<sup>26</sup> A smaller energy difference between the HOMO and LUMO leads to a larger paramagnetic shielding contribution. It is also interesting to note that the ionic/covalent character of the molecules follows the same trend, with population analyses indicating that AlF is essentially an ionically bound species, whereas AlCl

**Table 3.4:** Experimental and calculated aluminum-27 chemical shielding parameters for a series of linear Al-containing molecules

	Experimental (S.R. data) <sup>b</sup>	6-31G*(*) <sup>a</sup>		6-311G*(*) <sup>a</sup>	
		RHF	DFT (B3LYP)	RHF	DFT (B3LYP)
<b>AlNC:<sup>c</sup></b>					
$\sigma_1$ (ppm)	789.9	791.6	791.6	791.6	792.3
$\sigma_{\perp}$ (ppm)	384.3	460.5	422.6	414.9	374.9
$\sigma_{\text{iso}}$ (ppm)	519.5	570.9	545.6	540.5	514.0
$\Omega$ (ppm)	405.6	331.1	369.0	376.7	417.4
<b>AlNC:<sup>d</sup></b>					
$\sigma_1$ (ppm)	789.9	791.9	791.8	791.9	792.6
$\sigma_{\perp}$ (ppm)	384.3	442.7	404.6	394.0	354.1
$\sigma_{\text{iso}}$ (ppm)	519.5	559.1	533.7	526.7	500.2
$\Omega$ (ppm)	405.6	349.2	387.1	397.9	438.5
<b>AlCl:<sup>e</sup></b>					
$\sigma_1$ (ppm)	789.9	793.7	793.8	793.7	794.6
$\sigma_{\perp}$ (ppm)	312.5	373.8	330.0	309.0	257.6
$\sigma_{\text{iso}}$ (ppm)	471.6	513.8	484.6	470.6	436.7
$\Omega$ (ppm)	477.4	419.9	463.8	484.7	536.8
<b>AlCl:<sup>e</sup></b>					
$\sigma_1$ (ppm)	789.9	793.8	793.9	793.8	794.7
$\sigma_{\perp}$ (ppm)	312.5	371.7	328.5	306.2	255.6
$\sigma_{\text{iso}}$ (ppm)	471.6	512.4	483.6	468.7	435.3
$\Omega$ (ppm)	477.4	422.1	465.4	487.6	539.1

(continued next page)

Table 3.4 (cont'd)

	Experimental	6-31G*(*) <sup>a</sup>		6-311G*(*) <sup>a</sup>	
		RHF	B3LYP	RHF	B3LYP
AlH: <sup>f</sup>	n/a				
$\sigma_{\parallel}$ (ppm)		787.3	787.2	787.3	787.9
$\sigma_{\perp}$ (ppm)		-83.5	-163.4	-197.7	-290.6
$\sigma_{\text{iso}}$ (ppm)		206.8	153.5	130.6	68.9
$\Omega$ (ppm)		870.8	950.6	985.0	1078.5
AlF: <sup>g</sup>	n/a				
$\sigma_{\parallel}$ (ppm)		791.8	792.2	791.9	793.0
$\sigma_{\perp}$ (ppm)		501.6	457.4	462.0	417.9
$\sigma_{\text{iso}}$ (ppm)		598.3	569.0	572.0	542.9
$\Omega$ (ppm)		290.2	334.7	329.8	375.1

- a. For AlH, 6-31G\*\* and 6-311G\*\* basis sets were used so as to include polarization functions on the hydrogen atoms.
- b. The principal components of the <sup>27</sup>Al chemical shielding tensors are calculated from known nuclear spin-rotation coupling constants for AlNC and AlCl. Errors in these components are given in the text.
- c. Calculations performed on the MP2/6-311G\* geometry optimized structures:  $r(\text{Al,Cl}) = 2.1364 \text{ \AA}$ ,  $r(\text{Al,N}) = 1.8802 \text{ \AA}$ ,  $r(\text{N,C}) = 1.1936 \text{ \AA}$ .
- d. Calculations performed on the AlNC molecule using the experimentally determined Al,N and N,C bond lengths,  $r_{\text{o}}(\text{Al,N}) = 1.849 \text{ \AA}$  and  $r_{\text{o}}(\text{N,C}) = 1.171 \text{ \AA}$ .<sup>93</sup>
- e. Calculations performed on AlCl using the experimentally determined bond length,  $r_{\text{e}}(\text{Al,Cl}) = 2.1298$ .<sup>133</sup>
- f. Calculations performed on AlH using the experimentally determined bond length,  $r_{\text{e}}(\text{Al,H}) = 1.64738 \text{ \AA}$ .<sup>134b</sup>
- g. Calculations performed on AlF using experimental bond length,  $r_{\text{e}}(\text{Al,F}) = 1.65436 \text{ \AA}$ .<sup>135</sup>

and AlH have increasingly covalent bonding character.

Finally, experimental and theoretical values of  $C_Q(^{27}\text{Al})$  for all four systems are presented in Table 3.5. Values of  $C_Q$  obtained from RHF, DFT and MP2 calculations using the 6-311G\*(\*) basis set are quite close to experimental values with the exception of  $C_Q$  in AlH.<sup>137</sup> Nuclear quadrupole coupling constants vary due to distortions in molecular geometry which are dependent on the vibrational state of the molecule, isotopic substitution and intermolecular interactions.<sup>138</sup> However, MP2/6-311G\*\* calculations of  $C_Q(^{27}\text{Al})$  in AlH for varying bond lengths near  $r_e$  yield  $\partial C_Q/\partial r = -50 \text{ MHz/\AA}$ , indicating that rovibrational averaging cannot account for the difference in the experimental and theoretical  $C_Q$  (*vide infra*). Elimination of the polarization functions on the hydrogen atom has little effect on the calculated results (i.e., MP2/6-311G\* calculations). In some cases, corrections to quadrupolar and chemical shielding parameters must be made for vibrational motions and/or intermolecular interactions. This subject is addressed with regard to the aluminum chemical shielding in the next section of this chapter.

The difference between the experimental and theoretical  $C_Q(^{27}\text{Al})$  values may arise from several sources, such as some deficiency in the calculation of the electric field gradient, experimental uncertainty in the  $^{27}\text{Al}$  nuclear quadrupole moment, or an error in the reported value of  $C_Q(^{27}\text{Al})$ . Given that the calculated  $C_Q(^{27}\text{Al})$  for AlF, AlCl and AlNC are quite close to the experimental values, it is suspected that the analysis of the hyperfine structure in the microwave spectra of the  $J = 0 - 1$  transition in AlH may be incorrect.<sup>137</sup> In order to test this hypothesis, several calculations were carried out on HCl, for which experimental  $C_Q(\text{Cl})$  and nuclear

**Table 3.5:** Experimental and calculated aluminum-27 nuclear quadrupole coupling constants for a series of linear Al-containing molecules.<sup>a</sup>

	Experimental	6-31G*			6-311G*		
		RHF	B3LYP	MP2	RHF	B3LYP	MP2
AlH	-36.72(33) <sup>b</sup>	-40.16	-41.05	-39.46	-50.06	-51.68	-49.36
AlF	-37.6(1.0) <sup>c</sup>	-30.70	-29.86	-30.13	-37.72	-36.35	-37.04
AlCl	-29.2(2.0) <sup>d</sup> , -30.4081(27) <sup>e</sup>	-25.90	-24.08	-24.07	-32.93	-31.60	-30.84
AlNC	-35.6268(16) <sup>f</sup>	-30.50	-30.14	-29.26	-38.21	-38.17	-36.69

- a.* All  $C_Q$  reported in MHz. All values of  $\eta = 0$ . For all molecules, experimentally determined bond lengths were used in the calculations (see Table 3.4 for details).
- b.* Reference 137.
- c.* Reference 133.
- d.* Reference 95.
- e.* Reference 94.
- f.* Reference 93.

spin-rotation constants for H and Cl are known.<sup>139</sup> First, calculations at the MP2/6-311G\* level of theory yield  $C_Q(^{35}\text{Cl}) = -65.1$  MHz, which is close to the experimental  $C_Q(^{35}\text{Cl}) = -67.6$  MHz. Second, nuclear spin-rotation constants were determined from RHF/6-311G\* CS tensor calculations to be  $C_{\perp}(^1\text{H}) = -43.858$  kHz and  $C_{\perp}(^{35}\text{Cl}) = 53.724$  kHz, in good agreement with the experimental  $C_{\perp}(^1\text{H}) = -41.877$  kHz and  $C_{\perp}(^{35}\text{Cl}) = 53.829$  kHz.<sup>139</sup> The close agreement between theory and experiment suggests that there is not a major deficiency in the calculations. From the RHF/6-311G\* CS tensor calculations on AlH, nuclear spin-rotation coupling constants of  $C_{\perp}(^1\text{H}) = -18.3$  kHz and  $C_{\perp}(^{27}\text{Al}) = 300.3$  kHz are predicted. On the basis of these calculations it is apparent that in analyzing rotational spectra of AlH, one

must consider the  $^{27}\text{Al}$  and  $^1\text{H}$  spin-rotation interactions. Unfortunately, these interactions were not considered by Goto and Saito<sup>137</sup> in their study of the  $J = 0 - 1$  rotational transition of  $\text{AlH}$ .

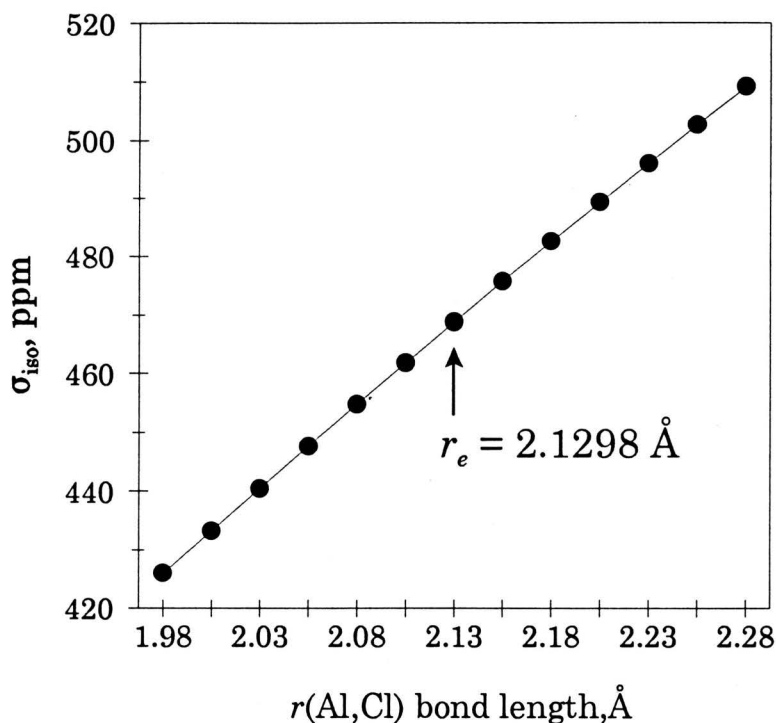


**Figure 3.16** Plot showing the linear relationship between the isotropic chemical shielding and the bond length in aluminum chloride. Calculations were carried out using the RHF/GIAO method with the 6-311G\* basis set, incrementing  $r(\text{Al,Cl})$  in 0.025 Å steps from the equilibrium bond length,  $r_e = 2.1298$  Å.

### 3.5 Rovibrational Corrections for Aluminum Chemical Shielding of $\text{AlCl}$

The magnetic shielding experienced by a nucleus in a molecule is known to be sensitive to subtle changes in molecular geometry. For example, the temperature dependence of nuclear magnetic shielding constants arises from varying populations of different allowed rotational and vibrational states.<sup>140,141</sup> Similarly, isotope effects

on magnetic shielding arise because of the different "average" structures of isotopomers.<sup>142</sup> The theoretical sensitivity of aluminum shielding to variations in bond length in aluminum chloride is shown in Fig. 3.16. First, it is clear that the derivative,  $\partial\sigma/\partial r$ , is positive, 278 ppm/Å at  $r_e$ . Positive values of  $\partial\sigma/\partial r$  have also been calculated for aluminum hydride,<sup>143</sup> but for group 14, 15, 16 and 17 hydrides this derivative is negative on the basis of theory and experiment.<sup>143,144</sup> Second, from the data shown in Fig. 3.16, one can estimate the rovibrational correction of the aluminum shielding constant, using the following expressions,

$$\langle\sigma\rangle_{v,J} - \sigma_e = \left(\frac{\partial\sigma}{\partial\xi}\right)_{\xi=0} \langle\xi\rangle_{v,J} + \left(\frac{1}{2}\right)\left(\frac{\partial^2\sigma}{\partial\xi^2}\right)_{\xi=0} \langle\xi^2\rangle_{v,J} \quad (3.12)$$

where  $\xi = (r - r_e)/r_e$  and the average values  $\langle\xi\rangle_{v,J}$  and  $\langle\xi^2\rangle_{v,J}$  are defined as follows:<sup>140,141</sup>

$$\langle\xi\rangle_{v,J} = -3a_1\left(\frac{B_e}{\omega_e}\right)\left[\frac{1}{2}\coth(hc\omega_e/2kT)\right] + 4(kT/hcB_e)\left(\frac{B_e}{\omega_e}\right)^2 \quad (3.13)$$

and

$$\langle\xi^2\rangle_{v,J} = [\coth(hc\omega_e/2kT)]\left(\frac{B_e}{\omega_e}\right) \quad (3.14)$$

where  $a_1$  is the cubic force constant,

$$-a_1 = \frac{\alpha_e\omega_e}{6B_e^2} + 1 \quad (3.15)$$

For AlCl,  $\alpha_1 = -3.1735$ .<sup>145</sup> Analysis of the data shown in Fig. 3.16 indicates  $(\partial\sigma/\partial\xi)_{\xi=0} = 592 \text{ ppm } \text{\AA}^{-1}$  and  $(\partial^2\sigma/\partial\xi^2)_{\xi=0} = -452 \text{ ppm } \text{\AA}^{-2}$ . Using the above expressions with  $B_e = 0.243942 \text{ cm}^{-1}$  and  $\omega_e = 481.67 \text{ cm}^{-1}$ ,<sup>145</sup> yields  $\langle\sigma\rangle_{v,J} - \sigma_e = 2.12 \text{ ppm}$ . Given that  $\sigma_{\parallel}$  is essentially independent of  $r$ ,  $\sigma_{\parallel}$  will be independent of temperature, and thus  $\langle\sigma_{\perp}\rangle_{v,J} - \sigma_{\perp,e} = 3.18 \text{ ppm}$ . In summary, the theoretical calculations indicate that the rovibrational averaging effects on aluminum shielding are relatively small, and not responsible for the discrepancies between theory and experiment.

### 3.6 Conclusions

In this chapter, several definitive examples of aluminum chemical shielding anisotropy have been presented. Solid-state  $^{27}\text{Al}$  NMR spectra of spinning and stationary samples provide detailed information on the nature of the chemical shielding and electric field gradient tensors. The tensor orientations within the molecular frame are inferred from a combination of molecular symmetry and NMR data. In terms of obtaining CS tensors with small CSAs from solid-state NMR spectra, it is clearly advantageous to obtain spectra at high magnetic fields. Our results demonstrate that anisotropic NMR interactions provide invaluable information about the local symmetry about NMR-active nuclei, since they are very sensitive to slight changes in molecular structure. Though these results increase the number of reported cases of  $^{27}\text{Al}$  CSA to eight, we believe that more work should be done characterizing  $^{27}\text{Al}$  CS tensors in order to better understand the nature of the chemical shielding interaction in aluminum and other group 13 elements.

It has been shown that it is beneficial to combine experimental and

theoretical data to characterize chemical shielding orientations in the molecular frame. Theoretical orientations of interaction tensors are in good agreement with experimental results, despite some small ambiguities in the octahedral complexes. Notably, experimentally determined and theoretically predicted CS and EFG tensor components along the unique symmetry axis of each molecule are in agreement. The 6-31G\* and 6-311G\* basis sets seem to be suitable for such calculations, since the employment of diffuse functions does not result in any significant differences in tensor parameters. Comparison of the calculated CS tensors to experimental results shows that further modification of current computational schemes is needed in order to calculate chemical shift parameters for second-row elements accurately.

Comparison of the CS tensors and EFG parameters in simple linear systems obtained from both experiment and theory reveal that it is possible to obtain relatively accurate theoretical CS parameters for simple molecules using present-day computational methods.

The  $^{31}\text{P}$  CS tensor in  $\text{Cl}_3\text{AlOPCl}_3$  was also characterized by solid-state NMR and computational methods. A brief summary of this work is given in Appendix A.

## Chapter 4

# Solid-State Phosphorus-31 NMR Study of

## Cobaloximes

### 4.1 Introduction

The recent solid-state NMR literature is replete with examples of the effects of the spin-spin coupling between spin-1/2 and quadrupolar nuclei on the NMR spectra of the spin-1/2 nuclei.<sup>146,147</sup> Much of this interest is derived from the fact that indirect spin-spin couplings between spin-1/2 and quadrupolar nuclei can often only be determined from NMR studies of solid samples, since quadrupolar relaxation times are relatively long in the solid state. For example, the first measurements of  $^1J(^{115}\text{In}, ^{31}\text{P})$  and  $^1J(^{101/99}\text{Ru}, ^{31}\text{P})$  were made in the  $^{31}\text{P}$  CPMAS NMR spectra of solid indium<sup>148</sup> and ruthenium<sup>149</sup> complexes. In solution, quadrupolar nuclei invariably undergo very efficient relaxation, resulting in "self-decoupling" from the spin-coupled spin-1/2 nucleus.<sup>17,150</sup> Although the effects of a self-decoupling quadrupolar nucleus on the solid-state line shapes of a neighbouring spin-1/2 nucleus have also been discussed,<sup>151,152</sup> few examples have been reported.<sup>153,154,155,156,157</sup> In each of these reports, only the direct dipolar interaction is considered; in this chapter, we discuss the first examples for which it is necessary to consider both direct dipolar and indirect spin-spin interactions.<sup>158</sup> These are also the first examples of self-decoupling of a quadrupolar nucleus in the solid state in which the quadrupolar nucleus remains stationary (i.e., the segment of the molecule containing the

quadrupolar nucleus does not undergo any jump-like or diffusional motion). The spin system of interest involves the cobalt-59 ( $S = 7/2$ ), phosphorus-31 ( $I = 1/2$ ) spin pair.

The series of complexes that are discussed in this report are the cobaloximes, which have been studied and characterized extensively over the past forty years.<sup>159,160,161</sup> Specifically, cobaloximes of the form  $LCo(DH)_2X$  (see Fig. 4.1) have been investigated, where L is a phosphine or phosphite, DH is the dimethylglyoxime anion, and X is one of the following anions:  $Cl^-$ ,  $Br^-$ ,  $CH_3^-$  ( $Me^-$ ), or  $N_3^-$ . Due to the large number of reported crystal structures for these compounds,<sup>160</sup> and the availability of  $^{59}Co$  NQR data,<sup>162</sup> cobaloximes are ideal candidates for study by  $^{31}P$  CPMAS NMR and the first-order perturbation theory which is outlined in Section 4.3.2.

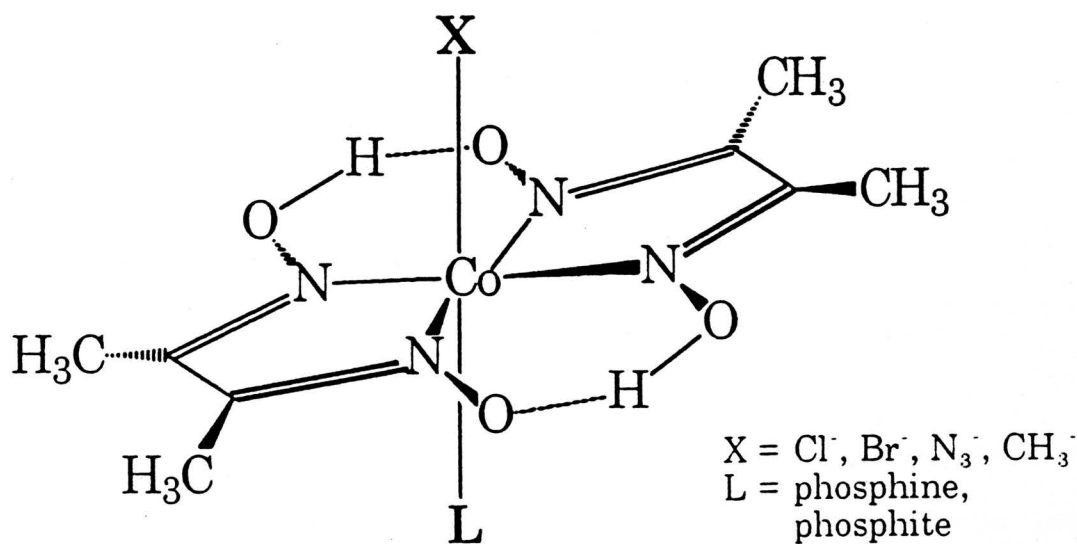


**Figure 4.1** The molecular structure of cobaloximes, with anionic species (X) and neutral ligands (L) substituted into the axial positions.

Phosphorus-31 CPMAS NMR spectra have been acquired at two applied magnetic fields (4.7 T and 9.4 T) for a series of cobaloximes. Since the phosphorus nucleus is indirectly spin-coupled to a cobalt nucleus, it is expected that a symmetric octet should be observed in the  $^{31}\text{P}$  MAS NMR spectrum; however, one observes an asymmetric eight-peak multiplet, with the size of the spacing between the peaks gradually increasing or decreasing (Fig. 4.2). Calculations of the  $^{31}\text{P}$  MAS NMR

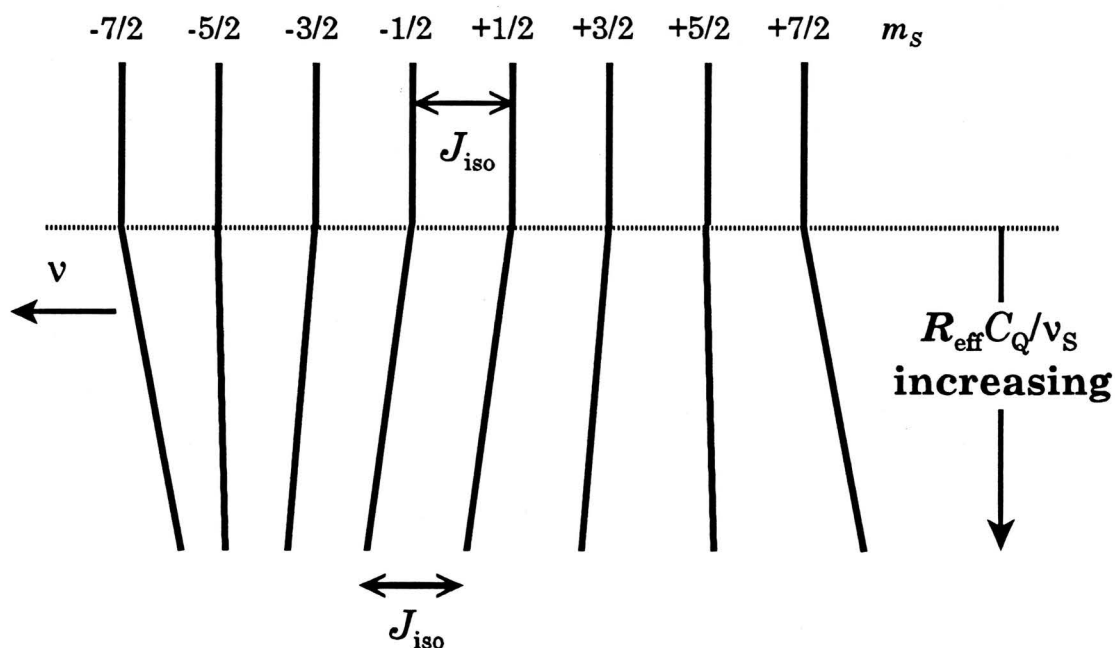


**Figure 4.2** Asymmetric splittings in the NMR spectrum of a spin-1/2 nucleus coupled to a quadrupolar nucleus with  $S = 7/2$ . Here, it is assumed that residual dipolar shift,  $d$ , is positive (see text). Note that to first order, separation between the transitions corresponding to  $m_s = +1/2$  and  $m_s = -1/2$  is equal to  $J_{\text{iso}}$ .

spectra are possible, allowing for the extraction of  $J_{\text{iso}}$ ,  $\delta_{\text{iso}}$  and the residual dipolar shift,  $d$  (*vide infra*). The origin of the asymmetric splitting observed in these spectra is also discussed in Section 4.3.2. New values of  $^1J(^{59}\text{Co}, ^{31}\text{P})$ , few of which have been obtained to date,<sup>163</sup> are reported in Section 4.4. To the best of our knowledge, there are only two other reports of  $^1J(^{59}\text{Co}, ^{31}\text{P})$  observed in the solid state.<sup>164,165</sup>

Several of the compounds exhibit broad, featureless peaks at room temperature; however, CPMAS NMR experiments at lower temperatures result in the gradual emergence of the eight-peak multiplet. The spin-lattice relaxation time of the cobalt nucleus decreases at higher temperatures, such that the cobalt nucleus effectively "self-decouples" from the indirectly spin-coupled phosphorus nucleus. Thus, at temperatures where the rate of cobalt of spin-lattice relaxation is fast enough, the multiplet disappears, and may even completely coalesce into a single peak. This phenomenon will be discussed in detail in Section 4.4.4.

## 4.2 Experimental

Cobaloximes were synthesized from standard literature methods<sup>159,166,167,168</sup> and new procedures described elsewhere.<sup>169</sup> Cobaloximes with L = PPh<sub>3</sub>, PBu<sub>3</sub> and X = Cl, Br, N<sub>3</sub> and Me were prepared in this laboratory. The remaining azido- and chloro-substituted cobaloximes were kindly provided by Prof. J.H. Nelson (University of Nevada at Reno). The remaining methylcobaloximes were provided by Dr. S. Moore and Prof. L.G. Marzilli (Emory University), and J.H. Nelson. Solid-state <sup>31</sup>P NMR spectra were acquired at 81.0 MHz (4.7 T) and 162.0 MHz (9.4 T) on Bruker MSL-200 and AMX-400 spectrometers, under conditions of cross polarization, magic-angle spinning and high-power proton decoupling. Microcrystalline samples were thoroughly powdered and packed tightly into 4 mm and 7 mm o.d. zirconium oxide rotors. Typical pulse widths, contact times and relaxation delays were 5 μs, 5 ms and 4 s, respectively. Spinning rates for the 7 mm rotors ranged from 2.0 to 4.5 kHz, and from 3.0 to 9.0 kHz for the 4 mm rotors.

Experiments required anywhere from 500 to 8000 scans, depending on the amount of sample available. Spectra were processed by applying lorentzian broadening of 20 to 60 Hz to the FID prior to Fourier transformation. All  $^{31}\text{P}$  NMR spectra were referenced with respect to 85%  $\text{H}_3\text{PO}_4$  (aq) by setting the phosphorus resonance of  $\text{NH}_4\text{H}_2\text{PO}_4$  (s) to 0.81 ppm. Low-temperature NMR experiments were performed using dry nitrogen gas from  $\text{N}_2$ (liq.) boil-off. Dry  $\text{N}_2$  was passed through a heat-exchange coil which was immersed in liquid nitrogen. The temperature of the probe was controlled by carefully adjusting the gas flow and heater in a complementary fashion, and was stable to within  $\pm 3$  K. Temperatures inside the MAS rotors were not calibrated with an internal NMR standard. Detailed investigation of relaxation dynamics would require careful temperature calibration, for which a number of standard samples are available.<sup>170</sup>

The spinning sidebands were summed to produce an isotropic MAS pattern representative of the centreband at an infinite spinning rate.<sup>171</sup> All spectra were analyzed with the WSolids program. We note that Olivieri has recently proposed a method of simulating the entire NMR spectrum of a spin-1/2 nucleus coupled to a spin-1 nucleus, including spinning sidebands at all spinning speeds and angles, for situations where residual dipolar coupling is present.<sup>172</sup>

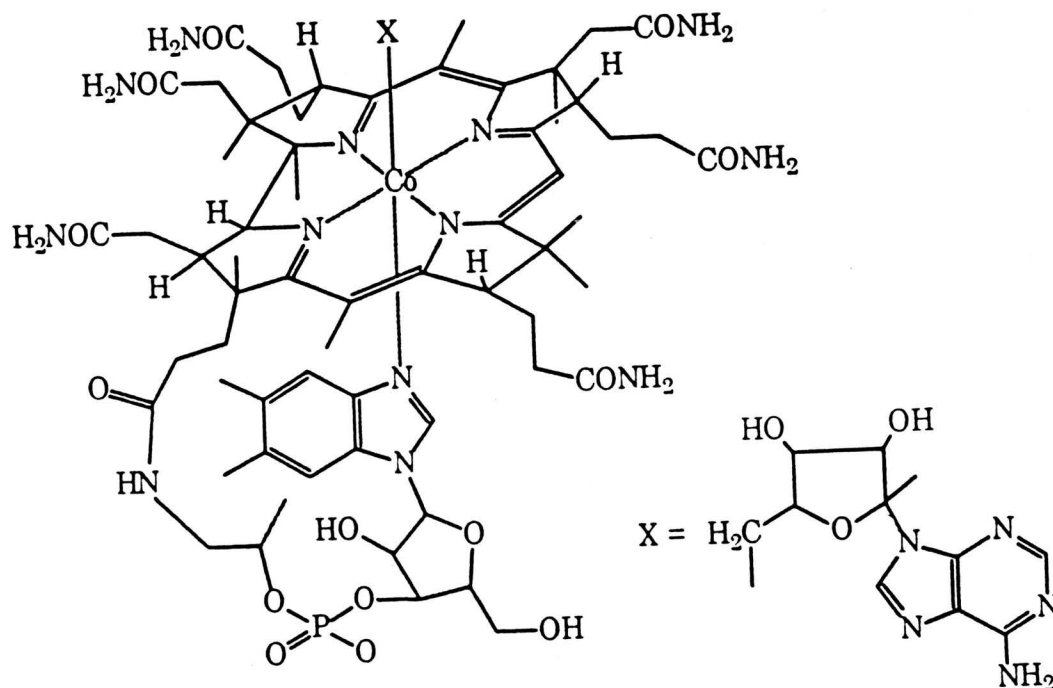


Figure 4.3 Structure of the vitamin-B12 coenzyme.

## 4.3 Background

### 4.3.1 Cobaloximes

In 1957, Dorothy Hodgkin and co-workers determined the crystal structure of the Vitamin B12 coenzyme, and found that it contains a cobalt-carbon sigma bond (Fig. 4.3).<sup>173</sup> The main interest in this complex is due to its catalytic activity, which is largely dependent upon the nature of the axial ligands and the conformational changes in the overall structure which trigger cleavage of the cobalt-carbon bond. Since this time, a large amount of chemistry has been developed around a class of compounds known as the cobaloximes, which have been used extensively as model compounds for the cobalamins, which are of great biological interest (i.e.,

organocobalamins adenosyl B<sub>12</sub> and coenzyme B<sub>12</sub>, and methylcobalamin B<sub>12</sub>).<sup>160,166,173,174,175</sup>

The cobaloximes have been thoroughly characterized over the last forty years by X-ray crystallography, multinuclear NMR, <sup>59</sup>Co NQR, kinetic equilibrium studies, UV-VIS spectrometry, electrochemical experiments and IR and Raman spectroscopy.<sup>160,161</sup> A compound is classified as a cobaloxime if it contains the Co(DH)<sub>2</sub> moiety, which is a cobalt (III) cation with two coordinated dimethylglyoxime anions which are hydrogen bonded to one another, such that there are four donor nitrogen atoms situated in an approximately rectangular plane about the Co centre (Fig. 4.1). Cobaloximes are of great interest because of their extensive coordination chemistry.<sup>160</sup> A number of variations on the nature of the axial ligands is possible, with the most common ligand being the dimethylglyoxime anion.<sup>160,161,176</sup> A variety of inorganic and organic ligands (either neutral or anionic) can be coordinated above and below the equatorial plane of nitrogens in the axial positions.<sup>160,177,178</sup> The ligand atoms assume a pseudo-octahedral arrangement about the cobalt centre, resulting in local C<sub>2v</sub> symmetry.

X-ray crystallography studies make up the bulk of the structural information available on these compounds in the solid state, with over 130 reported crystal structures. Some interesting general structural features of the cobaloximes have arisen from the culmination of all of the data from these studies.<sup>160</sup> For instance, it has been found that the geometry of the Co(DH)<sub>2</sub> moiety does not change significantly with substitution of various ligands into the axial positions. Much of the focus has been on the properties of the axial ligands, which seem to have the

largest influence on molecular structure.

A number of solution NMR studies have been conducted on the cobaloximes,<sup>162,174,179</sup> but there are only two solid-state NMR studies reported in the literature: the aforementioned <sup>31</sup>P NMR work,<sup>158</sup> and a detailed solid-state <sup>59</sup>Co NMR paper on cobaloximes and related complexes.<sup>160</sup> Proton NMR of solutions acts only as indirect probes of electronic changes at the cobalt nucleus.<sup>168,179a,h</sup> Similarly, the <sup>13</sup>C NMR shifts are not influenced by the cobalt nucleus in any particular way, though it is thought that they may qualitatively reflect changes in bonding between Co and the X ligands.<sup>179c,f</sup> Phosphorus-31 NMR studies of the directly bonded phosphorus nucleus provide more fruitful results.<sup>160,179e,181</sup> Phosphorus chemical shifts move to low frequency and high frequency for phosphine- and phosphite-substituted complexes, respectively, with the increasing *trans*-influencing ability of the X group. As well, the <sup>31</sup>P NMR shifts of phosphines are influenced by the steric size of the group, whereas the <sup>31</sup>P shifts of phosphites seem to depend more on the electronic nature of the ligand. The steric and electronic effects arising from both L and X groups are additive, thus making it unreasonable to draw exacting relationships between <sup>31</sup>P chemical shifts and the nature of the Co, P bond. Solution <sup>59</sup>Co NMR studies have also been reported, which correlate <sup>59</sup>Co chemical shifts with steric and electronic effects of different axial and equatorial ligands.<sup>162,174,182</sup>

Due to the short  $T_1$  of the <sup>59</sup>Co nucleus in solution, values of  $^1J(^{59}\text{Co}, ^{31}\text{P})$  in phosphorus-substituted cobaloximes are unavailable from solution NMR studies. In fact, there are no other reports of  $J$ -coupling between cobalt and axial ligands in the cobaloximes. Recently, work in this lab has demonstrated that  $^1J(^{59}\text{Co}, ^{31}\text{P})$  can be

readily determined in the solid state.<sup>158</sup> In this chapter and the following chapter, new examples of indirect spin-spin coupling involving cobalt are presented. The magnitudes of the  $J$ -coupling constants are qualitatively correlated to the molecular structure of the cobaloximes, and are dependent upon both steric and electronic effects of the axial ligands.

#### 4.3.2 MAS NMR Spectra of Spin-1/2 Nuclei Coupled to Quadrupolar Nuclei

##### A. Introduction

The origin of the asymmetric splitting in the MAS NMR spectrum of a spin-1/2 nucleus coupled to a quadrupolar nucleus is attributed to *residual dipolar coupling*. Residual dipolar coupling results from the failure of MAS to completely average the direct dipolar coupling between spin-1/2 and a quadrupolar nuclei, due to the presence of a large nuclear quadrupole interaction. The Zeeman interaction, under the high-field approximation, is much larger than the other NMR interactions. However, the quadrupolar interaction can range from almost zero to hundreds of MHz, and in some cases is much larger than the Zeeman interaction. Typical magnitudes of  $C_Q(^{59}\text{Co})$  in cobaloximes range from 24 to 80 MHz (the signs may be positive or negative), corresponding to  $\nu_Q$  from 1.7 to 5.7 MHz, which are smaller than the  $^{59}\text{Co}$  Larmor frequencies in this work:  $\nu_0 = 47.2$  MHz ( $B_0 = 4.7$  T) and 94.5 MHz ( $B_0 = 9.4$  T). For a quadrupolar nucleus with  $C_Q \neq 0$ , the high-field approximation is not strictly valid, and Zeeman states of the quadrupolar nucleus are not completely quantized in the direction of the magnetic field; rather, they must

be described by mixing of the pure Zeeman states of the quadrupolar nucleus. Thus, certain terms in the dipolar hamiltonian are not completely averaged by MAS. This is manifested in the spin-1/2 MAS NMR spectrum as a shift in the peaks of the multiplet, such that there is a constant change (i.e., increase or decrease) in the spacing between the peaks (Fig. 4.2). The multiplet is said to be affected by residual dipolar coupling.<sup>146</sup>

Residual dipolar coupling was first observed in the  $^{13}\text{C}$  MAS NMR spectra of solid proteins<sup>183</sup> and amino acids.<sup>184</sup> It was reported that MAS failed to average the dipolar interaction between the  $^{14}\text{N}$  ( $S = 1$ ) and  $^{13}\text{C}$  nuclei, and the  $^{13}\text{C}$  MAS NMR spectra appeared as 1:2 or 2:1 doublets. Soon after, several reports discussing the theoretical treatment of  $^{13}\text{C}$  NMR line shape calculations were published (*vide infra*). To account for the effects of a rotating sample, Zumbulyadis et al.<sup>185</sup> suggested a treatment based on the adiabatic approximation.<sup>186</sup> Other methods were applied to simulate the  $^{13}\text{C}$  MAS NMR spectra of several solid organic compounds and dipeptides containing  $^{14}\text{N}$ ,  $^{13}\text{C}$  spin pairs.<sup>187</sup> Hexem et al. discussed the effects of the magnetic field strength, the dipolar coupling and the magnitude, sign, asymmetry parameter and orientation of the  $^{14}\text{N}$  electric field gradient tensor on the  $^{13}\text{C}$  MAS NMR lineshape.<sup>188</sup> Spectra were simulated for a number of amino acids and organic compounds. Because of biological implications, the  $^{14}\text{N}$ ,  $^{13}\text{C}$  spin pair is still of interest in  $^{13}\text{C}$  CPMAS studies.<sup>189</sup> Recently, the first determination of the  $^1J(^{14}\text{N}, ^{13}\text{C})$  in the solid state was reported for a cadmium thiocyanate complex.<sup>190</sup>

The first reported case of residual dipolar coupling involving phosphorus and a quadrupolar transition metal nucleus was in the  $^{31}\text{P}$  MAS NMR spectra of the

triphenylphosphine copper complexes  $(\text{Ph}_3\text{P})_2\text{CuNO}_3$  and  $(\text{Ph}_3\text{P})_3\text{CuCl}$  ( $^{63/65}\text{Cu}$ ,  $^{31}\text{P}$  spin pair) by Veeman and co-workers.<sup>191</sup> Besides being the first reported spin pair other than  $^{14}\text{N}$ ,  $^{13}\text{C}$  to exhibit residual dipolar coupling in the spin-1/2 spectra, this case was unique in that the  $^{63/65}\text{Cu}$  ( $S = 3/2$ ) and  $^{31}\text{P}$  nuclei are also indirectly spin-spin coupled. Thus, the multiplet structure arising from indirect spin-spin coupling must also be considered. The  $^{31}\text{P}$  MAS NMR spectra appear as asymmetric quartets, with the outermost peaks displaying splittings due to the presence of both  $^{63}\text{Cu}$  and  $^{65}\text{Cu}$  isotopes (natural abundances, 69.1% and 30.9%, respectively). Menger and Veeman<sup>192</sup> presented a theoretical treatment involving the full diagonalization of the combined Zeeman-quadrupolar hamiltonian for the case where  $S = 3/2$  and  $\eta = 0$ , which also took into account the effects of indirect spin-spin interactions.

Cases of residual dipolar coupling have been reported for spin pairs involving a variety of spin-1/2 and quadrupolar nuclei, many of which are described in a comprehensive review by Harris and Olivieri.<sup>146</sup> Since then, there have been numerous reports of residual dipolar coupling. Several cases of residual dipolar coupling between an assortment of spin-1/2 nuclei and  $^{14}\text{N}$  have been reported, including the  $^{14}\text{N}$ ,  $^{13}\text{C}$  spin pair in acetanilide,<sup>193</sup> dipotassium tetracyanometalates,<sup>194</sup> and ruthenium-cyanate coordination polymers;<sup>195</sup> the  $^{14}\text{N}$ ,  $^{15}\text{N}$  spin pair in hydrazine sulfate and (diethylamino)-benzaldehyde diphenylhydrazone<sup>157</sup> and in 5-methyl-2-diazobenzenesulphonic acid hydrochloride;<sup>196</sup> the  $^{14}\text{N}$ ,  $^{31}\text{P}$  interactions in a phosphonium cation;<sup>197</sup> the  $^{14}\text{N}$ ,  $^{29}\text{Si}$  spin pair in polysilazanes;<sup>198</sup> and the  $^{14}\text{N}$ ,  $^{113}\text{Cd}$  spin pair in a series of cadmium thiocyanates.<sup>199</sup> Residual dipolar coupling involving the halogens,  $^{35/37}\text{Cl}$  ( $S = 3/2$ ),  $^{79/81}\text{Br}$  ( $S = 3/2$ ) and  $^{127}\text{I}$  ( $S = 5/2$ ), has been observed in

the  $^{13}\text{C}$  MAS NMR spectra of a number of compounds. Examples include the  $^{35/37}\text{Cl}$ ,  $^{13}\text{C}$  spin pair in sodium chloroacetates,<sup>156</sup> 5-chlorouracil,<sup>200</sup> chlorinated pyrazoles,<sup>201</sup> and in chloroketosulfones.<sup>202</sup> The  $^{79/81}\text{Br}$ ,  $^{13}\text{C}$  interactions in 5-bromouracil<sup>200</sup> and other bromoaromatic compounds;<sup>203</sup> and  $^{35/37}\text{Cl}$ ,  $^{79/81}\text{Br}$  and  $^{127}\text{I}$  effects in the  $^{13}\text{C}$  MAS NMR spectra of a series of *trans*-dihalobenzenes have also been reported.<sup>204</sup>

Residual dipolar coupling resulting from the presence of  $^2\text{H}$  ( $S = 1$ ) has also been observed in the  $^{13}\text{C}$  MAS NMR spectra of  $^2\text{H}$ ,  $^{13}\text{C}$ -enriched 3,4-dibenzyloxybenzaldehyde,<sup>205</sup> in urea and thiourea inclusion compounds,<sup>206</sup> and in methyl  $\alpha$ -*D*-glucopyranoside-2-*C-d*.<sup>207</sup> There are a number of reports involving quadrupolar transition metal nuclei, such as  $^{55}\text{Mn}$  ( $S = 5/2$ ),  $^{13}\text{C}$  and  $^{55}\text{Mn}$ ,  $^{31}\text{P}$  spin pairs in a series of octahedral manganese-carbonyl complexes;<sup>208</sup>  $^{55}\text{Mn}$ ,  $^{31}\text{P}$  interactions in acyl- and alkyltetracarbonyl-manganese(I) phosphines;<sup>209</sup> the  $^{55}\text{Mn}$ ,  $^{119}\text{Sn}$  spin pair in triaryltin(pentacarbonyl)-manganese(I) complexes;<sup>210</sup> the  $^{63}\text{Cu}$  ( $S = 3/2$ ),  $^{31}\text{P}$  spin pair in phosphine-substituted copper halides<sup>211</sup> and in copper(I)-phosphine complexes;<sup>212,213</sup> the  $^{93}\text{Nb}$  ( $S = 9/2$ ),  $^{31}\text{P}$  spin pair in half-sandwich niobium complexes;<sup>214</sup>  $^{99}\text{Ru}$  ( $S = 5/2$ ),  $^{31}\text{P}$  interactions in solid ruthenium compounds;<sup>149</sup> and the  $^{115}\text{In}$  ( $S = 9/2$ ),  $^{31}\text{P}$  spin pair in  $\text{Br}_3\text{InP}((p\text{-MeO})\text{C}_6\text{H}_4)_3$ .<sup>148</sup> The one-bond indirect spin-spin coupling was measured for the  $^{39}\text{K}$  ( $S = 3/2$ ),  $^{119}\text{Sn}$  spin pair, from solid-state  $^{119}\text{Sn}$  MAS NMR spectra of  $\text{KSn}(\text{CH}_2\text{Bu})_3(\eta^6\text{-PhMe})_3$ .<sup>215</sup> Of relevance to this thesis, residual dipolar couplings involving  $^{59}\text{Co}$  have been reported for  $^{59}\text{Co}$ ,  $^{13}\text{C}$  in  $\text{Co}_4(\text{CO})_{12}$  complexes,<sup>216</sup> and  $^{59}\text{Co}$ ,  $^{31}\text{P}$  in cluster compounds,<sup>164,165</sup> as well as the  $^{59}\text{Co}$ ,  $^{31}\text{P}$  interactions in the cobaloximes.<sup>158</sup>

## B. Theoretical Treatment

The effects of a quadrupolar nucleus on the solid-state MAS NMR spectrum of a direct dipolar and indirect spin-spin coupled spin-1/2 nucleus are now well understood.<sup>146,217,218</sup> A treatment based on first-order perturbation theory has been developed by Olivieri and co-workers<sup>219,220,221,222,223</sup> and others<sup>224</sup> which is valid in the limit  $C_Q/(4S(2S-1)) \ll \nu_S$ , where  $\nu_S$  is the Larmor frequency of the quadrupolar nucleus. Full treatments have also been developed for situations in which  $C_Q/(4S(2S-1)) \sim \nu_S$ , which include diagonalization of the combined Zeeman and quadrupolar hamiltonians.<sup>192,225</sup> For spin-7/2, spin-1/2 spin pairs, we are presently limited to cases in which  $\eta = 0$ ; thus only the first-order perturbation method is discussed here. For the majority of the complexes examined here, the first-order perturbation approach is adequate.

The transition frequencies in the MAS spectrum of an  $I$  nucleus,  $\nu_m$ , are shifted by a residual dipolar coupling,  $d$ , such that

$$\nu_m = \nu_{\text{iso}} - mJ_{\text{iso}} + \frac{S(S+1) - 3m^2}{S(2S-1)} d \quad (4.1)$$

where  $J_{\text{iso}}$  is the indirect spin-spin coupling constant,  $m = S, S-1, \dots, -S$ , and  $d$  is expressed as (in Hz)

$$d = \left( \frac{3C_Q R_{\text{eff}}}{20\nu_S} \right) [(3\cos^2\beta^D - 1) + \eta \sin^2\beta^D \cos 2\alpha^D] \quad (4.2)$$

In eq. 4.2,  $\alpha^D$  and  $\beta^D$  are polar angles describing the orientation of the  $I$ - $S$  dipolar

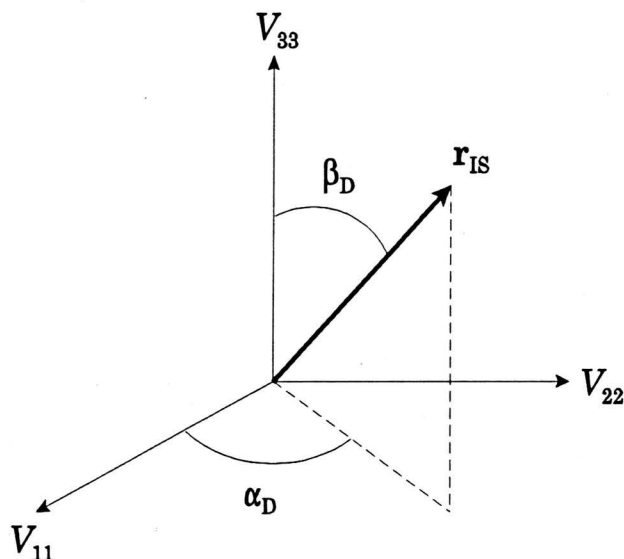


**Figure 4.4** Relative orientation of the dipolar vector,  $r_{IS}$ , and the EFG tensor.

vector,  $r_{IS}$ , with respect to the electric field gradient (EFG) tensor at the  $S$  nucleus (Fig. 4.4). The appearance of the asymmetric multiplet is therefore dependent upon (a) the nuclear quadrupole coupling constant,  $C_Q$ ; (b) the quadrupolar asymmetry parameter,  $\eta$ ; (c) the direct dipolar coupling constant,  $R_{dd}$ ; (d) the orientation of the dipolar vector,  $r_{IS}$  with respect to the EFG tensor; and (e) the Larmor frequency of the quadrupolar nucleus,  $\nu_S$ . If the spin-1/2 and quadrupolar nucleus are  $J$ -coupled, then (f) the magnitude of the isotropic  $J$ -coupling constant,  $J_{iso}$ ; and (g) the anisotropy of the  $J$ -coupling,  $\Delta J$ , must also be considered ( $\Delta J = J_{\parallel} - J_{\perp}$ ). As mentioned in Chapter 2,  $R_{dd}$  and  $\Delta J$  are assumed to be axially symmetric with the unique component directed along the internuclear vector.<sup>33,34</sup> It is impossible to separate contributions from  $R_{dd}$  and  $\Delta J$  to the residual dipolar shift, hence they are treated as an effective dipolar coupling constant,  $R_{eff} = R_{dd} - \Delta J/3$  (eq. 2.28).

For large values of  $C_Q$ , which may result from asymmetric environments, or

for large values of  $R_{dd}$ , which result from short internuclear distances, the multiplet structure becomes increasingly distorted (Fig. 4.2). Additionally, comparison of NMR spectra of the same complex at different applied magnetic fields reveals that the spectra acquired at lower fields exhibit a higher degree of distortion, as apparent from having  $\nu_s$  in the denominator of eq. 4.2.

The *sense* of the spectrum (i.e., the direction in which the spacings between peaks are increasing) is defined as follows: if the spacings between peaks increase from high to low frequency, the sense of the spectrum is positive, and  $d$  is positive (Fig. 4.2). Likewise, if the spacings decrease from high to low frequency, the spectral sense and  $d$  are negative. Eq. 4.2 also reveals that the sense of the spectrum can change depending on the sign of  $C_Q$ ,  $R_{eff}$  or the angular term (i.e.,  $\eta$ ,  $\beta^D$  and  $\alpha^D$ ). In the first-order treatment, the signs of  $R_{dd}$ ,  $\Delta J$ ,  $J_{iso}$  and  $\nu_s$  should have no effect on the sense of the spectrum, though this is not apparent for  $R_{dd}$  or  $\Delta J$  from the above equations. It is worth mentioning that in cases where  $\gamma_I$  is negative, the above equations do not hold (i.e., the sense of the spectrum is incorrectly reversed); accordingly, Olivieri has rewritten the above equations in a general expression which is valid for both positive and negative magnetogyric ratios.<sup>226</sup> Since we are considering the phosphorus-31 nucleus, which has a positive magnetogyric ratio, the above equations hold. The effects of the sign of  $\gamma_I$  are addressed in Chapter 5, where the  $^{15}\text{N}$  nucleus is considered. The origins of eqs. 4.1 and 4.2 are discussed in detail below.

The relative magnitudes of interactions relevant to this discussion are given by

$$|\mathcal{H}_Z^I| \sim |\mathcal{H}_Z^S| > |\mathcal{H}_Q^S| \gg |\mathcal{H}_{CS}^I| \sim |\mathcal{H}_D^{IS}| \sim |\mathcal{H}_J^{IS}| \quad (4.3)$$

According to the above relations, the nuclear quadrupole interaction is small enough to be treated as a perturbation on the Zeeman hamiltonians, but much larger than the remaining NMR interactions. However, in the presence of the quadrupolar interaction the axis of quantization of spin  $S$  is no longer directed along the magnetic field. The eigenstates of the quadrupolar nucleus are written as linear combinations of the pure Zeeman states:

$$|\Psi_m\rangle = \sum_n \alpha_{mn} |\varphi_n\rangle \quad (4.4)$$

where  $|\varphi_n\rangle$  are the pure Zeeman states (e.g., if  $S = 7/2$ , then  $|\varphi_1\rangle = |7/2\rangle$ ,  $|\varphi_2\rangle = |5/2\rangle$ ,  $|\varphi_3\rangle = |3/2\rangle$ , etc.), and  $\alpha_{mn}$  are defined below. Perturbation theory allows one to write the coefficients  $\alpha_{mn}$  as a linear expansion

$$\alpha_{mn} = {}^0\alpha_{mn} + {}^1\alpha_{mn} + \dots \quad (4.5)$$

which can be truncated at first order. The expansion coefficients, to first order, are written

$$\begin{aligned} {}^0\alpha_{mn} &= \delta_{mn} \\ {}^1\alpha_{mn} &= -Q_{mn}/(E_n - E_m) \\ {}^1\alpha_{mm} &= 0 \end{aligned} \quad (m \neq n) \quad (4.6)$$

where  $Q_{mn} = \langle m | \mathcal{H}_Q | n \rangle$ ,  $\delta_{mn}$  is the Kronecker delta, and  $E_n - E_m$  is the energy difference between the pure Zeeman levels. If the quadrupolar hamiltonian from eq. 2.34 is expressed in the Zeeman frame,

$$\begin{aligned} \mathcal{H}_Q &= (e^2 Q q_{zz} / 4S(2S - 1)) \{ 3(S_X \sin\theta + S_Z \cos\theta)^2 - S^2 \\ &+ \eta [(-S_X \cos\phi \cos\theta + S_Y \sin\phi + S_Z \cos\phi \sin\theta)^2 \\ &+ (-S_X \sin\phi \cos\theta - S_Y \cos\phi + S_Z \sin\phi \sin\theta)^2] \} \end{aligned} \quad (4.7)$$

and  $S_X$  and  $S_Y$  are rewritten in terms of raising and lowering operators,

$$\begin{aligned} S_X &= \frac{1}{2}(S_+ + S_-) \\ S_Y &= \frac{1}{2i}(S_+ - S_-) \end{aligned} \quad (4.8)$$

the first-order coefficients,  ${}^1a_{mn}$ , can be calculated. The general expression for the first-order coefficients are given as:<sup>146</sup>

$$\begin{aligned} {}^1a_{m,m-1} &= - \frac{\langle m-1 | \mathcal{H}_Q | m \rangle}{E_{m-1}^0 - E_m^0} \\ &= - \frac{C_Q(2m-1)[S(S+1) - m(m-1)]^{1/2}}{4v_S S(2S-1)} \cdot f(\phi, \theta, \eta) \\ {}^1a_{m,m+1} &= - \frac{\langle m+1 | \mathcal{H}_Q | m \rangle}{E_{m+1}^0 - E_m^0} \\ &= - \frac{C_Q(2m+1)[S(S+1) - m(m+1)]^{1/2}}{4v_S S(2S-1)} \cdot f(\phi, \theta, \eta) \end{aligned} \quad (4.9)$$

where

$$f(\phi, \theta, \eta) = \frac{3}{4} \sin 2\theta + \frac{1}{4} \eta \sin \theta [(1 - \cos \theta) e^{2i\phi} - (1 + \cos \theta) e^{-2i\phi}] \quad (4.10)$$

Once the coefficients are calculated, full expressions describing the mixed quadrupolar-Zeeman states,  $|\psi_m\rangle$ , are known. Now the effects of the dipolar interaction are considered, following the treatment of Harris and Olivieri.<sup>146</sup>

In treating this problem, it is necessary to consider the  $C$  and  $D$  terms of the dipolar hamiltonian in addition to the  $A$  term (see eq. 2.25). Since the eigenstates of the quadrupolar nucleus are described by mixing of the Zeeman states, and the  $C$  and  $D$  become secular (i.e., stationary) terms which commute with the Zeeman hamiltonian. The frequency shift of the  $I$  transitions resulting from the direct dipolar interaction is given as

$$\begin{aligned} \Delta v_m &= \langle \psi_m | R_{dd} [A + C + D] | \psi_m \rangle \\ &= - R_{dd} \langle \psi_m | S_z (1 - 3 \cos^2 \Theta) - \frac{3}{2} \sin \Theta \cos \Theta (S_+ e^{-i\Phi} + S_- e^{i\Phi}) | \psi_m \rangle \quad (4.11) \end{aligned}$$

The  $C$  and  $D$  terms are responsible for the residual dipolar shift since they are not averaged by MAS (*vide infra*). The effects of the indirect spin-spin coupling constant must also be considered. Since it is assumed that the anisotropy in  $\mathbf{J}$  has an identical orientation dependence to the dipolar interaction,<sup>146</sup>

$$\Delta v_m = - \langle \psi_m | JS_z + R_{\text{eff}} [S_z (1 - 3 \cos^2 \Theta) - \frac{3}{2} \sin \Theta \cos \Theta (S_+ e^{-i\Phi} + S_- e^{i\Phi})] | \psi_m \rangle \quad (4.12)$$

First-order terms involve the  $S_z$  operator, and considering both the indirect and

direct spin-spin coupling interactions, the first-order frequency shift is

$${}^1\Delta\nu_m = -mJ - mR_{\text{eff}}(1 - 3\cos^2\Theta) . \quad (4.13)$$

The second term of eq. 4.13 can be eliminated by rapid MAS. The second-order terms result from the operation of  $S_+$  and  $S_-$  on  $|\psi_m\rangle$ :

$$\begin{aligned} {}^2\Delta\nu_m &= \frac{3}{4}R_{\text{eff}}\sin 2\Theta \\ &\times \{ [S(S+1) - m(m+1)]^{1/2} ({}^1a_{m,m+1}e^{-i\Phi} + {}^1a_{m,m+1}e^{i\Phi}) \\ &+ [S(S+1) - m(m-1)]^{1/2} ({}^1a_{m,m-1}e^{-i\Phi} + {}^1a_{m,m-1}e^{i\Phi}) \} \\ &= \frac{3}{8} \frac{R_{\text{eff}}\chi}{v_s} \left[ \frac{S(S+1) - 3m^2}{S(2S-1)} \right] \\ &\times \sin 2\Theta \sin \theta [\cos \theta \cos \Phi (3 - \eta \cos 2\phi) - \eta \sin \Phi \sin 2\phi] . \end{aligned} \quad (4.14)$$

Eq. 4.14 is dependent upon both the orientations of the dipolar vector ( $\Theta, \Phi$ ) and the EFG tensor ( $\theta, \phi$ ) with respect to the magnetic field. The orientation of the dipolar vector is fixed with respect to the EFG, and their relative orientation can be given by the polar angles  $\alpha^D$  and  $\beta^D$  (Fig. 4.4). Trigonometric terms with  $\Theta$  and  $\Phi$  can be substituted by

$$\begin{aligned} \cos \Phi \sin \Theta &= \sin \theta \cos \beta^D + \sin \beta^D \cos \theta \cos(\alpha^D + \phi) \\ \sin \Phi \sin \Theta &= \sin \beta^D \sin(\alpha^D + \phi) \\ \cos \Theta &= \cos \theta \cos \beta^D - \sin \theta \sin \beta^D \cos(\alpha^D + \phi) . \end{aligned} \quad (4.15)$$

After much algebraic and trigonometric manipulation, it can be shown that the centre of mass of each transition is given by eq. 4.16:

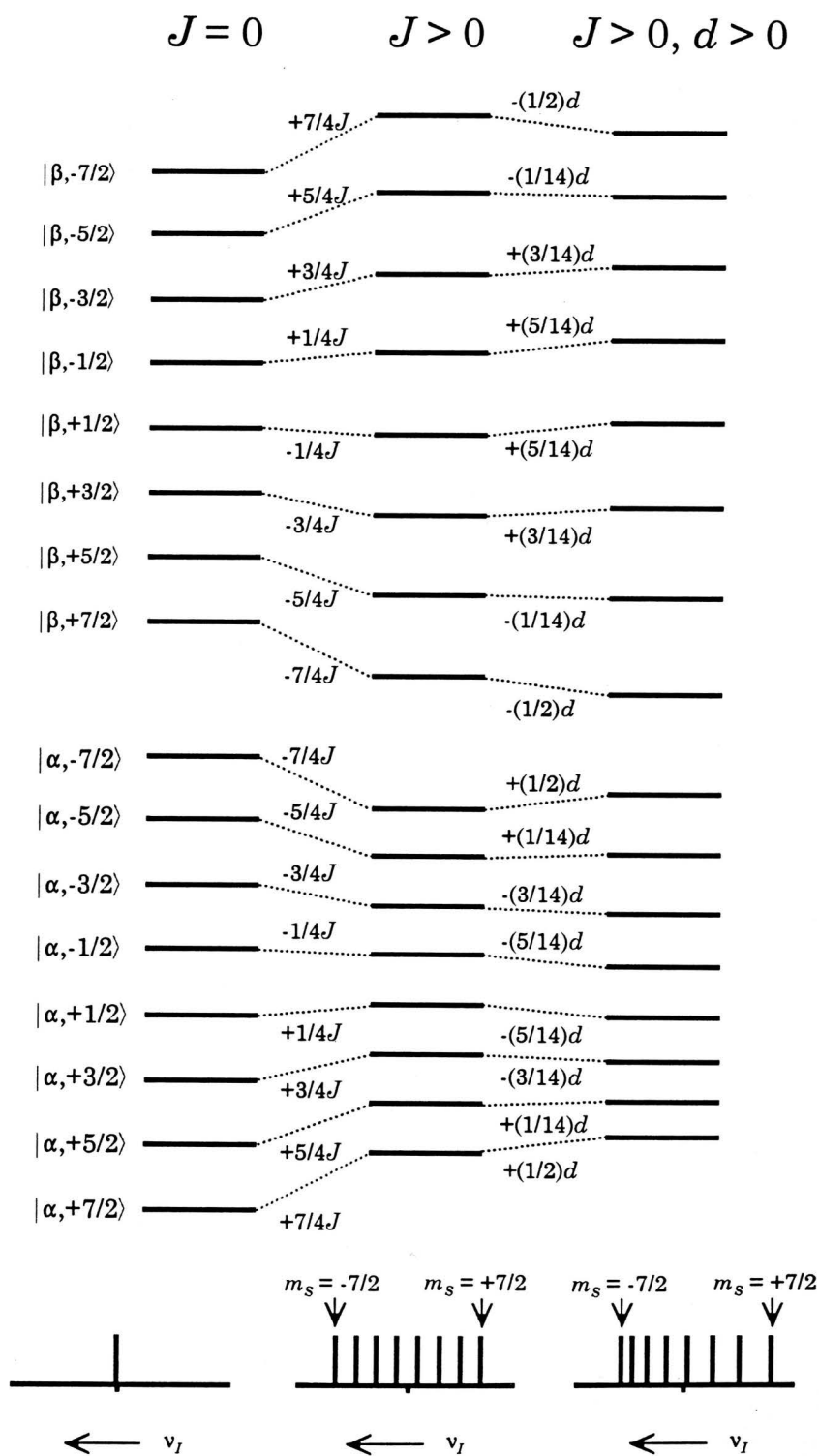


**Figure 4.5** Energy levels of the spin-1/2 nucleus coupled to a spin-7/2 nucleus, with corresponding stick spectra. Energy differences between the  $\alpha$  and  $\beta$  states are greatly understated.

$$\begin{aligned}
{}^2\Delta v_m &= \frac{1}{4\pi} \int_0^{\pi} \int_0^{2\pi} {}^2\Delta v_m(\theta, \phi) \sin\theta \, d\theta \, d\phi \\
&= \left( \frac{3C_Q R_{\text{eff}}}{20v_S} \right) [(3\cos^2\beta^D - 1) + \eta \sin^2\beta^D \cos 2\alpha^D] = d .
\end{aligned} \tag{4.16}$$

Thus, for the spin-7/2 nucleus (Fig. 4.5), the shifts of the spin-1/2 transition frequencies are given as

$$\begin{aligned}
v_{+7/2} &= - (7/2)J - d \\
v_{+5/2} &= - (5/2)J - (1/7)d \\
v_{+3/2} &= - (3/2)J + (3/7)d \\
v_{+1/2} &= - (1/2)J + (5/7)d \\
v_{-1/2} &= (1/2)J + (5/7)d \\
v_{-3/2} &= (3/2)J + (3/7)d \\
v_{-5/2} &= (5/2)J - (1/7)d \\
v_{-7/2} &= (7/2)J - d .
\end{aligned} \tag{4.17}$$

The MAS powder pattern can be generated by considering the orientation of the EFG with respect to the MAS frame, and the orientation of the MAS frame with respect to the Zeeman (lab) frame. The relative orientations of the EFG and MAS frames are described with polar angles  $\Xi$  and  $\xi$ , and the orientation of the MAS frame with respect to the Zeeman frame is described by polar angles  $\beta_M = 54.74^\circ$  and  $\omega_{\text{rot}}t$  (Fig. 4.6). The orientation relationships, if  $V_{33}$  is in the  $xz$  plane of the MAS frame, are given by:

$$\begin{aligned}
\cos\theta &= \cos\beta_M \cos\Xi + \sin\beta_M \sin\Xi \cos(\omega t) \\
\sin\theta \cos\phi &= -\cos\beta_M \sin\Xi \cos\xi + \sin\beta_M [\cos\Xi \cos\xi \cos(\omega t) + \sin\xi \sin(\omega t)] .
\end{aligned} \tag{4.18}$$

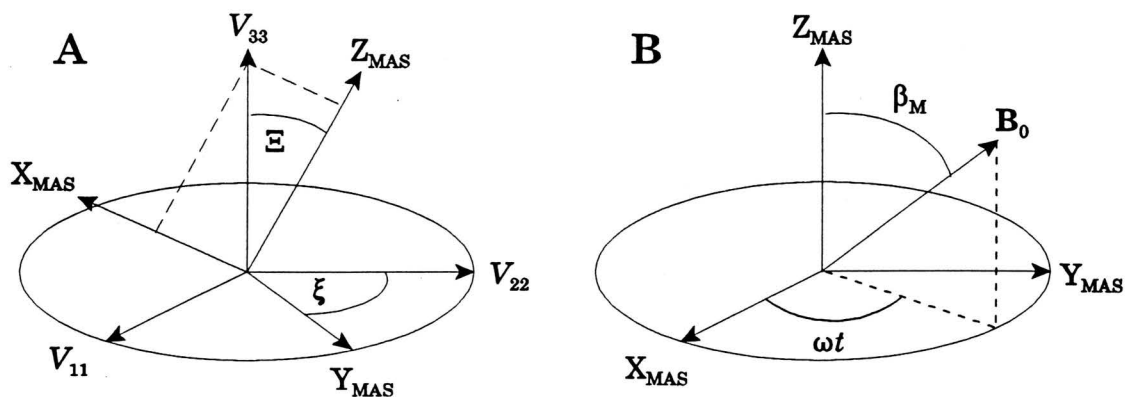


**Figure 4.6** Relative orientations of (A) the EFG and MAS frames ( $\Xi$ ,  $\xi$ ) and (B) the MAS frame and the applied magnetic field ( $\beta_M = 54.74^\circ$ ,  $\omega_{rot}t$ ).

The MAS powder patterns are generated as follows: First, angles  $\alpha^D$  and  $\beta^D$  are selected, fixing the dipolar vector with respect to the EFG PAS (other parameters such as  $C_Q$ ,  $\eta$ , etc. are chosen at this point). This allows substitution of eq. 4.15 into eq. 4.14, generating  ${}^2\Delta v_m(\theta, \phi)$ . For some orientation of the MAS frame relative to the EFG frame given by  $\Xi$  and  $\xi$ , the trigonometric functions of  $\theta$  and  $\phi$  (orientation of EFG in the Zeeman frame) in eq. 4.18 are formed. These functions are substituted into  ${}^2\Delta v_m(\theta, \phi)$ , from which the residual dipolar shift can be calculated. This is repeated for a number of equally spaced values of  $\omega_{rot}t$ , and averaged over one rotor cycle, which gives the shifts,  $\Delta v_m$ . This calculation has to be repeated thousands of times for different  $\Xi$  and  $\xi$  to generate a reasonable powder pattern. In choosing the angles  $\Xi$  and  $\xi$ , the surface of a sphere must be sampled at regular intervals. Alternative procedures exist for the generation of MAS NMR spectra, which reduce the computational time. An interpolation method has been developed which allows for the generation of a reasonable MAS spectrum with the sampling of 1 or 2 K of points.<sup>96</sup> Gaussian or lorentzian line broadening may also be applied. Unbroadened and convoluted powder patterns are shown in Fig. 4.7.

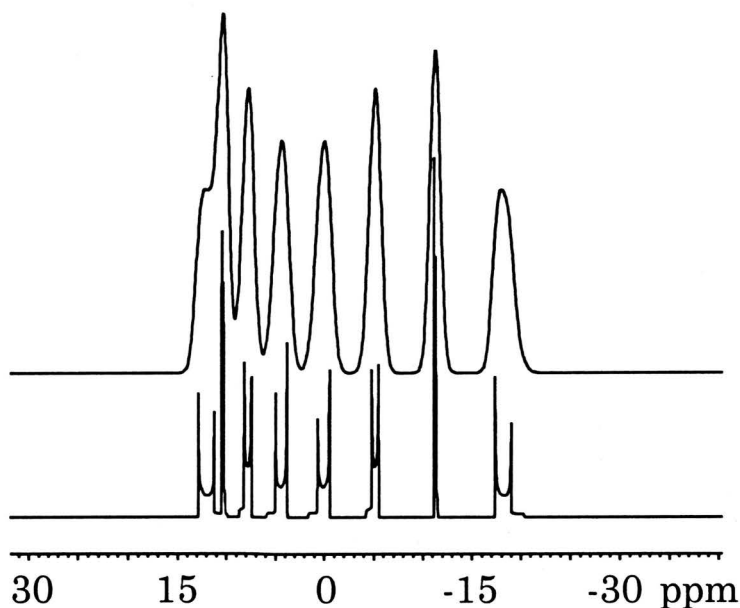


**Figure 4.7** MAS NMR spectrum of a spin-1/2 nucleus coupled to a spin-7/2 nucleus with no line broadening (lower trace) and gaussian broadening of 100 Hz (upper trace). Parameters are:  $J_{\text{iso}} = 300$  Hz,  $C_{\text{Q}} = 30$  MHz,  $R_{\text{eff}} = 1000$  Hz,  $\nu_0 = 47.24$  MHz,  $\beta^{\text{D}} = 0^\circ$ ,  $d = +95.3$  Hz.

## 4.4 Results and Discussion

### 4.4.1 Introduction

Phosphorus-31 CPMAS NMR parameters are presented for seventeen phosphine-substituted and two phosphite-substituted cobaloximes. In Section 4.4.2, spectra of cobaloximes for which quadrupolar parameters and X-ray crystallographic data are available are discussed. In Section 4.4.3, analysis is extended to systems for which no quadrupolar data is available. The relationship between  $^1J(^{59}\text{Co}, ^{31}\text{P})$  and the steric and electronic effects of the axial ligands is discussed. Difficulties in obtaining unique values of  $C_{\text{Q}}$ ,  $R_{\text{eff}}$ ,  $\beta^{\text{D}}$  and  $\alpha^{\text{D}}$  from the  $^{31}\text{P}$  CPMAS NMR spectra are

also illustrated in this section. The unique  $^{59}\text{Co}$  self-decoupling phenomena are discussed in Section 4.4.4.

#### 4.4.2 Well-Characterized Cobaloximes

In this section, the  $^{31}\text{P}$  CPMAS NMR spectra of three cobaloximes,  $\text{PPh}_3\text{Co}(\text{DH})_2\text{Me}$  (I),  $\text{PBu}_3\text{Co}(\text{DH})_2\text{Cl}$  (II) and  $\text{PPh}_3\text{Co}(\text{DH})_2\text{Cl}$  (III) (Bu = *n*-butyl), are analyzed (Table 4.1) using the first-order perturbation methods outlined above. The magnitudes of the nuclear quadrupole coupling constants and asymmetry parameters have been reported in a  $^{59}\text{Co}$  NQR study on the cobaloximes.<sup>162</sup>

**Table 4.1** NMR parameters for fully characterized cobaloximes.<sup>a</sup>

Compound $\text{LCo}(\text{DH})_2\text{X}$ (L, X)	$\delta_{\text{iso}}$ (ppm)	$R_{\text{eff}}$ (Hz) <sup>b</sup>	$^1J(^{59}\text{Co}, ^{31}\text{P})$ (Hz)	$\beta^{\text{D}}$	$\alpha^{\text{D}}$	$C_{\text{Q}}(^{59}\text{Co})$ (MHz) <sup>c</sup>	$\eta^c$	$d$ (Hz) <sup>d</sup>
$\text{PPh}_3$ , Me (I)	17.6(2)	810(20)	225(2)	90	0	+28.1	0.77	-8
$\text{PBu}_3$ , Cl (II)								
site 1	31.2(1)	995(15)	350(3)	90	90	-41.5	0.2	+79
site 2	29.8(1)	978(15)	352(3)	90	90	-40.9	0.35	+86
$\text{PPh}_3$ , Cl (III)	23.7(1)	910(20)	371(2)	90	90	-60.45	0.81	+158

*a.* Spectra of I and III acquired at 294 K, spectrum of II acquired at 155 K.

*b.*  $R_{\text{eff}} = R_{\text{dd}} - \Delta J/3$ , with  $R_{\text{dd}}$  calculated from known bond distances.  $\Delta J$  is assumed to be negligible. Uncertainties in  $R_{\text{eff}}$  are discussed in the text.

*c.* From ref. 157. Errors in  $C_{\text{Q}}$  are  $\pm 0.01$  MHz. Measurements made at room temperature.

*d.* Calculated for spectra at 9.4 T ( $\nu_{\text{S}} = 94.48$  MHz).

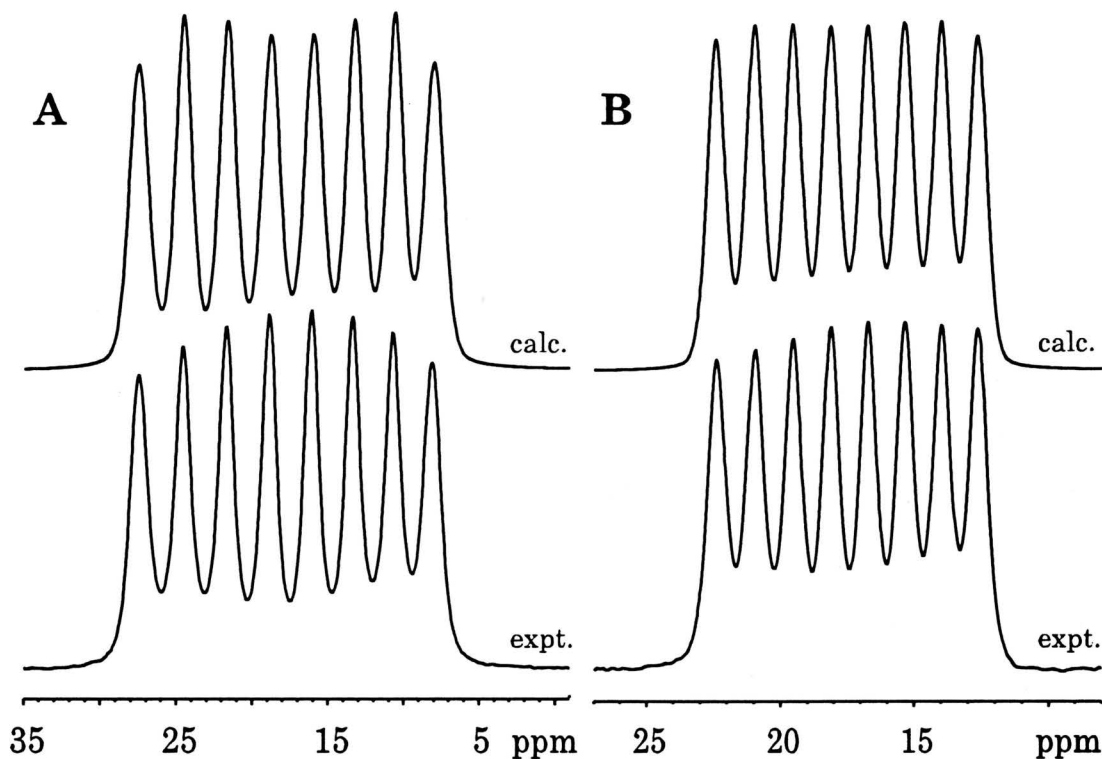


**Figure 4.8** Experimental and calculated  $^{31}\text{P}$  CPMAS NMR isotropic centrebands of  $\text{PPh}_3\text{Co}(\text{DH})_2\text{Me}$  (**I**) at (A) 4.7 T and (B) 9.4 T.

Phosphorus-31 CPMAS NMR spectra of **I** are pictured in Fig. 4.8. The one-bond indirect spin-spin coupling constant,  $^1J(^{59}\text{Co}, ^{31}\text{P})$ , measured from the splitting between the central peaks, is 225(2) Hz. To first order, these spectra are not dependent upon the sign of  $^1J(^{59}\text{Co}, ^{31}\text{P})$ , and therefore the sign cannot be determined from these analyses. It has been shown that the signs of one-bond  $J$ -couplings involving transition metals are dependent on the product of the magnetogyric ratios;<sup>227</sup> thus,  $^1J(^{59}\text{Co}, ^{31}\text{P})$  is assumed to be positive. The Co, P bond length in **I** is reported as 2.418(1) Å,<sup>228</sup> which means  $R_{\text{dd}} = 811(1)$  Hz. The values of  $C_{\text{Q}}$  and  $\eta$  have been reported as +28.1 MHz and 0.77.<sup>162</sup> The sign of  $C_{\text{Q}}$ , which is not available from NQR experiments, was determined from an empirical partial field gradient

(PFG) model, which takes into account relative contributions from axial and equatorial ligands. The PFG models were initially developed to explain the quadrupole splittings in Mössbauer spectra of tin and iron complexes.<sup>229</sup> According to this model, the total EFG at the metal centre is described as the sum of PFG parameters of the coordinating ligands. The PFG contribution from a ligand is calculated as

$$[L] = e^2Q \left[ \frac{q_L(1 - \gamma_r)}{r_L^3} + \frac{q'_L(1 - R)}{\langle r_L^{\beta} \rangle} \right] \quad (4.19)$$

where  $q_L$  is the charge at the ligand,  $\gamma_r$  and  $R$  are Sternheimer factors,<sup>230</sup>  $r_L$  is the separation between the metal and the ligand nuclei, and  $q'_L/r'_L{}^3$  is the effective charge donated into hybrid orbitals of the metal atom. In the model of LaRossa and Brown, the cobaloximes are treated as pseudo- $D_{2h}$  systems, in which one contribution to the EFG tensor originates from the equatorial ligands [N] and the other from an average of the partial field gradient contributions of the axial ligands  $[X] = \frac{1}{2}([A]+[B])$ . The actual values of [N] and [X] were not calculated; rather, the ratio [N]/[X] was plotted against  $C_Q$  and  $\eta$  to determine the sign of  $C_Q$  as well as the orientation of the EFG tensor components with respect to the molecular frame.<sup>162</sup> Their proposed orientation of the EFG tensor in I has  $V_{22}$  directed along the Co, P bond, with  $V_{11}$  bisecting the five-membered chelate rings, and  $V_{33}$  bisecting the inter-ring N-Co-N angles.

Information is not available from the <sup>31</sup>P CPMAS NMR spectra on all of the orientations of the EFG principal components with respect to the molecular frame;

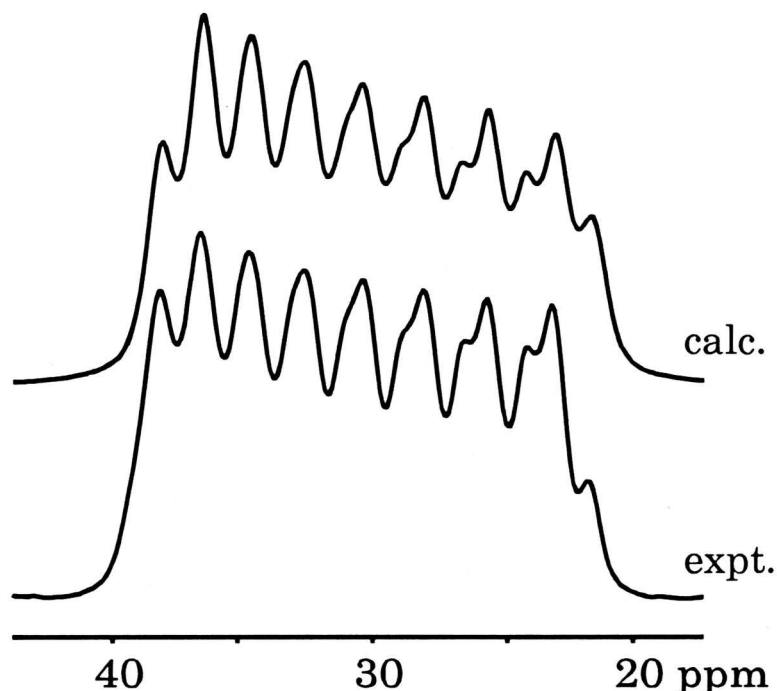


**Figure 4.9** Experimental and calculated  $^{31}\text{P}$  CPMAS NMR spectra of  $\text{PBu}_3\text{Co}(\text{DH})_2\text{Cl}$  (II) at 9.4 T and 155 K.

rather, it is possible to determine the orientations of the principal components with respect to the dipolar vector. The proposed orientation above corresponds to  $\beta^{\text{D}} = 90^\circ$ ,  $\alpha^{\text{D}} = 90^\circ$ , which means  $V_{11}$  and  $V_{33}$  are in the plane of the dimethylglyoxime ligands, and  $V_{22}$  is along the Co, P axis. Attempts to simulate the spectra using this proposed orientation were unsuccessful. However, it was found that with  $\beta^{\text{D}} = 90^\circ$  and  $\alpha^{\text{D}} = 0^\circ$  an excellent fit could be obtained. The spectra (Fig. 4.8) were calculated with the parameters given in Table 4.1. The spectra can be simulated with  $R_{\text{eff}} = R_{\text{dd}}$ , implying that the effects of  $\Delta J$  are negligible (*vide infra*).

At room temperature, the  $^{31}\text{P}$  CPMAS NMR spectra of II are broad and featureless. However, the fine structure originating from coupling to cobalt can be resolved at 155 K (Fig. 4.9). A detailed discussion of the temperature-dependent

phenomenon is given in Section 4.4.4. An X-ray diffraction study of **II** reveals that there are two crystallographically non-equivalent molecules in the unit cell. The Co, P bond lengths are reported as 2.272(2) Å and 2.289(2) Å,<sup>231</sup> corresponding to  $R_{\text{dd}}$  of 978(1) Hz and 956(1) Hz, respectively. From the  $^{59}\text{Co}$  NQR data and PFG model of LaRossa and Brown,  $C_{\text{Q}} = -41.5$  MHz and  $-40.9$  MHz, with  $\eta = 0.2$  and  $0.35$ . The proposed orientation of the EFG tensor has  $V_{22}$  along the Co, P bond (i.e.,  $\beta^{\text{D}} = 90^\circ$ ,  $\alpha^{\text{D}} = 90^\circ$ ). Using these parameters, and  $^1J(^{59}\text{Co}, ^{31}\text{P}) = 350(3)$  Hz and  $352(3)$  Hz, both sites are accounted for in the spectral calculations (Fig. 4.9). The experimentally-determined EFG tensor orientation is in agreement with that of LaRossa and Brown. The assignment of  $R_{\text{dd}}$  and  $C_{\text{Q}}$  to either set of transitions is arbitrary, since the appearance of the spectra is relatively insensitive to such a small differences in these parameters. Once again, it appears that the effects of  $\Delta J$  can be neglected.

The final example is compound **III**, for which  $r_{\text{Co,P}}$  is 2.327(4) Å ( $R_{\text{dd}} = 910(2)$  Hz),<sup>232</sup>  $C_{\text{Q}} = +60.45$  MHz,  $\eta = 0.81$ ,<sup>162</sup> and  $^1J(^{59}\text{Co}, ^{31}\text{P}) = 371(2)$  Hz. For this complex,  $V_{33}$  was previously proposed to be aligned with the Co, P bond axis.<sup>162</sup> However, simulations attempted with this EFG tensor orientation and the positive sign of  $C_{\text{Q}}$  reveal that the spectra cannot be simulated without a significant reduction in  $C_{\text{Q}}$  or  $R_{\text{eff}}$ . Attempts were made to simulate the spectra including  $J$ -anisotropy, without success. This was anticipated, given that  $\Delta J$  appears to be negligible in the previous examples. If the sign of  $C_{\text{Q}}$  is negative, and the orientation  $\beta^{\text{D}} = 90^\circ$ ,  $\alpha^{\text{D}} = 90^\circ$  is applied, the spectrum can be fit with the given quadrupolar and dipolar parameters (Fig. 4.10).

Concerning the data in Table 4.1, there are several interesting observations

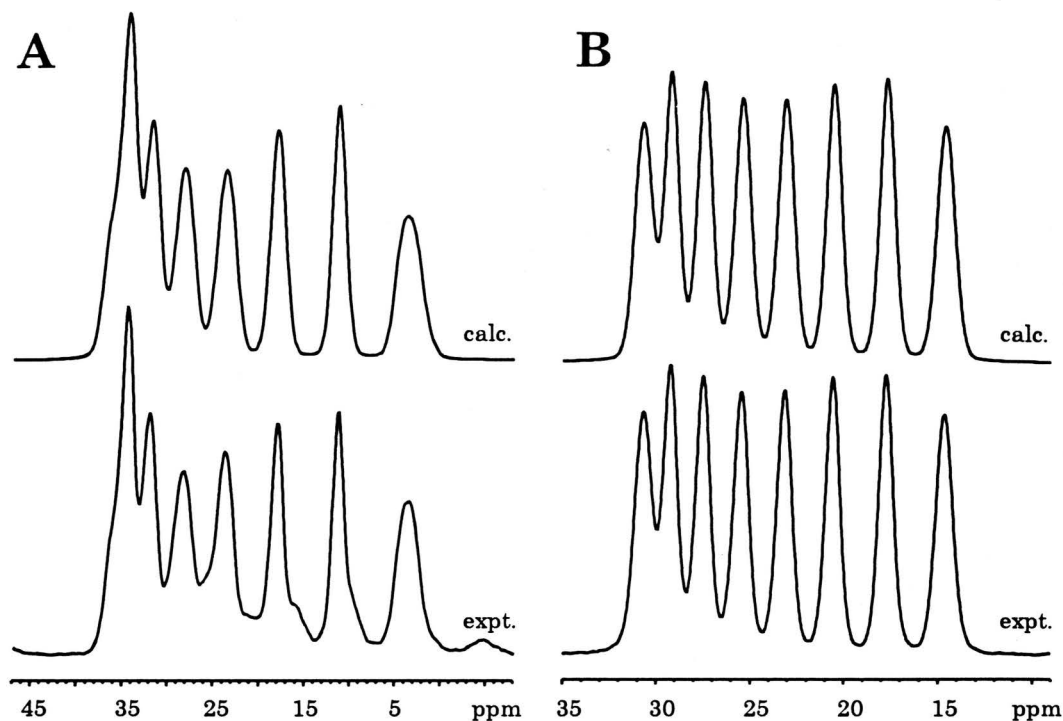


**Figure 4.10** Experimental and calculated  $^{31}\text{P}$  CPMAS NMR spectra of  $\text{PPh}_3\text{Co}(\text{DH})_2\text{CH}_3$  (**III**) at (A) 4.7 T and (B) 9.4 T. Small peaks arising from impurities in the sample are visible in the 4.7 T spectrum.

to note. First, the presence of the methyl group ( $X = \text{Me}^-$ ) results in a large decrease in  $^1J(^{59}\text{Co}, ^{31}\text{P})$  compared to the chloro-substituted cobaloximes ( $X = \text{Cl}^-$ ). Changing the nature of the phosphorus ligand results in much smaller variation in  $^1J(^{59}\text{Co}, ^{31}\text{P})$ . The sense of the spectra for **I** is negative (as indicated by  $d$ ), whereas for **II** and **III** the senses are positive. The magnitude of the residual dipolar shift is largest for **III**, which has the largest  $|C_Q|$ . However, other factors determine the size of  $d$ , such as  $R_{\text{eff}}$ , the EFG tensor orientation and  $\eta$ ; thus, direct correlation between the magnitudes of  $d$  and  $C_Q$  cannot be assumed. If  $\mathbf{r}_{\text{Co,P}}$  was coincident with  $V_{33}$  (i.e.,  $\beta^D = 0^\circ$ ), one might expect that such correlations may exist (*vide infra*).

The uncertainties in  $R_{\text{eff}}$  given in Table 4.1 reflect the degree to which  $R_{\text{eff}}$  can

be changed without creating any apparent differences between the calculated and experimental spectra. The residual dipolar shifts observed in the MAS spectra are not very sensitive to small changes in  $R_{\text{eff}}$  of ca. 20 or 30 Hz. If  $\Delta J$  is smaller than or on the order of the  ${}^1J({}^{59}\text{Co}, {}^{31}\text{P})$ , the maximum contribution would be ca. 100-125 Hz, which would be detectable given the quoted uncertainties in  $R_{\text{eff}}$ . If there is a contribution to  $R_{\text{eff}}$  from  $\Delta J$ , it must be less than 90 Hz (contribution to  $R_{\text{eff}}$  is  $\Delta J/3 = 30$  Hz).

#### 4.4.3 Cobaloximes for which Quadrupolar Data are Unknown

If  ${}^{59}\text{Co}$  quadrupolar data are unavailable, or reasonable assumptions cannot be made regarding the EFG tensor orientation, the only parameters available from the MAS NMR spectrum are  $\delta_{\text{iso}}$ ,  ${}^1J({}^{59}\text{Co}, {}^{31}\text{P})$  and  $d$ . The residual dipolar shift is proportional to  $C_{\text{Q}}$ ,  $R_{\text{eff}}$  and the angular factor in eq. 4.2, whose magnitude is dependent upon  $\eta$ ,  $\beta^{\text{D}}$  and  $\alpha^{\text{D}}$ . The covariance of these parameters means that it is possible to calculate identical MAS NMR spectra using markedly different parameters. In systems where the EFG tensor orientation is given by  $\beta^{\text{D}} = 0^\circ$ , the parameters  $\alpha^{\text{D}}$  and  $\eta$  do not play a role in determining the magnitude of  $d$ . In such cases, it is possible to gain information on either  $R_{\text{eff}}$  or  $C_{\text{Q}}$  if one of these parameters is known beforehand. For example, if the Co, P bond length is known,  $R_{\text{eff}}$  can be calculated (neglecting  $\Delta J$ ), and the spectrum simulated to determine the magnitude and sign of  $C_{\text{Q}}$ . The EFG tensor orientation varies in the first three cobaloximes, so general assumptions permitting this type of analysis are not possible. Nevertheless, valuable information is still available from these spectra.

In this section, the  $^{31}\text{P}$  CPMAS NMR spectra of cobaloximes for four different situations are examined. Cobaloximes with the anionic species  $\text{X} = \text{Cl}^-$  or  $\text{N}_3^-$  are considered first, followed by alkylcobaloximes ( $\text{X} = \text{Me}$ ). The effects of replacing phosphine ligands with phosphite groups are then discussed. Finally, several cases are presented in which the spectra cannot be simulated using first-order perturbation theory. The cobaloximes and the associated NMR parameters determined in this study are summarized in Table 4.2. A comparison of  $\delta_{\text{iso}}$ ,  $^1J(^{59}\text{Co}, ^{31}\text{P})$  and  $d$  with variations in molecular structure is given as a conclusion to this section.

Phosphorus-31 NMR spectra of stationary samples of the cobaloximes were also acquired. The powder patterns are very broad and convoluted by spin-spin interactions between  $^{31}\text{P}$  and  $^{59}\text{Co}$ . The combination of small chemical shielding anisotropy, large dipolar splittings and significant  $J$ -coupling makes analysis of the spectra difficult. Spectral simulations have been attempted without success, and are not reported here.

**Table 4.2** NMR parameters for phosphine- and phosphite-substituted cobaloximes,  $\text{LCo}(\text{DH})_2\text{X}$ , and uncoordinated neutral ligands, L.

Cobaloxime $\text{LCo}(\text{DH})_2\text{X}$ (L, X)	$\delta_{\text{iso}}$ , cobaloxime (ppm)	$\delta_{\text{iso}}$ , free ligand (ppm)	$\Delta$ (ppm)	$^1J(^{59}\text{Co}, ^{31}\text{P})$ (Hz)	$d$ (Hz) <sup>a</sup>	
$\text{PPh}_3$ , Me (I) <sup>b</sup>	17.6(2)	-10.3 <sup>e</sup>	27.9	225(2)	-8	
$\text{PBu}_3$ , Cl (II) <sup>b,c</sup>	site 1	31.2(1)	-30.9 <sup>f</sup>	62.1	350(3)	+79
	site 2	29.8(1)		60.7	352(3)	+86
$\text{PPh}_3$ , Cl (III) <sup>b</sup>	23.7(1)	-10.3 <sup>e</sup>	34	371(2)	+158	
$\text{P}(p\text{-tol})_3$ , Cl (IV)	27.9(2)	-10.4 <sup>e</sup>	38.3	362(1)	+147	
$\text{PPh}_3$ , $\text{N}_3$ (V)	23.0(1)	-10.3 <sup>e</sup>	33.3	348(2)	+122	
$\text{PMePh}_2$ , Cl (VI)	22.3(1)	-26.8 <sup>f</sup>	49.1	351(2)	+114	
$\text{PMe}_2\text{Ph}$ , $\text{N}_3$ (VII)	32.1(2)			344(3)	+121	
$\text{PBz}_3$ , Cl (VIII)	27.3(2)			357(2)	+116	
$\text{PBz}_3$ , $\text{N}_3$ (IX)	24.0(2)			345(5)	+72	
$\text{PMe}_3$ , Me (X)	site 1	-3.5(1)	-63 <sup>g</sup>	59.5	275(2)	-19
	site 2	-1.7(1)		64.7	275(2)	-20
$\text{P}(p\text{-FC}_6\text{H}_4)_3$ , Me (XI)	20.87(3)			226(2)	-12	
$\text{P}(p\text{-ClC}_6\text{H}_4)_3$ , Me (XII)	27.10(5)			228(2)	-24	
$\text{P}(\text{Me}_2\text{Ph})$ , Me (XIII)	10.15(3)			255(2)	-92	
$\text{P}(\text{Et}_2\text{Ph})$ , Me (XIV)	22.89(3)			254(1)	-72	
$\text{P}(\text{OEt})_3$ , $\text{N}_3$ (XV)	82.6(2)	139.2 <sup>f</sup>	-56.6	615(2)	+80	
$\text{P}(\text{OPh})_3$ , Me (XVI)	site 1	108.2(1)	119 <sup>h</sup>	-10.9	430(3)	-59
	site 2	106.8(2)		-12.2	420(2)	-61
$\text{PPh}_3$ , Br (XVII) <sup>d</sup>	24.3(3)	-10.3 <sup>e</sup>	34.6	372(9)	--	
$\text{PEt}_3$ , Me (XVIII) <sup>c,d</sup>	6.5(3)	-30.9 <sup>f</sup>	37.4	250(5)	--	
$\text{PBu}_3$ , $\text{N}_3$ (XIX) <sup>c</sup>	28.5(2)	-18.6 <sup>f</sup>	47.1	345(3)	+55	

$\alpha$ . Calculated for spectra at 9.4 T ( $\nu_s = 94.48$  MHz). Errors in  $d$  are as high as  $\pm 15$  Hz for spectra acquired at room temperature, and  $\pm 35$  Hz for low temperature spectra, due to the broadened peaks.

(continued next page)

**Table 4.2** footnotes (continued)

- b. NQR data available.
- c. Spectra acquired at 155 K.
- d. Spectra cannot be calculated using first-order perturbation theory.
- e.  $\delta_{\text{iso}}$  from solid-state NMR measurements.<sup>240</sup>
- f.  $\delta_{\text{iso}}$  from solution NMR measurements.<sup>179e</sup>
- g.  $\delta_{\text{iso}}$  from solid-state NMR measurements.<sup>233</sup>
- h.  $\delta_{\text{iso}}$  from solid-state NMR measurements.<sup>239</sup>

### A. Cobaloximes with X = Cl, N<sub>3</sub><sup>-</sup>

No structural or quadrupolar data are available for P(tol)<sub>3</sub>Co(DH)<sub>2</sub>Cl (IV) (tol = tolyl); however, the only difference between PPh<sub>3</sub>Co(DH)<sub>2</sub>Cl (III) and IV is the presence of the *para*-methyl groups on the phenyl rings of the phosphine ligand. The spectra of IV (Fig. 4.11) are remarkably similar to those of III, as evidenced by the spectral parameters. The isotropic chemical shifts and  $^1J(^{59}\text{Co}, ^{31}\text{P})$  are also very similar in these complexes. Another structurally similar cobaloxime is PPh<sub>3</sub>Co(DH)<sub>2</sub>N<sub>3</sub> (V). The crystal structure of this compound has been determined, with a reported Co, P bond length of 2.311(1) Å,<sup>234</sup> which corresponds to  $R_{\text{dd}} = 929(1)$  Hz. It has been suggested that the Co, P bond length is very similar to that in III since the N<sub>3</sub><sup>-</sup> species is a weak *trans*-influencing ligand<sup>235,236</sup> similar to Cl,<sup>234</sup> and hence should have comparable effects on molecular structure. The spectra of III, IV and V have positive residual dipolar shifts, similar  $\delta_{\text{iso}}$ , comparable  $^1J(^{59}\text{Co}, ^{31}\text{P})$  and the same sense. Given the structural similarity of these cobaloximes, it is likely that the EFG orientation is the same in all three complexes (i.e.,  $\beta^{\text{D}} = 90^\circ$ ,  $\alpha^{\text{D}} = 90^\circ$ ,  $V_{22}$  along the Co, P bond).

Parameters are presented for several other chloro- and azidocobaloximes in

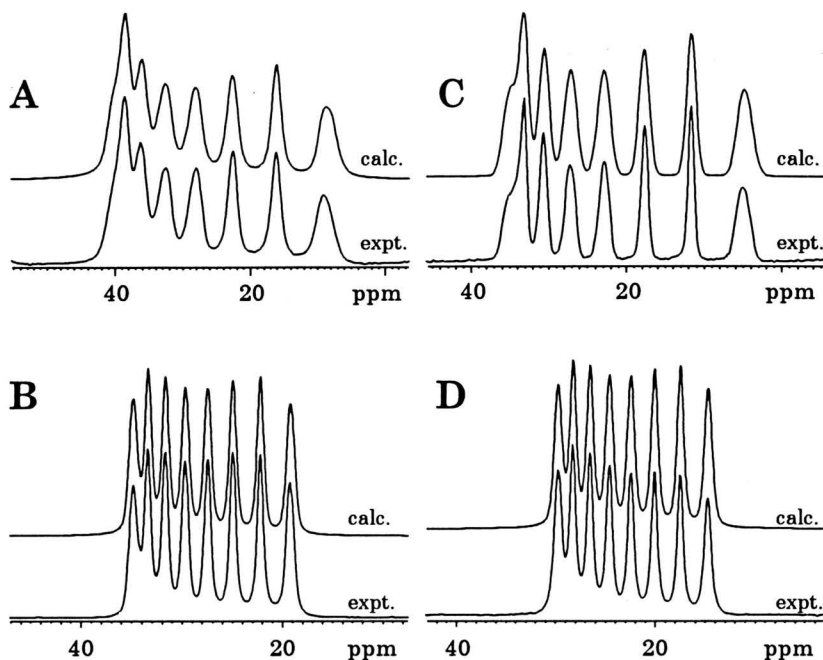


**Figure 4.11** Experimental and calculated  $^{31}\text{P}$  CPMAS NMR spectra of  $\text{P}(\text{tol})_3\text{Co}(\text{DH})_2\text{Cl}$  (IV) at (A) 4.7 T and (B) 9.4 T and  $\text{PPh}_3\text{Co}(\text{DH})_2\text{N}_3$  (V) at (C) 4.7 T and (D) 9.4 T.

Table 4.2. The magnitude of  $^1J(^{59}\text{Co}, ^{31}\text{P})$  and the  $\delta_{\text{iso}}$  in  $\text{PMePh}_2\text{Co}(\text{DH})_2\text{Cl}$  (VI) and  $\text{PMe}_2\text{PhCo}(\text{DH})_2\text{N}_3$  (VII) coincide with prior examples. Comparing  $\text{PBz}_3\text{Co}(\text{DH})_2\text{Cl}$  (VIII) and  $\text{PBz}_3\text{Co}(\text{DH})_2\text{N}_3$  (IX) (Bz = benzyl), reductions in both  $^1J(^{59}\text{Co}, ^{31}\text{P})$  and  $d$  are observed in the azidocobaloxime, similar to that observed for III and V.

### B. Cobaloximes with $\text{X} = \text{Me}^-$

Alkyl groups are strong electronic *trans*-influencing ligands<sup>235,236</sup> compared to the halides and azide anion. The presence of the axially-substituted methyl group results in a lengthening of the Co, L bond; this has been documented for a number of cobaloximes involving both phosphorus- and nitrogen-coordinated ligands.<sup>160,237</sup>

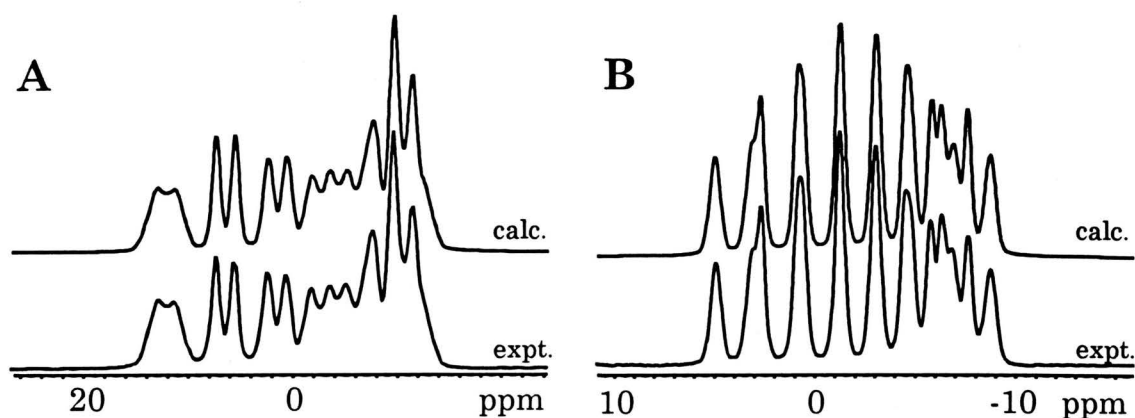


**Figure 4.12** Experimental and calculated  $^{31}\text{P}$  CPMAS NMR spectra of  $\text{PMe}_3\text{Co}(\text{DH})_2\text{Me}$  (**X**) at (A) 4.7 T and (B) 9.4 T.

Accordingly,  $R_{\text{dd}}(\text{Co},\text{P})$  is generally smaller (10 to 15%) in phosphorus-substituted alkyl cobaloximes.

$\text{PMe}_3\text{Co}(\text{DH})_2\text{Me}$  (**X**) has been structurally characterized in an X-ray crystallographic study,<sup>238</sup> however, no quadrupolar data are available. The Co, P bond length is reported as 2.293(1) Å,<sup>238</sup> corresponding to  $R_{\text{dd}} = 951(1)$  Hz. This bond length is uncommonly shorter than average Co, P bond lengths in phosphorus-substituted alkylcobaloximes ( $r_{\text{Co,P}} \geq 2.41$  Å), due to the small size of the  $\text{PMe}_3$  ligand. As a result,  $R_{\text{dd}}$  is on the order of those observed in the halogen- and azido-substituted cobaloximes. The value of  $^1J(^{59}\text{Co},^{31}\text{P})$  is ca. 70 Hz less than the smallest  $J$ -coupling in the halide- and azide-substituted cobaloximes, strongly indicating that bond length is not a factor in determining the magnitude of  $^1J(^{59}\text{Co},^{31}\text{P})$ .

The X-ray crystal study of **X** reveals that there are two crystallographically distinct molecules in the unit cell. This is also observed in the  $^{31}\text{P}$  CPMAS NMR spectra of **X** (Fig. 4.12), as two sites with distinct isotropic chemical shifts are

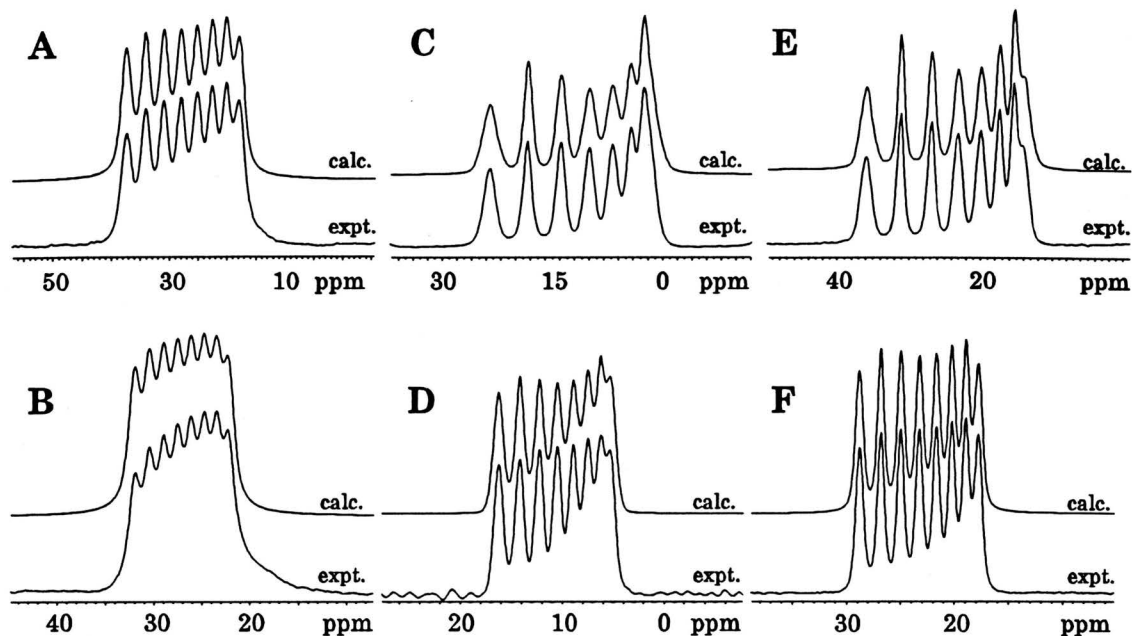


**Figure 4.13** Experimental and calculated  $^{31}\text{P}$  CPMAS NMR spectra of  $\text{P}(p\text{-ClC}_6\text{H}_4)_3\text{Co}(\text{DH})_2\text{Me}$  (**XII**) at (A) 4.7 T and (B) 9.4 T,  $\text{P}(\text{Me}_2\text{Ph})\text{Co}(\text{DH})_2\text{Me}$  (**XIII**) at (C) 4.7 T and (D) 9.4 T, and  $\text{P}(\text{Et}_2\text{Ph})\text{Co}(\text{DH})_2\text{Me}$  (**XIV**) at (E) 4.7 T and (F) 9.4 T.

resolved. The sites overlap with one another, resulting in a MAS NMR pattern of considerable complexity; however, excellent spectral fits are achieved at both fields.

It is noted that the sense of the spectrum is negative, as is the case for  $\text{PPh}_3\text{Co}(\text{DH})_2\text{Me}$  (**I**), and all spectra of the alkyl-substituted cobaloximes discussed in this chapter (*vide infra*). The phosphorus nucleus in **X** is the most shielded of all the examples reported in this chapter. This is expected, since uncoordinated  $\text{PMe}_3$  is considerably more shielded than other phosphine ligands considered in this work (see Table 4.2).

Spectral data are presented for several alkylcobaloximes which are similar to **I**, such as  $\text{P}(p\text{-FC}_6\text{H}_4)_3\text{Co}(\text{DH})_2\text{Me}$  (**XI**),  $\text{P}(p\text{-ClC}_6\text{H}_4)_3\text{Co}(\text{DH})_2\text{Me}$  (**XII**),  $\text{P}(\text{Me}_2\text{Ph})\text{Co}(\text{DH})_2\text{Me}$  (**XIII**) and  $\text{P}(\text{Et}_2\text{Ph})\text{Co}(\text{DH})_2\text{Me}$  (**XIV**) (Fig. 4.13). In the first

two cobaloximes,  ${}^1J({}^{59}\text{Co}, {}^{31}\text{P})$ ,  $\delta_{\text{iso}}$  and  $d$  are very similar to that observed in I. In the latter complexes, which have significantly different phosphine groups, the magnitude of  ${}^1J({}^{59}\text{Co}, {}^{31}\text{P})$  increases slightly, with a larger residual dipolar shift in comparison to I, XI and XII. This is indicative of either a substantial increase in  $C_Q$ , or a change in the orientation of the EFG tensor. In all cases, the values of  ${}^1J({}^{59}\text{Co}, {}^{31}\text{P})$  in the alkylcobaloximes are significantly smaller than in the chloro- and azide-substituted species. Reasons for this are discussed later in this section.

### C. Phosphite-substituted Cobaloximes

$\text{P(OEt)}_3\text{Co(DH)}_2\text{N}_3$  (XV) and  $\text{P(OPh)}_3\text{Co(DH)}_2\text{Me}$  (XVI), for which neither crystallographic nor quadrupolar data are available, are now considered. In XV,  ${}^1J({}^{59}\text{Co}, {}^{31}\text{P})$  is measured as 615(2) Hz, the largest for all of the cobaloximes considered here. In addition, the phosphorus nucleus is deshielded by ca. 50 ppm relative to the range of  $\delta_{\text{iso}}$  reported for the phosphine-substituted cobaloximes, in accordance with trends previously observed in solution  ${}^{31}\text{P}$  NMR studies.<sup>160,179e</sup> The spectra of XVI reveal that there are two crystallographically non-equivalent sites, with  ${}^1J({}^{59}\text{Co}, {}^{31}\text{P}) = 420(2)$  Hz and  $430(2)$  Hz, and  $\delta_{\text{iso}} = 108.2(1)$  ppm and  $106.8(1)$  ppm, respectively (Fig. 4.14). The values of  ${}^1J({}^{59}\text{Co}, {}^{31}\text{P})$  are large enough that the transitions arising from the two sites are completely separated, unlike in the spectra of II and X. The value of  ${}^1J({}^{59}\text{Co}, {}^{31}\text{P})$  is reduced compared to XV, undoubtedly due to the substitution of the Me into the axial position; notwithstanding,  ${}^1J({}^{59}\text{Co}, {}^{31}\text{P})$  in XVI is still larger than in all of the phosphine cobaloximes. In addition, the residual dipolar shifts are of opposite sign in these complexes, indicating either that the EFG

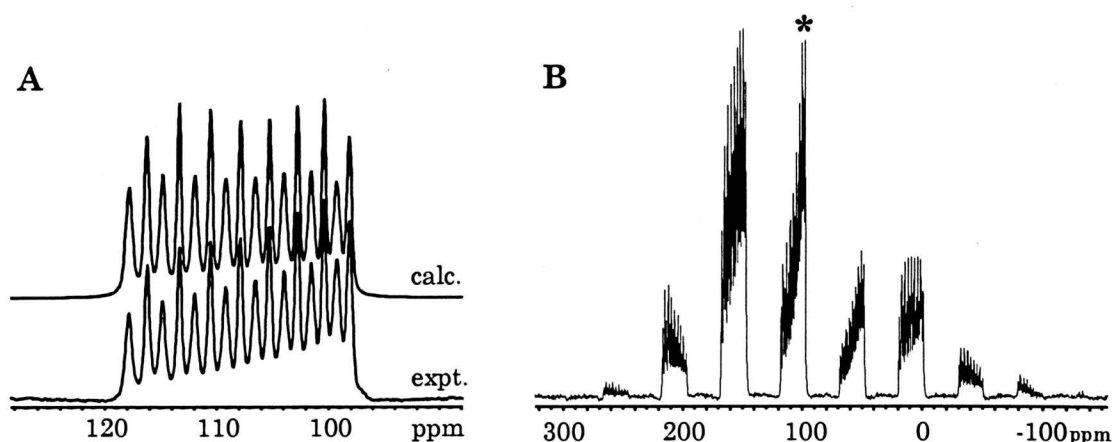


**Figure 4.14** (A) Experimental and calculated  $^{31}\text{P}$  CPMAS NMR isotropic transitions of  $\text{P}(\text{OPh})_3\text{Co}(\text{DH})_2\text{Me}$  (XVI) at 9.4 T. (B) Full spectrum, isotropic transitions marked with an asterisk ( $\nu_{\text{rot}} = 8$  kHz).

tensor orientations and/or the signs of  $C_Q$  are different.

Another interesting feature of the spectra of XV and XVI is the dramatic increase in phosphorus chemical shielding anisotropy (Fig. 4.14), which is apparent from the intensities of the spinning sidebands. In the spectra of the phosphine-substituted cobaloximes, usually only one or two sets of weakly resolved spinning sidebands are apparent ( $\Omega \sim 40$  to  $50$  ppm). In the phosphite-substituted cobaloximes, the span of the chemical shielding tensor is on the order of  $200$  ppm. This is concurrent with comparison of the spans measured in uncoordinated  $\text{P}(\text{OPh})_3$  ( $\Omega = 240(10)$  ppm)<sup>239</sup> and uncoordinated phosphines (e.g.,  $\text{PPh}_3$ ,  $\Omega = 51(1)$  ppm;  $\text{P}(p\text{-tol})_3$ ,  $\Omega = 41(1)$  ppm, etc.).<sup>80,240</sup>

#### D. Systems where First-Order Perturbation Theory Fails

Phosphorus-31 CPMAS NMR spectra of  $\text{PPh}_3\text{Co}(\text{DH})_2\text{Br}$  (XVII) acquired at

both 4.7 T and 9.4 T display an interesting anomaly; at the lower field, there are only six peaks resolved, and at the higher field, only seven. Eight peaks are resolved in the high-field spectra of all of the other cobaloximes, with seven or eight peaks resolved at the lower field, depending on the degree of residual dipolar coupling and the magnitude of  $^1J(^{59}\text{Co}, ^{31}\text{P})$ . Attempts to simulate the spectra of XVII at both fields were unsuccessful, as the degree of distortion in peak spacings could not be duplicated with the expressions derived from first-order perturbation theory. Calculations were attempted using full theory without success; however, we are presently limited to spectral simulations involving full diagonalization of the combined Zeeman and quadrupolar hamiltonian for cases in which  $\eta = 0$ . Interestingly, the crystal structure obtained for this compound reveals that  $r_{\text{Co,P}}$  is almost identical to that in  $\text{PPh}_3\text{Co}(\text{DH})_2\text{Cl}$  (III), with no significant deviations in molecular structure.<sup>241</sup> The magnitude of  $C_Q$  is assumed to be quite large in this complex, resulting in the severely distorted multiplet, though the source of the dramatic increase in  $V_{33}$  is unknown. Similar difficulties were encountered with  $\text{PEt}_3\text{Co}(\text{DH})_2\text{Me}$  (XVIII), which is one of the complexes exhibiting temperature-dependent  $^{59}\text{Co}$  self-decoupling (Section 4.4.4).

### E. Interpretation of Data from $^{31}\text{P}$ CPMAS NMR Spectra

General trends in the NMR parameters are as follows:

1. The magnitude of  $^1J(^{59}\text{Co}, ^{31}\text{P})$  is significantly reduced if the anionic species, X, is a methyl group, for both phosphine- and phosphite-substituted cobaloximes.

2. Examination of the complexes with the same L ligands and X = Cl<sup>-</sup> or N<sub>3</sub><sup>-</sup> (i.e., III and V, L = PPh<sub>3</sub>; VIII and IX, L = PBz<sub>3</sub>; II and XIX, L = PBu<sub>3</sub>), reveals that there is a small reduction in  $^1J(^{59}\text{Co}, ^{31}\text{P})$  in the azidocobaloximes compared to the corresponding chlorinated species (ca. 2 to 5 %).
3. For the phosphine alkylcobaloximes,  $^1J(^{59}\text{Co}, ^{31}\text{P})$  increases with decreasing steric bulk of the phosphine.
4. Values of  $^1J(^{59}\text{Co}, ^{31}\text{P})$  in phosphite-substituted cobaloximes are much larger than in phosphine-substituted cobaloximes.
5. The isotropic coordination chemical shifts are as follows: for phosphines, the coordination chemical shift,  $\Delta$ , is positive (i.e., the  $^{31}\text{P}$  nucleus becomes deshielded upon coordination to the cobaloxime). For the phosphites, it is negative. This is in accord with  $^{31}\text{P}$  coordination shifts measured in solution.<sup>179e</sup>
6. Isotropic  $^{31}\text{P}$  chemical shifts in the cobaloximes behave in an identical fashion to those of the corresponding uncoordinated ligands.  $\delta_{\text{iso}}(^{31}\text{P})$  moves to high frequency for the phosphite-substituted cobaloximes (i.e., phosphorus becomes deshielded), and the span of the chemical shift tensor increases. Phosphorus nuclei are most shielded with small phosphine groups and X = Me<sup>-</sup>.
7. In chloro- and azidocobaloximes,  $d$  is positive; for alkylcobaloximes,  $d$  is negative, and for several compounds, quite small.

Indirect spin-spin couplings between phosphorus and metal nuclei have often been interpreted in terms of the *Fermi-contact mechanism*, which is the dominant coupling mechanism for light nuclei such as protons and carbon. Ramsey proposed the first successful theory for the treatment of indirect spin-spin coupling constants in 1953.<sup>242</sup> The interactions between the nuclear spins are mediated by electrons, and are described by a non-relativistic, hyperfine hamiltonian which can be decomposed into terms characterizing individual contributions from (i) diamagnetic and paramagnetic interactions between the nuclear magnetic moments and the orbital motion of the electrons (orbital mechanism, OB), (ii) a dipolar interaction between the nuclear and electron spins (spin-dipolar mechanism, SD), and (iii) the Fermi-contact (FC) mechanism, which accounts for direct coupling between the electron and nuclear spins. There is also a FC×SD cross term which makes no contribution to  $J_{\text{iso}}$ , but can make significant contributions to the  $\mathbf{J}$  tensor. The OB and SD terms can make contributions to  $J_{\text{iso}}$  in addition to the anisotropic component of the  $\mathbf{J}$ -tensor. The Fermi contact term is isotropic, and contributions from this mechanism reflect the unpaired electron populations of  $s$  atomic orbitals of nuclei involved in the coupling. A simplified expression for a one-bond indirect spin-spin coupling between two nuclei,  $N$  and  $N'$ , in a complementary group of complexes is given by

$$J_{\text{iso}}(N, N') \propto \gamma_N \gamma_{N'} (\text{}^3\Delta E)^{-1} \alpha_N^2 \alpha_{N'}^2 |s_N(0)|^2 |s_{N'}(0)|^2 \quad (4.20)$$

where  $\text{}^3\Delta E$  is an average triplet excitation energy,  $\alpha_N$  is the  $s$ -character of the hybrid-orbital transmitting spin-coupling information to nucleus  $N'$ , and  $|s_N(0)|^2$  and

$|s_{N'}(0)|^2$  are the *s*-electron densities.

The assumption of the direct correspondence between *s*-character, the excitation energy and the magnitude of  $J_{\text{iso}}$  must be regarded with skepticism, since certain *J*-couplings between phosphorus and heavy nuclei which had previously been assumed to be dominated by the FC mechanism have been shown to have large contributions from other coupling mechanisms (*vide infra*). It has been proposed that the lengthening of the M, P bond (M = metal, for example Pt or Hg), say from the presence of a strong *trans*-influencing ligand, results in a reduction of *s*-character at the M atom, which consequently results in a decrease in the magnitude of  $J_{\text{iso}}$ , according to the FC mechanism.<sup>243</sup> Changes in the magnitude of *J* have also been attributed to decreasing or increasing *s*-character resulting from different hybrid molecular orbitals at the metal nucleus, which are dependent on the coordination number and electron-donating abilities of the coordinated ligands.<sup>243,244</sup> Conflicting results have been found regarding the correlation between  $J_{\text{iso}}$  and the "σ-donating ability" of various phosphorus ligands.<sup>243</sup> Solid-state <sup>31</sup>P NMR experiments on powder samples and single crystals have demonstrated that there are large *J*-anisotropies, and therefore contributions from mechanisms other than the FC mechanism in  $^1J(^{195}\text{Pt}, ^{31}\text{P})$  in square planar complexes,<sup>245</sup>  $^1J(^{199}\text{Hg}, ^{31}\text{P})$  in tetrahedral mercury phosphines<sup>246</sup> and  $^1J(^{63/65}\text{Cu}, ^{31}\text{P})$  in linear copper(I) phosphines.<sup>213</sup> For heavy atoms, relativistic effects, which may make a contribution to  $J_{\text{iso}}$ , cannot be ignored.<sup>247</sup>

Spectral simulations for cobaloximes in which dipolar and quadrupolar coupling constants are known reveal that  $\Delta J$  is probably less than 90 Hz; hence, it is

possible that the FC mechanism is dominant in  $^1J(^{59}\text{Co}, ^{31}\text{P})$ . However, the exact contributions of the SD and OB terms to  $^1J(^{59}\text{Co}, ^{31}\text{P})$  are unknown at this time. If the FC mechanism is dominant, a qualitative explanation of the changes in  $^1J(^{59}\text{Co}, ^{31}\text{P})$  may be formulated as follows. The presence of a methyl group, which is a strong  $\sigma$ -donor and *trans*-influencing ligand, may result in a decrease in the 4s-electron density concentrated in the Co, P bond, resulting in a reduced value of  $^1J(^{59}\text{Co}, ^{31}\text{P})$ . Similarly, the presence of a phosphite ligand may result in an increase in the 4s-electron density in the Co, P bond, resulting in an augmented value of  $^1J(^{59}\text{Co}, ^{31}\text{P})$ . In both cases, the average singlet-triplet excitation energy may play some role. Parallel effects of methyl, halide, phosphine and phosphite ligand substitution on  $^1J(\text{M}, \text{P})$  have been observed in a large number of cases for phosphorus bonded to transition metals.<sup>243</sup> Some examples include  $^1J(^{195}\text{Pt}, ^{31}\text{P})$  in square planar phosphine- and phosphite-substituted platinum (II) complexes,<sup>248</sup>  $^1J(^{183}\text{W}, ^{31}\text{P})$  in octahedral phosphine- and phosphite-substituted pentacarbonyl tungsten compounds,<sup>249</sup> and very close correspondence with  $^1J(^{103}\text{Rh}, ^{31}\text{P})$  from phosphorus NMR studies of the rhodium analogs of the cobaloximes, the rhodoximes (*vide infra*).<sup>250</sup>

In isostructural complexes with different metals in the same group of the periodic table, indirect spin-spin couplings  $^1J(\text{M}, \text{P})$  are normally compared by two different methods. The first is to consider the *reduced coupling constants*, given by

$$K(N, N') = 4\pi^2 J(N, N') / (h\gamma_N \gamma_{N'}) \quad (4.21)$$

which eliminates the dependence of the  $J$ -coupling on the magnitudes and signs of

the magnetogyric ratios.<sup>251</sup> It has also been proposed that  ${}^1J(M,P)$  for two different metals should be equivalent by the ratio of their *s*-electron densities and magnetogyric ratios,  $\gamma|s(0)|^2$ .<sup>243</sup> For comparison of couplings to phosphorus involving  ${}^{59}\text{Co}$  and  ${}^{103}\text{Rh}$ ,  ${}^1J({}^{59}\text{Co}, {}^{31}\text{P})$  is predicted to be 4.38 times larger than  ${}^1J({}^{103}\text{Rh}, {}^{31}\text{P})$ .<sup>227</sup> In Table 4.3,  ${}^1J({}^{59}\text{Co}, {}^{31}\text{P})$  and  ${}^1J({}^{103}\text{Rh}, {}^{31}\text{P})$  are compared in several cobaloximes and rhodoximes. The reduced coupling constants are two times as large in the rhodoximes, whereas the ratio of  $\gamma|s(0)|^2$  underestimates  ${}^1J({}^{59}\text{Co}, {}^{31}\text{P})$ . Qualitatively, the  ${}^1K({}^{59}\text{Co}, {}^{31}\text{P})$  and  ${}^1K({}^{103}\text{Rh}, {}^{31}\text{P})$  increase by the same factors in the alkylated cobaloximes and rhodoximes. The reduced coupling constant increases as the atomic number of the metal, *Z*, increases in a series of isostructural compounds.<sup>251</sup> This is thought to be due to increasing  $|s(0)|^2$  upon descending any group of the periodic table.

**Table 4.3:** Comparison of  ${}^1J({}^{59}\text{Co}, {}^{31}\text{P})$  and  ${}^1J({}^{103}\text{Rh}, {}^{31}\text{P})$  in cobaloximes and rhodoximes ( $\text{LRh}(\text{DH})_2\text{X}$ )

L, X	${}^1J({}^{59}\text{Co}, {}^{31}\text{P})$ (Hz)	${}^1K({}^{59}\text{Co}, {}^{31}\text{P})$ ( $\text{N A}^{-2} \text{ m}^{-3}$ ) $\times 10^{21}$	${}^1J({}^{103}\text{Rh}, {}^{31}\text{P})$ (Hz) <sup>a</sup>	${}^1K({}^{103}\text{Rh}, {}^{31}\text{P})$ ( $\text{N A}^{-2} \text{ m}^{-3}$ ) $\times 10^{21}$	${}^1J({}^{59}\text{Co}, {}^{31}\text{P})$ /4.38 (Hz)
$\text{PPh}_3, \text{Me}$	225	1.96	-66.0	4.28	51.4
$\text{PMe}_3, \text{Me}$	275	2.40	-78.1	5.07	62.8
$\text{P(OPh)}_3, \text{Me}$	430	3.75	-116.6	7.57	98.2
$\text{PPh}_3, \text{Cl}$	371	3.24	-120.0	7.79	84.7

*a.* Data from ref. 250.

The small negative values of the residual dipolar shift, *d*, in the

alkylcobaloximes likely result from a reduced angular factor,  $(3\cos^2\beta^D - 1 + \eta\sin^2\beta^D\cos 2\alpha^D)$ , and not simply from decreased  $C_Q$  in these cobaloximes. If  $\beta^D = 90^\circ$  and  $\alpha^D = 0^\circ$ , as in the case of **I**, the angular factor is  $-1 + \eta$ , which can be quite small. Alternatively, if  $\beta^D = 90^\circ$  and  $\alpha^D = 90^\circ$ , as in **II** and **III**, the angular factor is  $-1 - \eta$ . The fact that  $d$  is consistently positive and larger for the chloro- and azido-substituted cobaloximes, and negative and smaller for the majority of the methylcobaloximes, suggests that the EFG tensor orientations may be similar in each series of compounds.

#### 4.4.4 Temperature-Dependent Self-Decoupling of Cobalt

Most of the  $^{31}\text{P}$  CPMAS NMR spectra of the cobaloximes exhibit well-resolved eight-peak multiplets at room temperature; however, the spectra of several of the cobaloximes (i.e.,  $\text{PBu}_3\text{Co}(\text{DH})_2\text{Cl}$  (**II**),  $\text{PEt}_3\text{Co}(\text{DH})_2\text{Me}$  (**XVIII**) and  $\text{PBu}_3\text{Co}(\text{DH})_2\text{N}_3$  (**XIX**)) have broad peaks with little evidence of the expected multiplet structure. The line shapes observed in these complexes resemble spin-1/2 solution NMR spectra of a spin-1/2 nucleus coupled to a spin-7/2 nucleus where the spin-lattice relaxation rate of the quadrupolar nucleus,  $T_1(S)^{-1} \sim J(S,I)$  (*vide infra*). Variable-temperature  $^{31}\text{P}$  CPMAS NMR experiments have been conducted on **II**, **XVIII** and **XIX**, and will be the focus of discussion in this section.

Upon cooling **II** to 240 K, the octet in the  $^{31}\text{P}$  spectrum begins to appear (Fig. 4.15). Cooling to 155 K, the gradual emergence of the eight-peak multiplet (for each of the two  $^{31}\text{P}$  sites) from the broad peaks is observed. At 155 K, the spin-lattice relaxation time,  $T_1(^{59}\text{Co})$ , is long compared to  $^1J(^{59}\text{Co}, ^{31}\text{P})^{-1}$ , and the eight-peak

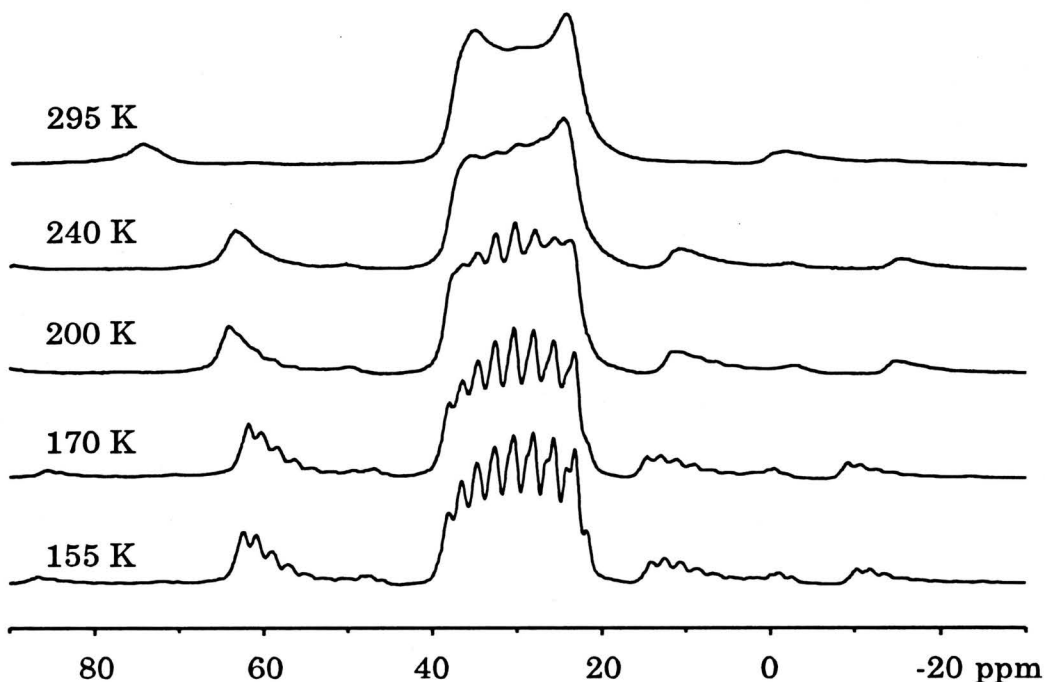


**Figure 4.15** Variable-temperature  $^{31}\text{P}$  CPMAS NMR spectra of  $\text{PBu}_3\text{Co}(\text{DH})_2\text{Cl}$  (II),  $\nu_{\text{rot}} = 3927$  Hz (155, 170 K), 4240 Hz (200, 240 K) and 5000 Hz (295 K) at 9.4 T.

multiplets are observed in the spectrum. As the temperature is increased,  $T_1(^{59}\text{Co})$  becomes comparable in magnitude to  $^1J(^{59}\text{Co}, ^{31}\text{P})^{-1}$ , and broadening of the peaks is observed. The peaks may completely coalesce into one narrow peak at  $\nu_{\text{iso}}$  if the rate of  $^{59}\text{Co}$  relaxation is rapid enough. The disappearance of the eight peak multiplet in the spectra of II is attributed to the self-decoupling of the direct dipolar and indirect spin-spin interactions between the cobalt and phosphorus nuclei due to the decrease of the  $T_1(^{59}\text{Co})$  at higher temperatures, and the dominance of *scalar relaxation of the second kind* (i.e., the  $T_2^{\text{SC}}$  spin-spin relaxation mechanism) at the phosphorus nucleus.<sup>17,150,252,253,254</sup>

Scalar relaxation of the second kind becomes the dominant spin-spin

relaxation mechanism at the  $I$  nucleus when it is indirectly spin-spin coupled to a rapidly relaxing quadrupolar nucleus through an interaction of the form  $J\mathbf{I}\cdot\mathbf{S}$ . If the  $S$  nucleus has a short relaxation time,  $T_1(S)$ , compared with the magnitude of  $J(S,I)^{-1}$ , then fluctuating magnetic fields arise which induce efficient spin-spin relaxation of  $I$ . As a result, the NMR spectrum of  $I$  will not exhibit the expected multiplet structure, but may have a broadened lineshape or be completely decoupled from  $S$ . The theory of scalar relaxation of the second kind as it pertains to isotropic liquids is well understood; it is often possible to estimate  $T_1(S)$  by simply measuring peak width at half height in the NMR spectrum of the  $I$  nucleus.<sup>254</sup> The rate expressions for spin-lattice and spin-spin scalar relaxation of the second kind in the extreme narrowing limit of motion in solution are written as

$$T_1^{\text{SC}}(I)^{-1} = \frac{8\pi^2 J(S,I)^2}{3} S(S+1) \left[ \frac{\tau_S}{1 + (\omega_I - \omega_S)^2 \tau_S^2} \right] \quad (4.22)$$

and

$$T_2^{\text{SC}}(I)^{-1} = \frac{4\pi^2 J(S,I)^2}{3} S(S+1) \left[ \tau_S + \frac{\tau_S}{1 + (\omega_I - \omega_S)^2 \tau_S^2} \right] \quad (4.23)$$

where  $\tau_S$  is the relaxation time of the quadrupolar nucleus. The contribution of the scalar relaxation mechanism to the overall  $T_1(I)$  is negligible unless  $\omega_I \approx \omega_S$ ; however, the contribution to  $T_2(I)$  can be substantial, affecting the line widths in the  $I$  spectrum, since  $(T_2(I))^{-1} \approx \pi \Delta\nu_{1/2}$  (where  $\Delta\nu_{1/2}$  is the line width at half-height). Relaxation at the quadrupolar nucleus is dominated by the quadrupolar relaxation

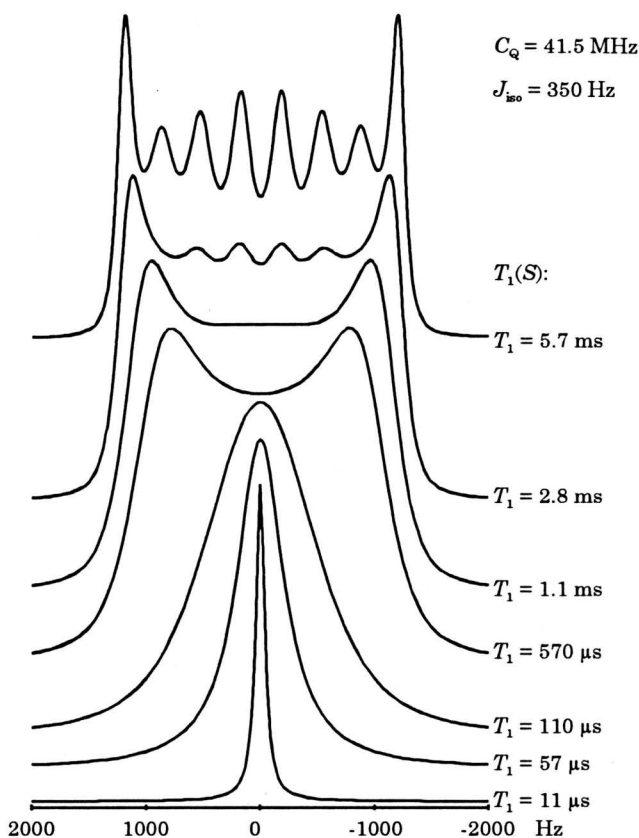


**Figure 4.16** Calculated variable-temperature solution NMR spectra of a spin-1/2 nucleus spin-coupled to a spin-7/2 nucleus.

mechanism, in which the relaxation rate is proportional to  $C_Q^2$  and, in solution, the rate of tumbling of the molecule. Expressions are given elsewhere.<sup>254</sup>

For rapid molecular tumbling in solution, the correlation time for molecular motion,  $\tau_c$ , is very small, and the  $T_1(S)$  of the quadrupolar nucleus increases. As a result, the full multiplet may appear in the  $I$  spectrum (Fig. 4.16). Decreasing the temperature results in longer  $\tau_c$  and a faster quadrupolar relaxation rate (i.e., shorter  $T_1(S)$ ); accordingly, since the coupled  $I$  nucleus is sensitive to the lifetime of each of the  $S$  spin states, broadening occurs in the  $I$  spectrum. Further decrease in

temperature results in an even longer  $\tau_c$ , and an even shorter  $T_1(S)$ , to the point where the spin-1/2 spectrum coalesces into a single peak.

Contrary to liquids, relaxation of quadrupolar nuclei in solids cannot generally be described by single exponential decays, even in the case of MAS experiments.<sup>23,255</sup> Nonetheless, it is still possible to obtain an approximate value for the effective  $^{59}\text{Co}$  spin-lattice relaxation time,  $T_1(^{59}\text{Co})^{\text{eff}}$ , at room temperature from qualitative analysis of the  $^{31}\text{P}$  NMR line shapes and comparison with the simulated solution spectra of these compounds. The effective  $^{59}\text{Co}$   $T_1$  at 155 K is estimated to be greater than 8 ms, and at 295 K can be estimated to be on the order of 500  $\mu\text{s}$ , from measurements of  $^{31}\text{P}$  NMR peak widths at half-height. From the X-ray structure,<sup>231</sup> it is clear that the cobaloxime molecules are not undergoing dynamic overall motion which would induce spin-lattice relaxation at the cobalt centre. The precise nature of the motion causing the fluctuating electric field gradient at  $^{59}\text{Co}$ , and therefore the increased rate of  $^{59}\text{Co}$  spin-lattice relaxation at room temperature in **II**, is unknown at this time.

An interesting similarity between the room-temperature solid-state and solution NMR spectra is the noticeable sharpening of the transitions corresponding to the  $\pm 7/2$  spin states of the quadrupolar nucleus. This is because quadrupolar relaxation of the  $\pm 7/2$  spin states is less efficient than for the other spin states, since there are only one single-quantum transition and one double-quantum transition possible from the  $\pm 7/2$  spin states, whereas for the remaining states there are four possible pathways for relaxation.<sup>150,252,256</sup>

Similar observations are made for **XVIII** and **XIX**, though the fine structure

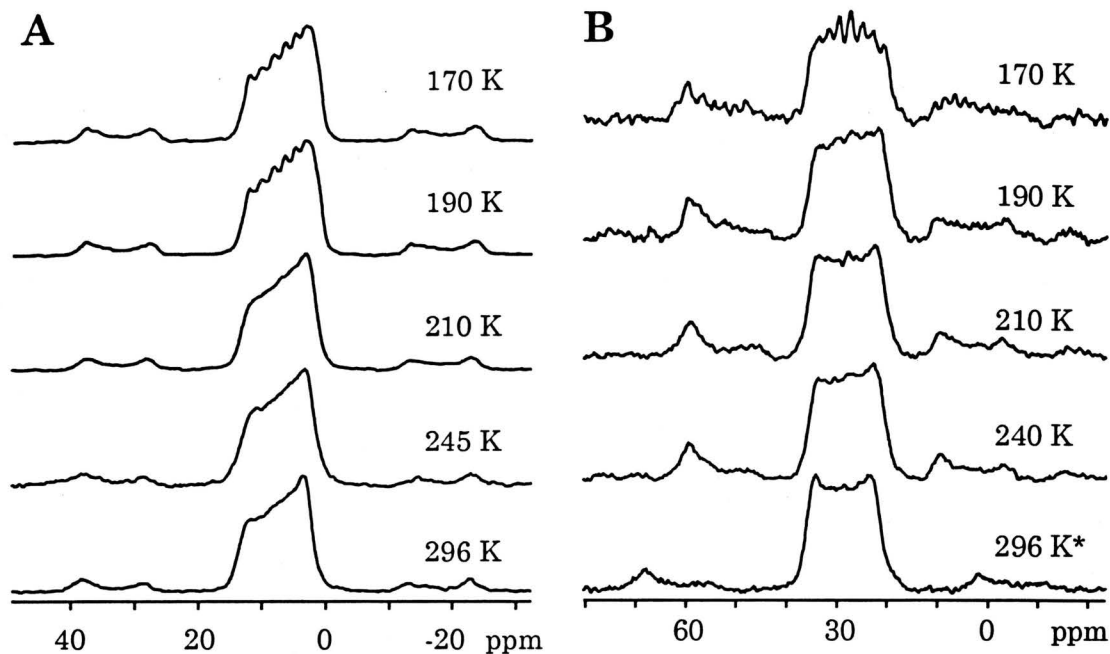


**Figure 4.17** Variable-temperature  $^{31}\text{P}$  CPMAS NMR of (A)  $\text{PEt}_3\text{Co}(\text{DH})_2\text{Me}$  (XVIII) and (B)  $\text{PBu}_3\text{Co}(\text{DH})_2\text{N}_3$  (XIX) at 9.4 T. All spectra of XVIII acquired with  $\nu_{\text{rot}} = 4136$  Hz. Spectrum marked with asterisk was acquired with  $\nu_{\text{rot}} = 5383$  Hz; for other spectra of XIX,  $\nu_{\text{rot}} = 4000$  Hz.

in the spectra can be resolved at 170 K (Fig. 4.17). Rough deconvolution of the room temperature powder patterns provide estimates of individual peak widths, from which upper limits on  $T_1(^{59}\text{Co})$  of 8 and 9 ms at 170 K are calculated for XVIII and XIX, respectively.

Spectral broadening akin to that observed in the  $^{31}\text{P}$  CPMAS NMR spectra of II, XVIII and XIX was also observed for  $\text{PBu}_3\text{Co}(\text{DH})_2\text{Me}$  and  $\text{P}(\text{OMe})_3\text{Co}(\text{DH})_2\text{N}_3$ ; variable-temperature NMR spectra of these complexes are not presented here. Raising the temperature of the sample by 30 K above room temperature had no noticeable effect on spectral appearance; it is likely that a large temperature increase would be needed to observe partial or full coalescence of the peaks. Low-temperature spectra were also acquired for  $\text{P}(p\text{-ClC}_6\text{H}_4)_3\text{Co}(\text{DH})_2\text{Me}$  (XII), which has

fairly broad MAS NMR patterns at room temperature, but still reveals the fine structure resulting from  $^1J(^{59}\text{Co}, ^{31}\text{P})$ . No changes were observed in these spectra down to 165 K. Peak-broadening mechanisms in the  $^{31}\text{P}$  CPMAS NMR spectra of the cobaloximes must arise from several sources other than the quadrupolar-dominated spin-lattice relaxation of the cobalt nucleus.

#### 4.5 Conclusions

NMR parameters determined from the  $^{31}\text{P}$  CPMAS NMR spectra of nineteen cobaloximes have been presented. The EFG tensor orientations and quadrupolar parameters vary with substitution of different axial ligands. The orientations of the EFG tensors have been determined for three cobaloximes for which complementary quadrupolar and structural data is available. In other systems for which such information is unavailable, the magnitudes and signs of the residual dipolar shifts can be used to infer EFG tensor orientations from comparison with the well-characterized compounds. In alkylcobaloximes,  $d$  is negative, suggesting an orientation in which  $V_{11}$  is along the Co, P bond. In chloro- and azidocobaloximes,  $d$  is positive, intimating that  $V_{22}$  is along the Co, P bond.

The magnitude of  $^1J(^{59}\text{Co}, ^{31}\text{P})$  varies according to the nature of the neutral and anionic axial ligands. Specific trends in  $^1J(^{59}\text{Co}, ^{31}\text{P})$  can be qualitatively related to the steric bulk and electronic nature of the neutral ligands and the *trans*-influencing ability of the anionic species. No correlation is found between the Co, P internuclear distance and the magnitude of  $^1J(^{59}\text{Co}, ^{31}\text{P})$ . The Fermi-contact mechanism can be used to qualitatively explain why  $^1J(^{59}\text{Co}, ^{31}\text{P})$  is reduced in

methylcobaloximes and increased in phosphite-substituted cobaloximes.

Variable-temperature  $^{31}\text{P}$  NMR experiments reveal that  $^{59}\text{Co}$  is partially self-decoupled at room temperature, and "re-coupled" at temperatures on the order of 170 K or lower, opposite to what is observed in the extreme-narrowing limit in solution. Upper limits on  $T_1(^{59}\text{Co})$  can be estimated from the line widths of the  $^{31}\text{P}$  MAS NMR spectra, assuming that scalar relaxation of the second kind is operative at the phosphorus nuclei.

Some  $^{13}\text{C}$  CPMAS NMR spectra and  $^{59}\text{Co}$  NMR spectra of stationary samples of cobaloximes have also been acquired. Difficulties associated with analysis and acquisition of these spectra are discussed in Appendix B.

## Chapter 5

# Solid-State Nitrogen-15 NMR Study of Cobaloximes with <sup>15</sup>N-labelled Pyridine and Aniline as Axial Ligands

### 5.1 Introduction

Nitrogen has two naturally-occurring isotopes, both of which are useful in NMR spectroscopy: <sup>14</sup>N ( $S = 1$ ) and <sup>15</sup>N ( $S = 1/2$ ). Nitrogen-14 is 99.635% naturally abundant, has a relatively small quadrupole moment, and is 5.7 times more receptive than <sup>13</sup>C in NMR experiments. However, in both solution and solid-state NMR experiments, the <sup>14</sup>N peaks are often very broad, such that fine structure (i.e.,  $J$ -couplings) is not observed. The development of new methods for acquiring <sup>14</sup>N NMR spectra<sup>257,258</sup> and the high magnetic fields available for dispersion of the <sup>14</sup>N signals have resulted in renewed interest in this nucleus.<sup>257,259</sup> Nitrogen-15 NMR, on the other hand, is capable of providing very high-resolution spectra in both solution and solid-state experiments. The pitfall, of course, is that due to the low natural abundance of <sup>15</sup>N (0.635 %, receptivity is  $2.19 \times 10^{-2}$  times that of carbon), hence isotopically enriched compounds are generally examined. This may be costly if the compounds of interest cannot be synthesized from <sup>15</sup>N-labelled nitric acid, ammonia or ammonium salts, which are relatively inexpensive. Nonetheless, solution and solid-state <sup>15</sup>N NMR have both found widespread use for the characterization of

countless materials containing nitrogen nuclei.<sup>257,260,261,262</sup>

Solid-state NMR studies on the cobaloximes have been extended to include cobaloximes with axially-substituted nitrogen-ligands. Solid-state  $^{15}\text{N}$  NMR spectra of spinning and stationary samples of four cobaloximes containing either pyridine- $^{15}\text{N}$  or aniline- $^{15}\text{N}$  as ligands are presented in this chapter. The cobaloximes investigated are  $^{15}\text{N}$ -py\*Co(DH) $_2$ Cl (I),  $^{15}\text{N}$ -anil\*Co(DH) $_2$ Cl (II),  $^{15}\text{N}$ -py\*Co(DH) $_2$ CH $_3$  (III) and  $^{15}\text{N}$ -py\*Co(DH) $_2$ Br (IV), where py = pyridine and anil = aniline.

Nitrogen-15 CPMAS NMR spectra exhibit  $^{59}\text{Co}$ ,  $^{15}\text{N}$  residual dipolar coupling, due to the breakdown of the high-field approximation for the  $^{59}\text{Co}$  nuclei. These spectra are analyzed to yield information on the magnitude of  $^1J(^{59}\text{Co}, ^{15}\text{N})$ , as well as the magnitude and sign of the  $^{59}\text{Co}$  nuclear quadrupole coupling constant,  $C_Q$ , and the orientation of the EFG tensor at the  $^{59}\text{Co}$  nucleus with respect to the molecular frame. There are only three reports of  $^1J(^{59}\text{Co}, ^{15}\text{N})$ , all obtained from solution  $^{15}\text{N}$  NMR studies. From  $^{15}\text{N}$  NMR spectra of  $^{15}\text{N}$ -labelled  $[\text{Co}(\text{NH}_3)_5(^{15}\text{NH}_3)]^{3+}$  and  $[\text{Co}(^{15}\text{NH}_2\text{CH}_2\text{CH}_2^{15}\text{NH}_2)_3]^{3+}$ , Yamasaki et al. measured  $|^1J(^{59}\text{Co}, ^{15}\text{N})| = 62.5 \pm 1.0$  Hz in the hexaammine complex and  $|^1J(^{59}\text{Co}, ^{15}\text{N})| = 63.8 \pm 1.0$  Hz in the tris(ethylenediamine) complex.<sup>263</sup> Very small values of  $^1J(^{59}\text{Co}, ^{15}\text{N})$ , 9 Hz, were reported from partially resolved octets in the solution  $^{15}\text{N}$  NMR spectra of the cobalt-nitrosyl complex  $\text{Co}(^{15}\text{NO})(\text{ketox})_2$ .<sup>264</sup> There are no other values of  $^1J(^{59}\text{Co}, ^{15}\text{N})$  available for comparison, with the closest analogies being  $^1J(^{103}\text{Rh}, ^{15}\text{N})$  values which have been reported for the rhodium analogues of cobaloximes, the rhodoximes,<sup>265</sup> and other six-coordinate rhodium complexes.<sup>266</sup>

Solid-state NMR spectra of stationary samples in which there is an isolated dipolar-coupled spin pair contain information on both the principal components of the chemical shielding (CS) tensor at the spin-1/2 nucleus and its orientation with respect to the internuclear vector between the dipolar coupled nuclei (i.e., the dipolar vector). *Dipolar-chemical shift NMR* has been used successfully for the characterization of the CS tensors in many instances.<sup>148,193,267,268,269,270,271,272</sup> A large number of nitrogen CS tensors in a variety of organic and inorganic complexes have been reported in the literature.<sup>80,257,273</sup> Nitrogen CS tensors of nuclei directly coordinated to transition metals have been reported in the literature as well,<sup>274,275,276,277,278,279</sup> however, there is no information available on the orientation of the CS tensors with respect to the molecular frame. If the magnitude of  $J$  can be determined from MAS NMR spectra, analysis of the stationary spectra can yield information on the sign of the indirect spin-spin coupling constant.

*Ab initio* calculations have been employed for the purpose of predicting the orientations of the nitrogen CS tensors in the molecular frame. Comparison is made between experimental CS tensors and theoretical CS tensors obtained from *ab initio* calculations using the gauge-including atomic orbital (GIAO) method (see experimental section for details). Furthermore, this allows for comparison of the nitrogen shielding tensors when the ligands, pyridine and aniline, are free and when they are coordinated to cobalt.

This chapter is organized as follows. The experimental details are given in Section 5.2. In Section 5.3, some theoretical background is provided on (i) the effects of a negative magnetogyric ratio on the appearance of MAS spectra exhibiting

residual dipolar coupling, and (ii) the dipolar chemical shift method. The  $^{15}\text{N}$  CPMAS NMR spectra of the four cobaloximes are discussed in Section 5.4. In Section 5.5, the nitrogen chemical shift tensors and their orientations with respect to the molecular frame are presented. A detailed account of how the analysis is conducted is given. Finally, in Section 5.6, GIAO *ab initio* calculations on compounds I, II and III, as well as on pyridine and aniline, are given. The principal components and orientations of the CS tensor are discussed in the context of Ramsey's equation for chemical shielding<sup>26</sup> and molecular orbital theory.

## 5.2 Experimental

Nitrogen-15 labelled (99%)  $\text{py}^*\text{Co}(\text{DH})_2\text{Cl}$  (I) and  $\text{anil}^*\text{Co}(\text{DH})_2\text{Cl}$  (II) were synthesized from  $\text{Co}(\text{DH})(\text{DH}_2)\text{Cl}_2$ <sup>168</sup> and  $^{15}\text{N}$ -labelled pyridine and aniline according to standard literature methods.<sup>179a,280</sup> Pyridine- $^{15}\text{N}$  and aniline- $^{15}\text{N}$  (99%) were obtained from Cambridge Isotope Laboratories and used without further purification.  $^{15}\text{N}$ - $\text{py}^*\text{Co}(\text{DH})_2\text{CH}_3$  (III) and  $^{15}\text{N}$ - $\text{py}^*\text{Co}(\text{DH})_2\text{Br}$  (IV) ( $^{15}\text{N}$ -labelling, ca. 25%) were synthesized from  $\text{Co}(\text{DH})(\text{DH}_2)\text{Br}$  and pyridine- $^{15}\text{N}$  using a recently published synthetic method.<sup>281</sup> Due to the small amounts of starting material for complexes III and IV (ca. 30-50 mg), the  $^{15}\text{N}$ -labelled compounds were mixed with freshly prepared, natural-abundance samples in order to provide enough material to fill the NMR rotors. All products were characterized by solution  $^1\text{H}$  and  $^{13}\text{C}$  NMR experiments. Crystalline samples were powdered and packed into 7 mm o.d. and 4 mm o.d. zirconium oxide rotors.

Solid-state  $^{15}\text{N}$  NMR spectra were acquired at both 20.3 MHz (4.7 T) and 40.5

MHz (9.4 T) on Bruker MSL-200 and AMX-400 NMR spectrometers under conditions of magic-angle spinning, cross-polarization and high-power proton decoupling. Typical spinning speeds for the 7 mm o.d. rotors were between 2.0 and 3.5 kHz; for the 4 mm rotors, spinning speeds ranged from 6.0 to 10.5 kHz. Contact times were set between 5 and 10 ms. Proton  $90^\circ$  pulses of 6.0 to 6.5  $\mu$ s and relaxation delays between 4 and 8 seconds were applied. Nitrogen-15 CPMAS NMR spectra were processed with an applied lorentzian broadening (LB) of ca. 20 to 30 Hz. CP NMR spectra of stationary samples were processed with LB from 80 to 200 Hz. CPMAS NMR spectra were acquired with ca. 2000-8000 scans, while spectra of stationary samples were acquired with 13000-22000 scans. All  $^{15}\text{N}$  NMR spectra were referenced with respect to liquid  $\text{NH}_3$  (20  $^\circ\text{C}$ ),  $\delta = 0$  ppm, by setting the ammonium  $^{15}\text{N}$  NMR signal of crystalline  $^{15}\text{NH}_4^{15}\text{NO}_3$  to 23.8 ppm.<sup>262,282</sup>

Prior to analysis of MAS spectra, the spinning sidebands were summed to produce a pattern representative of the isotropic MAS NMR spectrum.<sup>171</sup> All spectra were analyzed using the WSolids software package, which was developed in this laboratory.

*Ab initio* chemical shielding calculations were carried out on I, II and III, as well as pyridine and aniline, using a IBM RISC 6000 workstation using Gaussian 94.<sup>67</sup> The molecular structures used in the calculations on the cobaloximes were taken from reported X-ray structures.<sup>280,283,237</sup> For aniline and pyridine, CS calculations were done on the ground-state MP2/6-311G\* geometry-optimized structures, which are very close to experimentally determined geometries.<sup>284,285</sup> All chemical shielding calculations were performed using the GIAO method,<sup>66</sup> with both

restricted Hartree-Fock (RHF) and density functional theory (DFT) methods. Cobalt is a heavy fourth row element ( $Z = 27$ ), and is subject to relativistic effects;<sup>247</sup> thus, the cobalt atoms were treated with effective core potentials (ECPs), using the LANL2DZ basis set.<sup>72</sup> Due to the large size of the cobaloxime systems, locally dense basis sets were used.<sup>286</sup> In general, all atoms in direct contact with the cobalt centre, and atoms in the axial ligands were assigned large basis sets (6-31G\*\* and 6-311G\*\*). The remaining atoms were assigned the 3-21G basis set. DFT calculations (B3LYP) were carried out using Becke's three-parameter hybrid exchange functional<sup>98</sup> and the correlation functional of Lee, Yang and Parr.<sup>99</sup> Absolute chemical shieldings,  $\sigma$ , were converted to the  $^{15}\text{N}$  chemical shift scale relative to liquid  $\text{NH}_3$  ( $20^\circ$ ) with the formula  $\sigma_{\text{ref}} - \sigma$ , where  $\sigma_{\text{ref}} = 244.6$  ppm, the absolute chemical shielding of  $\text{NH}_3$  ( $l$ ) at  $20^\circ\text{C}$ .<sup>287</sup>

### 5.3 Theoretical Background

#### 5.3.1. Negative Magnetogyric Ratios and Residual Dipolar Coupling

Recall from Chapter 4, residual dipolar coupling resulting from the presence of a quadrupolar nucleus is manifested in the spin-1/2 spectrum as a shift in  $2S + 1$  the peaks of the multiplet, given by

$$\nu_m = \nu_{\text{iso}} - mJ + \frac{S(S + 1) - 3m^2}{S(2S - 1)} d \quad (5.1)$$

where

$$d = \left( \frac{3C_Q R_{\text{eff}}}{20\nu_S} \right) [(3\cos^2\beta^D - 1) + \eta \sin^2\beta^D \cos 2\alpha^D] \quad (5.2)$$

Recently, Olivieri and co-workers have emphasized that eqs. 5.1 and 5.2 are dependent upon the relative signs of the magnetogyric ratios of the spin-1/2 and quadrupolar nuclei.<sup>225,226</sup> Eqs. 5.1 and 5.2 may be combined and rewritten as<sup>226</sup>

$$\begin{aligned} \nu_m = \nu_{\text{iso}} - |\gamma_I| \left\{ -\frac{m\gamma_S K h}{4\pi^2} + \left( \frac{3C_Q h}{40\pi B_0} \right) \left( \frac{\mu_0}{4\pi r_{IS}^3} - \frac{\Delta K}{3} \right) \right. \\ \left. \times \left[ \frac{S(S+1) - 3m^2}{S(2S-1)} \right] \times (3\cos^2\beta^D - 1 + \eta \sin^2\beta^D \cos 2\alpha^D) \right\} \end{aligned} \quad (5.3)$$

where  $K = 4\pi^2 J/h\gamma_I\gamma_S$  and  $\Delta K = 4\pi^2 \Delta J/h\gamma_I\gamma_S$ . Spectral simulations employing this equation yield the correct shifts in the peak positions, regardless of the signs of  $\gamma_I$  and  $\gamma_S$ . If it is desired that  $d$  be used as a parameter describing the residual dipolar shift, eqs. 5.1 and 5.2 can be simply modified for the cases when  $\gamma_I$  is negative by simply (i) removing the negative sign from in front of " $mJ$ " in eq. 5.1, and (ii) placing a negative sign in front of the right-hand side of eq. 5.2. This insures that the transitions still correspond to the proper spin states of the quadrupolar nucleus, and the same definitions for the sense of the multiplet are maintained. On a final note, from these equations it can be seen that the signs of  $J$  and  $\Delta J$  cannot be determined from the analysis of MAS NMR spectra using first-order perturbation theory; however, a full theoretical treatment involving diagonalization of combined Zeeman and quadrupolar hamiltonian exhibits a dependence upon the signs of these parameters.<sup>225</sup>

### 5.3.2 The Dipolar Chemical Shift Method

In situations where an isolated direct-dipolar coupled spin pair is present, it is possible to gain information on the orientation of the CS tensor with respect to the internuclear dipolar vector, and therefore with respect to the molecular frame. This is due to the fact that the dipolar interaction, like the CS tensor, is orientation dependent. As discussed earlier, the dipolar tensor is traceless and almost always axially symmetric, with a unique component along the direction of the internuclear vector. In the case of an isolated spin pair which is direct-dipolar and indirect spin-spin coupled, both of these interactions must be considered in addition to the Zeeman and chemical shielding interactions.<sup>33,34</sup>

The dipolar vector is fixed with respect to the chemical shielding tensor, with the relative orientation described by polar angles  $\beta^C$  and  $\alpha^C$  (Fig. 5.1). The orientation of the chemical shielding tensor with respect to the magnetic field is described by the polar angles  $\vartheta$  and  $\varphi$ . Thus, the transition frequency for spin  $I$  can be computed from<sup>267,269,270</sup>

$$\nu_m(\vartheta, \varphi) = \nu_0 - \nu_{CS} - m\nu_D - mJ_{iso} \quad (5.4)$$

where  $\nu_0$  is the Larmor frequency of the bare  $I$  spin ( $\gamma_I B_0 / 2\pi$ ),

$$\nu_{CS} = \nu_0(\sigma_{11} \sin^2 \vartheta \cos^2 \varphi + \sigma_{22} \sin^2 \vartheta \sin^2 \varphi + \sigma_{33} \cos^2 \vartheta) \quad (5.5)$$

and

$$\nu_D = R_{eff} [1 - 3(\sin \beta^C \sin \vartheta \cos(\varphi - \alpha^C) + \cos \beta^C \cos \vartheta)^2] \quad (5.6)$$

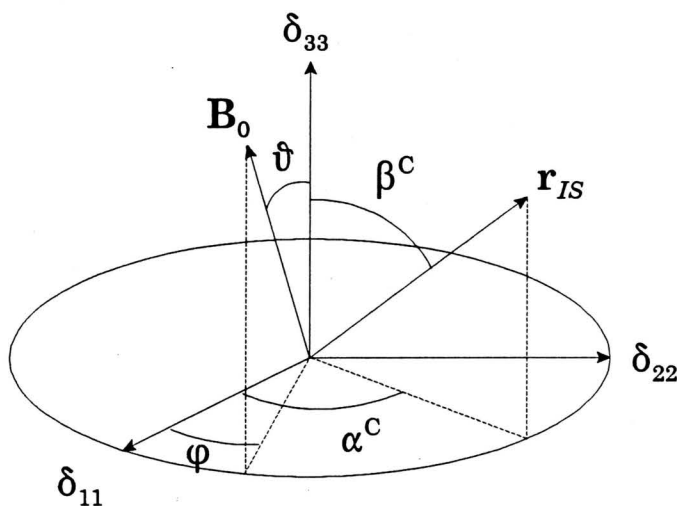


**Figure 5.1** The relative orientations of the magnetic field,  $B_0$ , and the dipolar vector,  $r_{IS}$ , with respect to the CS tensor.

where  $R_{\text{eff}}$  is defined in eq. 2.28. Application of these equations to the calculation of powder line shapes results in the usual anisotropic CS powder patterns. However, at each of the discontinuities corresponding to the principal components of the CS tensor, there will be  $2S + 1$  splittings present which are dependent upon the magnitudes and relative sign of  $R_{\text{eff}}$  and  $J_{\text{iso}}$ , and the orientation of the dipolar vector with respect to the chemical shielding tensor ( $\beta^C$ ,  $\alpha^C$ ), provided that  $|v_1 - v_2|$  and  $|v_2 - v_3|$  are greater than  $R_{\text{eff}}$ . The approximate dipolar splittings,  $\Delta v_{ii}$ , at each principal component,  $\delta_{ii}$ , are given by

$$\begin{aligned}
 \Delta v_{11} &= R_{\text{eff}}(1 - 3\cos^2\alpha^C\sin^2\beta^C) \\
 \Delta v_{22} &= R_{\text{eff}}(1 - 3\sin^2\alpha^C\sin^2\beta^C) \\
 \Delta v_{33} &= R_{\text{eff}}(1 - 3\cos^2\beta^C)
 \end{aligned}
 \tag{5.7}$$

These expressions are strictly valid cases where  $r_{IS}$  is aligned along any of the

three components of the CS tensor.<sup>193,205</sup> Asymmetric splittings may occur for other relative orientations of the CS tensor and dipolar vector. For example, if  $\mathbf{r}_{IS}$  lies in the plane of  $\delta_{11}$  and  $\delta_{22}$ , but not along either component, the splittings at  $\delta_{11}$  and  $\delta_{22}$  are asymmetric, while the splittings at  $\delta_{33}$  are symmetric.<sup>193</sup> Nonetheless, the expressions in eq. 5.7 can be utilized to provide a preliminary dipolar chemical shift analysis. In addition, the overall splitting at each discontinuity will also have a contribution from the isotropic  $J$ -coupling, if it is of appreciable magnitude with respect to  $\Delta\nu_{ii}$ .

As discussed earlier, in the presence of a quadrupolar interaction, orientation-dependent mixing of the pure Zeeman states of the quadrupolar nucleus occurs. It might be expected that if the nuclear quadrupolar interaction is on the order of the Zeeman interaction (i.e.,  $C_Q/(4S(2S - 1)) \sim \nu_S$ ), the splittings observed in the spin-1/2 NMR spectra would not be equally spaced. However, it has been demonstrated that large quadrupolar interactions have no effect on the positions of the CS principal components or spectral extremities; rather, some intensity redistribution over the powder pattern may occur.<sup>193,288</sup> Since the condition  $C_Q/(4S(2S - 1)) < \nu_S$  holds for the systems examined in this thesis, quadrupolar effects on the stationary spin-1/2 spectra can be safely neglected. Thus, if  $\mathbf{r}_{IS}$  is along the direction of one of the CS principal components, it is expected that eight  $(2S + 1)$  evenly spaced dipolar splittings should be observed at the discontinuities in the  $^{15}\text{N}$  NMR spectra of stationary samples. An idealized spectrum with well-dispersed CS principal components is shown in Fig. 5.2.

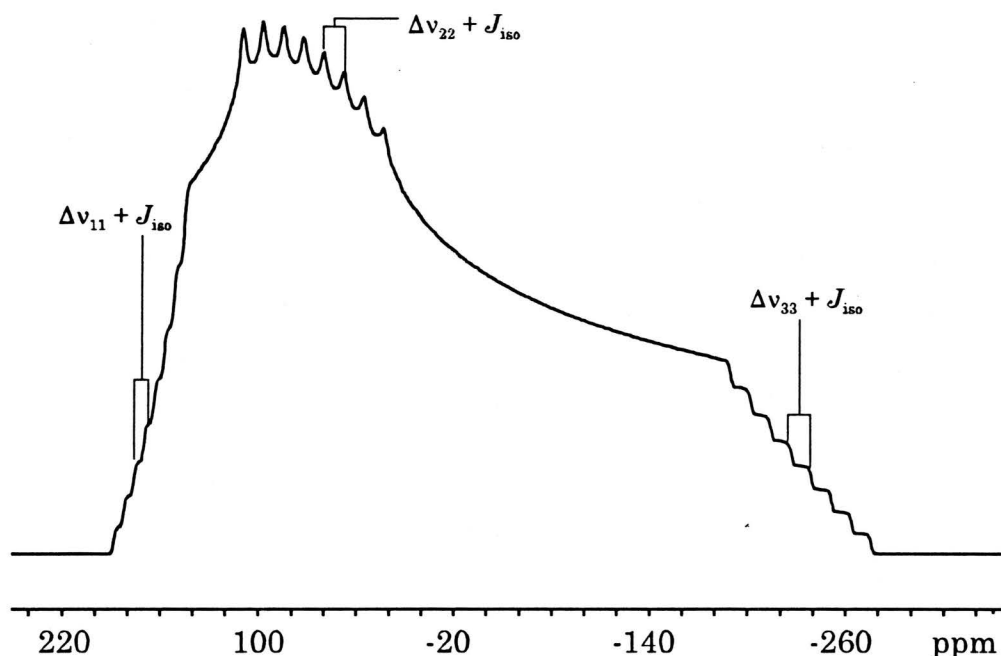


**Figure 5.2** Stationary powder pattern of a spin-1/2 nucleus dipolar- and  $J$ -coupled to a spin-7/2 nucleus. Here,  $\delta_{\text{iso}} = 0$  ppm,  $R_{\text{dd}} = 500$  Hz,  $J_{\text{iso}} = 500$  Hz,  $\Omega = 400$  ppm,  $\kappa = 0.5$ ,  $\beta^{\text{C}} = 90^\circ$  and  $\alpha^{\text{C}} = 0^\circ$ .

## 5.4 Nitrogen-15 CPMAS NMR Spectra of the Cobaloximes

### 5.4.1 $^{15}\text{N}$ -py\*Co(DH)<sub>2</sub>Cl (I)

Experimental and calculated  $^{15}\text{N}$  CPMAS NMR spectra of I at 4.7 T and 9.4 T are shown in Fig. 5.3. Rather than observing evenly-spaced octets, distorted multiplets result from the presence of residual dipolar coupling. Since the degree of distortion is inversely dependent upon the Larmor frequency, the 4.7 T spectrum is slightly more distorted than the corresponding spectrum at 9.4 T (i.e., five peaks are resolved in the 9.4 T spectrum, as opposed to four at 4.7 T). The spacing between

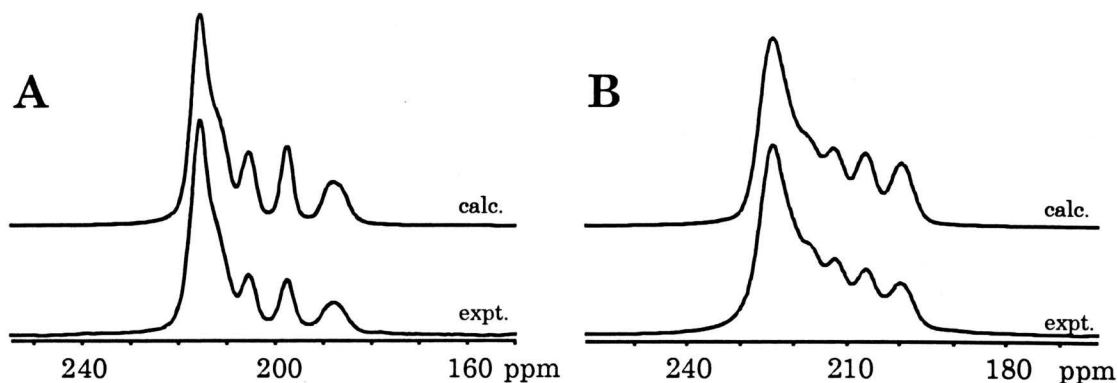


**Figure 5.3** Experimental and calculated  $^{15}\text{N}$  CPMAS NMR spectra of the isotropic peak of  $^{15}\text{N}$ -enriched  $\text{py}^*\text{Co}(\text{DH})_2\text{Cl}$  (I) at (A) 4.7 T and (B) 9.4 T.

the peaks increases from high to low frequency (left to right), meaning that the sense of the spectrum is positive. The parameters used to simulate these spectra are given in Table 5.1.

The analysis of the  $^{15}\text{N}$  CPMAS NMR spectra of I is aided by the availability of structural and nuclear quadrupole data obtained from various sources (*vide infra*). The dipolar coupling constant is calculated from the Co,  $\text{N}_{\text{ax}}$  internuclear distance,  $r(\text{Co}, \text{N}_{\text{ax}}) = 1.965(3) \text{ \AA}$ ,<sup>283</sup> to be  $R_{\text{dd}} = -378(1) \text{ Hz}$ . Values of  $C_Q = +64.82 \text{ MHz}$  and  $\eta = 0.63$  are reported for I, from the  $^{59}\text{Co}$  NQR study of LaRossa and Brown.<sup>162</sup> The largest component of the EFG,  $V_{33}$ , is proposed to be oriented along the L-Co-X axis of the molecule. The local  $C_{2v}$  symmetry at the cobalt atom dictates that if one of the EFG principal components is aligned in the direction of the axially bonded species, then the remaining components must lie in the plane of the DH moieties, with one component bisecting the dimethylglyoxime-cobalt ring, and the other bisecting the inter-ring N-Co-N bond angles.<sup>118</sup> This proposed orientation corresponds to  $\beta^D = 0^\circ$ , for which  $\alpha^D$  is undefined.

**Table 5.1:** Parameters obtained from the  $^{15}\text{N}$  CPMAS NMR spectra of  $^{15}\text{N}$ -labelled cobaloximes.

Compound	$\delta_{\text{iso}}$ (ppm)	$^1J(^{59}\text{Co}, ^{15}\text{N})$ (Hz) <sup>a</sup>	$R_{\text{eff}}$ (Hz) <sup>b</sup>	$C_Q$ (MHz)	$\eta$ <sup>c</sup>	$\beta^{\text{D}}$	$\alpha^{\text{D}}$	$d^{\text{d}}$ (Hz)
py*Co(DH) <sub>2</sub> Cl (I)	207.9(2)	74(2)	-378(20)	+64.82 <sup>c</sup>	0.63	0°	--	+78
anil*Co(DH) <sub>2</sub> Cl (II)	-7.9(1)	63(3)	-353(20)	+80(3)	n/a	0°	--	+90
py*Co(DH) <sub>2</sub> CH <sub>3</sub> (III)	265.7(2)	36(1)	-324(20)	+29.52 <sup>c</sup>	0.22	90°	0°	-12
py*Co(DH) <sub>2</sub> Br (IV)	213.0(3)	73(1)	-378(30)	+62(2)	n/a	0°	--	+74

*a.* The sign of  $^1J(^{59}\text{Co}, ^{15}\text{N})$  cannot be determined from analysis of the MAS NMR spectra.

*b.* Effective dipolar coupling constant,  $R_{\text{eff}} = R_{\text{dd}} - \Delta J/3$ .

*c.* Data from ref. 162. Obtained at room temperature.

*d.* Calculated for  $\nu_{\text{Co-59}} = 94.5$  MHz (9.4 T).

Several interesting comments should be made about some of the NMR parameters extracted from this analysis. The magnitude of  $|^1J(^{59}\text{Co}, ^{15}\text{N})|$ , 74(2) Hz, is comparable to the previously reported  $^1J(^{59}\text{Co}, ^{15}\text{N})$  of Yamasaki et al.<sup>263</sup> The spectrum can be simulated using the known EFG parameters,  $\beta^{\text{D}} = 0^\circ$ , and  $R_{\text{eff}} \approx R_{\text{dd}}$ ; thus,  $\Delta J$  is assumed to be negligible. This is a reasonable assumption, since in cases where  $\Delta J$  has been determined unambiguously,  $\Delta J \leq J$ .<sup>213, 245, 246</sup> If the same is true here, then the contribution from  $\Delta J$  is minimal (i.e.,  $\Delta J/3 \approx \pm 25$  Hz) compared to the much larger value of  $|R_{\text{dd}}|$ . This assumption is in place for the remainder of the complexes examined in this chapter. The angle  $\beta^{\text{D}}$  is  $0^\circ$ , indicating that the largest component of the EFG tensor,  $V_{33}$ , is oriented along the direction of the Co, N<sub>ax</sub> internuclear vector, in agreement with the proposed EFG tensor orientation of

LaRossa and Brown.<sup>162</sup> In cases where  $\beta^D = 0^\circ$ ,  $\eta$  has no effect on the appearance of the spectrum, since in the last term of eq. 5.2,  $\sin^2\beta^D = 0$ . The isotropic chemical shift of pyridine has been measured in the solid state as  $\delta_{\text{iso}} = 299(17)$  ppm<sup>289</sup> and 319(7) ppm.<sup>290</sup> The latter value is likely more reliable, since spectra were acquired using modern NMR pulse sequences at a higher applied field. In solution, nitrogen shifts of pyridine range from 286 to 328 ppm.<sup>290</sup> The coordination of pyridine to the cobalt centre in **I** results in a shielding of the nucleus by 111 ppm (coordination shift,  $\Delta = \delta_{\text{complex}} - \delta_{\text{free ligand}} = -111$  ppm). Further comparison of the anisotropic magnetic shielding tensors of pyridine and **I** are made in the Section 5.6.

#### 5.4.2. <sup>15</sup>N-anil\*Co(DH)<sub>2</sub>Cl (**II**)

From the X-ray structure of the anhydrous form of **II**<sup>280</sup>, the Co, N<sub>ax</sub> bond length is  $r(\text{Co}, \text{N}_{\text{ax}}) = 2.010(9)$  Å, corresponding to  $R_{\text{dd}} = -353(2)$  Hz  $\sim R_{\text{eff}}$ . Unlike compound **I**, <sup>59</sup>Co quadrupolar parameters are not available for this complex. Thus, analysis of the CPMAS NMR spectra requires some well-founded assumptions in order to determine the unknown quadrupolar parameters.

Comparison of the <sup>15</sup>N CPMAS NMR spectra of **I** and **II** (Fig. 5.4) reveals that there are increased quadrupolar-induced distortions in the spectra of **II**, possibly indicating that  $C_Q$  is larger in this complex (since  $R_{\text{dd}}$  in **II** is smaller than in **I**). A large number of trial spectral simulations yielded  $|^1J(^{59}\text{Co}, ^{15}\text{N})| = 63(3)$  Hz and  $\delta_{\text{iso}} = -7.9(1)$  ppm; however, there are several degenerate solutions which involve different values of  $C_Q$  and distinct EFG orientations relative to the dipolar vector. The first possible solution has  $C_Q = +80(3)$  Hz, with  $V_{33}$  along the Co,N internuclear vector ( $\beta^D$

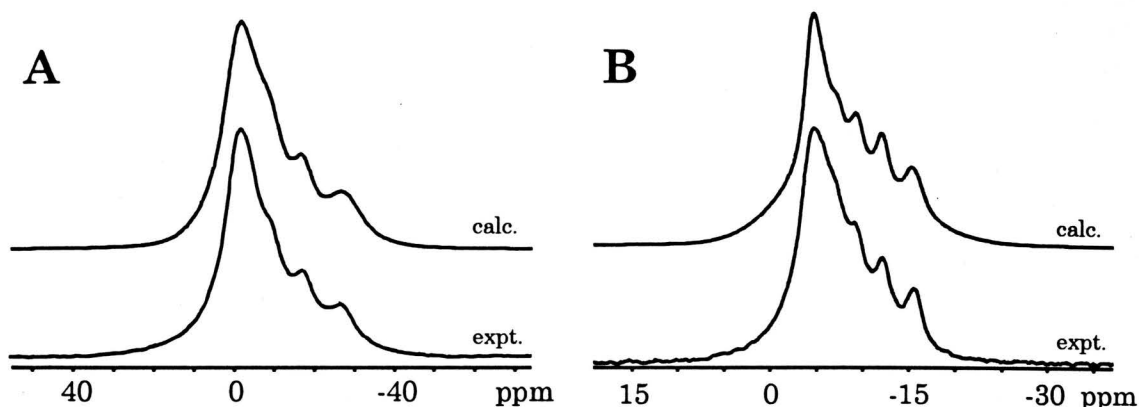


**Figure 5.4** Experimental and calculated  $^{15}\text{N}$  CPMAS NMR spectra of the isotropic peak of  $^{15}\text{N}$ -enriched anil\*Co(DH) $_2$ Cl (**II**) at (A) 4.7 T and (B) 9.4 T.

$= 0^\circ$ ). If  $\beta^D$  is  $90^\circ$ , there are a range of possible solutions involving changes in  $\alpha^D$  and  $\eta$ . If  $\alpha^D = 0^\circ$  ( $V_{11}$  along Co, N),  $\eta$  has no effect on the appearance of the MAS spectrum; however,  $C_Q = -160(4)$  MHz. Given the range of  $C_Q$  reported by LaRossa and Brown for octahedral cobaloxime complexes (i.e.,  $|C_Q(^{59}\text{Co})| = 28$  to  $76$  MHz), this solution seems untenable. When  $\alpha^D = 90^\circ$  ( $V_{22}$  along Co, N), a variety of  $C_Q$  and  $\eta$  can be used for spectral calculations, ranging from  $C_Q = -80$  MHz,  $\eta \sim 1$  to  $C_Q = -160$  MHz,  $\eta \sim 0$ . It is unlikely that  $\eta \sim 1$  in any of the cobaloximes, since this infers that there is no EFG component in one direction (i.e.,  $V_{11} \sim 0$ ). Decreasing the asymmetry parameter requires that the magnitude of  $C_Q$  be increased above the range of known values of  $C_Q$ . From all of the possible solutions, the best fit and the most feasible is the first, with  $\beta^D = 0^\circ$  ( $V_{33}$  along the Co, N bond) and  $C_Q = +80(3)$  MHz. The final parameters from this analysis are presented in Table 5.1.

The aniline nitrogen nucleus in **II**,  $\delta_{\text{iso}} = -7.9$  ppm, is extremely shielded compared to that observed in **I**. This is not surprising given that the axial nitrogen nuclei of **I** and **II** are in very different electronic environments.<sup>262</sup> Moreover,

comparison with the isotropic chemical shift of neat liquid aniline,  $\delta_{\text{iso}} = 58.2$  ppm,<sup>291</sup> demonstrates a similar coordination shift effect to that observed for I, with  $\Delta = -66$  ppm (i.e., the coordinated aniline is more shielded than the free ligand).

A detailed comparison of the molecular structures of I and II may provide a qualitative explanation for the larger value of  $C_Q$  in II.<sup>280,283</sup> The increased EFG in II can in part be attributed to the *s*-character involved in the Co, N bond, according to the theory of Townes and Dailey.<sup>292</sup> According to this model, as the *s*-bonding character in a covalent bond increases, the EFG at the nucleus decreases, according to

$$eq_{zz} = (1 - s - i - \pi)eq_{\text{at}} \quad (5.8)$$

where  $eq_{zz}$  is the largest component of the EFG tensor,  $eq_{\text{at}}$  is atomic EFG (obtainable from atomic data), and *s*, *i* and  $\pi$  are the *s*-, ionic and  $\pi$ -bond characters. In compound I, there is an  $sp^2$  nitrogen, which has considerably more *s*-character than the  $sp^3$  nitrogen in II. The increased *s*-bonding character in I results in a decrease in  $eq_{zz}$ , and therefore a decrease in  $C_Q$ . In addition, the presence of the aniline group in II reduces the overall symmetry of the molecule to less than  $C_{2v}$ , since the aromatic ring of aniline is tilted over one of the DH moieties, with  $\angle\text{Co-N}_{\text{ax}}\text{-C} = 120.7^\circ$ . The arrangement of the nitrogen atoms of the equatorial dimethylglyoxime moieties is less symmetrical in II, likely due to the positioning of the aniline ligand. The overall reduction of symmetry should lead to enhanced EFGs at the  $^{59}\text{Co}$  nucleus in II, also contributing to the increased  $C_Q$ .

### 5.4.3 $^{15}\text{N-py*Co(DH)}_2\text{CH}_3$ (III)

In this section, the consequences of axial substitution of a strong *trans*-influencing anion,  $\text{CH}_3^-$ , in cobaloximes and its effects on  $^{15}\text{N}$  CPMAS NMR spectra are discussed. As demonstrated in Chapter 4, replacement of weak *trans*-influencing anionic species such as halides with strong  $\sigma$ -donors such as  $\text{CH}_3^-$ , has significant effects on the structure of the cobaloxime, including a lengthening of the Co-L bond distance.<sup>160,235,237</sup> The analysis of the MAS NMR spectra of III is facilitated by the availability of both X-ray and quadrupolar data. LaRossa and Brown report  $C_Q = -29.52$  MHz and  $\eta = 0.22$  from their  $^{59}\text{Co}$  NQR study.<sup>162</sup> In addition, these authors suggest that the smallest component of the EFG tensor,  $V_{11}$ , is aligned along the direction of the Co,  $\text{N}_{\text{ax}}$  bond, which corresponds to  $\beta^D = 90^\circ$  and  $\alpha^D = 0^\circ$ . The magnitudes of the quadrupolar parameters were confirmed by a solid-state  $^{59}\text{Co}$  NMR study of Frydman et al., who report  $C_Q = 29.6(4)$  MHz and  $\eta = 0.3(2)$ .<sup>180</sup> Randaccio and co-workers report  $r(\text{Co}, \text{N}_{\text{ax}}) = 2.068(3)$  Å, corresponding to  $R_{\text{dd}} = -324(1)$  Hz.<sup>237</sup>

The  $^{15}\text{N}$  CPMAS NMR spectra of III (Fig. 5.5) are more symmetric in comparison to those of I and II, with seven of the eight peaks of the multiplet resolved at 9.4 T. This is in concordance with the smaller  $C_Q$  observed in III relative to the former compounds. In addition, the sense of the spectrum is negative, opposite to that for I and II. The spacings between the peaks are reduced, and in contrast to the previous two cases, the indirect spin-spin coupling can be measured directly from the splitting between the two central peaks of the multiplet, as  $|^1J(^{59}\text{Co}, ^{15}\text{N})| = 36(1)$  Hz. Using the proposed sign of  $C_Q$  and EFG orientations of

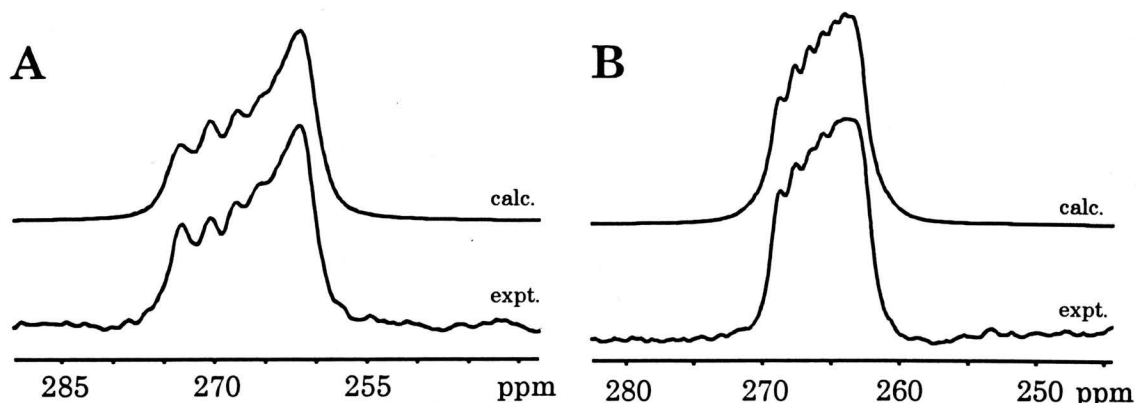


**Figure 5.5** Experimental and calculated  $^{15}\text{N}$  CPMAS NMR spectra of the isotropic transition of  $^{15}\text{N}$ -enriched  $\text{py}^*\text{Co}(\text{DH})_2\text{CH}_3$  (III) at (A) 4.7 T and (B) 9.4 T.

LaRossa and Brown, it appears to be impossible to properly simulate the MAS spectra; in fact, the entire sense of the spectrum is reversed. Our analyses reveal that  $V_{11}$ , is oriented along the Co, N internuclear vector (in agreement with LaRossa and Brown), but that the sign of  $C_Q$  is positive. Similar disagreement was found in the analysis of the  $^{31}\text{P}$  MAS NMR spectrum of  $\text{PPh}_3\text{Co}(\text{DH})_2\text{CH}_3$ , where it was found that  $V_{11}$ , as opposed to  $V_{22}$ , is oriented in the direction of the Co, P bond (Chapter 4).<sup>158</sup> The substitution of the methyl anion into the axial position clearly has a marked effect on both the magnitude of the  $J$ -couplings,  $C_Q$  and  $\eta$ , and the relative orientation of EFG and dipolar vector.

There is not enough data presently available to make any definitive statements about the correlation between molecular structure and the magnitude of  $^1J(^{59}\text{Co}, ^{15}\text{N})$ , though in this work we observe an increase in  $|^1J(^{59}\text{Co}, ^{15}\text{N})|$  with decreasing Co, N separation. This type of relationship has been found in some cases for indirect spin-spin couplings between light and heavy nuclei, where the Fermi-contact mechanism is thought to dominate.<sup>243,293</sup> Such correlations, as discussed in

Chapter 4, can be misleading in some instances, since there can be additional contributions in the  $\mathbf{J}$ -tensor which may affect the magnitudes of  $J_{\text{iso}}$  and  $\Delta J$ . As for  $^1J(^{59}\text{Co}, ^{31}\text{P})$  in the phosphine- and phosphite-substituted cobaloximes, it is observed that the substitution of Me into the axial position results in a reduction in the magnitude of  $^1J(^{59}\text{Co}, ^{15}\text{N})$ .

A comparison of  $^1J(^{59}\text{Co}, ^{15}\text{N})$  and  $^1J(^{103}\text{Rh}, ^{15}\text{N})$  in I and III and the isostructural rhodoximes<sup>265</sup> is given in Table 5.2. The reduced coupling constants increase for increasing atomic number,  $Z$ .<sup>251</sup> In this case, the differences between the two types of coupling constants are closely predicted by  $^1J(^{59}\text{Co}, ^{15}\text{N})/^1J(^{103}\text{Rh}, ^{15}\text{N}) = 4.38$ , which is apparently determined by a ratio of  $\gamma|s(0)|^2$  of the metal nuclei if the FC mechanism dominates.<sup>227</sup>

**Table 5.2:** Comparison of  $^1J(^{59}\text{Co}, ^{15}\text{N})$  and  $^1J(^{103}\text{Rh}, ^{15}\text{N})$  in cobaloximes and rhodoximes (LRh(DH)<sub>2</sub>X)

L, X	$^1J(^{59}\text{Co}, ^{15}\text{N})$ (Hz)	$^1K(^{59}\text{Co}, ^{15}\text{N})$ (N A <sup>-2</sup> m <sup>-3</sup> ) $\times 10^{21}$	$^1J(^{103}\text{Rh}, ^{15}\text{N})$ (Hz) <sup>a</sup>	$^1K(^{103}\text{Rh}, ^{15}\text{N})$ (N A <sup>-2</sup> m <sup>-3</sup> ) $\times 10^{21}$	$^1J(^{59}\text{Co}, ^{15}\text{N})$ /4.38 (Hz)
py, Me	-36	1.26	7.2	1.87	8.2
py, Cl	-75	2.62	17.8	4.62	17.1

*a.* Data from ref. 265.

The magnitudes of the nuclear quadrupolar coupling constant and asymmetry parameter are intimately related to chemical bonding and local symmetry at the quadrupolar nucleus. The values of  $C_Q$  and molecular structure of compounds I and III are compared below. The presence of an axially-substituted

methyl anion results in an increase in the Co, N<sub>ax</sub> bond length in III.<sup>160,237</sup> According to the Townes-Dailey model,<sup>292</sup> since the methyl anion is a strong  $\sigma$ -donor, it is expected that the 4s character of the cobalt atom involved in bonding will be substantially increased compared to that in the halide-substituted cobaloximes. Accordingly, the EFG is reduced at the cobalt atom, resulting in a much smaller value of  $C_Q$ . In addition, due to reduced steric interactions between pyridine and the dimethylglyoxime moieties resulting from the increased Co, N bond length, the nitrogen atoms in III adopt an increasingly planar arrangement with respect to one another.<sup>237</sup> An increasingly symmetric distribution of charge about the cobalt also results in a decreased EFG. Thus, the decrease in the  $C_Q$  of III is due to both electronic and steric effects of the axial ligands.

#### 5.4.4 <sup>15</sup>N-py\*Co(DH)<sub>2</sub>Br (IV)

In this final case, neither crystal data nor quadrupolar parameters are available from the literature. However, it is demonstrated below that a reasonable simulation of the <sup>15</sup>N MAS NMR spectra is possible, provided some prudent suppositions are made about the possible values of the unknown parameters. Slight structural changes have been observed in a comparison of the *trans*-influencing strengths of chlorine and iodine in pyCo(DH)<sub>2</sub>Cl and pyCo(DH)<sub>2</sub>I.<sup>294</sup> Thus, a comparable assumption is made for IV; that is, the bromine atom, like chlorine, acts as a weak *trans*-influencing ligand. Thus, it is expected that despite the larger size of the bromine, the overall effects on structure will be similar to that of chlorine, and  $R_{\text{da}}$  is assumed to be on the order of that for I. Comparison of the <sup>15</sup>N CPMAS NMR

spectra of I and IV (not shown) reveal that these spectra are remarkably similar in appearance, with the only noticeable difference being the isotropic  $^{15}\text{N}$  chemical shift, which is deshielded by 5 ppm in IV. Calculations of these spectra yield parameters which are, within experimental error, equal to those of I. This illustrates a limit on the ability of the fine structure in the  $^{15}\text{N}$  CPMAS NMR spectra to differentiate between molecules with *very* similar structures.

## 5.5 Analysis of $^{15}\text{N}$ NMR Spectra of Stationary Samples - Application of the Dipolar Chemical Shift Method to $^{59}\text{Co}$ , $^{15}\text{N}$ spin pairs

### 5.5.1 $^{15}\text{N}$ NMR of stationary samples of $^{15}\text{N}$ -labelled $\text{py}^*\text{Co}(\text{DH})_2\text{Cl}$ (I)

In this section, a detailed discussion of the interpretation of the stationary  $^{15}\text{N}$  NMR spectra of I is presented. The experimental and calculated  $^{15}\text{N}$  NMR spectra at 4.7 T and 9.4 T are pictured in Fig. 5.6. The measurement of the dipolar splittings and the fitting of the spectra is abetted by the use of first-derivative NMR spectra, also displayed in Fig. 5.6. It is useful to first consider what information is already known about the NMR parameters and molecular structure of I. As discussed earlier,  $R_{\text{eff}}$ , neglecting  $\Delta J$ , is calculated from the known Co, N bond distance to be  $R_{\text{eff}} = -378$  Hz. From the MAS NMR spectra,  $|^1J(^{59}\text{Co}, ^{15}\text{N})|$  is 74(2) Hz and  $\delta_{\text{iso}}$  is 207.9(2) ppm. Thus, the unknown parameters are the span and skew of the CS tensor ( $\Omega$  and  $\kappa$ ) and the relative orientation of the dipolar vector and CS tensor (given by  $\beta^{\text{C}}$  and  $\alpha^{\text{C}}$ ).

An excellent starting point for analysis of these spectra is to measure the

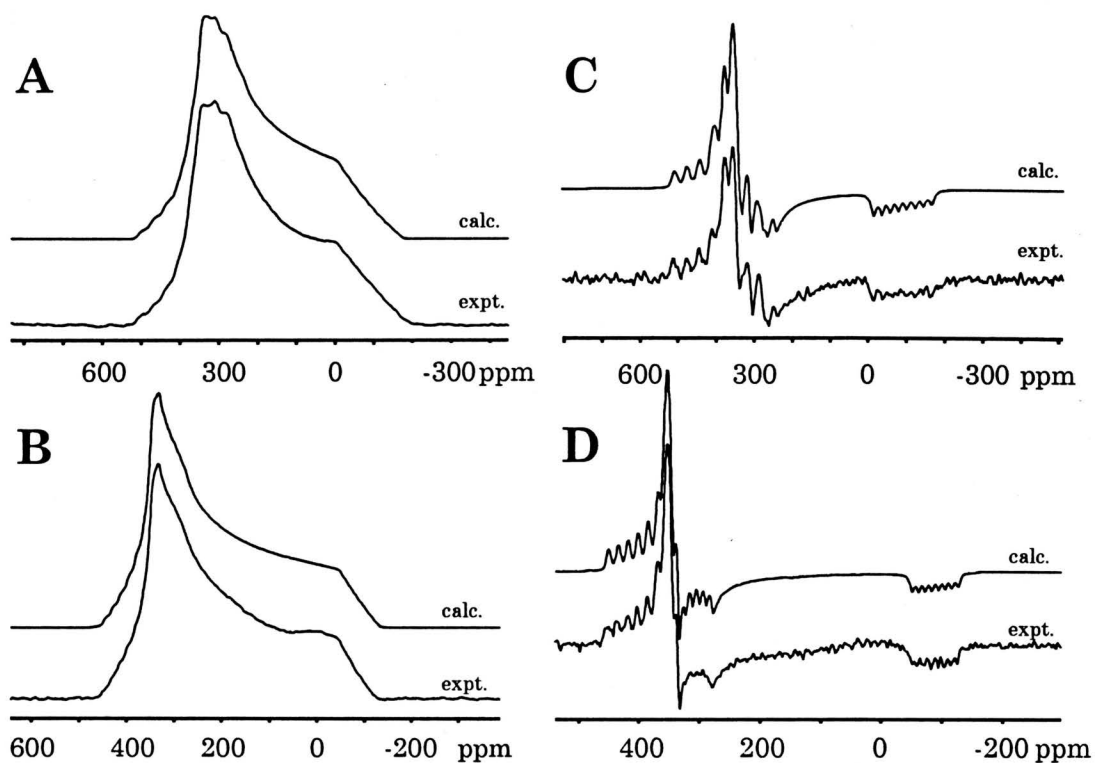


**Figure 5.6** Experimental and calculated  $^{15}\text{N}$  NMR spectra of stationary samples of  $^{15}\text{N}$ -enriched  $\text{py}^*\text{Co}(\text{DH})_2\text{Cl}$  at (A) 4.7 T and (B) 9.4 T. Corresponding first-derivative spectra are presented in (C) and (D).

splittings at the discontinuity corresponding to  $\delta_{33}$ . It must be kept in mind that the observed splittings at all of the discontinuities in the spectrum not only result from the orientation dependent dipolar interaction, but also from a constant contribution from  $J_{\text{iso}}$  (i.e.,  $\Delta\nu_{ii} + J_{\text{iso}}$ ). The measurement of splittings involves a significant error (5 to 8%), even in the first-derivative spectra, due to the mediocre signal to noise ratio. However, refinement of the spectral simulations in later stages of the analysis yields the principal components of the CS tensor and its orientation parameters. The splitting at  $\delta_{33}$  is measured as  $\pm 441(15)$  Hz. No information is initially available on the absolute signs of these splittings, but since the dipolar tensor is assumed to

be traceless, the sum of the measured  $\Delta v_{ii}$  must be equal to zero. The signs of the dipolar splittings quickly become apparent, as outlined below.

Considering both possible signs for  $^1J(^{59}\text{Co}, ^{15}\text{N})$ , potential values for  $\Delta v_{33}$  are  $\pm 367(15)$  Hz ( $J_{\text{iso}} = \pm 74(2)$  Hz) and  $\pm 515(15)$  Hz ( $J_{\text{iso}} = \mp 74(2)$  Hz). From eq. 5.7, the angle  $\beta^{\text{C}}$  can be calculated for the four possible values of  $\Delta v_{33}$ . With  $\Delta v_{33} = -367(15)$  Hz,  $\beta^{\text{C}} = 84.3^\circ$ , which places  $\delta_{33}$  approximately perpendicular to the dipolar vector. Other solutions are  $\Delta v_{33} = +367$ ,  $\beta^{\text{C}} = 35.8^\circ$ ;  $\Delta v_{33} = +515$  Hz,  $\beta^{\text{C}} = 27.5^\circ$ ; and, for  $\Delta v_{33} = -515$  Hz, there is no solution for  $\beta^{\text{C}}$ . Given the high symmetry of the cobaloxime complex, and the perpendicular positioning of the pyridine ring with respect to the planar DH moieties, one of the CS tensor components at the pyridine nitrogen is expected to be oriented in the direction of the Co, N internuclear vector, with another component perpendicular to the plane of the pyridine ring. Values of  $\beta^{\text{C}} = 35.8^\circ$  and  $27.5^\circ$  do not correspond to any local molecular symmetry about the pyridine nitrogen atom; thus the starting solution of  $\beta^{\text{C}} = 84.3^\circ$  with  $\Delta v_{33} = -367(15)$  Hz and  $^1J(^{59}\text{Co}, ^{15}\text{N}) = -74(2)$  Hz is assumed to be correct. Full analysis of the spectrum is required, however, to determine if this solution is valid and to refine the orientation parameters.

With the new information on the apparent signs of  $J$  and  $\Delta v_{33}$ , the angle  $\alpha^{\text{C}}$  can be determined from the measurements of the splittings at  $\delta_{11}$  or  $\delta_{22}$ , and eq. 5.7. The splittings at  $\delta_{22}$  are not well resolved compared to those at  $\delta_{11}$ ; thus, measurements were made at  $\delta_{11}$  yielding a splitting of  $\pm 666(15)$  Hz. This corresponds to two possible values for  $\Delta v_{11}$  of  $+740$  Hz and  $-592$  Hz. Since  $\sum \Delta v_{ii} = 0$ , this means that  $\Delta v_{22}$  is either  $-373$  Hz or  $+959$  Hz, respectively. The latter solution

is unlikely, as there are no splittings of this magnitude in the  $\delta_{22}$  region. As well, there is no solution for  $\alpha^C$  when  $\Delta\nu_{11} = -592$  Hz, indicating that the former solution is likely correct; thus,  $\alpha^C$  is calculated to be ca.  $4^\circ$ , corresponding to an orientation in which  $\delta_{11}$  is aligned approximately along the direction of the Co, N bond.

In addition to all of this, initial predictions of the principal components of the CS tensor must be made. Normally, these components are readily available from Herzfeld-Berger analysis of the spinning sideband manifold of the MAS NMR spectrum.<sup>48</sup> However, since residual dipolar coupling is modulating the sideband intensities in addition to the chemical shielding interaction, spinning-sideband analysis can only be used in a very rough sense to provide an initial guess for these parameters.

The calculated spectrum was refined by varying the parameters at both applied magnetic field strengths, with the final results from analysis of the  $^{15}\text{N}$  NMR spectra presented in Table 5.3, and best fit spectra shown in Fig. 5.6. The close agreement of the experimental and calculated spectra is especially apparent from examination of the first-derivative spectra. Best fit spectra were obtained with  $^1J(^{59}\text{Co}, ^{15}\text{N}) = -75(2)$  Hz. The powder pattern approaches axial symmetry as indicated by the skew,  $\kappa = 0.70(2)$ . The span observed at the pyridine nitrogen in I,  $\Omega = 484(2)$  ppm, is notably reduced compared to that observed in the low-temperature solid-state NMR spectra of pyridine ( $\Omega = 622(7)$  ppm).<sup>290</sup>

Several comments should be made about the correctness of the sign of  $J$  and the signs of the dipolar splittings. Spectral simulations using the other possible values for  $\beta^C$  were attempted, but none of the simulated spectra were even remotely

close in appearance to the experimental spectra. If  ${}^1J({}^{59}\text{Co}, {}^{15}\text{N}) = +75$  is utilized in calculating the spectra, an increase in the magnitude of the splitting at  $\delta_{11}$  is observed, while the splittings at  $\delta_{22}$  and  $\delta_{33}$  decrease. Given that  $\beta^{\text{C}} = 85(2)^\circ$  is required to properly simulate spectra at both fields, this confirms that the sign of  ${}^1J({}^{59}\text{Co}, {}^{15}\text{N})$  is negative, and that the signs of the dipolar splittings are as stated.

The polar angle  $\beta^{\text{C}}$ ,  $85(2)^\circ$ , indicates that  $\delta_{11}$  is approximately oriented along the direction of the Co, N bond, and  $\delta_{33}$  is nearly perpendicular to the dipolar vector. The small value of  $\alpha^{\text{C}}$  ( $3^\circ$ ) and the high symmetry at the pyridine nitrogen imply that  $\delta_{22}$  and  $\delta_{33}$  are oriented such that one component is approximately perpendicular and the other approximately parallel to the plane of the pyridine ring. Based on the CS tensor orientations from the solid-state  ${}^{15}\text{N}$  NMR study of pyridine,<sup>289,290</sup> it is likely that  $\delta_{33}$  is the component oriented perpendicular to the pyridine ring plane. This is supported by the theoretical calculations presented in Section 5.6.

**Table 5.3:** Parameters obtained from dipolar chemical shift analysis of the  $^{15}\text{N}$  NMR spectra of stationary samples of  $^{15}\text{N}$ -labelled cobaloximes.

Compound	$\delta_{\text{iso}}$ (ppm) <sup>a</sup>	$\Omega$ (ppm)	$\kappa$	$\delta_{11}$ (ppm)	$\delta_{22}$ (ppm)	$\delta_{33}$ (ppm)	$\beta^{\text{C}}$ ( $^{\circ}$ )	$\alpha^{\text{C}}$ ( $^{\circ}$ )	$R_{\text{eff}}$ (Hz)	$^1J(^{59}\text{Co}, ^{15}\text{N})$ (Hz)
$^{15}\text{N}$ -py*Co(DH) <sub>2</sub> Cl (I)	207(1)	484(2)	0.70(2)	393	320	-92	85	3	-375	-75(2)
$^{15}\text{N}$ -an*Co(DH) <sub>2</sub> Cl (II)	-7.0(3.0)	175(3)	0.18(2)	75	3.5	-100	88	3	-353	-63(3)
$^{15}\text{N}$ -py*Co(DH) <sub>2</sub> CH <sub>3</sub> (III)	265(4)	488(10)	0.97(5)	430	423	-58	90	- <sup>b</sup>	-324	-36(7)
$^{15}\text{N}$ -py*Co(DH) <sub>2</sub> Br (IV)	212.5(2.0)	485(7)	0.72(2)	396	328	-89	88	2	-372	-73(2)

- a.*  $^{15}\text{N}$  chemical shifts are referenced with respect to liquid  $\text{NH}_3$  at  $20^{\circ}\text{C}$  ( $\delta_{\text{iso}} = 0.0$  ppm) by setting the isotropic chemical shift of the  $^{15}\text{N}$  ammonium resonance of  $\text{NH}_4\text{NO}_3$  (s) to 23.8 ppm.
- b.*  $\alpha^{\text{C}}$  not determined, since  $\delta_{11} \approx \delta_{22}$ .

### 5.5.2 $^{15}\text{N}$ NMR of stationary samples of $^{15}\text{N}$ -labelled anil\*Co(DH)<sub>2</sub>Cl (II)

The analyses of the  $^{15}\text{N}$  NMR spectra of II were conducted in much the same manner as for I, so a full description is not given here. However, there are some substantial differences in the analysis of the spectra for I and II that should be addressed. For instance, the least shielded regions of the  $^{15}\text{N}$  powder patterns at both applied magnetic fields (Fig.5.7) are "smeared out", with no well-defined splittings, making the fitting of this spectrum difficult. The lack of spectral definition may be due to incompletely decoupled dipolar interactions between  $^{15}\text{N}$  and  $^1\text{H}$  ( $R_{\text{dd}} > 12$  kHz). Nonetheless, the regions of the powder pattern corresponding to  $\delta_{22}$  and  $\delta_{33}$  display well-defined splittings which are easily measured, and from these the approximate orientations of the CS tensor can be ascertained. No experimental information is available on the orientation of CS tensors in uncoordinated aniline; therefore, assumptions about the orientation dependence of the chemical shielding cannot be made as easily as in the case of I.

From the parameters obtained from analysis of the  $^{15}\text{N}$  MAS NMR spectra, and from measurement of the dipolar splittings, the final parameters defining the  $^{15}\text{N}$  CS tensor of the aniline nitrogen in II are given in Table 5.3. The span of the CS tensor decreases by over 300 ppm relative to I. Splittings in the  $\delta_{22}$  and  $\delta_{33}$  regions are decreased when a positive  $^1J(^{59}\text{Co}, ^{15}\text{N})$  is used for spectral simulations; accordingly, the value of  $^1J(^{59}\text{Co}, ^{15}\text{N})$  is negative as in I. The angles  $\beta^{\text{C}} = 88^\circ$  and  $\alpha^{\text{C}} = 3^\circ$  reveal that  $\delta_{11}$  is aligned approximately along the direction of the Co, N bond, with  $\delta_{33}$  nearly perpendicular to the dipolar vector. It is likely that one of  $\delta_{22}$  or  $\delta_{33}$  bisects the H-N-H bond angle, with the other component perpendicular to this

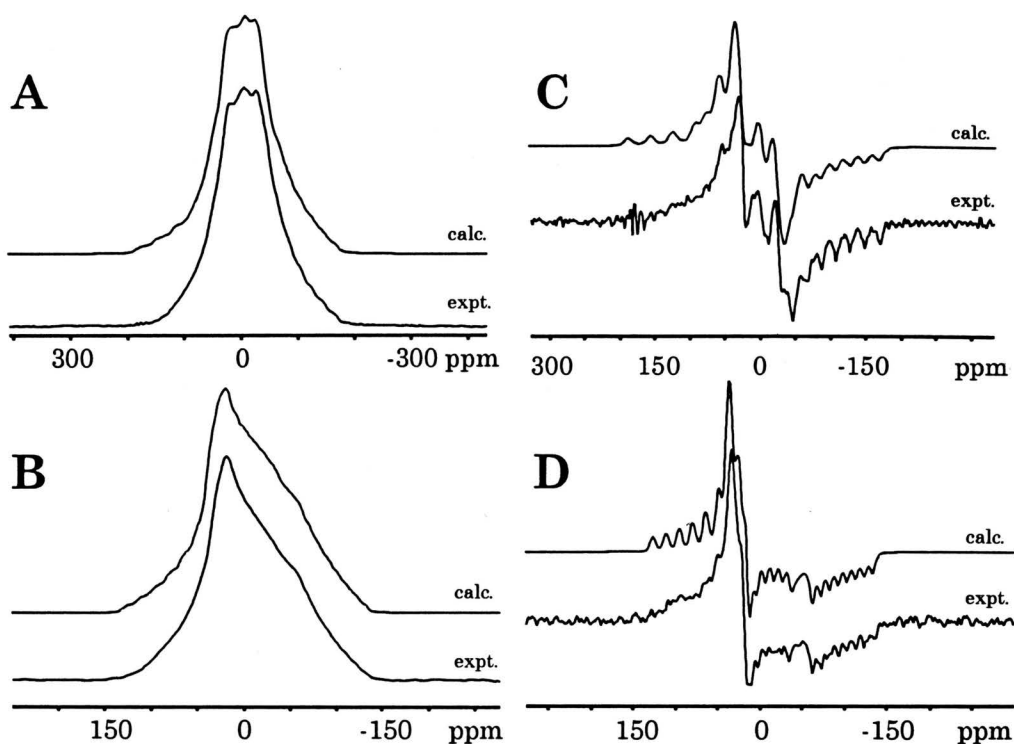


**Figure 5.7** Experimental and calculated  $^{15}\text{N}$  NMR spectra of stationary samples of  $^{15}\text{N}$ -enriched  $\text{anil}^*\text{Co}(\text{DH})_2\text{Cl}$  at (A) 4.7 T and (B) 9.4 T. Corresponding first-derivative spectra are presented in (C) and (D).

direction. Again, no further information on the orientations of the other principal components with respect to the molecular frame can be gained from analysis of these spectra, although *ab initio* calculations of the  $^{15}\text{N}$  CS tensors in **II**, presented in Section 5.6, suggest possible tensor orientations.

### 5.5.3. $^{15}\text{N}$ NMR of stationary samples of $^{15}\text{N}$ -enriched $\text{py}^*\text{Co}(\text{DH})_2\text{CH}_3$ (**III**)

Due to the small amount of sample available, it was not possible to obtain solid-state  $^{15}\text{N}$  NMR spectra of the same quality (i.e., higher signal-to-noise ratio) as those for **I** and **II**. As a result, dipolar splittings are not clearly resolved in the

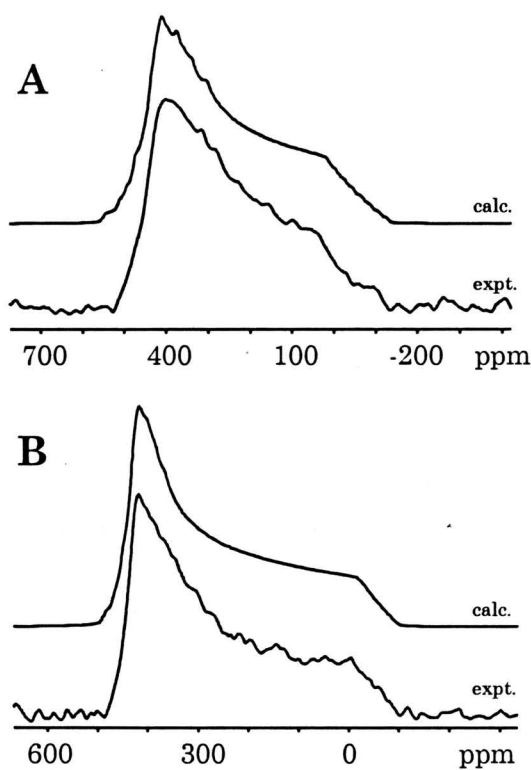


**Figure 5.8** Experimental and calculated  $^{15}\text{N}$  NMR spectra of stationary samples of  $^{15}\text{N}$ -enriched  $\text{py}^*\text{Co}(\text{DH})_2\text{CH}_3$  at (A) 4.7 T and (B) 9.4 T.

stationary powder patterns at either field. Nonetheless, it was still possible to obtain spectra which allow for extraction of fairly accurate CS tensor components and prediction of the orientation of the  $^{15}\text{N}$  CS tensor. The experimental and calculated  $^{15}\text{N}$  NMR spectra of **III** at two fields are pictured in Fig. 5.8. Due to the aforementioned low S/N ratios, first derivative spectra are not shown since they serve no purpose in this analysis. Final parameters from this analysis are given in Table 5.3.

The span of the  $^{15}\text{N}$  CS tensor is very similar to that observed in **I**, indicating that the presence of the axial methyl group does not influence the magnitude of the

span significantly. However, the appearance of the spectra indicates that the  $^{15}\text{N}$  CS tensor is very close to axial symmetry, as indicated by the skew,  $\kappa = 0.97(5)$ . The pyridine nitrogen nucleus in **III** is deshielded by ca. 58 ppm ( $\delta_{\text{iso}} = 265(4)$  ppm) with respect to that in **I**. The intermediate component,  $\delta_{22}$ , is 103 ppm larger in **III**, whereas  $\delta_{11}$  and  $\delta_{33}$  are about 35 ppm larger. Despite the absence of resolved dipolar splittings, the spectra can only be simulated with  $\beta^{\text{C}}$  set to  $90^{\circ}(4^{\circ})$ , indicating that the orientation of the CS tensor is similar to that in **I**. Variations in  $\alpha^{\text{C}}$  from  $0^{\circ}$  to  $90^{\circ}$  do not seem to have any discernible effects on spectral appearance, since  $\delta_{11}$  is very close to  $\delta_{22}$ . Changing the sign of  $^1J(^{59}\text{Co}, ^{15}\text{N})$  from negative to positive does not have a drastic effect on the spectral simulations, but given the sign of the previously determined  $J$ -couplings it is assumed that the sign of  $^1J(^{59}\text{Co}, ^{15}\text{N})$  in **III** is negative.

#### 5.5.4. $^{15}\text{N}$ NMR of stationary samples of $^{15}\text{N}$ -enriched $\text{py}^*\text{Co}(\text{DH})_2\text{Br}$ (**IV**)

The small amount of sample again limited the quality of the acquired  $^{15}\text{N}$  NMR spectra; however, at 9.4 T, it was possible to partially resolve the dipolar splittings and therefore obtain accurate information on the CS tensor orientation and the sign of  $^1J(^{59}\text{Co}, ^{15}\text{N})$ . The  $^{15}\text{N}$  CS tensor parameters and orientation are almost identical to those of **I**. The similarity of all of the NMR parameters of **I** and **IV** from spectra of both spinning and stationary samples indicates that the substitution of bromine for chlorine into the axial position has very little effect on the molecular structure of the cobaloxime. This is further affirmed by the marked sensitivity of the CS and quadrupolar parameters to changes in both the axial anions ( $\text{CH}_3^-$ ) and neutral ligands (aniline). The similarity between the  $^{15}\text{N}$  NMR

spectra of spinning and stationary samples of I and IV stands in stark contrast to the  $^{31}\text{P}$  CPMAS NMR spectra of  $\text{PPh}_3\text{Co}(\text{DH})_2\text{Cl}$  and  $\text{PPh}_3\text{Co}(\text{DH})_2\text{Br}$  in Chapter 4, where the  $^{31}\text{P}$  spectra of the latter compound could not be calculated using first-order perturbation theory.

## 5.6 *Ab initio* Chemical Shielding Calculations

In this section, comparison is made between experimental and calculated nitrogen CS tensors (Table 5.4). Some of the theoretical results are in good qualitative agreement with experiment. The calculations correctly predict a negative coordination shift (i.e. decreased nitrogen shielding in the free ligand) for I, II and III, and larger nitrogen CSA for uncoordinated pyridine with respect to that in I and III. Qualitative explanations are given for the observed changes in the nitrogen CS tensors upon coordination to the cobalt atom.

The RHF calculations overestimate the span of the  $^{15}\text{N}$  CS tensor in I by over 100 ppm, with most of the contribution to the span arising from the  $\delta_{33}$  component, which is calculated to be ca. 75 ppm less than the experimental value (note, a smaller chemical shift principal component indicates shielding at the nitrogen nucleus along the direction of that component; conversely, an increase in the principal component indicates deshielding along that direction). Moreover, the nitrogen nucleus is predicted to be shielded by 44 ppm (6-31G\*) and 20 ppm (6-311G\*). In the B3LYP/6-311G\* calculations, the span is closer to the experimental value, resulting from an overestimation of  $\delta_{33}$ , and a corresponding increase in  $\delta_{\text{iso}}$  by ca. 70 ppm. The skews predicted by all of the calculations are in

reasonable agreement with the experimental skew, confirming that the quasi-unique component is  $\delta_{33}$ . Given that these calculations are conducted on large, isolated molecules using a number of approximations (given in the experimental section), the qualitative agreement between theory and experiment is quite reasonable.

**Table 5.4:** Comparison of experimental and calculated  $^{15}\text{N}$  chemical shielding tensors.<sup>a</sup>

	$\delta_{\text{iso}}$ (ppm)	$\Omega$ (ppm)	$\kappa$	$\delta_{11}$ (ppm)	$\delta_{22}$ (ppm)	$\delta_{33}$ (ppm)
<b>py*Co(DH)<sub>2</sub>Cl (I)</b>						
Experimental	207(1)	484(2)	0.70(2)	393	320	-92
RHF/6-31G*	163.7	595.3	0.43	418.6	249.3	-176.7
RHF/6-311G*	187.7	622.8	0.44	453.3	279.3	-169.5
B3LYP/6-311G*	272.6	505.5	0.85	453.7	415.9	-51.8
<b>anil*Co(DH)<sub>2</sub>Cl (II)</b>						
Experimental	-7.0(3.0)	175(3)	0.18(2)	75	3.5	-100
RHF/6-31G*	-88.8	246.2	-0.30	46.5	-113.1	-199.7
RHF/6-311G*	-79.6	242.2	-0.23	50.9	-98.3	-191.3
B3LYP/6-311G*	7.8	83.2	0.74	39.2	28.3	-44
<b>py*Co(DH)<sub>2</sub>CH<sub>3</sub> (III)</b>						
Experimental	265(4)	488(10)	0.97(8)	430	423	-58
RHF/6-31G*	230.5	541.6	0.72	436.5	360	-105.1
RHF/6-311G*	256.8	569.8	0.73	472.3	395.7	-97.5
B3LYP/6-311G*	290.6	533.1	0.75	490.9	423.1	-42.2

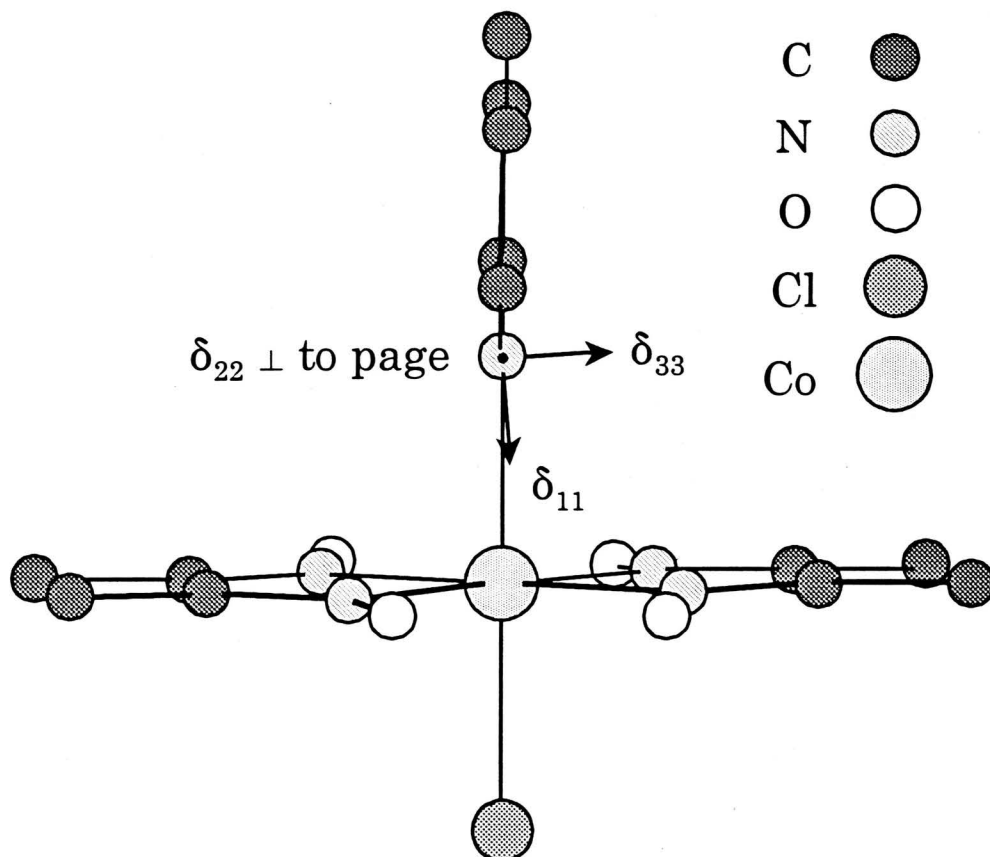
(continued next page)

Table 5.4 (continued)

	$\delta_{\text{iso}}$ (ppm)	$\Omega$ (ppm)	$\kappa$	$\delta_{11}$ (ppm)	$\delta_{22}$ (ppm)	$\delta_{33}$ (ppm)
pyridine						
Experimental <sup>b</sup>	299.2	782.0	0.44	633	414	-149
Experimental <sup>c</sup>	318.9	622.0	0.46	582	415	-40
RHF/6-31G*	321.2	694.2	0.40	623	413	-72
RHF/6-311G*	352.8	737.5	0.39	674	448	-64
B3LYP/6-311G*	352.3	719.5	0.34	671	435	-49
LORG/[3s3p1d/2s] <sup>d</sup>	316.5	664.0	0.30	616	383	-49
SOLO/[3s3p1d/2s] <sup>d</sup>	337.8	691.0	0.40	638	430	-54
IGLO/[3s3p1d/2s] <sup>d</sup>	348.7	721.0	0.43	658	451	-63
aniline						
Experimental <sup>e</sup>	58.2	--	--	--	--	--
RHF/6-31G*	26.3	75.5	0.79	54	46	-21
RHF/6-311G*	34.7	91.2	0.86	67	61	-24
B3LYP/6-311G*	55.8	102.9	0.92	92	87	-11

- a.* Absolute chemical shieldings,  $\sigma$ , were converted to the  $^{15}\text{N}$  chemical shift scale with the formula  $\sigma_{\text{ref}} - \sigma$ , where  $\sigma_{\text{ref}} = 244.6$  ppm, the absolute chemical shielding of  $\text{NH}_3$  at  $20^\circ\text{C}$ .<sup>287</sup>
- b.* Data from ref. 289.
- c.* Data from ref. 290.
- d.* Data from ref. 295.
- e.* Data from ref. 291.

The most interesting results of these calculations are the CS tensor orientations in the molecular frame. In the RHF calculations with both basis sets,  $\delta_{11}$  is oriented  $0.7^\circ$  from the Co, N bond, in good agreement with the experimentally determined orientations (see Fig. 5.9). The most shielded component,  $\delta_{33}$ , is found to



**Figure 5.9** Nitrogen chemical shielding tensor orientation in  $^{15}\text{N-py}^*\text{Co}(\text{DH})_2\text{Cl}$  as determined by experimental methods and GIAO calculations. Side view of the molecule, with the pyridine ring perpendicular to the page.

lie perpendicular to the pyridine ring ( $88.2^\circ$ ), in agreement with the experimental observation of  $\beta^{\text{C}} = 85^\circ$  and concomitant with the experimentally determined CS tensor orientations in uncoordinated pyridine.<sup>289,290</sup> This leaves  $\delta_{22}$  oriented approximately in the ring plane ( $0.9^\circ$ ). The B3LYP/6-311G\* calculation, however, predicts that  $\delta_{22}$  is  $0.7^\circ$  from the Co, N bond, with  $\delta_{11}$  at  $0.7^\circ$  with respect to the pyridine ring, corresponding to polar angles of  $\beta^{\text{C}} = 90^\circ$  and  $\alpha^{\text{C}} = 90^\circ$ . Spectral simulations were attempted with this relative tensor orientation without success, suggesting that the RHF calculations correctly predict the  $^{15}\text{N}$  CS tensor orientations.

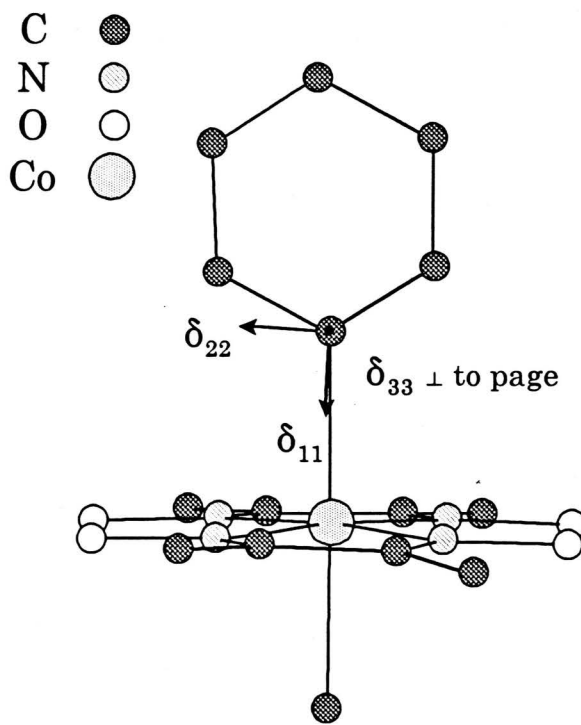


**Figure 5.10** Nitrogen chemical shielding tensor orientation in  $^{15}\text{N-py}^*\text{Co}(\text{DH})_2\text{CH}_3$  as determined by experimental methods and GIAO calculations. Side view of the molecule, with the pyridine ring in the plane of the paper.

The best correspondence between theory and experiment is found for III.

RHF and DFT calculations all come very close to predicting the span, skew and isotropic shifts, with RHF calculations underestimating  $\delta_{33}$ , and DFT calculations overestimating  $\delta_{33}$ . Once again, the RHF calculations predict that  $\delta_{11}$  is along the Co, N bond, with  $\delta_{33}$  perpendicular to the pyridine ring plane, and  $\delta_{22}$  in the plane of the ring (Fig. 5.10). The B3LYP/DFT calculation places  $\delta_{22}$  along the Co, N bond, and  $\delta_{11}$  in the ring plane, leaving  $\delta_{33}$  perpendicular to the ring plane. The predicted orientations from RHF calculations are in excellent agreement with the experimental results. The calculations also predict the overall deshielding of the

nitrogen nucleus in **III** compared to **I**, in agreement with experimental results.

In order to qualitatively explain the nitrogen CS tensor orientations in **I** and **III**, it is worthwhile to consider the shielding in uncoordinated pyridine. *Ab initio* nitrogen CS tensors in pyridine are in very good agreement with the experimental values of Solum and co-workers,<sup>290</sup> which is a more recent solid-state <sup>15</sup>N NMR measurement than that of Schweitzer and Spiess.<sup>289</sup> There is also close agreement with the nitrogen CS tensors of pyridine calculated using other methods (Table 5.4).<sup>295</sup> All of the calculations predict a larger span and deshielding at the uncoordinated pyridine nitrogen relative to **I** and **III**, in accordance with experimentally observed results. The predicted orientation of the CS tensor has  $\delta_{33}$  perpendicular to the ring plane, and  $\delta_{22}$  and  $\delta_{11}$  in the plane with  $\delta_{22}$  bisecting the ring (in the direction of the lone pair of electrons at nitrogen, Fig. 5.11). Upon coordination, the least shielded component is now in the direction of the nitrogen lone pair, with  $\delta_{22}$  in the ring plane. The orientation of  $\delta_{33}$  remains perpendicular to the pyridine ring.

Solum and co-workers<sup>290</sup> have explained the nitrogen shielding tensor orientation in pyridine by considering contributions to chemical shielding from mixing of the ground- and excited-state molecular orbitals by the angular momentum operators in Ramsey's equations for chemical shielding (see Chapter 3).<sup>26</sup> The paramagnetic contribution to shielding is inversely proportional to the energy difference between the relevant ground- and excited-state orbitals; thus, the smaller the energy difference, the larger the paramagnetic shielding contribution (i.e., deshielding) at the nucleus. Due to the nature of the angular momentum operators,

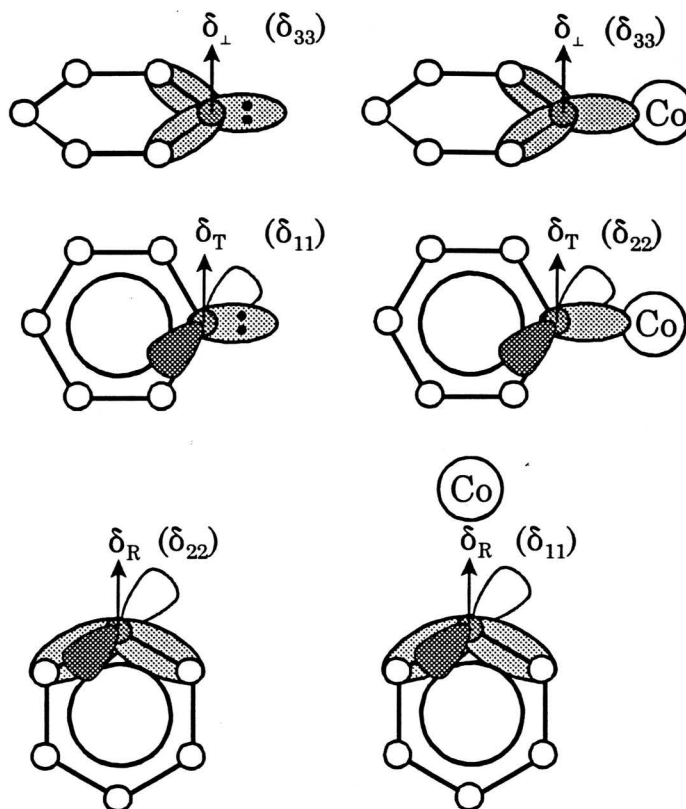


**Figure 5.11** Perpendicular ( $\delta_{\perp}$ ), tangential ( $\delta_{\text{T}}$ ) and radial ( $\delta_{\text{R}}$ ) components of the nitrogen shielding tensor in pyridine. See text for discussion.

the principal components of the CS tensor are oriented perpendicular to the molecular orbitals which mix (*vide infra*).

In pyridine, three generalized CS principal components are shown in Fig.5.11:  $\delta_{\perp}$ , which is perpendicular to the ring plane;  $\delta_{\text{T}}$ , which is in the plane of the ring and perpendicular to the nitrogen lone pair of electrons (tangential component); and  $\delta_{\text{R}}$ , which is along the direction of the lone pair and also in the plane of the ring (radial component).<sup>290</sup> The tangential component is dominated by contributions from the  $n\text{-}\pi^*$  transition (mixing orbitals are highlighted in the figure), the radial

component by the  $\sigma_{\text{N-C}} \rightarrow \pi^*$  transition, and the perpendicular component by the  $\sigma$ -framework of the pyridine ring. Since the  $n \rightarrow \pi^*$  transition energy is the smallest, the largest component (direction of least shielding),  $\delta_{11}$ , is oriented in the tangential direction. The  $\sigma_{\text{N-C}} \rightarrow \pi^*$  energy is higher, and accordingly,  $\delta_{22} = \delta_{\text{R}}$ . Finally, there are no low-lying transitions contributing to paramagnetic deshielding perpendicular to the plane of the nitrogen ring, so  $\delta_{33} = \delta_{\perp}$ , and is much less than  $\delta_{11}$  and  $\delta_{22}$ .

Upon coordination to cobalt, the nitrogen lone pair is occupied in a high-energy bonding orbital with the cobalt nucleus. The absence of the low-energy  $n \rightarrow \pi^*$  transition means that the nitrogen nucleus is generally more shielded in **I** and **III** than in pyridine. The nitrogen nucleus is deshielded along the direction of the Co, N bond. Here,  $\delta_{11} = \delta_{\text{R}}$ , with contributions from  $\sigma_{\text{N-C}} \rightarrow \pi^*$  transition dominating. The tangential direction is not as deshielded as in the uncoordinated pyridine, since it is dominated by the  $\sigma_{\text{N-Co}} \rightarrow \pi^*$  transition, which is slightly higher in energy than the corresponding  $\sigma_{\text{N-C}} \rightarrow \pi^*$  transition; thus,  $\delta_{22} = \delta_{\text{T}}$ . Finally, the orientation of  $\delta_{33}$  remains the same, since there are still no low-energy transitions contributing to paramagnetic deshielding.

The qualitative molecular orbital picture above can also be used to rationalize the differences in the principal components between **I** and **III**. The  $\delta_{11}$  and  $\delta_{22}$  components are larger in **III**; notably  $\delta_{22}$  is increased by 123 ppm (Table 5.4). The presence of the axial methyl group results in a decrease in the energy of the  $\sigma_{\text{N-C}} \rightarrow \pi^*$  and  $\sigma_{\text{N-Co}} \rightarrow \pi^*$  transitions, resulting in deshielding in the  $\delta_{\text{R}}$  and  $\delta_{\text{T}}$  directions. There is increased paramagnetic deshielding in the direction of  $\delta_{22}$ , since the  $\sigma_{\text{N-C}} \rightarrow \pi^*$  and  $\sigma_{\text{N-Co}} \rightarrow \pi^*$  transitions are similar in energy.

Calculations for **II** yield NMR parameters which are somewhat further from experimental results than those for **I**. However, the N, H bond lengths reported with the crystal structure were used at the aniline nitrogen atom. Calculations are currently underway which incorporate N, H bond lengths from the structure of uncoordinated aniline.<sup>284</sup> RHF calculations overestimate the span by more than 65 ppm, and the DFT calculation underestimates the span by 92 ppm. In the former case, the  $\delta_{22}$  and  $\delta_{33}$  components are much less than the experimental values, accounting for the larger span and increased nitrogen shielding. The DFT calculation suffers from an overestimation of  $\delta_{33}$ , and an underestimation of  $\delta_{11}$ , resulting in the reduced span. None of the calculations predict the skew accurately.

RHF calculations once again predict a CS tensor orientation in good agreement with experimental data, with  $\delta_{11}$  oriented  $4.7^\circ$  from the Co, N bond. The  $\delta_{33}$  component is predicted to bisect the H-N-H bond angle of the aniline, and lies perpendicular to the Co, N bond (Fig. 5.12). The B3LYP calculation yields a tensor orientation that seems to have very little correspondence to the geometry of the molecule; thus, it is suggested that the orientations predicted by the RHF calculations are likely correct. From the *ab initio* calculations on **I**, **II** and **III**, it is seen that the RHF level of theory is superior to the DFT/B3LYP method for systems such as these.

At this time, there is no nitrogen chemical shielding tensor information for aniline, though there have been shielding tensors calculated with IGLO (individualized gauge for local orbitals) methods.<sup>296</sup> Our calculations reveal that  $\delta_{11}$  is within three degrees of being perpendicular to the ring plane (Fig. 5.13). All

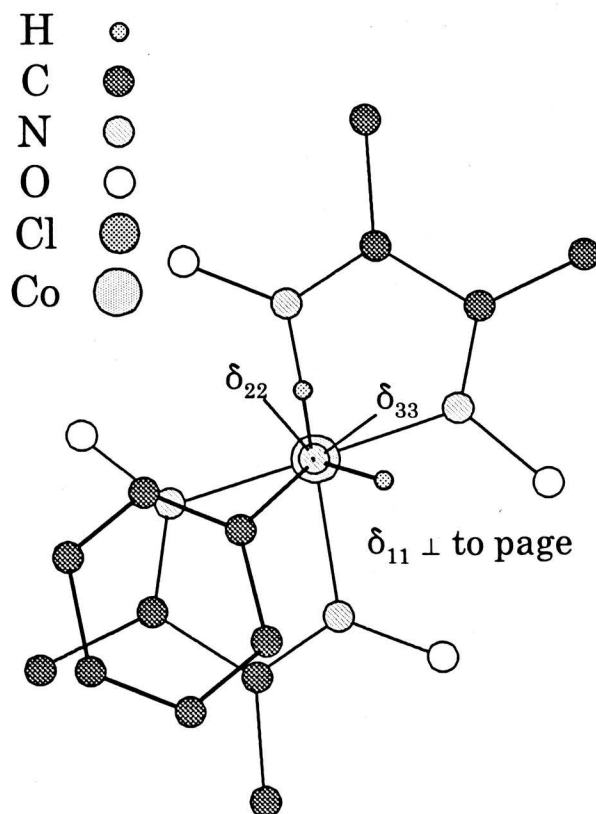


**Figure 5.12** Nitrogen chemical shielding tensor orientation in  $^{15}\text{N-anil*Co}(\text{DH})_2\text{Cl}$  as determined by experimental methods and GIAO calculations. Top view of the molecule, with the dimethylglyoxime moieties in the plane of the page.

calculations predict that  $\delta_{22}$  is  $2.1^\circ$  out of the aromatic plane, and sits perpendicular to the N, C bond. Finally,  $\delta_{33}$  is seen to bisect the H-N-H bond angle, and is approximately  $6^\circ$  from the plane of the ring. Thus, according to theory the nitrogen CS tensor of aniline changes only slightly upon coordination in a cobaloxime complex, with  $\delta_{11}$  assuming an orientation along the direction of the nitrogen lone pair (and the Co, N bond).

A qualitative explanation of the CS tensor orientations in aniline and in **II** is

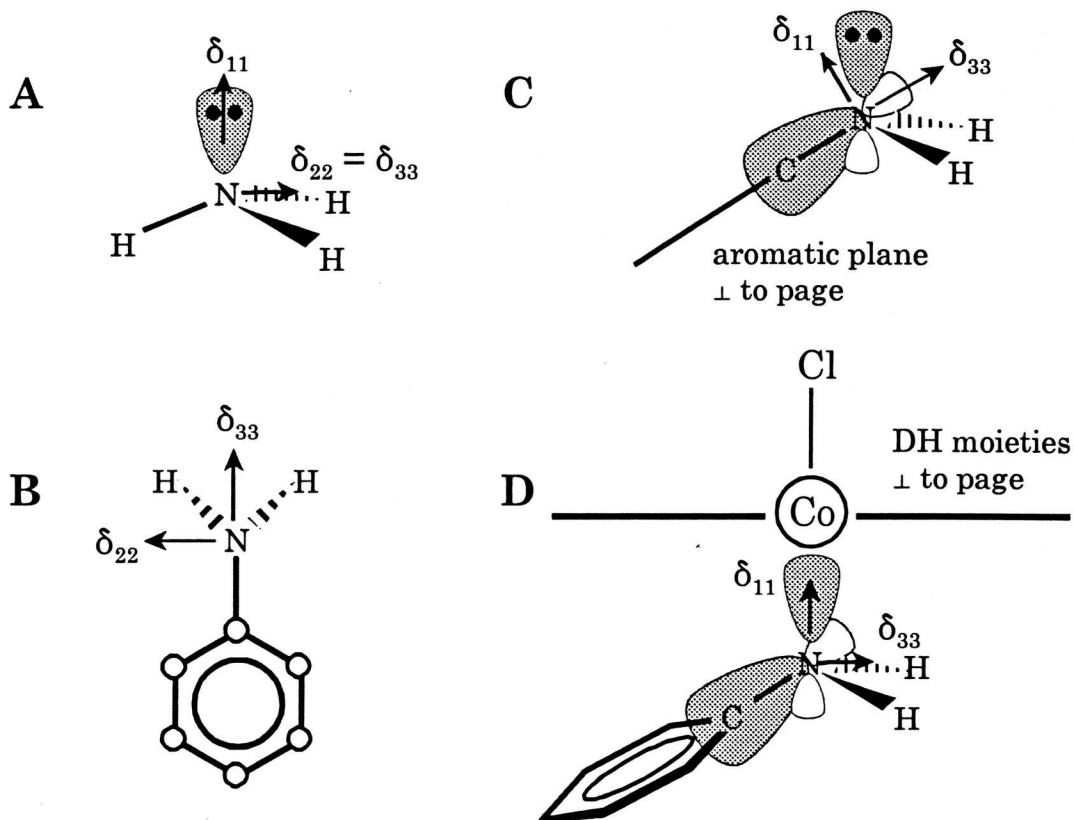


**Figure 5.13** (A) The nitrogen CS tensor in ammonia. (B) The nitrogen CS tensor in aniline, top view. (C) The nitrogen CS tensor in aniline, side view, aromatic ring is perpendicular to page. (D) The nitrogen CS tensor in anil\*Co(DH)<sub>2</sub>Cl (II), DH moieties perpendicular to the page, with slight twisting of the aromatic ring.

somewhat more complicated than for pyridine, I and III, since there is not a perpendicular arrangement of molecular orbitals and CS tensor principal components. As a starting point, it is useful to consider ammonia, which has chemical shift components  $\delta_{11} = 26.9$  ppm and  $\delta_{22} = \delta_{33} = -13.4$  ppm.<sup>297</sup> The least shielded component of the chemical shift tensor,  $\delta_{11}$ , is along the direction of the lone pair, and is dominated by  $\sigma \rightarrow \sigma^*$  transitions (Fig. 5.13A). There is even less of a paramagnetic shielding contribution perpendicular to the lone pair, with  $\delta_{22}$  and  $\delta_{33}$  dominated by higher energy  $n \rightarrow \sigma^*$  transitions. The lone pair in ammonia has very

little  $p$ -character,<sup>273</sup> and as a result, the nitrogen nucleus in ammonia is quite shielded.

In aniline, none of the components is along the direction of the lone pair. There is increased  $p$ -character at the nitrogen atom, since it is bound to an aromatic carbon (Fig. 5.13B,C). Thus  $\delta_{11}$  and  $\delta_{22}$  are similar in magnitude, with  $\delta_{11}$  governed by lower energy  $\sigma_{N-C} \rightarrow \sigma^*$  and  $\sigma_{N-C} \rightarrow \pi^*$  transitions, and  $\delta_{22}$  by a low energy  $n \rightarrow \pi^*$  transition.<sup>261,296</sup> The nitrogen nucleus of aniline is therefore deshielded compared to that of ammonia. In the direction of the N, C bond, there are no low-energy transitions contributing to paramagnetic shielding, and hence  $\delta_{33}$  is oriented in this direction.

When aniline is coordinated to cobalt, the magnitude of  $\delta_{11}$  does not change significantly, but it is oriented along the direction of the Co, N bond (Fig 5.13D). Magnetic shielding increases perpendicular to the Co, N bond, with reductions in both  $\delta_{22}$  and  $\delta_{33}$ . This is due to the presence of the higher energy  $\sigma_{N-Co} \rightarrow \pi^*$  transition, which accounts for the decreased isotropic shift in II relative to unbound aniline. There is still some paramagnetic shielding contribution from the  $\sigma_{N-C} \rightarrow \pi^*$  transition, which accounts for  $\delta_{11}$  being along the Co, N bond, and the large difference between  $\delta_{22}$  and  $\delta_{33}$ .

## 5.7 Conclusions

The analysis of solid-state  $^{15}\text{N}$  NMR spectra of both spinning and stationary samples of the  $^{15}\text{N}$ -enriched cobaloximes has yielded much information on the  $^{59}\text{Co}$ ,  $^{15}\text{N}$  spin pair. The analysis of solid-state NMR spectra of a spin-1/2 nucleus coupled

to a quadrupolar nucleus once again demonstrates that much more information can be gained from such spectra which is not available from analogous solution NMR experiments. The magnitudes and signs of four new values of  $^1J(^{59}\text{Co}, ^{15}\text{N})$  have been determined using a combination of  $^{15}\text{N}$  MAS NMR spectra influenced by residual dipolar coupling and  $^{15}\text{N}$  NMR spectra of stationary samples exhibiting dipolar splittings resulting from coupling to the  $^{59}\text{Co}$  nucleus. Information is also provided on the magnitude of the quadrupolar interaction and orientation of the EFG tensor at the  $^{59}\text{Co}$  nucleus.

The orientations and chemical shift parameters of four  $^{15}\text{N}$  CS tensors have been determined; this is the first report of  $^{15}\text{N}$  CS tensor orientations for a nitrogen nucleus directly bound to a transition metal centre. As well, since nitrogen shielding tensors have not been determined for uncoordinated aniline, this is a preliminary glimpse at what the magnetic shielding may be like in this molecule. The NMR parameters elicited from these spectra are very dependent upon the local and overall molecular geometry, as well as electronic structure. The nitrogen nuclei in pyridine and aniline experience greater shielding upon coordination to the cobalt centre, which is explained qualitatively through the chemical shielding equations of Ramsey. This negative nitrogen coordination shift is analogous to the phosphorus coordination shift observed for the phosphite-substituted cobaloximes (Chapter 4).

Comparison of experimental CS tensors and those obtained via *ab initio* methods aids in confirming CS tensor orientations in the cobaloximes. There is considerable disparity between the experimental and theoretical CS principal components; nonetheless, the qualitative predictions made by the theoretical results

(notably, the RHF calculations) are in agreement with our experimental observations. *Ab initio* calculations of magnetic shielding are clearly very useful for predicting the orientations of the CS tensors, as well as providing explanations as to why a nucleus is shielded or deshielded in a particular manner.

Many systems like the cobaloximes that have been thoroughly investigated by a variety of methods, such as solution NMR, X-ray crystallography, IR and Raman spectroscopy, etc. have not been characterized by solid-state NMR techniques. It is hoped that this work will encourage further effort in determining NMR parameters from these solid-state methods, since they are capable of evoking detailed information on complex molecules.

On a final note,  $^{13}\text{C}$  CPMAS NMR spectra have been acquired for a  $^{13}\text{C}$ -labelled sample of **III**. A brief discussion of this spectrum is given in Appendix B.

## Chapter 6

### Ongoing Projects and Future Work

#### 6.1 Aluminum and Gallium Chemical Shielding Anisotropy

Due to the deficiency of information on chemical shielding anisotropy of group 13 elements such as aluminum and gallium, several new examples are currently being investigated in our laboratory. Since octahedral and tetrahedral aluminum complexes have already been considered (cf. Chapter 3), it is suggested that NMR studies be extended to include aluminum in a different coordination environment. An interesting candidate is aluminum phthalocyanine chloride (Fig. 6.1), which has aluminum in a pentacoordinate environment. Isostructural dyes containing metals such as cobalt and chromium<sup>298</sup> are very common, but are more toxic than the related aluminum complexes.<sup>299</sup> Recently, a multinuclear solution and solid-state NMR study of aluminum (III) complexes of azo dyes was reported.<sup>299</sup> Aluminum-27 MAS NMR spectra of these octahedral complexes are presented which exhibit line shapes influenced by the second-order quadrupolar interaction; however, no spectra of stationary samples are reported. Thus, it is proposed that <sup>27</sup>Al studies be carried out on these systems. Another group of molecules under investigation are aluminum halide phosphines (i.e., X<sub>3</sub>AlPR<sub>3</sub>; X = Cl, Br; R = Ph, Me, Bu, etc.). Since the aluminum and phosphorus are directly bonded, it is possible to obtain information on the chemical shift and EFG tensors, from both <sup>27</sup>Al and <sup>31</sup>P solid-state NMR experiments.

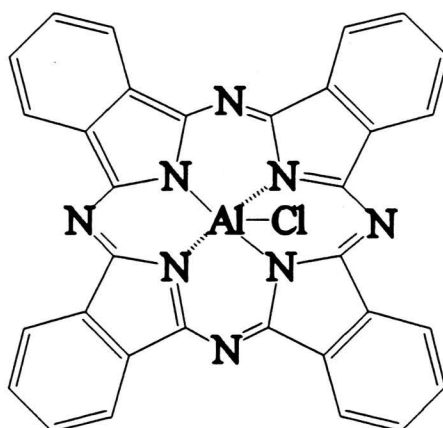


**Figure 6.1** Structure of aluminum phthalocyanine.

Work is currently underway investigating the gallium-69 and gallium-71 solid-state NMR spectra of complexes analogous to those discussed in Chapter 3 (*vide infra*). Gallium-69 is the abundant isotope (60.2 % n.a.), but has a larger quadrupole moment ( $Q = 0.19 \times 10^{-28} \text{ m}^2$ ); thus, NMR studies are usually conducted on gallium-71 (39.8 % n.a.,  $Q = 0.12 \times 10^{-28} \text{ m}^2$ ), which also has a larger magnetogyric ratio ( $\gamma_{\text{Ga-71}} = 1.27\gamma_{\text{Ga-69}}$ ). The gallium quadrupole moments are comparable to that of aluminum; however, since  $^{69}\text{Ga}$  and  $^{71}\text{Ga}$  are spin-3/2 nuclei, the second-order quadrupole broadening of the central transition is much greater than in corresponding  $^{27}\text{Al}$  spectra.<sup>55,105</sup> It is not unusual for the line widths to exceed 300 kHz, rendering acquisition of such spectra difficult. As a result, there are not many reports of solid-state  $^{69/71}\text{Ga}$  NMR compared to  $^{27}\text{Al}$  NMR, despite the common substitution of gallium for aluminum in many systems, such as garnets and zeolites.<sup>300,301</sup> There is a single report of gallium chemical shielding anisotropy, from a single-crystal  $^{71}\text{Ga}$  NMR study of the garnet  $\text{Y}_3\text{Ga}_5\text{O}_{12}$ .<sup>302</sup>

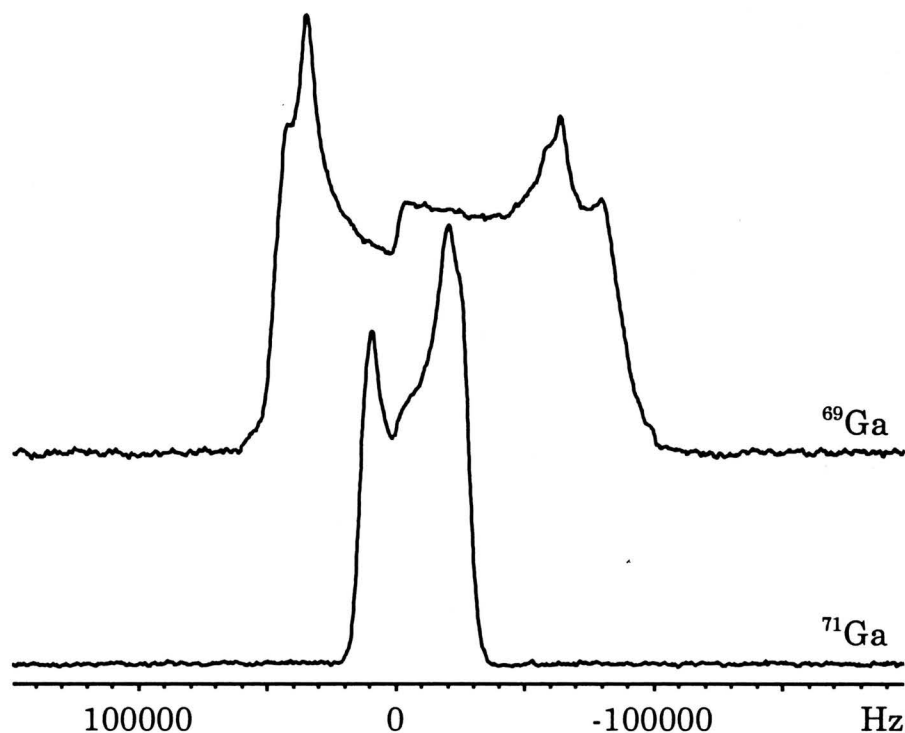


**Figure 6.2** Solid-state  $^{69}\text{Ga}$  and  $^{71}\text{Ga}$  NMR spectra of stationary samples of  $\text{Ga}(\text{acac})_3$  at 9.4 T.

Preliminary studies have been conducted on tris(acetylacetonate)gallium(III),  $\text{Ga}(\text{acac})_3$ , and further work will include  $\text{Ga}(\text{trop})_3$  and  $\text{Cl}_3\text{GaOPCl}_3$ . Solid-state  $^{69}\text{Ga}$  and  $^{71}\text{Ga}$  NMR spectra of  $\text{Ga}(\text{acac})_3$  (not recrystallized) are pictured in Fig. 6.2. Gallium spectra were acquired with a simple Hahn-echo sequence,  $\pi/2 - \tau_1 - \pi - \tau_2 - \tau_{\text{AQ}}$ . It is apparent from the  $^{69}\text{Ga}$  NMR spectrum that there are two sites present. The crystal structure of  $\text{Ga}(\text{acac})_3$  recrystallized from methanol (space group  $P2_1/c$ ) reveals that there is only one crystallographically distinct site per unit cell,<sup>303</sup> which would result in a single transition in the gallium NMR spectrum. NMR spectra of the recrystallized complex will be acquired in the near future. Rough analysis of these spectra yield  $C_Q(^{69}\text{Ga}) = 9.3(5)$  MHz,  $C_Q(^{71}\text{Ga}) = 5.9(5)$  MHz,  $\delta_{\text{iso}} = -2.5(8)$  ppm,  $\Omega = 25(8)$  ppm and  $\kappa = 1.0(1)$ . The chemical shifts are referenced with respect to 1 M

$\text{Ga}(\text{NO}_3)_3$  (aq). The values of  $C_Q$  are in reasonable agreement with those determined in a  $^{13}\text{C}$  solution NMR relaxation study, where  $C_Q(^{69}\text{Ga}) = 11$  MHz and  $C_Q(^{71}\text{Ga}) = 6.9$  MHz.<sup>304</sup> The relative orientation of the EFG and CS tensors is given by  $\alpha = 90^\circ$ ,  $\beta = 90^\circ$  and  $\gamma = 0^\circ$ , which corresponds to  $\delta_{11}$  aligned along the direction of  $V_{33}$ . This orientation is the same as that observed for the aluminum CS tensor in  $\text{Al}(\text{acac})_3$ . The acquisition of  $^{69}\text{Ga}$  and  $^{71}\text{Ga}$  NMR spectra at 9.4 T is akin to having  $^{69}\text{Ga}$  spectra acquired at 9.4 T and 23.5 T (i.e., the effects of second-order quadrupolar broadening in the  $^{69}\text{Ga}$  NMR spectrum would be reduced at 23.5 T, such that the spectrum would appear as a  $^{71}\text{Ga}$  NMR spectrum at 9.4 T, in the absence of gallium CSA). Since the  $C_Q$  and  $\eta$  are directly related in each spectrum, the effects of gallium CSA can be accurately determined by comparison of calculated  $^{69}\text{Ga}$  and  $^{71}\text{Ga}$  NMR spectra.

## 6.2 Solid-State $^{31}\text{P}$ NMR Investigations of $^{31}\text{P}$ , $^{59}\text{Co}$ Spin Pairs

Investigations of spin interactions of the isolated  $^{31}\text{P}$ ,  $^{59}\text{Co}$  spin pair have been extended (cf. Chapter 4) to include exohedrally-substituted organometallic buckminsterfullerenes,<sup>305</sup> such as  $(\text{PPh}_3)_2(\text{NO})\text{Co}(\eta^2\text{-C}_{60})$  (Fig. 6.3), and the starting material for synthesis of this complex,  $(\text{PPh}_3)_3\text{Co}(\text{NO})$ .<sup>306,307</sup> The  $^{31}\text{P}$  CPMAS NMR spectra of these two complexes are pictured in Fig. 6.4. Solid-state NMR studies have been conducted on a variety of buckminsterfullerenes,<sup>308</sup> but none on this class of fullerenes. Due to the presence of two or three phosphine groups, more than one phosphorus transition is observed in the  $^{31}\text{P}$  CPMAS NMR spectra. From preliminary analysis, for  $(\text{PPh}_3)_3\text{Co}(\text{NO})$ ,  $^1J(^{59}\text{Co}, ^{31}\text{P}) = 605(5)$  Hz, with three slightly

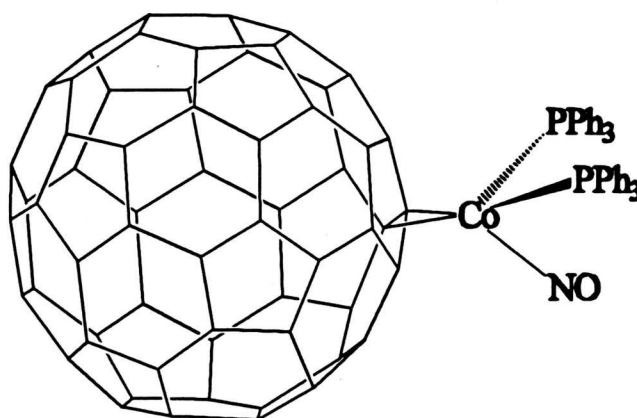


**Figure 6.3** Structure of  $(\text{PPh}_3)_2(\text{NO})\text{Co}(\eta^2\text{-C}_{60})$ .

different isotropic chemical shifts of 61.2(5) ppm, 60.7(5) ppm and 59.4(5) ppm. This is expected, since the phosphorus nuclei of each phosphine group should be in slightly differing environments due to the pyramidal symmetry of the complex. From rough simulations of this spectrum, a residual dipolar shift of  $d = -105$  Hz (negative sense) has been measured. The appearance of the  $^{31}\text{P}$  CPMAS NMR spectrum of  $(\text{PPh}_3)_3(\text{NO})\text{Co}(\eta^2\text{-C}_{60})$  is quite complicated. Despite the resemblance of the high-frequency portion of the isotropic transition with that of  $(\text{PPh}_3)_3\text{Co}(\text{NO})$ , it is not expected that the presence of any starting material is contributing to the appearance of this spectrum. The fullerene was thoroughly washed with methanol, in which the starting material is extremely soluble.<sup>306</sup> Rough simulations provide an estimate of  $^1J(^{59}\text{Co}, ^{31}\text{P}) = 550(20)$  Hz, and  $\delta_{\text{iso}} = 57$  and 40.5 ppm. Further work is required on the interpretation of these spectra.

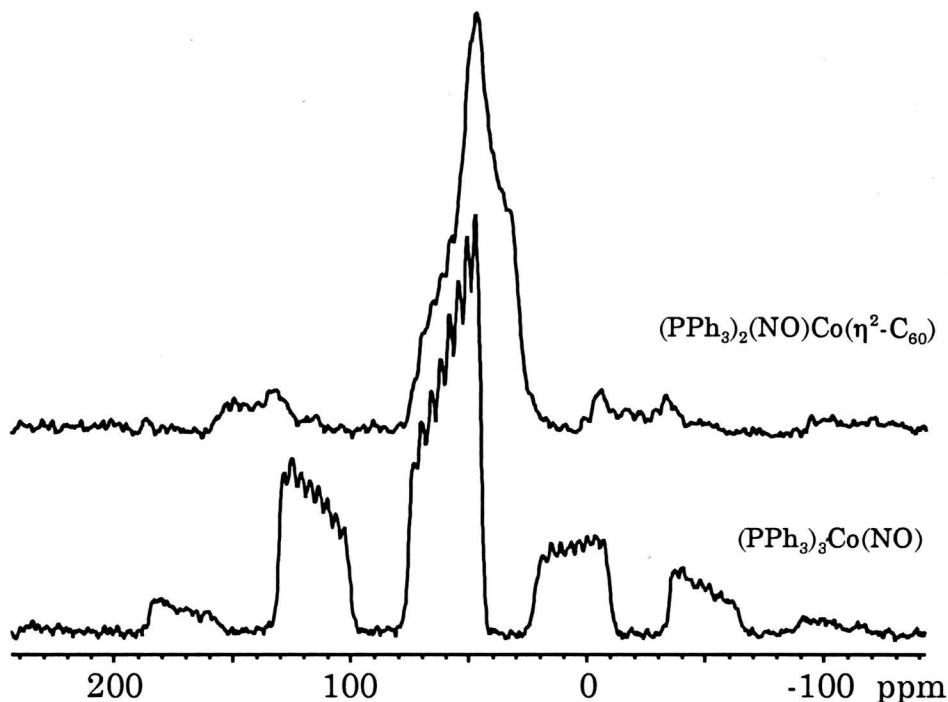


**Figure 6.4** Solid-state  $^{31}\text{P}$  CPMAS NMR spectra of  $(\text{PPh}_3)_2(\text{NO})\text{Co}(\eta^2\text{-C}_{60})$ ,  $\nu_{\text{rot}} = 13593$  Hz, and  $(\text{PPh}_3)_3\text{Co}(\text{NO})$ ,  $\nu_{\text{rot}} = 8921$  Hz at 9.4 T.

### 6.3 Characterization of the Nitrogen Chemical Shift Tensor in Aniline

Since the nitrogen CS tensor orientation has been determined in an aniline-substituted cobaloxime (Chapter 5), it would be of great interest to determine the nitrogen CS tensor in uncoordinated  $^{15}\text{N}$ -labelled aniline. Aniline is a liquid at room temperature, but freezes at  $-6.3^\circ\text{C}$ . The principal components of the nitrogen CS tensor can, in principle, be determined from a low temperature solid-state  $^{15}\text{N}$  NMR spectrum; however, no orientation information is available. If the  $^{15}\text{N}$ -aniline is labelled with a single deuteron, then the dipolar chemical shift method can be applied to determine the orientation of the nitrogen CS tensor with respect to the N, D bond. Isotopic enrichment is accomplished by proton-deuteron exchange with  $\text{D}_2\text{O}$ .

## Chapter 7

### Concluding Remarks

The usefulness of solid-state NMR for the investigation of systems involving quadrupolar nuclei is evident in the examples presented in this thesis. First, it was shown that by directly observing the solid-state NMR spectra of quadrupolar nuclei (i.e.,  $^{27}\text{Al}$ ), it is possible to characterize both electric field gradient and chemical shielding tensors at the quadrupolar nucleus. It is clear that characterization of CS tensors for a variety of nuclei in different chemical environments is essential for proper understanding of the nature of chemical shielding. It has been also been illustrated that much information can be gained on a variety of NMR interaction tensors in isolated spin pairs by indirect observation of quadrupolar nuclei (i.e.,  $^{59}\text{Co}$ ) via solid-state NMR spectra of spin-1/2 nuclei (i.e.,  $^{31}\text{P}$  and  $^{15}\text{N}$ ). The quadrupolar, chemical shielding, dipolar and indirect spin-spin interactions are intimately related to subtle changes in molecular structure and chemistry. Solution NMR spectra of quadrupolar nuclei or of spin-1/2 nuclei which are spin-coupled to quadrupolar nuclei generally provide little information in comparison. *Ab initio* calculations of chemical shielding and electric field gradient tensors are invaluable in aiding in the determination of the orientation of the interactions tensors in the frame of the molecule, as well as providing insight into their origin and nature.

Rather than being a hindrance to the acquisition and interpretation of NMR spectra, the effects of quadrupolar nuclei in solid-state NMR spectra provide a

plethora of valuable chemical and structural information. "What can be done now with obstreperous quadrupoles is really astounding!"<sup>309</sup>

*Nunc est bibendum*

## Appendix A

### Characterization of the Phosphorus Chemical

### Shielding Tensor in $\text{Cl}_3\text{AlOPCl}_3$

#### 1. Solid-State Phosphorus-31 NMR of $\text{Cl}_3\text{AlOPCl}_3$

Phosphorus-31 MAS NMR spectra of  $\text{Cl}_3\text{AlOPCl}_3$  were acquired, yielding an isotropic  $^{31}\text{P}$  chemical shift of 33.8(3) ppm. In the  $^{31}\text{P}$  NMR spectrum of the stationary sample (Fig. A1), there are small splittings and considerable broadening about  $\delta_{33}$ , which is evidence of direct dipolar  $^{27}\text{Al}$ ,  $^{31}\text{P}$  coupling (the internuclear Al,P distance is 3.336(2) Å, which corresponds to a dipolar coupling of 342(1) Hz). Assuming that the magnitude of  $^2J(^{27}\text{Al}, ^{31}\text{P})$  is very small (i.e.,  $^2J(^{27}\text{Al}, ^{31}\text{P})$  between 7 and 20 Hz),<sup>79</sup> it follows that  $\Delta J$  is very small. Therefore, the effective dipolar coupling is set at  $R_{\text{eff}} = 342$  Hz. The  $^{31}\text{P}$  NMR spectrum of the stationary sample is calculated from the following parameters:  $\delta_{11} = 59(2)$  ppm,  $\delta_{22} = 59(2)$  ppm,  $\delta_{33} = -16(1)$  ppm, with the polar angle  $\beta^{\text{C}} = 0^\circ$ . This means that  $\delta_{33}$  is approximately coincident with the P, Al dipolar vector. The non-unique components,  $\delta_{11}$  and  $\delta_{22}$ , are oriented perpendicular to the P-O-Al axis, with one component in the mirror plane of the molecule, and one perpendicular to the mirror plane (see Chapter 3, and Fig. A.2). The  $^{31}\text{P}$  CS tensor is axially symmetric within experimental error,  $\kappa = 0.97(3)$ , concomitant with the high local symmetry at the phosphorus nucleus.

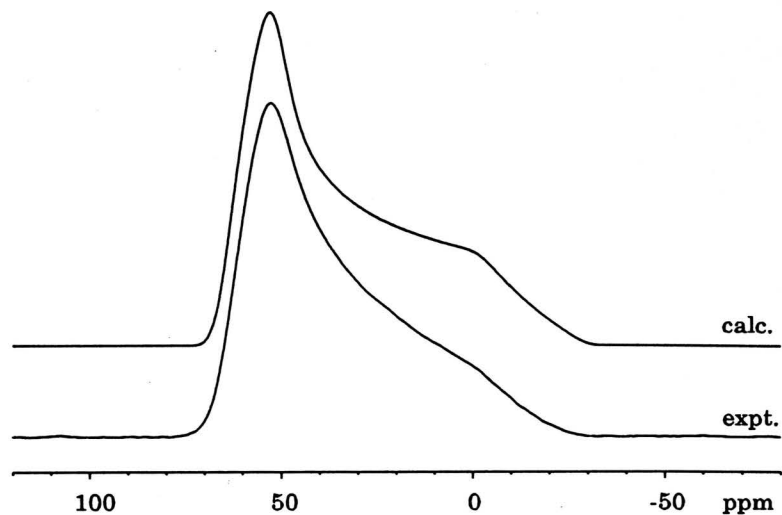


**Figure A.1** Experimental and calculated solid-state  $^{31}\text{P}$  NMR spectra of a stationary sample of  $\text{Cl}_3\text{AlOPCl}_3$  at 9.4 T.

**Table A.1:** Experimental and Calculated Phosphorus Chemical Shift Tensors

	$\delta_{11}(\text{ppm})$	$\delta_{22}(\text{ppm})$	$\delta_{33}(\text{ppm})$	$\delta_{\text{iso}}(\text{ppm})$	$\Omega(\text{ppm})$	$\kappa$
Experimental	59	58	-16	34	75	0.97
RHF						
6-31G*	2.0	0.6	-60.6	-19.3	62.6	0.95
6-31+G*	-5.1	-7.0	-76.8	-29.6	71.7	0.95
6-311G*	37.6	35.8	-41.1	10.7	78.7	0.95
6-311+G*	39.1	37.2	-42.1	11.4	81.1	0.95
DFT(B3LYP)						
6-31G*	30.5	28.9	-39.9	6.5	70.4	0.96
6-31+G*	24.4	22.2	-59.6	-4.3	84.0	0.95
6-311G*	86.1	84.1	-4.0	55.4	90.1	0.96
6-311+G*	87.3	85.2	-3.1	56.5	90.4	0.95

## 2. *Ab initio* Calculations of the $^{31}\text{P}$ Chemical Shielding Tensor

The experimental and theoretical CS tensor orientations are in good agreement, as shown in Fig. A.2. The spans and skews of the phosphorus CS tensor are predicted with relative accuracy by the majority of the calculations; however, correspondence between the experimental and theoretical CS tensor principal components is quite poor.

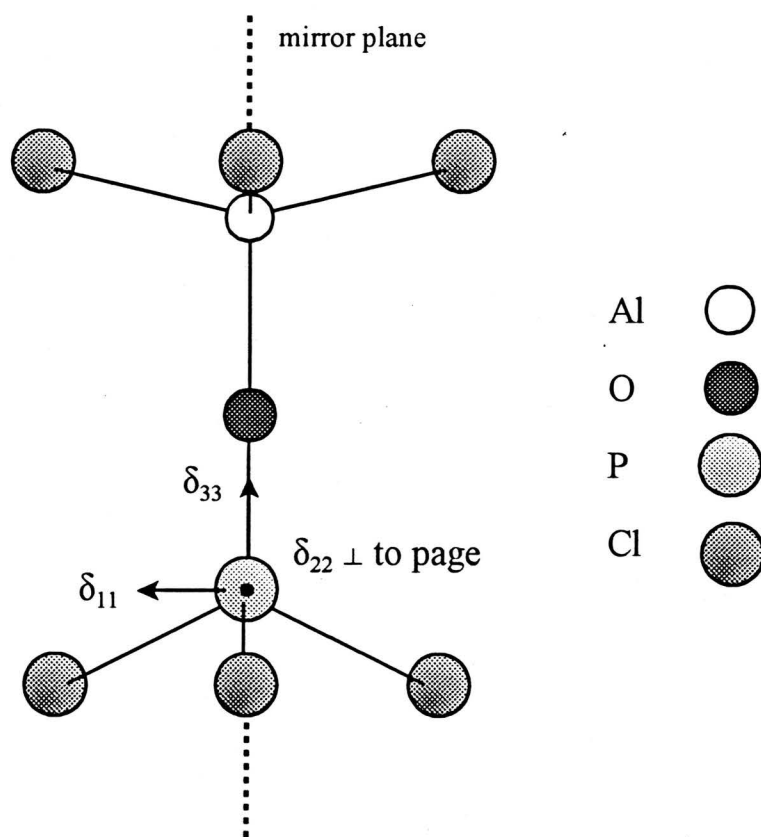


**Figure A.2** Experimental and theoretical phosphorus CS tensor orientations in  $\text{Cl}_3\text{AlOPCl}_3$ .

## 3. Experimental

Phosphorus-31 NMR spectra of stationary and spinning samples were obtained at both 4.7 T and 9.4 T on Bruker MSL-200 and AMX-400 NMR

spectrometers, respectively. Crystals of  $\text{AlCl}_3 \cdot \text{OPCl}_3$  were powdered and packed into 4 mm and 7 mm o.d. zirconium oxide rotors under an inert atmosphere. MAS spectra were acquired with spinning rates between 2.5 and 8 kHz. The  $^{31}\text{P}$  chemical shifts were referenced with respect to 85%  $\text{H}_3\text{PO}_4(\text{aq})$  by setting the chemical shift of the solid reference compound,  $\text{NH}_4\text{H}_2\text{PO}_4$ , to 0.81 ppm. Typical  $90^\circ$   $^{31}\text{P}$  pulse widths were set between 3 and 4  $\mu\text{s}$ . Relaxation delays of 4 to 6 s were applied. NMR spectra were simulated with the WSolids program.

*Ab initio* calculations were carried out as described in Section 3.2.3 of this thesis. Phosphorus-31 chemical shifts were referenced with respect to 85%  $\text{H}_3\text{PO}_4(\text{aq})$  by setting the chemical shielding of the reference to 328.35 ppm.<sup>32</sup>

## Appendix B

# Solid-State Carbon-13 and Cobalt-59 NMR of Cobaloximes

Representative examples of  $^{13}\text{C}$  and  $^{59}\text{Co}$  NMR spectra of cobaloximes are presented in this appendix. Carbon-13 NMR spectra of  $^{13}\text{C}$ -enriched  $\text{PPh}_3\text{Co}(\text{DH})_2\text{*CH}_3$  and  $\text{pyCo}(\text{DH})_2\text{*CH}_3$  are discussed in Section B.1, and the  $^{59}\text{Co}$  NMR spectrum of  $\text{PPh}_3\text{Co}(\text{DH})_2\text{*CH}_3$  is discussed in Section B.2.

### 1. Carbon-13 CPMAS NMR of Cobaloximes

The  $^{13}\text{C}$  CPMAS NMR spectrum of 25%  $^{13}\text{C}$ -labelled  $\text{PPh}_3\text{Co}(\text{DH})_2\text{*CH}_3$  is pictured in Fig. B.1. Multiplet structure resulting from  $^1J(^{59}\text{Co}, ^{13}\text{C})$  is observed in the broad transition at ca. 30 ppm, with the two peaks at ca. 15 and 11 ppm assigned to the methyl groups of the dimethylglyoxime moieties. The shape of the transition at 30 ppm is typical of all of the  $^{13}\text{C}$  CPMAS NMR spectra run on methylcobaloximes. The odd appearance of this multiplet in comparison with those observed in the  $^{31}\text{P}$  and  $^{15}\text{N}$  CPMAS NMR spectra is not due to multiple sites, since the known crystal structure<sup>228</sup> and the  $^{31}\text{P}$  and  $^{15}\text{N}$  CPMAS NMR spectra all establish that there is only one crystallographically distinct site in the unit cell. The indirect spin-spin coupling is roughly estimated as  $^1J(^{59}\text{Co}, ^{13}\text{C}) = 68(6)$  Hz, with no further information available on the sense of the spectrum.

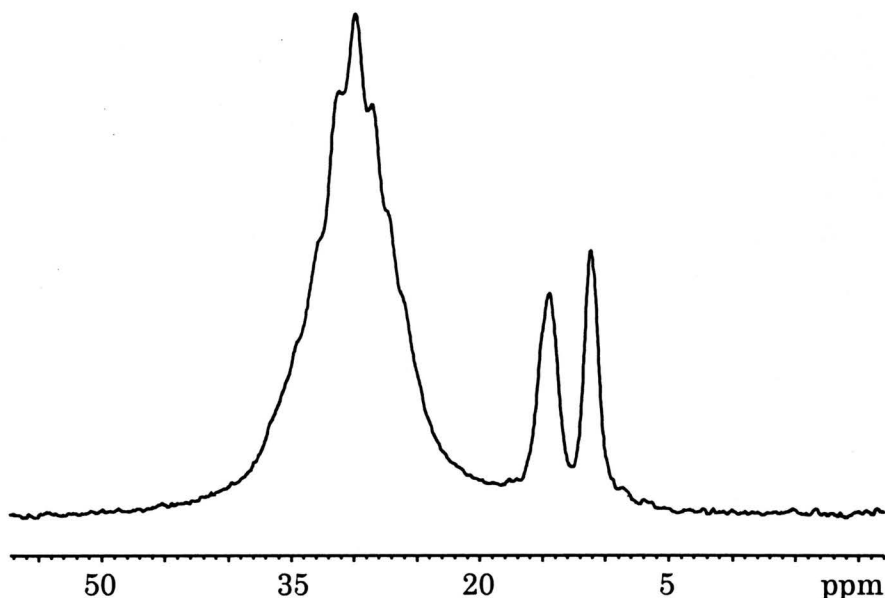


**Figure B.1** Solid-state  $^{13}\text{C}$  CPMAS NMR spectrum of 25%  $^{13}\text{C}$ -enriched  $\text{PPh}_3\text{Co}(\text{DH})_2\cdot\text{CH}_3$  at 4.7 T. Peaks at 15 and 11 ppm correspond to equatorial methyl groups.

Matters are further complicated for the  $^{13}\text{C}$  CPMAS NMR spectra of 30%  $^{13}\text{C}$ -enriched  $\text{pyCo}(\text{DH})_2\cdot\text{CH}_3$ , since the transitions corresponding to the axial and equatorial methyl groups overlap (Fig. B.2). Attempts to simulate the spectra failed; however, a rough estimate of  $^1J(^{59}\text{Co}, ^{13}\text{C})$  of 83(9) Hz is possible from preliminary spectral calculations. In addition, the sense of the spectrum is negative, as observed in the corresponding  $^{15}\text{N}$  CPMAS NMR spectra. This verifies that the sign of the dipolar coupling constant does not affect the sense of the spectrum (i.e.,  $R_{\text{dd}}(\text{Co}, \text{N})$  is negative,  $R_{\text{dd}}(\text{Co}, \text{C})$  is positive).

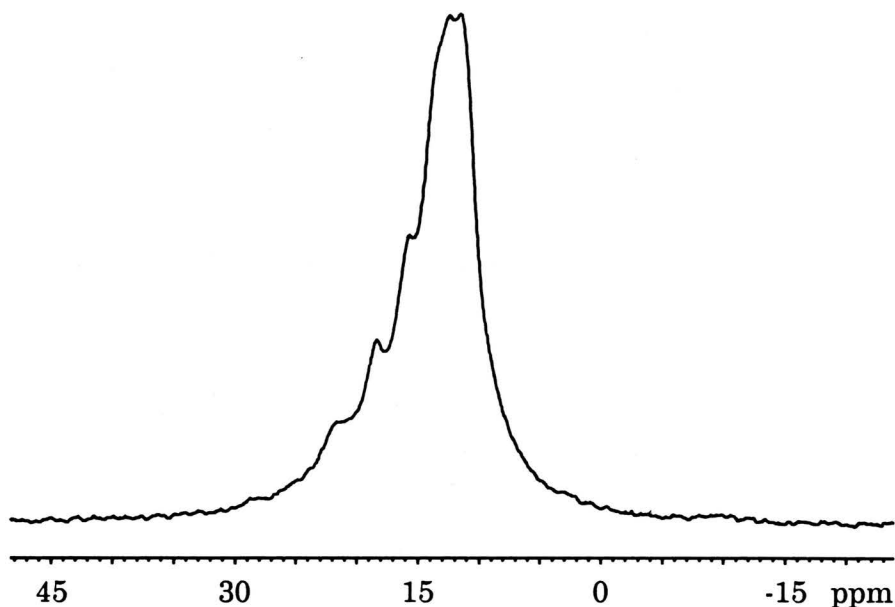


**Figure B.2** Solid-state  $^{13}\text{C}$  CPMAS NMR spectrum of 30%  $^{13}\text{C}$ -enriched  $\text{pyrCo}(\text{DH})_2 \cdot \text{CH}_3$  at 4.7 T.

## 2. Cobalt-59 NMR of the Cobaloximes

Solid-state  $^{59}\text{Co}$  NMR spectra were acquired for stationary samples of several of the cobaloximes, with limited success. Due to the large widths of the central transitions (i.e., 350 kHz and larger), acquisition of  $^{59}\text{Co}$  NMR spectra is quite difficult, since only partial excitation of the transition is possible. In addition, single-pulse experiments could not be used, since the spin-lattice relaxation time of the cobalt nucleus is very short. This means that much of the signal decays during the probe dead time prior to acquiring the signal. This problem is circumvented by the use of spin-echo sequences, with suitable phase cycling.<sup>310</sup>

Some spectra were uninterpretable due to spectral distortions, while others could not be simulated due to lack of quadrupolar data. Interpretation of the

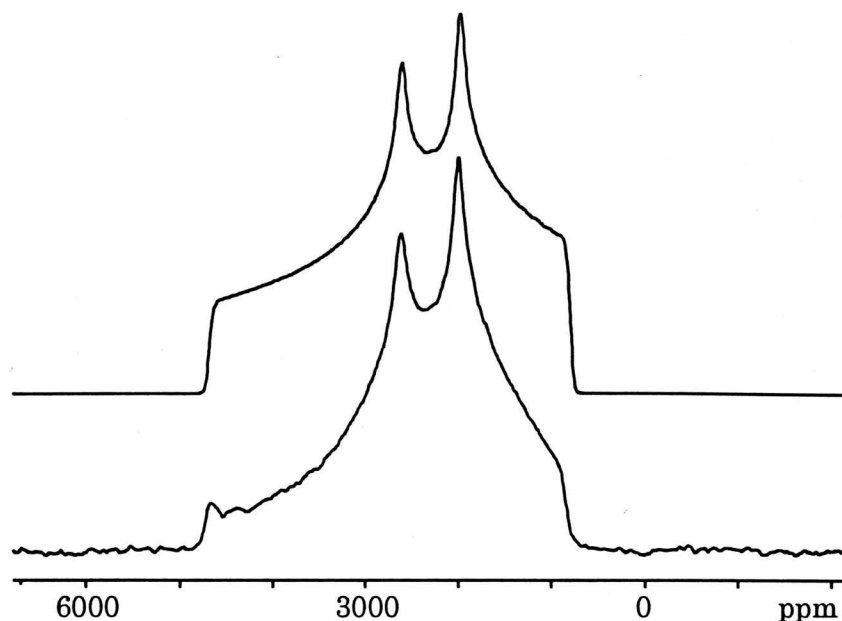


**Figure B.3** Experimental (bottom) and calculated (top) solid-state  $^{59}\text{Co}$  NMR spectra of  $\text{PPh}_3\text{Co}(\text{DH})_2\text{CH}_3$  at 9.4 T.

spectra is further convoluted by the spectral dependence on the cobalt CS tensor and its orientation relative to the EFG tensor at cobalt. Cobalt chemical shielding is very sensitive to slight changes in structure, and spans a range of greater than 18,000 ppm.<sup>163</sup> Cobalt nuclei in even slightly asymmetric environments experience large chemical shift anisotropy. Nonetheless,  $^{59}\text{Co}$  spectra were analyzed for  $\text{PPh}_3\text{Co}(\text{DH})_2\text{CH}_3$ , with the experimental and calculated spectra presented in Fig. B.3.

For  $\text{PPh}_3\text{Co}(\text{DH})_2\text{CH}_3$ , the following quadrupolar data are known:  $|C_Q| = 28.1$  MHz and  $\eta = 0.77$ . Simulations of the spectra yielded  $\delta_{11} = 4080(15)$  ppm,  $\delta_{22} = 2450(15)$  ppm and  $\delta_{33} = 1950(15)$  ppm, which corresponds to  $\delta_{\text{iso}} = 2827(26)$  ppm,  $\Omega = 2130(25)$  ppm and  $\kappa = -0.53(7)$ . The relative orientation of the CS and EFG tensors

is given by the Euler angles  $\alpha = \beta = \gamma = 0^\circ$ , which corresponds to coincidence of the two interaction tensors (i.e.,  $\delta_{33}$  along  $V_{33}$ , etc.).

### 3. Experimental

Solid-state  $^{13}\text{C}$  CPMAS NMR spectra were acquired at  $B_0 = 4.7$  T and 9.4 T on Bruker MSL-200 and AMX-400 spectrometers, under conditions of high-power proton decoupling. Samples were powdered and packed into 7-mm o.d. (MSL-200) and 4-mm o.d. zirconium oxide rotors. The proton  $90^\circ$  pulse, contact time and relaxation delay were 5.2  $\mu\text{s}$ , 10 ms and 8 s, respectively. Sample spinning rates ranged from 3 to 4.5 kHz. Carbon shifts were referenced to tetramethylsilane (TMS) at 0 ppm by setting the carbon resonances of solid adamantane to 38.56 ppm ( $\text{CH}_2$ ) and 29.50 ppm (CH).

Solid-state  $^{59}\text{Co}$  NMR spectra of stationary samples of the cobaloximes were obtained at 9.4 T using a Bruker solenoid probe. Samples were powdered and packed into small 5 mm o.d. NMR tubes approximately 2.5 cm in length. Spectra were referenced with respect to 1 M  $\text{K}_3\text{Co}(\text{CN})_6$  in  $\text{D}_2\text{O}$ ,  $\delta_{\text{iso}}(^{59}\text{Co}) = 0$  ppm. The length of the  $\pi/2$  pulse was determined to be 4  $\mu\text{s}$  in solution, corresponding to  $\nu_1 = 62.5$  kHz. Solid state spectra were acquired with the Hahn-echo pulse sequence:  $\pi/2 - \tau_1 - \pi - \tau_2 - \tau_{\text{AQ}}$ , with a  $\pi/2$  pulse of 1  $\mu\text{s}$  ( $1/(S + 1/2)$  times the solution  $\pi/2$  pulse length). Echo delay times,  $\tau_1$  and  $\tau_2$ , were set to 50  $\mu\text{s}$  and 20  $\mu\text{s}$ , respectively. The spectral width was set to 1.67 MHz, with a time domain size of 8 K. The spectra were left-shifted to the top of the echo signal and prior to Fourier transformation. Line-broadening of 4000 Hz was applied.

## References

1. An excellent review of the "pre-history" of NMR can be found in: Ramsey, N.F. *Bull. Magn. Reson.* **1985**, *7*, 94.
2. (a) Gorter, C.J. *Physica*, **1936**, *3*, 995. (b) Gorter, C.J.; Broer, I.F.J. *Physica*, **1942**, *9*, 591.
3. Purcell, E.M.; Torrey, H.C.; Pound, R.V. *Phys. Rev.* **1946**, *69*, 37.
4. Bloch, F.; Hansen, W.W.; Packard, M. *Phys. Rev.* **1946**, *69*, 127.
5. Pake, G.E. *J. Chem. Phys.* **1948**, *16*, 327.
6. Pound, R.V. *Phys. Rev.* **1950**, *79*, 685.
7. (a) Proctor, W.G.; Yu, F.C. *Phys. Rev.* **1950**, *77*, 717. (b) Dickinson, W.C. *Phys. Rev.* **1950**, *77*, 736.
8. Gutowsky, H.S.; McCall, D.W.; Slichter, C.P. *J. Chem. Phys.* **1953**, *21*, 279.
9. Jonas, J.; Gutowsky, H.S. *Ann. Rev. Phys. Chem.* **1980**, *31*, 1.
10. (a) Andrew, E.R.; Bradbury, A.; Eades, R.G. *Nature* **1958**, *182*, 1659. (b) Lowe, I.J. *Phys. Rev. Lett.* **1959**, *2*, 285. (c) Andrew, E.R.; Newing, R.A. *Proc. Phys. Soc. (London)* **1958**, *72*, 959.
11. Waugh, J.S.; Huber, L.M.; Haeberlen, U. *Phys. Rev. Lett.* **1968**, *20*, 180.
12. Pines, A.; Gibby, M.G.; Waugh, J.S. *J. Chem. Phys.* **1973**, *59*, 569.
13. Hartmann, S.R.; Hahn, E.L. *Phys. Rev.* **1962**, *128*, 2042.
14. Schaefer, J.; Stejskal, E.O. *J. Am. Chem. Soc.* **1976**, *98*, 1031.
15. Andrew, E.R.; Szczesniak, E. *Progr. Nucl. Magn. Spectrosc.* **1995**, *28*, 11.
16. Clayden, N.J. *Ann. Rep. NMR. Spectrosc.* **1992**, *24*, 1.
17. Abragam, A. *The Principles of Nuclear Magnetism*; Clarendon Press: Oxford, 1986.
18. Mehring, M. *Principles of High Resolution NMR in Solids, Second Edition*; Springer-Verlag: New York, 1983.
19. Wind, R.A. *Modern NMR Techniques and Their Application in Chemistry*; Popov, A.I.; Hallenga, K., Eds. Marcel Dekker, Inc.: New York, 1991; pp. 125-216.

20. Dye, J.L.; Ellaboudy, A.S.; Kim, J. *Modern NMR Techniques and Their Application in Chemistry*; Popov, A.I.; Hallenga, K., Eds. Marcel Dekker, Inc.: New York, 1991; pp. 217-322.
21. Harris, R.K. *Multinuclear Magnetic Resonance in Liquids and Solids - Chemical Applications - NATO ASI Series*; Granger, P.; Harris, R.K., Eds. Kluwer Academic Publishers: Dordrecht, 1990; vol. 322, pp. 269-290.
22. Grimmer, A.-R.; Blümich, B. *NMR Basic Principles and Progress*; Diehl, P.; Fluck, E.; Günther, H.; Kosfeld, R.; Seelig, J., Eds. Springer-Verlag: Berlin, 1994; vol. 30, pp. 1-62.
23. Freude, D.; Haase, J. *NMR Basic Principles and Progress*; Diehl, P.; Fluck, E.; Günther, H.; Kosfeld, R.; Seelig, J., Eds. Springer-Verlag: Berlin, 1993; vol. 29, pp. 1-90.
24. Gerstein, B.C.; Dybowski, C.R. *Transient Techniques in NMR of Solids*; Academic Press, Inc.: Orlando, 1985.
25. Harris, R.K. *Nuclear Magnetic Resonance Spectroscopy - A Physicochemical View*; John Wiley & Sons: New York, 1987.
26. Ramsey, N.F. *Phys. Rev.* **1950**, *78*, 699.
27. Anet, F.A.L.; O'Leary, D.J. *Concepts in Magn. Reson.* **1991**, *3*, 193 and references therein.
28. (a) Kennedy, M.A.; Ellis, P.D. *Concepts in Magn. Reson.* **1989**, *1*, 35. (b) Kennedy, M.A.; Ellis, P.D. *Concepts in Magn. Reson.* **1989**, *1*, 109.
29. Mason, J. *Solid State Nucl. Magn. Reson.* **1993**, *2*, 285.
30. Jameson, C.J.; Mason, J. *Multinuclear NMR*; Mason, J. Ed. Plenum Press: New York, 1987; pp. 51-88.
31. Jameson, C.J. *Encyclopedia of Nuclear Magnetic Resonance*; Grant, D.M.; Harris, R.K., Eds. John Wiley & Sons: Chichester, U.K., 1996; pp. 1273-1281.
32. Jameson, C.J.; De Dios, A.; Jameson, A.K. *Chem. Phys. Lett.* **1990**, *167*, 575.
33. Wasylshen, R.E. *Encyclopedia of Nuclear Magnetic Resonance*; Grant, D.M.; Harris, R.K., Eds. John Wiley & Sons: Chichester, U.K., 1996; pp. 1685-1695.
34. (a) Tutunjian, P.; Waugh, J.S. *J. Magn. Reson.* **1982**, *49*, 155. (b) Penner, G.H.; Power, W.P.; Wasylshen, R.E. *Can. J. Chem.* **1988**, *66*, 1821.

35. Amoureux, J.P.; Fernandez, C.; Granger, P. *Multinuclear Magnetic Resonance in Liquids and Solids - Chemical Applications - NATO ASI Series*; Granger, P.; Harris, R.K., Eds. Kluwer Academic Publishers: Dordrecht, 1990; vol. 322, pp. 409-424.
36. Smith, J.A.S. *Ber. Bunsenges. Phys. Chem.* **1987**, *91*, 1145.
37. See for instance, Pyykkö, P. *Z. Naturforsch.* **1992**, *47a*, 189.
38. Cohen, M.H.; Reif, F. *Solid St. Phys.* **1957**, *5*, 321.
39. Lucken, E.A.C. *Nuclear Quadrupole Coupling Constants*; Academic Press, Inc.: London, 1969.
40. Man, P.P. *Encyclopedia of Nuclear Magnetic Resonance*; Grant, D.M.; Harris, R.K., Eds.; John Wiley & Sons: Chichester, U.K., 1996, pp. 3838-3848.
41. Ramsey, N.F. *Nuclear Moments*; Wiley Interscience: New York, 1953.
42. Taulelle, F. *Multinuclear Magnetic Resonance in Liquids and Solids - Chemical Applications - NATO ASI Series*; Granger, P.; Harris, R.K., Eds. Kluwer Academic Publishers: Dordrecht, 1990; vol. 322, pp. 393-407.
43. Vega, A.J. *Encyclopedia of Nuclear Magnetic Resonance*; Grant, D.M.; Harris, R.K., Eds.; John Wiley & Sons: Chichester, U.K., 1996, pp. 3869-3889.
44. (a) Samoson, A.; Lippmaa, E.; Pines, A. *Mol. Phys.* **1988**, *65*, 1013. (b) Llor, A.; Virlet, J. *Chem. Phys. Lett.* **1988**, *152*, 248.
45. Mueller, K.T.; Sun, B.Q.; Chingas, G.C.; Zwanziger, J.W.; Terao, T.; Pines, A. *J. Magn. Reson.* **1990**, *86*, 470.
46. (a) Frydman, L.; Harwood, J.S. *J. Am. Chem. Soc.* **1995**, *117*, 5367. (b) Medek, A.; Harwood, J.S.; Frydman, L. *J. Am. Chem. Soc.* **1995**, *117*, 12779.
47. Fyfe, C.A. *Multinuclear Magnetic Resonance in Liquids and Solids - Chemical Applications - NATO ASI Series*; Granger, P.; Harris, R.K., Eds. Kluwer Academic Publishers: Dordrecht, 1990; vol. 322, pp. 311-337.
48. (a) Herzfeld, J.; Berger, A.E. *J. Chem. Phys.* **1980**, *73*, 6021. (b) Maricq, M.M.; Waugh, J.S. *J. Chem. Phys.* **1979**, *70*, 3300.
49. (a) VanderHart, D.L.; Earl, W.L.; Garroway, A.N. *J. Magn. Reson.* **1981**, *44*, 361. (b) Garroway, A.N.; Vanderhart, D.L.; Earl, W.L. *Philos. Trans. R. Lond. A* **1981**, *299*, 609.
50. Waugh, J.S. *J. Magn. Reson.* **1982**, *50*, 30.

51. Bennett, A.E.; Rienstra, C.M.; Auger, M.; Lakshmi, K.V.; Griffin, R.G. *J. Chem. Phys.* **1995**, *103*, 6951.
52. Sachleben, J.R.; Caldarelli, S.; Emsley, L. *J. Chem. Phys.* **1996**, *104*, 2518.
53. Burum, D.P. *Encyclopedia of Nuclear Magnetic Resonance*; Grant, D.M.; Harris, R.K., Eds.; John Wiley & Sons: Chichester, U.K., **1996**, pp. 1535-1543.
54. Engelke, F. *Encyclopedia of Nuclear Magnetic Resonance*; Grant, D.M.; Harris, R.K., Eds.; John Wiley & Sons: Chichester, U.K., **1996**, pp. 1529-1535.
55. Kentgens, A.P.M. *Geoderma*, **1997**, *80*, 271.
56. Fukushima, E.; Roeder, S.B.W. *Experimental Pulse NMR - A Nuts and Bolts Approach*; Addison-Wesley Publishing Company: Reading, MA, 1981.
57. Foerster, H. *Solids Experiments on AVANCE DMX/DSX Spectrometers*; Bruker Analytik GmbH: Rheinstetten, 1995, preliminary version 7.6.95.
58. Gerstein, B.C. *Encyclopedia of Nuclear Magnetic Resonance*; Grant, D.M.; Harris, R.K., Eds.; John Wiley & Sons: Chichester, U.K., **1996**, pp. 1835-1840.
59. Webb, G.A. *Nuclear Magnetic Shielding and Structure - NATO ASI Series*; Tossell, J.A., Ed.; Kluwer Academic Publishers, Dordrecht: The Netherlands, 1993, vol. 386, pp. 1-26.
60. De Dios, A.C. *J. Progr. Nucl. Magn. Reson. Spectrosc.* **1996**, *29*, 229.
61. Facelli, J.C. *Encyclopedia of Nuclear Magnetic Resonance*; Grant, D.M.; Harris, R.K., Eds.; John Wiley & Sons: Chichester, U.K., **1996**, pp. 4299-4307.
62. Webb, G.A. *Encyclopedia of Nuclear Magnetic Resonance*; Grant, D.M.; Harris, R.K., Eds.; John Wiley & Sons: Chichester, U.K., **1996**, pp. 4307-4318.
63. Fukui, H. *Progr. Nucl. Magn. Reson. Spectrosc.* **1997**, *31*, 317.
64. Jameson, C.J. *Specialist Periodical Reports - Nuclear Magnetic Resonance*; Webb, G.A., Ed.; The Royal Society of Chemistry: London, 1980 - 1996; vols. 8-26.
65. Several articles on this subject can be found in: *Nuclear Magnetic Shielding and Structure - NATO ASI Series*; Tossell, J.A., Ed.; Kluwer Academic

Publishers, Dordrecht: The Netherlands, 1993; vol. 386.

66. (a) Wolinski, K.; Hinton, J.F.; Pulay, P. *J. Am. Chem. Soc.* **1990**, *112*, 8251. (b) Ditchfield, R. *Mol. Phys.* **1974**, *27*, 789.
67. Gaussian 94, Revision B.2: Frisch, M.J.; Trucks, G.W.; Schlegel, H.B.; Gill, P.M.W.; Johnson, B.G.; Robb, M.A.; Cheeseman, J.R.; Keith, T.; Petersson, G.A.; Montgomery, J.A.; Raghavachari, K.; Al-Laham, M.A.; Zakrewski, V.G.; Ortiz, J.V.; Foresman, J.B.; Cioslowski, J.; Stefanov, B.B.; Nanayakkara, A.; Challacombe, M.; Peng, C.Y.; Ayala, P.Y.; Chen, W.; Wong, M.W.; Andres, J.L.; Replogle, E.S.; Gomperts, R.; Martin, R.L.; Fox, D.J.; Binkley, J.S.; Defrees, D.J.; Baker, J.; Stewart, J.P.; Head-Gordon, M.; Gonzalez, C.; Pople, J.A., Gaussian, Inc., Pittsburgh PA, 1995.
68. Frisch, M.J.; Frisch, A.; Foresman, J.B. *Gaussian 94 User's Reference*; Gaussian Inc.: Pittsburgh, 1996.
69. (a) Kutzelnigg, W. *Isr. J. Chem.* **1980**, *19*, 193. (b) Kutzelnigg, W.; Fleischer, U.; Schindler, M. *NMR Basic Principles and Progress*; Diehl, P.; Fluck, E.; Günther, H.; Kosfeld, R.; Seelig, J., Eds. Springer-Verlag: Berlin, 1991; vol. 23, pp. 165-262.
70. Hansen, A.E.; Bouman, T.D. *J. Chem. Phys.* **1985**, *82*, 5035.
71. (a) Keith, T.A.; Bader, R.F.W. *Chem. Phys. Lett.* **1992**, *194*, 1. (b) Keith, T.A.; Bader, R.F.W. *Chem. Phys. Lett.* **1992**, *210*, 223. (c) Keith, T.A.; Bader, R.F.W. *Can. J. Chem.* **1996**, *74*, 185.
72. (a) Hay, P.J.; Wadt, W.R. *J. Chem. Phys.* **1985**, *82*, 270. (b) Wadt, W.R.; Hay, P.J. *J. Chem. Phys.* **1985**, *82*, 284. (c) Hay, P.J.; Wadt, W.R. *J. Chem. Phys.* **1985**, *82*, 299. (d) Russo, T.V.; Martin, R.L.; Hay, P.J. *J. Phys. Chem.* **1995**, *99*, 17085.
73. Huber, H. *J. Chem. Phys.* **1985**, *83*, 4591.
74. Smith, M.E. *Appl. Magn. Reson.* **1993**, *4*, 1.
75. Bastow, T.J. *Z. Naturforsch.* **1994**, *49a*, 320.
76. Klinowski, J. *Anal. Chim. Acta* **1993**, *283*, 929.
77. Alemany, L.B. *Appl. Magn. Reson.* **1993**, *4*, 179.
78. Delpuech, J.J. *NMR of Newly Accessible Nuclei - Volume 2: Chemically and Biochemically Important Elements*; Laszlo, P., Ed. Academic Press: New York, 1983; pp. 153-195.

79. Akitt, J.W. *Progr. NMR Spectrosc.* **1989**, *21*, 1.
80. (a) Duncan, T.M. *Principal Components of Chemical Shift Tensors: A Compilation, Second Edition*; Farragut Press: Chicago, 1994. (b) Duncan, T.M. *J. Phys. Chem. Ref. Data* **1987**, *16*, 125.
81. Samoson, A.; Sarv, P.; van Braam Houckgeest, J.P.; Kraushaar-Czarnetzki, B. *Appl. Magn. Reson.* **1993**, *4*, 171.
82. Vosegaard, T.; Jakobsen, H.J. *J. Magn. Reson.* **1997**, *128*, 135.
83. For a review on the Knight shift and references to original articles, see: Knight, W.D.; Kobayashi, S. *Encyclopedia of Nuclear Magnetic Resonance*; Grant, D.M.; Harris, R.K., Eds.; John Wiley & Sons: Chichester, U.K., 1996, pp. 2672-2679.
84. (a) Smith, M.E.; Gibson, M.A.; Forwood, C.T.; Bastow, T.J. *Philosoph. Mag. A* **1996**, *74*, 791. (b) Bastow, T.J.; Smith, M.E.; West, G.W. *J. Phys. Condens. Matter* **1997**, *9*, 6085.
85. (a) Sykes, D.; Kubicki, J.D.; Farrar, T.C. *J. Phys. Chem. A* **1997**, *101*, 2715. (b) Nakatsuji, H.; Hada, M.; Tejima, T.; Nakajima, T.; Sugimoto, M. *Chem. Phys. Lett.* **1996**, *249*, 284. (c) Schneider, U.; Ahlrichs, R. *Chem. Phys. Lett.* **1994**, *226*, 491. (d) Gauss, J.; Schneider, U.; Ahlrichs, R.; Dohmeier, C.; Schnöckel, H. *J. Am. Chem. Soc.* **1993**, *115*, 2402. (e) Kanzaki, M. *J. Ceram. Soc. Jpn.* **1997**, *105*, 98. (f) Tossell, J.A. *Nuclear Magnetic Shieldings and Molecular Structure - NATO ASI Series*; Tossell, J.A., Ed. Kluwer Academic Publishers: Dordrecht, 1993; vol. 386, pp. 279-296. (g) O'Reilly, D.E. *J. Chem. Phys.* **1960**, *32*, 1007.
86. (a) Kaupp, M.; Malkina, O.L.; Malkin, V.G. *J. Chem. Phys.* **1997**, *106*, 9201. (b) Cheeseman, J.R.; Trucks, G.W.; Keith, T.A.; Frisch, M.J. *J. Chem. Phys.* **1996**, *104*, 5497.
87. (a) Chesnut, D.B.; Byrd, E.F.C. *Heteroatom Chem.* **1996**, *7*, 307. (b) Kaupp, M. *Chem. Ber.* **1996**, *129*, 535.
88. Schurko, R.W.; Wasylishen, R.E.; Phillips, A.D. *J. Magn. Reson.* In press.
89. See for instance, (a) Burford, N. *Coord. Chem. Rev.* **1992**, *112*, 1. (b) Burford, N.; Royan, B.W.; Spence, R.E. v.H.; Cameron, T.S.; Linden, A.; Rogers, R.D. *J. Chem. Soc. Dalton Trans.* **1990**, 1521.
90. Birkneder, F.; Berg, R.W.; Bjerrum, N.J. *Acta Chem. Scand.* **1993**, *47*, 344.
91. Burford, N.; Phillips, A.D.; Schurko, R.W.; Wasylishen, R.E.; Richardson, J.F. *Chem. Commun.* **1997**, 2363.

92. Schurko, R.W.; Wasylshen, R.E.; Foerster, H. *J. Phys. Chem.* **1998**, *In press*.
93. Robinson, J.S.; Apponi, A.J.; Ziurys, L.M. *Chem. Phys. Lett.* **1997**, *278*, 1.
94. Walker, K.A.; Gerry, M.C.L. *Chem. Phys. Lett.* **1997**, *278*, 9.
95. Hensel, K.D.; Styger, C.; Jäger, W.; Merer, A.J.; Gerry, M.C.L. *J. Chem. Phys.* **1993**, *99*, 3320.
96. Alderman, D.W.; Solum, M.S.; Grant, D.M. *J. Chem. Phys.* **1986**, *84*, 3717.
97. Muetterties, E.L.; Wright, C.M. *J. Am. Chem. Soc.* **1964**, *86*, 5132.
98. Becke, A.D. *J. Chem. Phys.* **1993**, *98*, 5648.
99. Lee, C.; Yang, W.; Parr, R.G. *Phys. Rev. B* **1988**, *37*, 785.
100. (a) Rahman, A.; Nizamuddin Ahmed, S.; Khair, M.A.; Zangrando, E.; Randaccio, L. *J. Bangladesh. Acad. Sci.* **1990**, *14*, 161. (b) Hon, P.K.; Pfluger, C.E. *J. Coord. Chem.* **1973**, *3*, 67. (c) McClelland, B.W. *Acta Cryst.* **1975**, *B31*, 2496.
101. Muetterties, E.L.; Guggenberger, L.J. *J. Am. Chem. Soc.* **1972**, *94*, 8046.
102. Nöth, H. *Z. Naturforsch.* **1980**, *35b*, 119.
103. Tarasov, V.P.; Kirakosyan, G.A. *Russ. J. Inorg. Chem.* **1997**, *42*, 1223.
104. (a) Brown, R.D.; Head-Gordon, M.P. *Mol. Phys.* **1987**, *61*, 1183. (b) Cummins, P.L.; Bacskey, G.B.; Hush, N.S. *Mol. Phys.* **1987**, *62*, 193.
105. Samoson, A.; Kundla, E.; Lippmaa, E. *J. Magn. Reson.* **1982**, *49*, 350.
106. For  $\text{AlCl}_3$ -tetrahydrofuran, the  $\delta_{\text{iso}}(^{27}\text{Al})$  is reported as 99 ppm from solid-state experiments. O.H. Han and E. Oldfield, *Inorg. Chem.* **1990**, *29*, 3666.
107. Several complexes of  $\text{AlCl}_3$  and  $\text{PMe}_3$  were investigated, with  $\delta_{\text{iso}}(^{27}\text{Al})$  of 111.5(2) and 54.3(2) ppm. P.J. Chu, A. de Mallmann and J.H. Lunsford, *J. Phys. Chem.* **1991**, *95*, 7362.
108. Barrie, P.J. *Chem. Phys. Lett.* **1993**, *208*, 486.
109. Dechter, J.J.; Henriksson, U.; Kowalewski, J.; Nilsson, A.-C. *J. Magn. Reson.* **1982**, *48*, 503.
110. Cotton, F.A.; Wilkinson, G. *Advanced Inorganic Chemistry*, 4<sup>th</sup> Ed.; John Wiley & Sons: New York, 1980; pp. 166-170.

111. Baugher, J.F.; Taylor, P.C.; Oja, T.; Bray, P.J. *J. Chem. Phys.* **1969**, *50*, 4914.
112. Taylor, P.C.; Baugher, J.F.; Kriz, H.M. *Chem. Rev.* **1975**, *75*, 203.
113. (a) Cheng, J.T.; Edwards, J.C.; Ellis, P.D. *J. Phys. Chem.* **1990**, *94*, 553. (b) Power, W.P.; Wasylishen, R.E.; Mooibroek, S.; Pettitt, B.A.; Danchura, W. *J. Phys. Chem.* **1990**, *94*, 591.
114. Koons, J.M.; Hughes, E.; Cho, H.M.; Ellis, P.D. *J. Magn. Reson. A*, **1995**, *114*, 12.
115. Zare, R.N. *Angular Momentum - Understanding Spatial Aspects in Chemistry and Physics*; John Wiley & Sons: New York, 1988.
116. Van Vleck, J.H. *Phys. Rev.* **1948**, *74*, 1168.
117. Woessner, D.E.; Timken, H.K.C. *J. Magn. Reson.* **1990**, *90*, 411.
118. Weil, J.A., Buch, T., Clapp, J.E. *Adv. Magn. Reson.* **1973**, *6*, 183.
119. Reynhardt, E.C. *J. Phys. C: Solid State Phys.* **1974**, *7*, 4135.
120. Eichele, K.; Chan, J.C.C.; Wasylishen, R.E.; Britten, J.F. *J. Phys. Chem. A* **1997**, *101*, 5423.
121. Veeman, W.S. *Progr. NMR Spectrosc.* **1984**, *16*, 193.
122. Ditchfield, R. *Critical Evaluation of Chemical and Physical Structural Information*; Lide, D.R.; Paul, M.A., Eds.; National Academy of Sciences: Washington, D.C., 1974; pp. 565-590.
123. Segleken, W.G.; Torrey, H.C. *Phys. Rev.* **1955**, *98*, 1537.
124. Dewar, M.J.S.; Patterson, D.B.; Simpson, W.I. *J. Chem. Soc. Dalton Trans.* **1973**, 2381.
125. For another example, see Rauhut, G.; Puyear, S.; Wolinski, K.; Pulay, P. *J. Phys. Chem.* **1996**, *100*, 6310.
126. Malli, G.; Froese, C. *Int. J. Quantum. Chem.* **1967**, *1S*, 95.
127. (a) Flygare, W.H. *Chem. Rev.* **1974**, *74*, 653. (b) Gierke, T.D.; Flygare, W.H. *J. Am. Chem. Soc.* **1972**, *94*, 7277. (c) Flygare, W.H.; Goodisman, J. *J. Chem. Phys.* **1968**, *49*, 3122.
128. Figure adapted from Grutzner, J.B. *Recent Advances in Organic NMR Spectroscopy*; Lambert, J.B.; Rittner, R., Eds.; Norell Press: Landisville, NJ,

1987; pp. 17-42.

129. (a) Christiansen, O.; Gauss, J.; Stanton, J.F. *Chem. Phys. Lett.* **1997**, *266*, 53. (b) Gauss, J.; Ruud, K. *Int. J. Quantum Chem.* **1995**, *29*, 437.
130. (a) Schreckenbach, G.; Dickson, R.M.; Ruiz-Morales, Y.; Ziegler, T. *Chemical Applications of Density-Functional Theory*; Laird, B.B.; Ross, R.B.; Ziegler, T., Eds. American Chemical Society: Washington, D.C., 1996; vol. 629, p. 328. (b) Malkin, V.G.; Malkina, O.L.; Casida, M.E.; Salahub, D.R. *J. Am. Chem. Soc.* **1994**, *116*, 5898.
131. (a) Müller, H.S.P.; Gerry, M.C.L. *J. Chem. Phys.* **1995**, *103*, 577. (b) Baker, M.R.; Anderson, C.H.; Ramsey, N.F. *Phys. Rev.* **1964**, *133*, A1533.
132. Gatehouse, B.; Müller, H.S.P.; Gerry, M.C.L. *J. Chem. Phys.* **1997**, *106*, 6916 and references therein.
133. Lide, D.R. *J. Chem. Phys.* **1965**, *42*, 1013.
134. (a) Holst, W.; Hulthén, E. *Z. Physik* **1934**, *90*, 712. (b) Deutsch, J.L.; Neil, W.S.; Ramsay, D.A. *J. Mol. Spectrosc.* **1987**, *125*, 115. (c) White, J.B.; Dulick, M.; Bernath, P.F. *J. Chem. Phys.* **1993**, *99*, 8371. Calculations were performed using bond length from ref (b).
135. (a) Lide, D.R. *J. Chem. Phys.* **1963**, *38*, 2027. (b) Wyse, F.C.; Gordy, W.; Pearson, E.F. *J. Chem. Phys.* **1970**, *52*, 3887.
136. Carpenter, J.F.; Weinhold, F. *J. Mol. Struct. (Theochem)* **1988**, *169*, 41 and references therein.
137. Goto, M.; Saito S. *Astrophys. J. Lett.* **1995**, *452*, 147.
138. Lucken, E.A. *Adv. Nucl. Quadrupole Reson.* **1983**, *5*, 83.
139. Klaus, Th.; Belov, S.P.; Winnewisser, G. *J. Mol. Spectrosc.* **1998**, *187*, 109.
140. Buckingham, A.D. *J. Chem. Phys.* **1962**, *36*, 3096.
141. Jameson, C.J. *J. Chem. Phys.* **1977**, *66*, 4977.
142. Jameson, C.J. *J. Chem. Phys.* **1977**, *66*, 4983.
143. Chesnut, D.B. *Chem. Phys.* **1986**, *110*, 415.
144. (a) Jameson, C.J.; de Dios, A.C. *J. Chem. Phys.* **1993**, *98*, 2208. (b) de Dios, A.C.; Jameson, C.J. *Ann. Rep. NMR Spectrosc.* **1994**, *29*, 1.
145. Wyse, F.C.; Gordy, W. *J. Chem. Phys.* **1972**, *56*, 2130.

146. For a recent review, see: Harris, R.K.; Olivieri, A.C. *Progr. NMR Spectros.* **1992**, *24*, 435.
147. Power, W.P.; Wasylishen, R.E. *Ann. Rep. on NMR Spectrosc.* **1991**, *23*, 1
148. Wasylishen, R.E.; Wright, K.C.; Eichele, K.; Cameron, T.S. *Inorg. Chem.* **1994**, *33*, 407.
149. Eichele, K.; Wasylishen, R.E.; Corrigan, J.F.; Doherty, S.; Sun, Y.; Carty, A.J. *Inorg. Chem.* **1993**, *32*, 121.
150. (a) Pople, J.A. *Mol. Phys.* **1958**, *1*, 168. (b) Sanders, J.C.P.; Schrobilgen, G.J. in *Multinuclear Magnetic Resonance in Liquids and Solids - Chemical Applications - NATO ASI Series*; Granger, P.; Harris, R.K., Eds.; Kluwer Academic Publishers: Dordrecht, The Netherlands, 1990; vol. 322, pp. 157-186.
151. (a) Jonsen, P. *J. Magn. Reson.* **1988**, *77*, 348. (b) Olivieri, A.C. *J. Magn. Reson.* **1989**, *82*, 342.
152. Olivieri, A.C. *J. Chem. Soc. Perkins Trans. 2* **1990**, 85.
153. Spiess, H.W.; Haeberlen, U.; Zimmermann, H. *J. Magn. Reson.* **1977**, *25*, 55.
154. Fleming, W.W.; Fyfe, C.A.; Lyerla, J.R.; Vanni, H.; Yannoni, C.S. *Macromolecules* **1980**, *13*, 460.
155. Harris, R.K.; Root, A. *Mol. Phys.* **1989**, *66*, 993.
156. (a) Alarcón, S.H.; Olivieri, A.C.; Carss, S.A.; Harris, R.K. *Angew. Chem. Int. Ed. Engl.* **1994**, *33*, 1624. (b) Alarcón, S.H.; Olivieri, A.C.; Carss, S.A.; Harris, R.K.; Zuriaga, M.J.; Monti, G.A. *J. Magn. Reson. Ser. A* **1995**, *116*, 244.
157. Hoelger, C.-G.; Rössler, E.; Wehrle, B.; Aguilar-Parrilla, F.; Limbach, H.-H. *J. Phys. Chem.* **1995**, *99*, 14271.
158. Schurko, R.W.; Wasylishen, R.E.; Nelson, J.H. *J. Chem. Phys.* **1996**, *100*, 8057.
159. Schrauzer, G.N. *Inorg. Synth.* **1968**, *11*, 61 and references therein.
160. Bresciani-Pahor, N.; Forcolin, M.; Marzilli, L.G.; Randaccio, L.; Summers, M.F.; Toscano, P.J. *Coord. Chem. Rev.* **1985**, *63*, 1.
161. (a) Randaccio, L.; Bresciani-Pahor, N.; Zangrando, E.; Marzilli, L.G. *Chem. Soc. Rev.* **1989**, *18*, 225. (b) Randaccio, L.; Geremia, S.; Zangrando, E.; Ebert, C. *Inorg. Chem.* **1994**, *33*, 4641.

162. (a) LaRossa, R.A.; Brown, T.L. *J. Am. Chem. Soc.* **1974**, *96*, 2072. (b) Brown, T.L. *Acc. Chem. Res.* **1974**, 408.
163. (a) Pregosin, P.S. *Transition Metal Nuclear Magnetic Resonance*; Pregosin, P.S., Ed.; Elsevier: Amsterdam, 1991; pp. 143-176. (b) Lucken, E.A.C.; Noack, K.; Williams, D.F. *J. Chem. Soc. A* **1967**, 148. (c) Yamasaki, A.; Aoyama, T.; Fujiwara, S.; Nakamura, K.; *Bull. Chem. Soc. Jpn.* **1978**, *51*, 643. (d) Weiss, R.; Verkade, J.G. *Inorg. Chem.* **1979**, *18*, 529. (e) Socol, S.M.; Lacelle, S.; Verkade, J.G. *Inorg. Chem.* **1987**, *26*, 3221. (f) Granger, P.; Elbayed, K.; Raya, J.; Kempgens, P.; Rosé, J. *J. Magn. Reson. A* **1995**, *117*, 179.
164. Gobetto, R.; Harris, R.K.; Apperley, D.C. *J. Magn. Reson.* **1992**, *96*, 119.
165. Kempgens, P.; Hirschinger, J.; Elbayed, K.; Raya, J.; Granger, P.; Rosé, J. *J. Phys. Chem.* **1996**, *100*, 2045.
166. Schrauzer, G.N.; Windgassen, R.J. *J. Am. Chem. Soc.* **1966**, *88*, 3738.
167. (a) Toscano, P.J.; Chiang, C.C.; Kistenmacher, T.J.; Marzilli, L.G. *Inorg. Chem.* **1981**, *20*, 1513. (b) Stewart, R.C.; Marzilli, L.G. *J. Am. Chem. Soc.* **1978**, *100*, 817. (c) Trogler, W.C.; Marzilli, L.G. *Inorg. Chem.* **1975**, *14*, 2942.
168. Trogler, W.C.; Stewart, R.C.; Epps, L.A.; Marzilli, L.G. *Inorg. Chem.* **1974**, *13*, 1564.
169. Moore, S.J.; Marzilli, L.G. *Inorg. Chem.* **1998**, In press.
170. (a) van Gorkom, L.C.M.; Hook, J.M.; Logan, M.B.; Hanna, J.V.; Wasylishen, R.E. *Magn. Reson. Chem.* **1995**, *33*, 791. (b) Mildner, T.; Ernst, H.; Freude, D. *Solid State Nucl. Magn. Reson.* **1995**, *5*, 269. (c) Bielecki, A.; Burum, D.P. *J. Magn. Reson. Ser. A* **1995**, *116*, 215. (d) van Moorsel, G.-J.M.P.; van Eck, E.R.H.; Grey, C.P. *J. Magn. Reson. Ser. A* **1995**, *113*, 159. (e) Haw, J.F.; Crook, R.A.; Crosby, R.C. *J. Magn. Reson.* **1986**, *66*, 551.
171. Wu, G.; Wasylishen, R.E. *J. Phys. Chem.* **1993**, *97*, 7863 and references therein.
172. Olivieri, A.C. *Solid State Nucl. Magn. Reson.* **1997**, *10*, 19.
173. Hodgkin, D.C.; Kamper, J.; Lindsey, J.; MacKay, M.; Pickworth, J.; Robertson, J.H.; Schoemaker, C.B.; White, J.G.; Prosen, R.J.; Trueblood, K.N. *Proc. Roy. Soc. (London) A* **1957**, *242*, 228.
174. Tavagnacco, C.; Balducci, G.; Costa, G.; Täschler, K.; von Philipsborn, W. *Helv. Chim. Acta* **1990**, *73*, 1469.

175. Ochiai, E.-I. *Bioinorganic Chemistry - An Introduction*; Allyn and Bacon, Inc.: Boston, 1977; pp. 311-356.
176. Marzilli, L.G.; Polson, S.M.; Hansen, L.; Moore, S.J.; Marzilli, P.A. *Inorg. Chem.* **1997**, *36*, 3854.
177. Samus, N.M.; Ablov, A.V. *Coord. Chem. Rev.* **1979**, *28*, 177.
178. Toscano, P.J.; Marzilli, L.G. *Progr. Inorg. Chem.* **1984**, *31*, 105.
179. (a) Hill, H.A.O.; Morallee, K.G. *J. Chem. Soc. (A)* **1969**, 554. (b) Gaus, P.L.; Crumbliss, A.L. *Inorg. Chem.* **1976**, *15*, 739. (c) Stewart, R.C.; Marzilli, L.G. *Inorg. Chem.* **1977**, *16*, 424. (d) Cartano, A.V.; Ingraham, L.L. *Bioinorg. Chem.* **1977**, *7*, 351. (e) Kargol, J.A.; Creceley, R.W.; Burmeister, J.L.; Toscano, P.J.; Marzilli, L.G. *Inorg. Chim. Acta* **1980**, *40*, 79. (f) Huet, J.; Gaudemer, A. *Org. Magn. Reson.* **1982**, *20*, 4. (g) Brown, K.L.; Satyanarayana, S. *J. Am. Chem. Soc.* **1992**, *114*, 5674. (h) Moore, S.J.; Iwamoto, M.; Marzilli, L.G. *Inorg. Chem.* **1998**, *37*, 1169.
180. Medek, A.; Frydman, V.; Frydman, L. *Proc. Natl. Acad. Sci. USA* **1997**, *94*, 14237.
181. (a) Bresciani-Pahor, N.; Randaccio, L.; Zangrando, E.; Summers, M.F.; Ramsden, J.D.; Marzilli, P.A.; Marzilli, L.G. *Organometallics*, **1985**, *4*, 2086. (b) Randaccio, L.; Bresciani-Pahor, N.; Orbell, J.D.; Calligaris, M. *Organometallics* **1985**, *4*, 469.
182. von Phillipsborn, W. *Pure Appl. Chem.* **1986**, *58*, 513.
183. Opella, S.J.; Frey, M.H.; Cross, T.A. *J. Am. Chem. Soc.* **1979**, *101*, 5856.
184. Groombridge, C.J.; Harris, R.K.; Packer, K.J.; Say, B.J.; Tanner, S.F. *J. Chem. Soc. Chem. Commun.* **1980**, 174.
185. Zumbulyadis, N.; Henrichs, P.M.; Young, R.H. *J. Chem. Phys.* **1981**, *75*, 1603.
186. Messiah, A. *Quantum Mechanics, Vol. 2*; John Wiley & Sons: New York, 1966; pp. 739-759.
187. Naito, A.; Ganapathy, S.; McDowell, C.A. *J. Magn. Reson.* **1982**, *48*, 367.
188. Hexem, J.G.; Frey, M.H.; Opella, S.J. *J. Chem. Phys.* **1982**, *77*, 3847.
189. For example, Naito, A.; Root, A.; McDowell, C.A. *J. Phys. Chem.* **1991**, *95*, 3578.
190. Eichele, K.; Wasylshen, R.E. *Solid State Nucl. Magn. Reson.* **1992**, *1*, 159.

191. Diesveld, J.W.; Menger, E.M.; Edzes, H.T.; Veeman, W.S. *J. Am. Chem. Soc.* **1980**, *102*, 7935.
192. Menger, E.M.; Veeman, W.S. *J. Magn. Reson.* **1982**, *46*, 257.
193. Eichele, K.; Lumsden, M.D.; Wasylishen, R.E. *J. Phys. Chem.* **1993**, *97*, 8909.
194. Wu, G.; Kroeker, S.; Wasylishen, R.E. *Inorg. Chem.* **1995**, *34*, 1595.
195. Davies, N.A.; Harris, R.K.; Olivieri, A.C. *Mol. Phys.* **1996**, *87*, 669.
196. Challoner, R.; Harris, R.K. *Solid State Nucl. Magn. Reson.* **1995**, *4*, 65.
197. Burford, N.; Cameron, T.S.; Clyburne, J.A.C.; Eichele, K.; Robertson, K.N.; Sereda, S.; Wasylishen, R.E.; Whitla, W.A. *Inorg. Chem.* **1996**, *35*, 5460.
198. Li, H.; Butler, I.S.; Gilson, D.F.R.; Harrod, J.F.; Morin, F.G. *J. Phys. Chem.* **1995**, *99*, 8490.
199. Eichele, K.; Wasylishen, R.E. *Inorg. Chem.* **1994**, *33*, 2766.
200. Nagasaka, B.; Takeda, S.; Nakamura, N. *Chem. Phys. Lett.* **1994**, *222*, 486.
201. Olivieri, A.C.; Elguero, J.; Sobrados, I.; Cabildo, P.; Claramunt, R.M. *J. Phys. Chem.* **1994**, *98*, 5207.
202. Eichele, K.; Wasylishen, R.E.; Grossert, J.S.; Olivieri, A.C. *J. Phys. Chem.* **1995**, *99*, 10110.
203. Alarcón, S.; Olivieri, A.C.; Carss, S.A.; Harris, R.K. *Magn. Reson. Chem.* **1995**, *33*, 603.
204. Aliev, A.E.; Harris, K.D.M.; Barrie, P.J.; Camus, S. *J. Chem. Soc. Faraday Trans.* **1994**, *90*, 3729.
205. Wu, G.; Lumsden, M.D.; Ossenkamp, G.C.; Eichele, K.; Wasylishen, R.E. *J. Phys. Chem.* **1995**, *99*, 15806.
206. Aliev, A.E.; Harris, K.D.M.; Apperley, D.C.; Harris, R.K.; Sünnetçöğü, M.M. *J. Chem. Soc. Faraday Trans.* **1993**, *89*, 3791.
207. Jonsen, P.; Olivieri, A.C.; Tanner, S.F. *Solid State Nucl. Magn. Reson.* **1996**, *7*, 121.
208. Rentsch, D.; Hany, R.; von Philipsborn, W. *Magn. Reson. Chem.* **1997**, *35*, 832.

209. Christendat, D.; Markwell, R.D.; Gilson, D.F.R.; Butler, I.S.; Cotton, J.D. *Inorg. Chem.* **1997**, *36*, 230.
210. Christendat, D.; Wharf, I.; Morin, F.G.; Butler, I.S.; Gilson, D.F.R. *J. Magn. Reson.* **1998**, *131*, 1.
211. Bowmaker, G.A.; Hanna, J.V.; Hart, R.D.; Healy, P.C.; White, A.H. *Aust. J. Chem.* **1994**, *47*, 25.
212. Asaro, F.; Camus, A.; Gobetto, R.; Olivieri, A.C.; Pellizer, G. *Solid State Nucl. Magn. Reson.* **1997**, *8*, 81.
213. Kroeker, S.; Hanna, J.V.; Wasylshen, R.E.; Ainscough, E.W.; Brodie, A.M. *J. Magn. Reson.* In press.
214. Gibson, V.C.; Gobetto, R.; Harris, R.K.; Langdale-Brown, C.; Siemeling, U. *J. Organomet. Chem.* **1994**, *479*, 207.
215. Hitchcock, P.B.; Lappert, M.F.; Lawless, G.A.; Royo, B. *J. Chem. Soc. Chem. Comm.* **1993**, 554.
216. Aime, S.; Botta, M.; Gobetto, R.; Hanson, B.E. *Inorg. Chem.* **1989**, *28*, 1196.
217. Harris, R.K. *Encyclopedia of Nuclear Magnetic Resonance*; Grant, D.M.; Harris, R.K., Eds.; John Wiley & Sons: Chichester, U.K., **1996**, pp.2909-2914.
218. McDowell, C.A. *Encyclopedia of Nuclear Magnetic Resonance*; Grant, D.M.; Harris, R.K., Eds.; John Wiley & Sons: Chichester, U.K., **1996**, pp. 2901-2908.
219. Olivieri, A.C.; Frydman, L.; Diaz, L.E. *J. Magn. Reson.* **1987**, *75*, 50.
220. Olivieri, A.C.; Frydman, L.; Grasselli, M.; Diaz, L. *Magn. Reson. Chem.* **1988**, *26*, 615.
221. Olivieri, A.C. *J. Magn. Reson.* **1989**, *81*, 201.
222. Olivieri, A.C. *J. Am. Chem. Soc.* **1992**, *114*, 5758.
223. Grondona, P.; Olivieri, A.C. *Concepts Magn. Reson.* **1993**, *5*, 319.
224. Apperley, D.C.; Haiping, B.; Harris, R.K. *Mol. Phys.* **1989**, *68*, 1277.
225. Alarcón, S.H.; Olivieri, A.C.; Harris, R.K. *Solid. State Nucl. Magn. Reson.* **1993**, *2*, 325.
226. Olivieri, A.C. *Magn. Reson. Chem.* **1996**, *34*, 365.

227. Goodfellow, R.J. *Multinuclear NMR*; Mason, J. Ed. Plenum Press: New York, 1987; pp. 521-561.
228. Bresciani-Pahor, N.; Calligaris, M.; Randaccio, L.; Marzilli, L.G. *Inorg. Chim. Acta* **1979**, *32*, 181
229. (a) Parish, R.V. *Progr. Inorg. Chem.* **1972**, *15*, 101. (b) Bancroft, G.M.; Garrod, R.E.B.; Maddock, A.G. *J. Chem. Soc. (A)* **1971**, 3165.
230. Sternheimer, R. *Phys. Rev.* **1951**, *84*, 244.
231. Bresciani-Pahor, N.; Calligaris, M.; Randaccio, L. *Inorg. Chim. Acta* **1980**, *39*, 173.
232. Brückner, S.; Randaccio, L. *J. Chem. Soc. Dalton Trans.* **1974**, 1017.
233. Jameson, C.J.; de Dios, A.; Jameson, A.K. *Chem. Phys. Lett.* **1990**, *167*, 575.
234. Nelson, J.H.; Takach, N.E.; Bresciani-Pahor, N.; Randaccio, L.; Zangrando, E. *Acta Cryst.* **1984**, *C40*, 742.
235. Appleton, T.G.; Clark, H.C.; Manzer, L.E. *Coord. Chem. Rev.* **1973**, *10*, 335.
236. Zumdahl, S.S.; Drago, R.S. *J. Am. Chem. Soc.* **1968**, *90*, 6669 and references therein.
237. Bigotto, A.; Zangrando, E.; Randaccio, L. *J. Chem. Soc. Dalton Trans.* **1976**, 96.
238. Bresciani-Pahor, N.; Randaccio, L.; Toscano, P.J.; Sandercock, A.C.; Marzilli, L.G. *J. Chem. Soc. Dalton Trans.* **1982**, 129.
239. Huang, Y.; Uhm, H.L.; Gilson, D.F.R.; Butler, I.S. *Inorg. Chem.* **1994**, *33*, 804.
240. Penner, G.H.; Wasylshen, R.E. *Can. J. Chem.* **1989**, *67*, 1909.
241. Bresciani-Pahor, N.; Calligaris, M.; Nardin, G.; Randaccio, L. *Gazz. Chim. Ital.* **1981**, *111*, 147.
242. Ramsey, N.F. *Phys. Rev.* **1953**, *91*, 303.
243. Pregosin, P.S.; Kunz, R.W. *<sup>31</sup>P and <sup>13</sup>C NMR of Transition Metal Complexes; in NMR Basic Principles and Progress*; Diehl, P.; Fluck, E.; Kosfeld, R., Eds.; Springer-Verlag: Berlin, 1979; vol. 16, pp. 1-153.
244. See for example, Buergi, H.B.; Kunz, R.W.; Pregosin, P.S. *Inorg. Chem.* **1980**, *19*, 3707 and references therein.

245. Power, W.P.; Wasylishen, R.E. *Inorg. Chem.* **1992**, *31*, 2176.
246. (a) Lumsden, M.D.; Wasylishen, R.E.; Britten, J.F. *J. Phys. Chem.* **1995**, *99*, 16602. (b) Power, W.P.; Lumsden, M.D.; Wasylishen, R.E. *J. Am. Chem. Soc.* **1991**, *113*, 8257. (c) Penner, G.H.; Power, W.P.; Wasylishen, R.E. *Can. J. Chem.* **1988**, *66*, 1821.
247. Pyykkö, P. *Chem. Rev.* **1988**, *88*, 563.
248. (a) Allen, F.H.; Pidcock, A. *J. Chem. Soc. A* **1968**, 2700. (b) Grim, S.O.; Keiter, R.L.; McFarlane, W. *Inorg. Chem.* **1967**, *6*, 1133. (c) Ahmad, N.; Aiscough, E.W.; James, T.A.; Robinson, S.D. *J. Chem. Soc. Dalton Trans.* **1973**, 1148.
249. (a) Grim, S.O.; Wheatland, D.A.; McFarlane, W. *J. Am. Chem. Soc.* **1967**, *89*, 5573. (b) Grim, S.O.; McAllister, P.R.; Singer, R.M. *J. Chem. Soc. Chem. Commun.* **1969**, 38.
250. (a) Asaro, F.; Garlatti, R.D.; Pellizer, G.; Tauzher, G. *Inorg. Chim. Acta* **1993**, *211*, 27. (b) Ludwig, M.; Öhrström, L.; Steinborn, D. *Magn. Reson. Chem.* **1995**, *33*, 984.
251. Jameson, C.J. *Multinuclear NMR*; Mason, J. Ed. Plenum Press: New York, 1987; pp. 89-131.
252. Suzuki, M.; Kubo, R. *Mol. Phys.* **1964**, *7*, 201.
253. Mlynárik, V. *Progr. NMR Spectrosc.* **1986**, *18*, 277.
254. (a) Farrar, T.C.; Becker, E.D. *Pulse and Fourier Transform NMR*; Academic Press, Inc.: New York, 1971. (b) Wasylishen, R.E. *Practical Spectroscopy Series*; Dybowski, C.; Lichter, R.L., Eds.; Marcel Dekker, Inc.: New York, 1987; vol.5, pp. 45-91. (c) Werbelow, L.G.; Allouche, A.; Pouzard, G. *J. Chem. Soc., Faraday Trans. 2* **1987**, *83*, 871. (d) Werbelow, L.G.; London, R.E. *J. Chem. Phys.* **1995**, *102*, 5181.
255. Torchia, D.A.; Szabo, A. *J. Magn. Reson.* **1982**, *49*, 107.
256. Kofod, P. *J. Magn. Reson.* **1996**, *119*, 219 and references therein.
257. Mason, J. *Encyclopedia of Nuclear Magnetic Resonance*; Grant, D.M.; Harris, R.K., Eds.; John Wiley & Sons: Chichester, U.K., **1996**, pp. 3222-3251.
258. (a) Lee, D.-K.; Ramamoorthy, A. *Chem. Phys. Lett.* **1998**, *286*, 398. (b) Lee, D.-K.; Ramamoorthy, A. *Chem. Phys. Lett.* **1998**, *286*, 403.

259. Laszlo, P. *Encyclopedia of Nuclear Magnetic Resonance*; Grant, D.M.; Harris, R.K., Eds.; John Wiley & Sons: Chichester, U.K., 1996, pp. 3858-3869.
260. Martin, G.J.; Martin, M.L.; Gouesnard, J.-P. <sup>15</sup>N-NMR Spectroscopy; in *NMR Basic Principles and Progress*; Diehl, P.; Fluck, E.; Kosfeld, R., Eds.; Springer-Verlag: Berlin, 1979; vol. 18, pp. 1-382.
261. Levy, G.C.; Lichter, R.L. *Nitrogen-15 Nuclear Magnetic Resonance Spectroscopy*; John Wiley & Sons: New York, 1979.
262. Witanowski, M.; Stefaniak, L.; Webb, G.A. *Ann. Rep. NMR Spectrosc.* **1993**, *25*, 1.
263. Yamasaki, A.; Miyakoshi, Y.; Fujita, M.; Yoshikawa, Y.; Yamatara, H. *J. Inorg. Nucl. Chem.* **1979**, *41*, 473.
264. (a) Bell, L.K.; Mingos, D.M.P.; Tew, D.G.; Larkworthy, L.F.; Sandell, B.; Povey, D.C.; Mason, J. *J. Chem. Soc. Chem. Commun.* **1983**, 125. (b) Bultitude, J.; Larkworthy, L.F.; Mason, J.; Povey, D.C.; Sandell, B. *Inorg. Chem.* **1984**, *23*, 3629.
265. Rentsch, G.H.; Kozminski, W.; von Philipsborn, W.; Asaro, F.; Pellizer, G. *Magn. Reson. Chem.* **1997**, *35*, 904.
266. Bose, K.S.; Abbott, E.H. *Inorg. Chem.* **1977**, *16*, 3190.
267. Wasylishen, R.E.; Curtis, R.D.; Eichele, K.; Lumsden, M.D.; Penner, G.H.; Power, W.P.; Wu, G. *Nuclear Magnetic Shieldings and Molecular Structure - NATO ASI Series*; Tossell, J.A., Ed.; Kluwer Academic Publishers: Dordrecht, The Netherlands, 1993; vol. 386, pp. 297-314.
268. Oas, T.G.; Hartzell, C.J.; McMahon, T.J.; Drobny, G.P.; Dahlquist, F.W. *J. Am. Chem. Soc.* **1987**, *109*, 5956.
269. Harris, R.K.; Packer, K.J.; Thayer, A.M. *J. Magn. Reson.* **1985**, *62*, 284.
270. Zilm, K.W.; Grant, D.M. *J. Am. Chem. Soc.* **1981**, *103*, 2913.
271. VanderHart, D.L.; Gutowsky, H.S. *J. Chem. Phys.* **1968**, *49*, 261.
272. Some other papers from our research group on the dipolar chemical shift method: (a) Eichele, K.; Wasylishen, R.E. *J. Magn. Reson. A* **1994**, *106*, 46. (b) Power, W.P.; Wasylishen, R.E.; Curtis, R.D. *Can. J. Chem.* **1989**, *67*, 454. (c) Wasylishen, R.E.; Penner, G.H.; Power, W.P.; Curtis, R.D. *J. Am. Chem. Soc.* **1989**, *111*, 6082.

273. Mason, J. *Nuclear Magnetic Shieldings and Molecular Structure - NATO ASI Series*; Tossell, J.A., Ed.; Kluwer Academic Publishers: Dordrecht, The Netherlands, 1993; vol. 386, pp. 449-471.
274. Mason, J.; Mingos, D.M.P.; Schaefer, J.; Sherman, D.; Stejskal, E.O. *J. Chem. Soc. Chem. Commun.* **1985**, 444.
275. Santos, R.A.; Chien, W.-J.; Harbison, G.S.; McCurry, J.D.; Roberts, J.E. *J. Magn. Reson.* **1989**, *84*, 357.
276. Groombridge, C.J.; Larkworthy, L.F.; Marécaux, A.; Povey, D.C.; Smith, G.W.; Mason, J. *J. Chem. Soc. Dalton Trans.* **1992**, 3125.
277. Groombridge, C.J.; Larkworthy, L.F.; Mason, J. *Inorg. Chem.* **1993**, *32*, 379.
278. Strohmeier, M.; Orendt, A.M.; Facelli, J.C.; Solum, M.S.; Pugmire, R.J.; Parry, R.W.; Grant, D.M. *J. Am. Chem. Soc.* **1997**, *119*, 7114.
279. Salzmann, R.; Wojdelski, M.; McMahan, M.; Havlin, R.H.; Oldfield, E. *J. Am. Chem. Soc.* **1998**, *120*, 1349.
280. Solans, X.; Font-Bardia, M.; López, C.; Alvarez, S. *Acta Cryst.* **1996**, *C52*, 63.
281. Jameson, D.L.; Grzybowski, J.J.; Hammels, D.E.; Castellano, R.K.; Hoke, M.E.; Freed, K.; Basquill, S.; Mendel, A.; Shoemaker, W.J. *J. Chem. Ed.* **1998**, *75*, 447 and references therein.
282. Hayashi, S.; Hayamizu, K. *Bull. Chem. Soc. Jpn.* **1991**, *64*, 688.
283. López, C.; Alvarez, S.; Aguiló, M.; Solans, X.; Font-Altaba, M. *Inorg. Chim. Acta* **1987**, *127*, 153.
284. Lister, D.G.; Tyler, J.K. *J. Chem. Soc. Chem. Commun.* **1966**, 152.
285. Bak, B.; Hansen-Nygaard, L.; Rastrup-Andersen, J. *J. Mol. Spectrosc.* **1958**, *2*, 361.
286. (a) Chesnut, D.B.; Moore, K.D. *J. Comput. Chem.* **1989**, *10*, 648. (b) Chesnut, D.B.; Rusiloski, B.E.; Moore, K.D.; Egolf, D.A. *J. Comput. Chem.* **1993**, *14*, 1364.
287. Jameson, C.J.; Jameson, A.K.; Oppusunggu, D.; Wille, S.; Burrell, P.M.; Mason, J. *J. Chem. Phys.* **1981**, *74*, 81.
288. (a) Casabella, P.A. *J. Chem. Phys.* **1964**, *41*, 3793. (b) VanderHart, D.L.; Gutowsky, H.S.; Farrar, T.C. *J. Am. Chem. Soc.* **1967**, *89*, 5056.
289. Schweitzer, D.; Speiss, H.W. *J. Magn. Reson.* **1974**, *15*, 529.

290. Solum, M.S.; Altmann, K.L.; Strohmeier, M.; Berges, D.A.; Zhang, Y.; Facelli, J.C.; Pugmire, R.J.; Grant, D.M. *J. Am. Chem. Soc.* **1997**, *119*, 9804.
291. Lichter, R.L.; Roberts, J.D. *Org. Magn. Reson.* **1974**, *6*, 636.
292. Dailey, B.P.; Townes, C.H. *J. Chem. Phys.* **1955**, *23*, 118.
293. Kunz, R.W. *Helv. Chim. Acta* **1980**, *63*, 2054.
294. Geremia, S.; Dreos, R.; Randaccio, L.; Tazzer, G.; Antolini, L. *Inorg. Chim. Acta* **1994**, *216*, 125.
295. Bouman, T.D.; Hansen, A.E. *Chem. Phys. Lett.* **1992**, *197*, 59.
296. Schindler, M. *J. Am. Chem. Soc.* **1987**, *109*, 5950.
297. (a) Jameson, C.J.; de Dios, A.C.; Jameson, A.K. *J. Chem. Phys.* **1991**, *95*, 1069. (b) Kukolich, S.G. *J. Am. Chem. Soc.* **1975**, *97*, 5704.
298. Price, R. *The Chemistry of Synthetic Dyes*; Venkataraman, K., Ed.; Academic Press: New York, 1970, Vol. III, Chapt. VII.
299. Lyčka, A.; Rys, P.; Skrabal, P. *Magn. Reson. Chem.* **1998**, *36*, 279.
300. Massiot, D.; Farman, I.; Gautier, N.; Trumeau, D.; Trokner, A.; Coutures, J.P. *Solid State Nucl Magn. Reson.* **1995**, *4*, 241.
301. Fredoueil, F.; Massiot, D.; Poojary, D.; Bujoli-Doeuff, M.; Clearfield, A.; Bujoli, B. *J. Chem. Soc. Chem. Commun.* **1998**, 175.
302. Vosegaard, T.; Massiot, D.; Gautier, N.; Jakobsen, H.J. *Inorg. Chem.* **1997**, *36*, 2446.
303. Dymock, K.; Palenik, G.J. *Acta. Cryst.* **1974**, *B30*, 1364.
304. Dechter, J.J.; Henriksson, U.; Kowalewski, J.; Nilsson, A.-C. *J. Magn. Reson.* **1982**, *48*, 503.
305. (a) Stephens, A.H.H.; Green, M.L.H. *Adv. Inorg. Chem.* **1997**, *44*, 1. (b) Fagan, P.J.; Calabrese, J.C.; Malone, B. *Acc. Chem. Res.* **1992**, *25*, 134.
306. Chernega, A.N.; Green, M.L.H.; Haggitt, J.; Stephens, A.H.H. *J. Chem. Soc. Dalton Trans.* **1998**, 755.
307. La Monica, G.; Navazio, G.; Sandrini, P.; Cenini, S. *J. Organomet. Chem.* **1971**, *31*, 89.

308. For example, (a) He, H.; Barras, J.; Foulkes, J.; Klinowski, J. *J. Phys. Chem. B* **1997**, *101*, 117. (b) Saunders, M.; Jiménez-Vázquez, H.A.; Khong, A. *J. Phys. Chem.* **1996**, *100*, 15968. (c) Fowler, P.W.; Lazzeretti, P.; Malagoli, M.; Zanasi, R. *J. Phys. Chem.* **1991**, *95*, 6404. (d) Yannoni, C.S.; Bernier, P.P.; Bethune, D.S.; Meijer, G.; Salem, J.R. *J. Am. Chem. Soc.* **1991**, *113*, 3190.
309. Schaefer, T. *Private communication*, 1998.
310. Kunwar, A.C.; Turner, G.L.; Oldfield, E. *J. Magn. Reson.* **1986**, *69*, 124.